EFFECTS OF LIGHTWEIGHT FLY ASH AGGREGATE PROPERTIES ON THE PERFORMANCE OF LIGHTWEIGHT CONCRETES

by

Niyazi Uğur Koçkal

B.S., Civil Engineering, Süleyman Demirel University, 1999

M.S., Civil Engineering, Akdeniz University, 2002

Submitted to the Institute for Graduate Studies in
Science and Engineering in partial fulfillment of
the requirements for the degree of
Doctor of Philosophy

Graduate Program in Civil Engineering

Boğaziçi University

2008

EFFECTS OF LIGHTWEIGHT FLY ASH AGGREGATE PROPERTIES ON THE PERFORMANCE OF LIGHTWEIGHT CONCRETES

APPROVED BY:

Prof. Turan Özturan …….
(Thesis Supervisor)

Prof. Gökhan Baykal ……

Prof. Cengiz Karakoç ……

Prof. Hulusi Özkul …….

Prof. Mehmet Ali Taşdemir ……..

DATE OF APPROVAL.....

ACKNOWLEDGEMENTS

I would like to thank to my thesis supervisor, Prof. Turan Ozturan, for his valuable guidance, suggestions and continuous support throughout my graduate study. I greatly appreciate all the support that he has given on this thesis.

I am grateful to the members of the supervisory committee, Prof. Gökhan Baykal, Prof. Cengiz Karakoç, Prof. Hulusi Özkul and Prof. Mehmet Ali Taşdemir for their help and suggestions.

I would also like to thank to my friends Osman, Bülent and Selçuk and other assistants and technicians for their support.

My special appreciation goes to my parents whose love and care have brought me to this level. Their substantial encouragements and support have helped me to succeed in finishing my program.

ABSTRACT

EFFECTS OF LIGHTWEIGHT FLY ASH AGGREGATE PROPERTIES ON THE PERFORMANCE OF LIGHTWEIGHT CONCRETES

Only a very small content of ash is being used for the construction applications. As large quantities of the fly ash remain unutilized in most countries of the world, the manufacture of light-weight fly ash aggregates is an appropriate step to utilize a large quantity of fly ash. Structural lightweight concrete mixtures can be designed to obtain similar mechanical and durability performance as normalweight concrete.

The study is divided into two parts. In the first part of the study, the characteristics of different lightweight fly ash aggregates were investigated. Specific gravity, water absorption, porosity, thermal behaviour, crushing strength and microstructural changes of these aggregates were determined. The properties and microstructure of aggregates were modified by different sintering agents and heat treatments. The strength and specific gravity of all aggregates decreased with increasing the binder content (disregarding binder type) at high temperature. Aggregates with low water absorption and high strength can be attributed to the discontinuous porosity, dense structure and small pore size. In the second part of the study, the influence of properties of lightweight aggregate types on the behaviour of concrete mixtures were discussed. The compressive strength, modulus of elasticity, splitting tensile strength tests, water impermeability test, rapid chloride permeability test, accelerated corrosion studies and rapid freeze/thaw cycling test were performed on lightweight and normalweight concretes. The results of this study revealed the possibility of manufacturing high-strength air-entrained lightweight aggregate concretes using sintered and cold-bonded fly ash aggregates. The use of lightweight aggregates instead of normalweight aggregates in concrete production decreased the strength as expected but improved the resistance to permeability and freeze-thaw of the concretes.

ÖZET

HAFİF UÇUCU KÜL AGREGA ÖZELLİKLERİNİN HAFİF BETON PERFORMANSINA ETKİLERİ

Uçucu külün çok az bir miktarı inşaat sektöründe kullanılmaktadır. Çoğu ülkede çok yüksek miktarlarda uçucu külün kullanılamadığından, bunların hafif uçucu kül agregası olarak üretilmesi tüketimin artmasında önemli bir adım olacaktır. Yapısal hafif betonlar normal betonların benzer mekanik ve durabilite özelliklerini elde edebilecek biçimde tasarlanabilmektedir.

Çalışma iki bölümden oluşmaktadır. Birinci bölümde, farklı yöntemlerle üretilen agregaların özellikleri incelenmiştir. Bu agregaların özgül ağırlıkları, su emme ve poroziteleri, sıcaklık etkisinde davranışları, dayanımları ve mikroyapı değişimleri tayin edilmiştir. Agregaların özellikleri ve mikroyapıları farklı bağlayıcılar ve sıcaklıklarla değişmiştir. Bütün agregaların dayanım ve özgül ağırlıkları yüksek sıcaklıkta bağlayıcı miktarının artmasıyla azalmıştır. Agregaların düşük su emme ve yüksek dayanımı, boşlukların küçük ve süreksiz olmasının yanında yoğun yapısından kaynaklanmaktadır. Çalışmanın ikinci bölümünde, hafif uçucu kül agrega özelliklerinin beton davranışına etkileri araştırılmıştır. Normal ağırlıklı betonun ve hafif betonların üzerinde basınç dayanımı, elastisite modülü, yarmada çekme dayanımı, basınçlı su geçirimlilik, hızlı klor geçirimliliği, hızlandırılmış korozyon ve hızlı donma-çözülme çevrimi deneyleri yapılmıştır. Deney sonuçları, soğuk bağlanmış ve sinterlenmiş uçucu kül agregalarıyla yüksek dayanımlı hava sürüklenmiş hafif betonların üretilmesinin mümkün olabileceğini ortaya koymuştur. Betonda hafif uçucu kül agregalarının normal ağırlıklı agregalarla yer değiştirmeleri, beklenildiği gibi, dayanımı bir miktar düşürmelerine rağmen, betonların geçirimliliğe ve donma-çözülme çevrimine dirençlerini arttırmıştırlardır.

TABLE OF CONTENTS

LIST OF FIGURES

LIST OF TABLES

LIST OF SYMBOLS/ABBREVIATIONS

a	coefficient
A	Air content (percentage of voids) in the concrete
A	Mass of oven dry specimen, g
b	Coefficient
B	Mass of pycnometer filled with water, to calibration mark, g
c	binder content
C	Mass of pycnometer filled with specimen and water to calibration mark, g
d	Pore width
d	Depth of water penetration in mm
D	Density (unit weight) of concrete, kg/m^3
D	Durability factor of the test specimen
E	Chord modulus of elasticity, MPa
Ec	Calculated equilibrium density
f_c	Cylinder compressive strength
G	Mass of the aggregate plus the measure, kg,
k	Coefficient
l	Length, mm
M	Bulk density of the aggregate, kg/m^3
M	Total mass of all materials batched, kg
m_d	Mass of oven-dry test sample in air, g,
m_s	Mass of saturated-surface-dry test sample in air, g,
m_w	Apparent mass of saturated test sample in water, g.
M_1	Mass of the test specimen (in g)
M_2	Mass of the material passing the 2.36 mm test sieve (in g).
M_c	Mass of the measure filled with concrete, kg
M_m	Mass of the measure, kg
Mdf	Mass of dry fine aggregate in batch, kg
Mdc	Mass of dry coarse aggregate in batch, kg
Mct	Mass of cement in batch, kg

n	Fundamental transverse frequency at 0 cycles of freezing and thawing
n_1	Fundamental transverse frequency after c cycles of freezing and thawing
Oc	Calculated oven-dry density, kg/m^3
P	Fracture load
P	Net pressure across the mercury meniscus at the time of the cumulative intrusion measurement,
P_c	Relative dynamic modulus of elasticity, after c cycles of freezing and thawing, percent
P_d	relative dynamic modulus of elasticity at N cycles, %
P_l	Maximum applied load indicated by the testing machine, N
Q	Charge passed (coulombs)
S	Mass of saturated surface-dry specimen, g
SS	Sum of squares
t	Sintering temperature
T	Mass of the measure, kg
T_i	Target value of ith response
v	Volume of permeable pore space in %
V	Volume of concrete produced by the batch m^3
V_m	Volume of the measure, m^3
w	Water absorption in %
W	Density of water, 998 kg/m^3
w/c	water-cement ratio
w_c	Air dry density of concrete
x	Factor
X	Distance between loading points
y	Response function
ε	Error
ε_2	Longitudinal strain produced by stres σ_2
γ	Density of concrete

γ_t	Surface tension
μ	Specific gravity
σ	Compressive strength of concrete
σ_a	Crushing strength of aggregate
σ_t	Splitting tensile strength in MPa
σ_1	Stress corresponding to a longitudinal strain, ε_1, of 50 millionths, MPa
σ_2	Stress corresponding to 40 % of ultimate load
δ	Aggregate crushing value %
θ	Contact angle between mercury and the pore wall

ACI	American Concrete Institute
ACV	Aggregate crushing value
ANOVA	Analysis of variance
ASTM	American Society for Testing and Materials
BS	British Standard
DF	Degree of freedom
DTA/TGA	Differential thermal analysis-Thermal gravimetric analysis
ITZ	Interfacial transition zone
LVDT	Linear variable differential transformers
MS	Mean squares
RSM	Response surface methodology
SEM	Scanning electron microscobe
TS	Turkish Standard
XRD	X-Ray Diffraction

1. INTRODUCTION

The large amounts of fly ash are generated from thermal coal-fired power plants and some smaller proportions are used for a variety of purposes. Fly ash consists essentially of small spherical particles of aluminosilicate glass which is produced on combustion of pulverized coal in thermal power plants. Large quantity of fly ash is still disposed of in landfills and storage lagoons. Fly ash leads to problems of disposal as well as environmental damage by causing air and water pollution on a large scale. Approximately 15 million tonnes of fly ash is being produced annually in Turkey. By the year 2020, ash production is expected to reach 50 million tons per year. Only a very small content of ash is being used for the construction applications. As large quantities of the fly ash remain unutilized in most countries of the world, the manufacture of light-weight fly ash aggregates is an appropriate step to utilize a large quantity of fly ash. Also, normalweight natural coarse and fine aggregates supplied from natural rock, river beds and coastal regions are used to manufacture concretes with density of approximately 2400 kg/m^3. The way of providing materials for normalweight concrete damages environment. Recently, the use of mineral admixtures such as fly ash and silica fume has remarkably increased in different applications due to an increase in environmental awareness.

Dynamic loads such as earthquake forces which affect structures are proportional to their mass, therefore decreasing selfweight of constructions and cross section of structural elements is necessary to ensure its resistance to earthquake disaster. Structural lightweight concrete mixtures can be designed to obtain similar mechanical and durability performance as normalweight concrete. Lighter and stronger concrete decreases self weight of the construction, the quantity of material needed, the energy used in transportation and handling (permit larger precast units to be handled), as well as foundation size and construction costs. Concrete with lower density also has good thermal insulation. Thinner structural elements lead to more space for occupancy. Lightweight concrete can also increase the span length for structures such as bridges.

Durability carries vital significance for structures, besides the strength/weight ratio. The permeability of concrete determines its long-term durability. The permeable concrete

is vulnerable and sensitive to water and harmful substances it contains and this phenomenon causes deterioration of concrete and reinforcement. The interfacial zone between aggregate and the cement matrix influences the properties of concrete such as strength, stiffness and durability. However, the resistance of lightweight fly ash concretes to permeability and freeze-thaw is still unclear.

Lightweight aggregates have a particle density of less than 2.0 g/m^3 or a dry loose bulk density of less than 1.1 g/cm^3, as defined in ASTM specification C330. Normal weight aggregates from gravel, sand, and crushed stone, for example, generally have bulk specific gravities of from about 2.4 to about 2.9 (both oven dry and saturated surface dry), and bulk densities of up to about 1.7 g/cm^3 [1]. High quality LWAs have a strong but low density porous sintered ceramic core of uniform structural strength and a dense, continuous, relatively impermeable surface layer to inhibit water absorption. They are physically stable, durable, and environmentally inert. LWAs should also be nearly spherical, to improve concrete properties and provide good adherence to concrete paste.

While LWA concrete may be 20-30% lighter than conventional concrete, it may be just as strong [1]. Even when it is not as strong as conventional concrete, the LWA concrete may have reduced structural dead loads enabling the use of longer spans, narrower cross-sections, and reduced reinforcement in structures. The lower weight of the LWA concrete facilitates handling and reduces transport, equipment, and manpower costs. LWA concrete may be particularly useful in construction slabs in high rise buildings and in concrete arch bridges, for example. LWA concrete may also have improved insulating properties, freeze-thaw performance, fire resistance, and sound reduction. LWAs can also be used in the construction of other structures, in highways, and as soil fillers.

As these results indicate, when these lightweight aggregates will be used as aggregates for concretes, we can expect not only the reduction of self-weight and other positive effects of concretes but also the protection of environmental pollution and the recycling of waste resources.

Taking into consideration all the above factors, durable high-strength air-entrained lightweight fly ash concrete can be an attractive construction material which possesses

required properties for structural materials used in the applications mentioned, however the available literature from this field is insufficient and it is clear that it is difficult to find published papers related with the properties of high-strength LWC with sintered and cold bonded fly ash aggregates.

The objective of the investigation was to study the characteristics and mineralogy of the lightweight fly ash aggregates produced by different binders and temperature treatments and determine their effects on concrete performance (strength and durability).

At present, little is known about the effects of the chemical composition of Çatalağzı fly ash on the optimum sintering conditions and the properties of sintered products. Therefore, the present study was also undertaken to search thoroughly into this subject. Çatalağzı fly ash was also utilized in other studies for other purposes and it is noted that its chemical properties does not change so much. Also, it is notable that Çatalağzı fly ash is the one which has Class F type properties specified in ASTM C 618 in Turkey. Çatalağzı fly ash was tested and the sintering process of this material was aimed at manufacturing sintered products for use as concrete aggregates. Addition of different binders was attempted to improve the chemical and mechanical characteristics of sintered products.

The study is divided into two parts; first one is investigating the lightweight fly ash aggregate properties, second one is about the effects of aggregate properties on the lightweight agregate concrete performance.

In the first part of the study, the characteristics of lightweight fly ash aggregates (LWA) with various binders produced by different heat treatments were investigated. The different amounts of binders were mixed with fly ash and put into the pelletization disc. Bentonite (B) and glass powder (G) were added as sintering agents at 5 % and 10 %, individually, by weight of fly ash (FA). Fly ash without a binder and fly ash with the combination of these two binders (B 7,5 %+G 7,5 %) were also prepared. Additionally, a mixture of fly ash and 10% portland cement as replacement of fly ash, by weight, was prepared for cold-bonding process. Irregular particles were obtained when 15 % bentonite was added into the fly ash mixture. Also, pelletizing fly ash with 15 % glass powder resulted in particles with larger diameter. For these reasons, the upper limits of contents for

both bentonite and glass powder were selected as 10 %. After pelletization, fly ash-cement mixture aggregates were put in plastic bags and maintained in a curing room at 25 ^{o}C temperature and 70 % R.H. for cold-bonding. The other pellets were first put in a furnace to be dried at 110 °C, drying was provided because sintering wet pellets in a kiln may result in cracking and exploding of the pellets due to rapid temperature changes and then sintered for 1 hour at three different temperatures (1100, 1150 and 1200 °C) with a heating rate of 6.7 ^{o}C/ min. Then, the aggregates were left in the furnace to cool in a slow rate. In trial production treatments, when fly ash lightweight pellets were sintered below 1100 ^{o}C, the aggregates contained loosely bounded particles and weak matrix. Therefore, a temperature of 1100 ^{o}C was chosen as lower sintering limit. Both fully densification of only fly ash aggregates and bloating of aggregates with binders were observed at the temperature of 1200 ^{o}C. Thus, 1200 ^{o}C was the upper sintering limit. The modification of properties and microstructure of aggregates by different binders and heat treatments was observed. Specific gravity, porosity (water absorption for open porosity, mercury intrusion porosimetry (MIP) for total and closed porosity and for critical pore diameter and pore size distribution), crushing strength, thermal behaviour (differential thermal analysis (DTA) and thermal gravimetric analysis (TGA)) and microstructural changes (X-Ray diffraction (XRD) analysis for crystal structure and scanning electron microscope (SEM) for morphology to explain the reason of the results) of these aggregates were determined.

This study also aimed to employ Response Surface Methodology (RSM) to relate the aggregate manufacturing input parameters (temperature, agent content and agent type) to the three responses (specific gravity, porosity and strength) using Design Expert software. Two different designs were applied: D-Optimal Design and Historical Data Design .The main challenge was how to choose the process input parameters that would produce a high strength lightweight concrete. The aim was to study the parameters which had significant effect on aggregate characteristics and to find the optimal production combination that would maximize both the porosity and strength while keeping the water absorption and specific gravity minimum. The selected aggregate types with the highest desirability values were used in concrete productions.

In the second phase of the study, the influence of aggregates on the behaviour of concrete mixtures were discussed. Lightweight concrete can be produced with a

combination of fine and coarse lightweight aggregate or coarse lightweight aggregate and normalweight fine aggregate. In this study, coarse lightweight aggregates were fully replaced with normalweight aggregate in concretes. The performance characteristics of the lightweight concretes and the normalweight concrete were investigated through compressive strength, modulus of elasticity, and splitting tensile strength representing the mechanical behavior; through water permeability and rapid chloride permeability representing the transport properties and through accelerated corrosion of embedded rebars and rapid freeze/thaw cycling representing the durability of concrete. In order to investigate the aggregate-cement matrix interfacial transition zone (ITZ), SEM observations were performed.

Regression and graphical analysis of the data obtained for concrete properties were also performed. Analysis of variance (ANOVA) is a useful technique for analyzing experimental data. Thus, a software TableCurve 3D V4.0 was used for analyzing hardened concrete properties. The software offers a large number of graphical and numerical tools to enable the user to choose the best equation for particular needs. The validity of predicted values of different models specified by standards and literature, derived in this study and suggested by software was compared and discussed.

2. LITERATURE SURVEY

The lightweight aggregates have been manufactured in this study by making use of fly ash, bentonite, glass powder and portland cement in different percentages.

2.1. Fly Ash

Fly ash is a byproduct of coal-fired electric generating plants. The coal is pulverized and blown into burning chambers for immediate combustion. Heavier ash particles (bottom ash or slag) fall to the bottom of the burning chamber and the lighter ash particles (fly ash) fly out with the exhaust gas, thus the term fly ash. Before leaving the stack, these fly ash particles are removed and collected by electrostatic precipitators, bag houses or other methods.

Fly ash is a pozzolan, meaning it is a siliceous and aluminous material, that in the presence of moisture, will combine with the lime liberated during the hydration of cement to form cementitious materials. In other words, fly ash is a siliceous or a siliceous and aluminous material that, in the presence of water, will combine with an activator (lime, Portland cement or kiln dust) to produce a cementitous material.

Fly ash particles are mostly spherical in shape and range from less than 1 μm to 100 μm with a specific surface area, typically between 250 and 600 m^2/kg [2]. Physical properties of fly ash mainly depend on the type of coal burned and the burning conditions.

Fly ash contains valuable oxide resources such as SiO_2, Al_2O_3, CaO, Fe_2O_3, and other oxides [3]. These oxides have been mainly considered as a low cost material resource for the ceramic industry. Moreover, fly ash is presented as a fine dust so it can be directly incorporated into ceramic pastes, with almost no pre-treatment. Therefore, coal fly ash is a good candidate for the ceramic industry as a raw material resource.

ASTM C 618 defines two major classes of fly ash, on the basis of their chemical composition, Class F and Class C. Class F FA, which comprises siliceous and sometimes

aluminous material, is normally produced from burning anthracite or bituminous coal and has little or no cementitious value. Class C FA, which is normally produced from the burning of subbituminous coal and lignite, usually contains significant amount of calcium hydroxide (CaOH) or lime (CaO). Class C FA has some cementitious properties. The majority of PFA produced is currently disposed in landfills at a great cost and risk of leakage of heavy metals that could contaminate underground aquifers.

Class F: Fly ash is normally produced from burning anthracite or bituminous coal. It is known like fly ash with low content CaO. This class of fly ash has pozzolanic properties.

Class C: Fly ash is normally produced from lignite or subbituminous coal. Class C is known like fly ash with high content CaO. This class of fly ash, in addition to having pozzolanic properties, also has some cementitious properties.

$$\text{Class F has } SiO_2 + Al_2O_3 + Fe_2O_3 > 70\% \quad (2.1)$$

$$\text{Class C has } SiO_2 + Al_2O_3 + Fe_2O_3 > 50\% \quad (2.2)$$

For the establishment of model of fly ash and Portland cement mixture hydration, it is important to point out that the pozzolanic reactions, which are primary (the most important) reactions of fly ash in cement (eq. 1-3) in respect to the Portland cement hydration reaction, are much slower reactions and occur in a noticeable extent only after one or two weeks [4].

$$2SiO_2 + 3Ca(OH)_2 = 3CaO.2SiO_2 \,.\, 3H_2O(C_3S_2H_3) \quad (2.3)$$

$$Al_2O3 + CaSO4.2H_2O + 3Ca(OH)_2 + 7H_2O = 4CaO.Al_2O_3.SO_3 \,.12H_2O\ (C_4ASH_{12}) \quad (2.4)$$

$$Al_2O_3 + 4Ca(OH)_2 + 9H_2O = 4\ CaO.Al_2O_3 \,.13H_2O(C_4AH_{13}) \quad (2.5)$$

The entire Portland cement and fly ash mixture hydration process can be divided into several phases, depending on the time segment of the process. However, there is a difference in the hydration process of the cement mixtures depending on the content of CaO in the fly ash. If the content of CaO is less than 10% this fly ash is treated as the one

with a low content of CaO (FAL) with significant pozzolanic characteristics. Ashes with a high CaO content may have cement characteristics if CaO content is higher than 20%, FAH, but if the presence is within 10 – 20%, then we talk about cement and pozzolanic materials (FAM) (FA with a middle content of CaO). Pozzolanic materials require the presence of $Ca(OH)_2$ in order to form a solid product, while cement materials contain sufficient quantities of CaO and can present only hydraulic activity. Usually, the content of CaO in ash is not sufficient for the reaction with the total quantity of pozzolanic components, and thus it has a pozzolanic activity (pozzolanic and cement materials).

Fly ash mineralogy varies greatly from one sample to another depending on the source of the coal or municipal solid waste and the combustion conditions. Likewise, mineralogy of the sintered bodies varies depending on the raw materials used. In general the mineral phases present in the fly ash are quartz (SiO_2), mullite ($3Al_2O_3.2SiO_2$), plagioclase ($Na,Ca(Si,Al)4O_8$), gehlenite ($Ca_2Al[AlSiO_7]$), anhydrite ($CaSO_4$), hematite (Fe_2O_3), halite (NaCl), sylvite (KCl), and calcite ($CaCO_3$). After sintering, some of these phases remain the same, some are changed in their amount, and some new phases are formed. For example, sintering of lignite coal fly ash reduced the amount of glass, quartz, gehlenite, and anhydrite, but increased the formation of anorthite ($CaAl_2Si_2O_8$), mullite, hematite, and cristobalite (SiO_2). Mollah et al. studied the effect of temperature on the mineralogy and microstructure of sintered lignite fly ash. They found that formation of cristobalite was enhanced by increasing the sintering temperature, along with the formation of hematite. Other XRD studies showed reduction in quartz amount and formation of cristobalite, and kyanite ($Al_2(SiO_4)O$).

Coal fly ash has many uses including as a cement additive, in masonry blocks, as a concrete admixture, as a material in lightweight alloys, as a concrete aggregate, in flowable fill materials, in roadway/runway construction, in structural fill materials, as roofing granules, and in grouting.

2.2. Bentonite

Due to its sorptive and catalytic properties, bentonite is widely used in a variety of industrial applications [5]. The clay is utilized as a pesticide carrier, an animal waste

adsorbent, a catalyst and catalyst support, and a decolorizing agent in oil refining, and in the pharmaceutical industries. It is well known that bentonites in their natural state have limited sorbing capacity. This ability is greatly enhanced by treatment with strong acids. When bentonites are acid-activated by hot mineral acid solutions, hydrogen ions attack the aluminosilicate layers via the interlayer region. This process alters the structure, chemical composition, and physical properties of the clay while increasing its adsorption capacity.

Two conditions necessary for bloating of clay for the production of lightweight aggregates are:

- The clayey material must produce a high temperature glassy phase with sufficient viscosity to trap gases,
- Some substance such as a carbonate must be present in the clayey material that will liberate a gas at a temperature at which a glassy phase forms.

Riley proposed a composition diagram of the major oxides (SiO_2, Al_2O_3, and fluxing oxides) showing the area in which the clays fire to a mass viscous enough to ensure good bloating [6].

Clay is a cheap and appropriate binder to impart cohesive strength to the pelletized nodules [7]. Sintered fly ash light-weight aggregates can be produced by mixing fly ash with clay and then by nodulizing it in a pelletizer with proportionate quantity of water.

Bentonite is a clayey material consisting mainly of montmorillonite. Montomorillonite has one exceptional property, it can take up water into the interlayer space. This is connected with the typical swelling ability of bentonite, which is important for balling because it enhances the cohesion of particles in the ball and the ball strength depends on cohesion of particles [8, 9].

2.3. Glass Powder

Over the last few years considerable progress has been made in the development of new building materials from waste glass [10]. There are innumerable environmental

reasons why sustained efforts should be made to reduce the amount of glass in the solid waste stream. Unlike other forms of waste, such as paper and organic constituents of garbage, it does not decompose when dumped on the land and constitutes a high proportion of incinerator residue.

Glass is produced in many forms, including packaging or container glass (bottles and jars), flat glass (windows and windscreens), bulb glass (light globes) and cathode ray tube glass (TV screens, monitors, etc.), all of which have a limited life in the form they are produced and need to be reused/recycled to avoid environmental problems that would be created if they were to be stockpiled or sent to landfill [11]. Postconsumer glass containers have traditionally been disposed of either in domestic refuse, which ends up in landfill, collected in designated collection spots for reuse/recycling, or collected from kerbside and then transported to collection sites. The major aim of environmental authorities is to reduce, as far as possible, the disposal of postconsumer glass in landfill and diversion to economically viable glass product streams.

Glass is a unique inert material that could be recycled many times without changing its chemical properties. In other words, bottles can be crushed into cullet then melted and made into new bottles without significant changes to the glass properties. Most of the glass produced is in the form of containers, and the bulk of what is collected postconsumer is again used for making containers. The efficiency of this process depends on the method of collecting and sorting glass of different colours. If different colour glass (clear, green and amber) could be separated, then they could be used for manufacturing similar colour glass containers. However, when the glass colours get mixed, they become unsuitable for use as containers and are then used for other purposes or sent to landfill. Reindl reported the many noncontainer uses of glass cullet, which included road construction aggregate, asphalt paving, concrete aggregate, building applications (glass tiles and bricks, wall panels, etc.), fibre glass insulation, glass fibre, abrasive, art glass, agricultural fertiliser, landscaping, reflective beads, tableware, hydraulic cement, among other applications.

A major concern regarding the use of glass in concrete is the chemical reaction that takes place between the silica-rich glass particles and the alkali in the pore solution of concrete, alkali-silica reaction (ASR). This reaction can be very detrimental to the stability of concrete, unless appropriate precautions are taken to minimise its effects. Such

preventative actions could be achieved by incorporating a suitable pozzolanic material such as fly ash, silica fume (SF) or ground blast furnace slag in the concrete mix at appropriate proportions.

The susceptibility of glass to alkali implies that coarse glass or glass fibres could undergo ASR in concrete, possibly with deleterious effects. However, it would be expected that fine ground glass (i.e., glass powder, GLP) would exhibit pozzolanic properties such as those of the materials named above and would be an effective ASR suppressant, preventing ASR damage to concrete in the presence of reactive aggregates.

Waste glass can be finely ground and used as a pozzolanic material since it contains a high amount of silica (SiO_2). Shayan and Xu reported that ground waste glass can be used as a 30% replacement of cement to produce concrete with a satisfactory strength development and an acceptable drying shrinkage value. Also, the potential deleterious alkali-silica reaction can be avoided if waste glass is ground sufficiently [12].

Use of recycled materials in construction is among the most attractive options because of the large quantity consumptions of the materials, relatively low quality requirements and widespread construction sites [13]. The main applications include a partial replacement for aggregate in asphalt concrete, as fine aggregate in unbond base course, pipe bedding, landfill gas venting systems and gravel backfill for drains.

Attempts have been made for a long time to try to use mixed waste glasses as aggregates in cement concrete, but it seems that the concrete with waste glasses always cracks. Very limited work has been conducted for the use of ground glass as a cement replacement in concrete. Recently, some attempts have been made to use the waste glasses as raw siliceous materials for the production of Portland cement. The introduction of waste glasses in cement production will definitely increase the alkali content in the cement. It was also noticed it could result in flash setting due to the high alkali content and the formation of compound $2CaSO_4.K_2SO_4$.

2.4. Lightweight Aggregate Types

The use of lightweight aggregate in concrete has many advantages [14, 15]. These include:

- Reduction of dead load that may result in reduced footings sizes and lighter and smaller upper structure. This may result in reduction in cement quantity and possible reduction in reinforcement.
- Lighter and smaller pre-cast elements needing smaller and less expensive handling and transporting equipment.
- Reductions in the sizes of columns and slab and beam dimensions that result in larger space availability.
- Improved cyclic loading structural response
- Longer spans
- Greater design flexibility and lower costs
- High thermal insulation.
- Enhanced fire resistance.

Furthermore, certain structures, specifically offshore structures which are mostly used for oil production, require lightweight elements which can be towed easily and have the greatest buoyancy. But perhaps the most significant potential advantage of the use of lightweight aggregates for concrete and building in general is the environmental value. When the raw materials needed for lightweight production are derived from industrial byproducts, the environment and economy of the producing locality and country are deemed to benefit. Already, stringent environmental limitations are imposed on mining of natural aggregates in various parts of the world. Such production would result in benefits to the community, the environment, and the building industry. Among these benefits are the following:

- Efficient recyclable disposal of the fly ash.
- Helping to conserve the natural and sometimes scarce materials of coarse aggregates and sand.

- Sparing the country side, river beds and beaches from the scarring and damaging activities of aggregate mining.
- Producing aggregates much lighter than the natural aggregates. This would result in the production of significantly lighter concrete whose advantages have been mentioned above.
- Significantly reducing the emission of green house gases by reducing the need of large quantities of cement whose production is a major contributor to CO_2 emission.
- Establishing an industry with export potential especially to countries where natural aggregates are depleted.

There are many types of aggregates available which are classed as lightweight, and their properties cover wide ranges [16]. Figure 2.1. indicates the approximate 28-day, air-dry unit weight range of three types of lightweight aggregate concretes along with the use to which each type is generally associated. The indicated dividing weights of these types (and the end points of each bar for each of the aggregates) are generally valid but should not be considered precise.

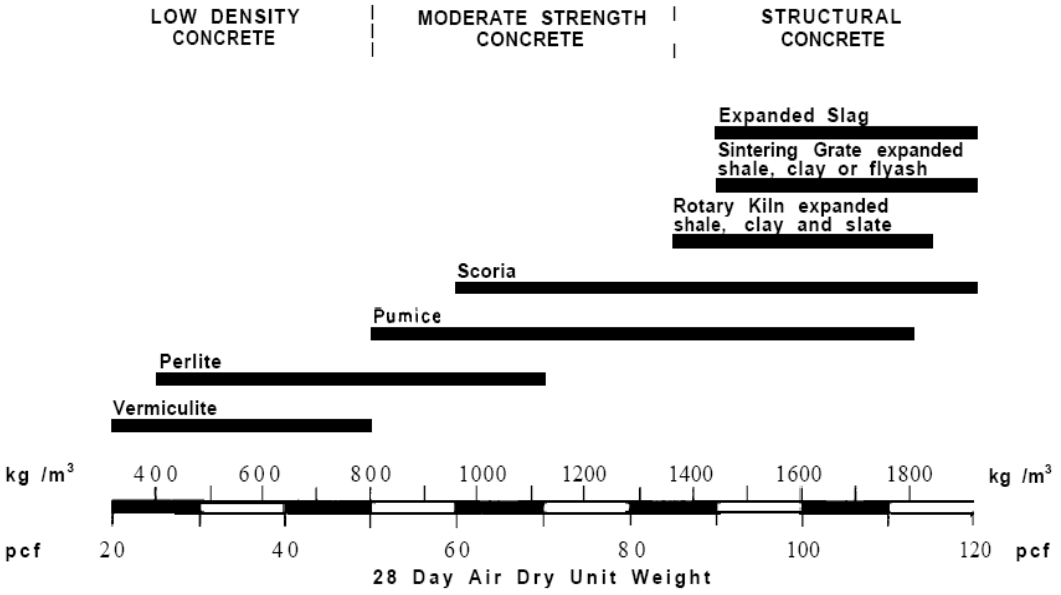

Figure 2.1. Approximate unit weight and use classification of lightweight aggregate concretes [16]

Low density concretes- These very light nonstructural concretes are employed chiefly for insulation purposes. With low unit weights, seldom exceeding 800 kg/m^3, thermal conductivity is low. Compressive strengths, ranging from about 0.7 to 7 MPa, are characteristic.

Structural concretes - These concretes contain aggregates that fall on the other end of the scale and that are generally made with expanded shales, clays, slates, slags, pumice and scoria. Minimum compressive strength, by definition, is 17 MPa. Most structural lightweight aggregates are capable of producing concretes with compressive strengths in excess of 35 MPa and with many of these, concretes can be made with strengths considerably greater than 41 MPa. Since the unit weights of structural lightweight aggregate concretes are considerably greater than those of low-density concretes, insulation efficiency is lower. However, thermal conductivity values for structural lightweight concrete are substantially better than for normal weight concrete.

Moderate strength concretes-The use of these concretes requires a fair degree of compressive strength, and thus they fall about midway between the structural and low density concretes. These are sometimes designated as "fill" concretes. Compressive strengths are approximately 7 to 17 MPa and insulation characteristics are intermediate.

2.5. Production Methods of Lightweight Fly Ash Aggregates

Sintering, cold bonding and autoclaving (hydrothermal treating) are the three methods generally used for the hardening of fly ash pellets [8, 17].

Cold Bonded Fly Ash Aggregates: Cold bonding is a type of bonding which accounts for the ability of fly ash to react with calcium hydroxide at ordinary temperatures to form a water resistant bonding material, which accounts for the pozzolanic reactivity of fly ash. Pelletized or extruded aggregates made with fly ash, Portland cement and water are cured for several days to produce an aggregate.

Autoclaved (Hydrothermal Treated) Fly Ash Aggregate: Autoclaving uses pressurized saturated steam curing for hardening of fly ash pellets. The manufacture of autoclaved fly ash aggregates typically involves using 45% quartz sand, 47% fly ash, 4.5%

lime, 2.0% additives and 1.5% water by weight. All of the mixture is pelletized and then heated in a high humidity environment and then heated for 6.5 hours at 200 °C to produce lightweight aggregate that finds its primary use in masonry units.

Sintered Fly Ash Aggregates: Sintering process hardens the pellets by fusing the fly ash particles together at the points of mutual contact. The manufacture of sintered fly ash aggregates involves two main operations. The first is to pelletize the fly ash by spraying a water-fly ash slurry onto an inclined rotating pan (pan pellitization) and then to sinter the pellets on a traveling grate that runs through an ignition chamber where the 5 to 8% coal in the fly ash is ignited. In the burning process a temperature of from 1050 to 1250°C is reached. These aggregates can be used to produce structural concrete.

The principle to make lightweight aggregate by the expansion of raw materials is explained as follows: A part of the raw materials is melted at a high temperature, attains a proper viscosity, and generates a gas [18]. The melted raw materials are expanded and then formed into a lightweight aggregate when the gas pressure is slightly higher than that required to resist the viscosity of the melted raw materials. The expansion at high temperature depends on their viscosity. The proper viscosity can be determined from the chemical compositions of the raw materials used.

The advantage of fly-ash over other lightweight aggregates is that it promotes fuel efficiency because the carbon in the ash provides sufficient heat needed to evaporate the moisture in the pellets and bring the pellets to the sintering temperature [19]. The suitability of fly-ash for the pelletization and sintering processes is difficult to predict because many physico-chemical factors are involved.

Many countries like the UK, USA, Germany, Poland and Russia are producing light-weight aggregates commercially under different trade names, such as Terlite, Lytag, Waylite corsonalite, sinterlite, etc [7]. A techno-commercial feasibility study was undertaken on the production of the light-weight aggregates from fly ash by Verma et al. The study described the production method, pilot plant investigations, process engineering of a demonstrative unit, major plant and equipment specifications, cost-economics, etc. Also, Nabozny et al. [20] suggested that processing of by-products (ash, slag) from power generation by sintering in shaft furnace seemed to be one of the most valuables options for

treatment of such residues. The requirements for an efficient process were described and their influence on effectiveness of the sintering was presented. Influence of temperature and combustion speed was investigated more deeply.

2.6. Physical Properties of Lightweight Aggregates

Physical properties of lightweight aggregates such as specific gravity, water absorption and porosity values of different ceramic powders such as sewage sludge ash, fly ash, zeolitic tuff, clay, municipal solid waste fly ash etc. were obtained and compared by many researchers. The sintering temperatures generally varied from 1000 to 1300 ^{o}C in experimental studies.

Cheeseman and Virdi [21, 22] compared the sintered sewage sludge ash (SSA) and municipal solid waste incinerator bottom ash (IBA) pellets to the commercially available lightweight aggregate Lytag. Maximum density occurred for samples sintered between 1040 and 1060 ^{o}C, with higher temperatures resulting in reduced densities. Water absorption data for sintered SSA continuously decreased with increasing firing temperature indicating a reduction in the volume of water accessible surface connected porosity. It appeared that SSA needed to be sintered at around 1050 ^{o}C to have similar water absorption properties to Lytag, and sintering above 1060 ^{o}C produced pellets with very low water absorption. Comparing the density and water absorption data clearly indicated a change in the nature of the porosity as the sintering temperature increased.

Generally the heat and polymer treatments reduced porosity in both types of measurements (water saturation and mercury) [23]. The relative reduction however was greater in the water saturation values. In all of the aggregates the mercury porosimetry pore volume values were greater than those of the water saturation. The change in the density of the solids showed consistent trends: (i) It reduced with increase in the temperature of heat treatment, which could be accounted for by transformation of the crystalline products to more glassy ones, (ii) For the same temperature of heat treatment, 1300 ^{o}C, the rapid cooling resulted in lower solid density compared to the slow cooling (iii) The lower solid density of the polymer treated aggregate relative to the original one could be attributed to the presence of a solid which was essentially a mixture of higher density inorganic material

and lower density polymeric material. The trends of reduced absorption and absorption rate with increase in temperature of heat treatment and with the polymer treatment was evident, and in agreement with the marked reduction in the open porosity values.

Li-xiong et al. presented a research on a sintered fly ash aggregate[24]. The aggregate was manufactured through material orthogonal test and quick chilled firing schedule test. Pellets were produced by extruding. Water ratio of pellets was 25%, and size fraction of pellets was 5-20 mm. Drying schedule of green-compact was temperature 140 ^{o}C and time 4 hours, and presintering schedule of green-compact was temperature 700°C and time 25 minutes. Sintering schedule of green-compact was that pellets were sintered at temperature 1250 degrees for 15 min, then at temperature from 1250 to 1200°C for 20 minutes, and then discharged from high temperature furnace. The aggregate displayed high strength (7.8 MPa) and low water absorption (4.2 %) with a bulk density of 843 kg/m^3.

The aggregates, both expanded clay and sintered fly ash types, were preconditioned to different initial moisture contents, both by drying from a high initial moisture situation, and by wetting from an initially dry situation [25]. The results demonstrated that LWA based on expanded clay produces a significant absorption hysteresis. This meaned that the 1-hour water absorption for a given initial moisture content was clearly lower in a pre-wetted state than in a drying state. This hysteresis was not found for the sintered fly ash aggregate.

The densification and mass loss behavior of pellets produced from zeolitic tuff with respect to heating temperature were investigated [26]. Above 1000 ^{o}C the density of the pellets showed a decreasing trend due to volume expansion. The volume expansion was not related to mass loss since the mass of the pellets decreased up to 1000 ^{o}C and did not change with further heating to higher temperatures. Above 1000 ^{o}C, while the mass of pellets was constant, the diameter and thickness of pellets increased due to volume expansion. The maximum density obtained at 1000 ^{o}C (2.28 g/cm^3) was still lower than the measured skeleton density value (2.4 g/cm^3) of zeolitic tuff and it was comparable to the value of 2.375 g/cm^3 for aluminum silicate based ceramics sintered at 1350 ^{o}C which was observed by Tulyaganov et al. Further increase in temperature caused deformation of the shape of pellets and decrease in density because of formation of pores.

Researchers [27] stated that all the internal gas was released before the surface becomes completely vitrified, thus affecting the quality of the LWA produced. The results revealed that the lowest specific gravity of LWA is fabricated at sintering of 1150 ^{o}C for 15 min with raw aggregate pellets fed at 750 ^{o}C. The rapidly vitrified surface enveloped the gas produced with the increase in internal temperature resulting in a specific gravity of 0.6. At feeding temperature of 850 ^{o}C, the LWA sintered at 1150 ^{o}C has specific gravity below 0.5. Further increase in feeding temperature to 950 ^{o}C led to rapid vaporization of moisture, causing the pellets to burst.

Sintered lightweight aggregate from sewage sludge was experimentally manufactured with various mass ratios of clay to sewage sludge by a rotary kiln [18]. The density of the lightweight aggregate decreased with the increase in sewage sludge content. The decrease in density was attributed to the internal sintering due to the calorification and combustion of organic materials and the accelerated expansion due to gas generation. The water absorption of the lightweight aggregate tended to gradually decrease with the increase in the sewage sludge content and with the decrease in the density. The water absorption–density relationship of the lightweight aggregate differed from that of ordinary lightweight aggregate. The reason resulted from the formation of a melted glass phase made by the thermal decomposition in the foamed clay–sewage sludge mixture.

Researchers studied the recycling of the fine sediments of Shih-Men Reservoir to manufacture lightweight aggregate [28]. The particle density of sintered lightweight aggregate decreased when the sintering temperature increases especially above 1200 °C due to phase transformation and formation of a vitrified layer on the surface through subsequent dehydration, bloating and collapsing stages.

Ordinary Portland cement, Na–bentonite and powdered limestone were used as binders in 10%, 20%, and 30% by weight of fly ash for pelletization [8]. After pelletization, the aggregates were dried before sintering at a temperature of 1100 ^{o}C for 1-h duration in a muffle furnace. The specific gravity increased when binders were used. The addition of bentonite, which contained a higher amount of very fine organic matters, increased the quantity of gases evolved during sintering thereby reducing the density of the aggregates. The 24 h water absorption of sintered fly ash aggregate without binders is in

the range of 21–22%. Addition of lime reduces the water absorption marginally. Cement performs relatively better than lime as a binder in reducing water absorption. Beyond 20% dosage, the binders did not exhibit further reduction in water absorption.

Thermal power plant fly ashes were used to investigate the sintering behavior of fly ashes [3]. For this purpose, coal fly ash samples were sintered to form ceramic materials without the addition of any inorganic additives or organic binders. Pressed fly ash samples were heat treated at the temperature of 1175 ^{o}C on the basis of preliminary experimental trials. The color of fly ash sample changed from light to dark grey when the heat treatment process applied on the pressed sample. The surface of the sample was smooth and shiny dark grey. It was observed that the pressed fly ash sample from other thermal power plant was grey color, which tended to become pale brown after the heat treatment process. The surface of the sintered sample was smooth with a glassy appearance. Color and the texture of the other pressed fly ash sample also changed with the heat treatment process. Densities of the sintered samples were in the range of 2.43–2.58 g/cm^3. The low density and high water absorption values are the indicatives of a porous material.

The sinterability of a class F fly ash was investigated as a function of processing conditions including sintering temperature (1050–1200 ^{o}C) and sintering time (0–90 min) [2]. For each temperature, the sintered density generally increased as the sintering time increased, though, there was a suggestion of a local optima at 1100 ^{o}C and 60 min. In the case of 1050 ^{o}C, the sintered density was below the green density due to the oxidative volatilization of the sugar binder and the native carbon, the decomposition of calcite and negligible change in the dimensions of the sample. A maximum density of 1708 kg/m^3 (a relative density of 0.723) was observed in the case of 1200 ^{o}C and 90 min of sintering time. Bulk density and water absorption are independent measures of densification, the greater the density, the lower should be the water absorption. Visual surface inspection of sintered samples did not vary much from sample to sample, yet, fracture surfaces were found to be vastly different, varying in color from orange to black.

Sewage sludge ash (SSA), with similar characteristics to expansive clay, was used as the principal material and sewage sludge (SS) as the admixture to sinter lightweight aggregate and to study the influences of raw material composition on pelletising, sintering

effect and aggregate properties [29]. Spherical particles were combusted in furnace at 1050, 1100 and 1150 ^{o}C for 10 and 20 min, respectively, to sinter aggregates. The appearance of pellets of the four samples were in rounded and spherical shape. In the process of sintering lightweight aggregates with mixture of SS and SSA, weight loss occurred, probably because of water evaporation, high temperature oxidization of organic matters, decomposition of inorganic salts or emission of volatile heavy metals. The emission and decomposition of the before-mentioned substances affected the macro properties and microstructure of the lightweight aggregates. At 1100 ^{o}C, with the increase in amount of SS, the bulk density of the aggregates dropped significantly. However, when the temperature was increased to 1050 ^{o}C, due to the sintering effect, the bulk density of aggregates only slightly decreased. However, the bulk density decreased to 1.35– 1.39 g/cm^3 at 1150 ^{o}C; meanwhile, a glassy texture was formed on the surface of SSALA.

Firing of the aggregates at the temperatures of 1000 and 1100°C generally displayed particle density of values ranging from 2.0 to 2.9 g/cm^3, which increased with increasing sludge content [30]. The highest particle density occurred when pure sludge was sintered at 1000°C. Good lightweight properties were observed on the aggregates fired at the temperatures of 1200 and 1300°C. Aggregate samples containing sludge content of less than 50%, displayed an expansion effect on the aggregates and lower particle densities when sintered at 1300°C, as when compared with those sintered at 1200°C. It should be noted that although the lightweight aggregates had a very porous structure, they exhibited relatively low water absorption characteristics. This indicated that true density depended on the sample size and the measurement methods as the aggregates form intracellular voids that are impervious to surface water.

2.7. Mechanical Properties of Lightweight Aggregates

The strength of natural coarse aggregate can be obtained empirically by testing the bedrock; however, it is not easy to obtain the strength of artificial lightweight aggregate in the same way. Thus, the strength of lightweight aggregate can be evaluated from indirect tests such as the Los Angeles abrasion test (ASTM C 131), hardness test, aggregate crushing value test (ACV) (BS 812-110) and ten per cent fines value test (BS 812-111).

A numerical approach was proposed for estimating the compressive strength of lightweight coarse aggregate and predicting the trend of strength variation for different volume fractions of aggregates using a micromechanics method by Yang and Huang [31]. Nilsen et al. suggested that the specific energy dissipation due to a stress cycle can be used to assess the quality of lightweight aggregates. Chang and Su proposed a method to estimate the compressive strength of an aggregate particle by using the theory of granular mechanics. Tangtermsirikul and Wijeyewickrema [32] proposed a strength estimation method for cold-bonded fly ash aggregate. The equation for computing tensile stress at the tensile failure plane at the breaking point load was adopted. This tensile stress was utilized to represent the tensile strength of the FAA. It was found that the tensile strength of the fly ash aggregate was higher when the equivalent CaO content of the raw materials used to produce the fly ash aggregate increased and the time-dependent tensile strength of the fly ash aggregate from ages 14 to 91 days could be fairly estimated from the maturity of the aggregate based on the 30-day tensile strength. The following equation was proposed:

$$\sigma_t = \frac{0.2 * P}{R_0^{\,2}} \tag{2.6}$$

Where σ_t is the tensile stress at the center of tensile failure plane at the time of pellet breaking (MPa), P is the point load at the time of pellet breaking (N), R_0 is the mean radius computed from three measurements in three normal direction of the FAA pellet (mm).

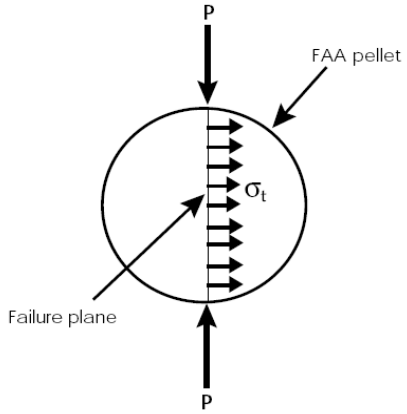

Figure 2.2. Point load and tensile stress at the center of tensile failure plane (14)

An estimate for the mechanical quality of the aggregates was obtained by a crushing strength test reported in a previous study [23]. Oven-dried sample of the aggregates was placed in a steel cylinder with internal diameter of 57mm and height of 87mm. The aggregates were filled up to an upper incision mark in the cylinder and afterwards covered with a steel puncheon that was pressed until the upper level of the aggregate was reduced by a prescribed distance. The crushing strength value was calculated in stress units as the ratio between the load and the cross section area of the cylinder.

Cheeseman and Virdi [21, 22] revealed that Lytag was considered a relatively high strength lightweight aggregate and sintered sewage sludge ash produced pellets with comparable strengths when fired between 1050 and 1070 ^{o}C. Average strengths of IBA pellets sintered at all temperatures were lower than those obtained for Lytag.

Regardless of the type of municipal solid waste (MSW) fly ash tested, all the sintered specimens exhibited low strength (4.2–6.3 N/mm^2) [33]. The poor properties of the sintered products made with untreated MSW fly ashes were essentially related to the adverse chemical characteristics of these fly ashes in terms of water-soluble compounds (chlorides and sulfates) and vitrifying oxides, and a preliminary washing treatment of MSW fly ash with water could greatly reduce the content of water-soluble compounds and, at the same time, could increase the concentration of vitrifying oxides. Therefore, the sintering of preliminarily washed MSW fly ash could be a suitable way of manufacturing sintered products with proper chemical and mechanical characteristics for reuse as concrete aggregates.

The crushing strength value for the aggregate (Lytag) sintered at 1300 ^{o}C and then rapid cooled was extremely low and this could be accounted for by numerous cracks observed on its surface, reflecting probably the influence of thermal gradients [23]. The differences in crushing strength could not be correlated only with differences in porosity. For example, aggregates sintered at 1250 ^{o}C and 1300 ^{o}C (rapid cooled) had lower porosity than the original Lytag aggregate, but their strength was lower. This may be due to several influences: change in the mineralogical composition and cracks and internal defects due to thermal stresses.

Heat treatment effect on zeolitic tuff mainly containing clinoptilolite was investigated [26]. The heat treatment conditions for maximum density and hardness were determined. The original structure unchanged up to 800 ^{o}C hence the zeolitic tuff can be used for applications at moderate temperatures. Further heating caused complex structural transformations occurring with breakdown of the three-dimensional network structure of the zeolitic tuff. The hardness of the pellets increased considerably by heating from 700 to 1000 ^{o}C. However, further heating lowers the values of hardness and density but increases the size and number of the pores. The hardness test of the pellets by Vicker's Hardness Tester showed the hardness increased from 75 to 387 Hv by heating from 700 to 1000 ^{o}C. Further heating caused decrease of the hardness to 135 Hv due to volume expansion.

During the sintering process, after heating, particles of municipal solid waste incinerator (MSWI) fly ash binded to one another giving greater strength [34]. However, the driving force required to reach the sintered state at the ash powder contact points was proportional to the surface area of the ash particles, and was thus affected by the particle size of the MSWI fly ash. Specimens made with small ash particles showed a higher compressive strength after sintering at 400–1000 °C for 1 and 4 h. All the specimens showed a similar compressive strength trend, that is the compressive strength first increased when the temperature increased from 400–800 °C, then peaked at 800 °C, and then decreased from 800–1000 °C. Since smaller particles give a larger total surface area, small ash particles may result in a larger change in the surface area during sintering, and in turn, a larger change of free energy. The densification, and thus the development of the compressive strength is thermodynamically more likely to occur for ash with a smaller particle size. As observed in the study, specimens made from small particle sizes showed a higher compressive strength, which is consistent with, and explained by, the above reasoning.

Five types of lightweight aggregate with sewage sludge and clay manufactured on trial and a commercial lightweight aggregate for nonstructural concrete (imported from a European country) were tested for comparison [18]. The abrasion loss, crushing value and impact value of the lightweight aggregate decreased with increasing the clay to sewage sludge ratios of 100:100, 100:200 and 100:300 and had similar or less abrasion loss, crushing value and impact value compared to the commercial lightweight aggregate.

For lightweight aggregate, as crushing value test was not appropriate (aggregate would get compacted before the full load of 40 t was applied and hence the amount of crushing during later stages of the test was reduced), a 10% fine value was used to compare the strength of aggregates [8]. Ordinary Portland cement, Na–bentonite and powdered limestone were used as binders in 10 %, 20 %, and 30 % by weight of fly ash for sintering at a temperature of 1100 ^{o}C for 1-h duration. Addition of lime did not improve the 10 % fines value but it has been found that it helped in appreciable improvement of the ballability of the material. Addition of cement resulted in marginal improvement in 10% fines value. It was also found that this increase was pronounced at higher dosage. Bentonite was observed to enhance the 10 % fines value of aggregates significantly and the maximum value was obtained with 20 % dosage. Beyond this dosage, there was no further enhancement in the 10 % fines value of sintered aggregate.

More dense and tiny crystalline structure caused better mechanical properties [3]. Large and irregular shaped crystallites, glassy phase and porosity decrease the mechanical properties of the materials. It was also known that the mullite properties (low thermal expansion, high hardness, low thermal conductivity) make it an ideal candidate for making ceramic bodies. Rockwell hardness value of fly ash sample was 82 at the major load of 1 kg. fly ash sample had the highest hardness value among all other sintered fly ash samples obtained in this study.

Sintered class F fly ash samples (sintering temperature (1050–1200 ^{o}C) and sintering time (0–90 min)) were characterized for mechanical properties [2]. In the case of 1050 ^{o}C, the effect of sintering time has little effect on the splitting tensile strength (STS). In other cases, the STS reached a maximum value and then dropped with increasing sintering time. The optimum in density, however, was not necessarily coincident with the optimum in STS and the data indicated that though the density was increasing, the STS was decreasing for some samples. While bloating was a possible mechanism, in some cases the density was actually increasing. Unfortunately, strength was not necessarily a simple function of one materials property alone, bulk density, for instance. Rather, strength was the result of the interplay between numerous properties. Though density increased, this did not necessarily imply that the size of the strength controlling flaw was decreasing proportionally.

The sintered sewage sludge ash (SSA), and expansive clay with the weight percentage of SS to that of total solids (SS + SSA) 0%, 10%, 20% and 30%, respectively, named MA, MB, MC and MD accordingly were tested [29]. At 1050 ^{o}C, the failure point loadings of SSALA of MA and MB were only 12.29–17.45 and 10.74–12.96 kgf individually. This was because the SSALA had not reached the sintering temperature, and there was still powdery film on the surface. The failure point loadings of SSALA of MC and MD were 95.10–96.87 and 81.07–82.55 kgf, respectively, because the sintering reaction has happened at this moment. Sintering temperature had a more significant effect on aggregate characteristics than retention period. Besides, 10 min of retention period was sufficient, but prolonging the retention period to 20 min would lower the failure point loading of SSALA.

2.8. Microstructural Analysis of Lightweight Aggregates

2.8.1. X-Ray Diffraction Studies on Lightweight Aggregates

Comparison of XRD data for as-received sewage sludge ash and sewage sludge ash pellets sintered at 1020 ^{o}C and 1070 ^{o}C demonstrated that no significant crystallographic changes had occurred. The major crystalline phases present were again quartz, whitlockite ($Ca_7Mg_2P_6O_{24}$) with some hematite (Fe_2O_3) [21].

XRD data for IBA sintered at 1030 ^{o}C showed that this material contained wollastonite ($CaSiO_3$), diopside ($CaMgSi_2O_6$) and clinoenstatite ($Mg_2Si_2O_6$) as the principal mineral phases, together with reduced levels of quartz and some hematite [22]. A number of the XRD peaks detected could not be unambiguously identified.

Wasserman found that the original aggregate (Lytag) contained several crystalline phases: quartz, mullite, anorthite and hematite [23]. The hump in the X-ray diffraction pattern was characteristic of a glassy phase. It could be seen that the increase in the temperature of treatment was associated with a marked reduction in the quartz peak, with only mild increase in the mullite peak. A semi-quantitative estimate of these changes suggested that the quantity of quartz being reduced was greater than that consumed in the formation of other crystalline phases. This implies that the part of the reduction in quartz

content was accompanied by formation of additional glassy phase. The mineralogical changes due to the heat treatments are sensitive to the alkali content of the glass. Therefore, different trends may be obtained with fly ash of different compositions.

X-Ray patterns of the zeolitic tuff samples were analyzed considering the peaks within the 10 and 40^{o} 2θ range [26]. In addition to zeolitic phase (80 %) presence of quartz, cristobalite and K-feldspar was reported for the same zeolitic tuff. Heating up to 800 ^{o}C did not produce any structural changes detectable by X-Ray with regard to the original sample, while further increase in the temperature produced decrease in main peaks of clinoptilolite. Finally, the disappearance of the characteristic peaks of clinoptilolite was observed with further increase in temperature, which indicated the transformation of zeolite into an amorphous phase. On the other hand, both the original and the heated samples contained SiO_2 as a crystalline phase, which did not change by heating, indicated by the peak at 2θ value of 21.88.

The X-ray diffraction analysis of sewage sludge was done by Mun [18]. Quartz peaks were dominantly and remarkably visible, followed by feldspar, muscovite and chlorite peaks.

The relative performance of three binders, viz., cement, lime and bentonite, on the properties of sintered fly ash aggregate was reported by Ramamurthy and Harikrishnan [8].The main chemical compositions of the fly ash identified through XRD and chemical analysis were SiO_2, Al_2O_3, MgO, and CaO. Representative XRD patterns of sintered fly ash aggregate samples with bentonite and lime (20% by weight of fly ash) carried out that the XRD peak was characterized by the presence of SiO_2 along with trace amounts of MgO and CaO. Irrespective of the binders used, the overall XRD pattern remained unaltered, indicating that there were no major variation, in the chemical composition of the product and no new compounds were formed. Hence, it could be concluded that the enhancement in properties of aggregates could be attributed to the binding ability of binders and all properties, including density, water absorption, and strength of a porous material, were influenced by the internal pore structure of the material.

In order to investigate the nature of phases resulting from thermal treatment, the XRD patterns of samples heat treated at different temperatures were compared [3]. The main crystalline phase occurred in the fly ash sample was mullite ($Al_6Si_2O_{13}$). Enstatite and anorthite phases in the as-received fly ash sample disappeared in the sintered sample. Fly ash sample belonged to mainly SiO_2–Al_2O_3–Fe_2O_3 system. The other sintered fly ash sample showed the presence of mullite ($Al_6Si_2O_{13}$) and anorthite ($CaAl_2Si_2O_8$) while the untreated fly ash sample comprised of the quartz, mullite, anorthite and enstatite phases. The intensity of the anorthite peaks was higher than the intensity of the mullite peaks. The composition of this fly ash was in the SiO_2–Al_2O_3–CaO–Fe_2O_3 system. The compositions of these two fly ash samples were similar to each other. However, CaO content of latter fly ash was higher than former fly ash. The formation of the anorthite phase could be explained by the high CaO content of other fly ash. The presence of anorthite was generally associated with the substitution of Ca ion into the SiO_2–Al_2O_3 couple at high temperatures.

X-ray microanalysis was used to identify the elements present in different particles of the raw fly ash and sintered fly ash to see if there was any elemental composition change due to thermal treatment [2]. Normalized atomic percentages were obtained for the elements Al, Si, and Ca. While subtle, the data suggested that the SiO_2 and Al_2O_3 in the glass phase was redistributed by the sintering process. Initially, there were islands of highly enriched SiO_2 and glassy mixtures of SiO_2 and Al_2O_3 clustering between a Si/Al ratio of 0.5 and 0.8 with the distribution tending towards a composition of 0.5. After heat treatment, a more uniform distribution of Si/Al ratios was observed with some points as low as a Si/Al ratio of 0.4. The amount of mullite increased with increasing temperature and time, while the quartz content was decreasing. It also appeared that the overall crystalline content was increasing, e.g. increased peak intensities with increasing temperature over a entire range of 2θ angles, 5–85^o 2θ. The occurrence of crystalline inclusions, likewise, could contribute to residual stress development since crystallization in this case was accompanied by a significant change in volume, e.g. the specific gravity of the nominal glass is 2.3 while that of quartz and mullite is 2.65 and 2.8, respectively.

2.8.2. Scanning Electron Microscope Observations on Lightweight Aggregates

SEM micrographs of fracture surfaces of sewage sludge ash lightweight aggregate pellet samples prepared using the organic binder that were sintered at 1020, 1060 and 1070 ^{o}C. These clearly show the microstructural changes induced by increasing the sintering temperature [21]. The sintered microstructure at 1060 ^{o}C showed a well-formed, dense matrix material that contained a significant volume of isolated approximately spherical porosity. These pores appeared to be predominantly in the 1–10 μm diameter range, although there was evidence of some much larger pores. The microstructure results from extensive liquid phase sintering with partial softening of the glassy phase, together with some decomposition reactions producing internal pore pressure that causes the finely bubbled microstructure observed.

Sintering IBA at 1020 ^{o}C resulted in material containing significant glassy phase with isolated, irregularly shaped pores [22]. Samples sintered at 1050 ^{o}C appeared to contain approximately spherical pores, typically 5–10μm in diameter. These are believed to form when the residual glass viscosity is low enough for gas-forming decomposition reactions to produce the voids observed.

SEM observations at low magnifications showed that in all the aggregates (sintered 1200,1250,1300 ^{o}C for 30 minutes) distinction could be made between the core and external shell, ~500-1000 μm thick [23]. Large pores bigger than 10 μm were usually located in the core, whereas the pores in the shell were smaller. At higher magnifications, it is possible to see a more uniform distribution of smaller pores in the higher temperature treated aggregate (1300 ^{o}C vs. 1200°C). Observations of the external shell of the aggregates clearly showed the particulate nature of the sintered fly ash particles in the untreated Lytag aggregate whereas in the heat treated aggregate they became more fused together. In the aggregate treated with the polymer the spaces between the sintered fly ash particles seemed to have become impregnated and their structure can no longer be resolved.

Researchers investigated the microstructural development of a well-characterized zeolitic tuff during heat treatment [26]. The formation of porous structure might be due to

volatilization and decomposition of any thermally unstable material and/or the water vapor present in the zeolitic tuff. However, the size and number of the pores in pellets sintered at 1200 ^{o}C were much more than expected while comparing the factors of heating processes in literature such as heating rate, soaking time and sintering temperature. Hence, higher heating rates may cause larger expansion of pellets due to a rapid derivation of gases. The derived vapor partially trapped by viscous body could cause the formation of pores, which leads to decrease in density and the deformation of pellets. The pores were closed and distributed homogeneously.

Artificial lightweight aggregate (LWA) manufactured from recycled resources was investigated [27]. Residues from mining, fly ash from an incinerator and heavy metal sludge from an electronic waste water plant were mixed into raw aggregate pellets and fed into a tunnel kiln to be sintered and finally cooled rapidly. In the case of LWA sintered at 1150 ^{o}C, there were abundant pores present in the center, which were even and with thin boundary, while away from the center, the pores become smaller and more densified. It was revealed that the higher the sintering temperature, the smaller and fewer the pores.

The microstructures of lightweight aggregate with the clay to sewage sludge ratios of 100:100, 100:300 and 100:500 showed that during the expansion of the spherically formed lightweight aggregate in the sintering process, thin layers with dense microstructures were formed on the surfaces of the aggregate, which prevented the adhesion [18]. The thickness of the layers tended to decrease with the increase in the sewage sludge content. The diameters of pores inside the lightweight aggregate with the ratio of clay:sewage sludge = 100:100 were 500 μm or less, but those of pores inside the lightweight aggregate with the ratios of clay:sewage sludge = 100:300 and 100:500 were 500–1500 μm. The decomposition of organic materials in the sewage sludge caused calorification and gas generation in the formed mixtures. These generations led to a decrease in the melted ingredient viscosity and an increase in the gas pressure due to the increased inner temperature. The thickness of the thin layers formed on the lightweight aggregate and the diameters of the pores inside them depend on the balance of the melted ingredient viscosity and gas pressure. Increasing the inner temperature and the excessive generation of the melted ingredients in the formed mixtures effectively accelerate the formation of a glass phase. Accordingly, although the larger pores inside the lightweight aggregate were

formed by increasing the sewage sludge content, the formation of the glass phase was found to prevent the decrease in the strength and the increase in water absorption.

Researchers reported that the shapes of pores in general were irregular, spherical, and discrete, while others were elongated and interconnected in the structure of sintered fly ash aggregate without binders [8]. There were a few relatively large voids. Lack of binding among the grains could be the reason for the lower strength of fly ash aggregate. Relatively smaller pores distributed uniformly in the aggregates indicated that cement and lime improved the binding ability. But the presence of some large voids resulted in higher water absorption and lower strength of these aggregates. The dosage of bentonite affected the microstructure. With 10% bentonite, the presences of large voids were reduced. The use of 20% bentonite resulted in minute pores distributed uniformly as compared to all other cases. This corroborated well with strength and water absorption characteristics of aggregates.

SEM investigations were conducted on the sintered coal fly ash samples obtained from thermal power plants to investigate the microstructural evolution of the samples [3]. SEM observations of sample indicated that the mullite crystallites formed in the microstructure of the sintered sample. Prismatic, equiaxed mullite crystallites embedded in a fine-grained matrix formed by solid state reactions. The crystallites strictly interlocked together to form a more dense structure. The crystallites occurred in the other fly ash sample were small equiaxed crystals and some irregular shaped crystallites were also observed. Small equiaxed crystallites interlocked together to form a more dense well-sintered microstructure with a uniform distribution of crystals.

The microstructure of the sintered Class F fly ash specimens was characterized using scanning electron microscopy [2]. Samples treated at 1050 ^{o}C exhibited poorly sintered structure with very few necks between the particles, resulting in poor mechanical properties, low density and high water absorption. With increasing temperature, fly ash particles coalesced forming necks among the particles and resulting in higher density and under some conditions good mechanical properties. The neck growth rate and neck size increased greatly starting at 1150 ^{o}C. Similarly, microstructural development increases with increasing sintering time at constant temperature.

Sewage sludge ash (SSA), with similar characteristics to expansive clay was used to sinter lightweight aggregate. The weight percentage of dried SS to that of total dried solids (SS + SSA) was 0%, 10%, 20% and 30%, respectively, named MA, MB, MC and MD accordingly [29]. MA became sintered and expansive at 1150 ^{o}C. MB became sintered between 1100 and 1150 ^{o}C, and its expansion was obvious at 1150 ^{o}C. At 1100 ^{o}C, MC achieved the sintered and expansive stage simultaneously, and MD became sintered at 1050 ^{o}C, and significantly expansive at 1100 ^{o}C. Thus, it was concluded that increasing the amount of SS could effectively lower the sintering temperature, enhance the bloating effect, and save energy.

The SEM micrographs indicating the interior of the aggregates of various mix ratios fired at 1200 °C are illustrated in micrographs [30]. The interior structure exhibited, to a large extent, a heterogeneous appearance when more clay was present. With sludge as the main raw material, the sample exhibited a smoother interior. The SEM images show that bloating and expansion of the aggregates were more evident as the sludge content increased. The fine and densely spaced pores seen in the micrograph of the sample with 100% clay content were no longer present in the sample that contained only sludge. From the SEM observation, the sample interior was of a heterogeneous structure, particularly when the clay content was high.

2.8.3. Thermal Behavior

In general, two essential physical–chemical changes in ash at elevated temperature need to exist simultaneously for gaseous bubbles to be generated and trapped inside the pyro-plastic mass, including the development of a glassy phase and evolution of gases from the dissociation of mineral components [35]. The most observed gas-producing reactions of incinerated sludge ash at elevated temperature are:

• Oxidation of sulfide substances at 400 ^{o}C to produce SO_2.
• Dissociation and evaporation of crystallized water in clay at 600 ^{o}C to produce water vapor.
• Oxidation of carbon containing substances at 700 ^{o}C to produce CO_2.
• Release of O_2 from Fe_2O_3 at 1000–1100 ^{o}C.

Mangialardi used fly ashes that came from MSW incineration plants located at four different Italian cities (Bologna, Forlı, Modena, and Reggio Emilia). These fly ashes were designated by notations indicating the respective place of origin (BO, FO, MO, and RE) [33]. The TGA–DSC thermograms of untreated fly ashes revealed that all the fly ashes melted over a wide temperature range, as evidenced by the large endothermic peak located at a peak temperature of 1200–1250^{o}C, depending on the type of fly ash tested. For all the fly ashes, some endothermic peaks associated with relatively low percentage weight losses (2.0–3.9%) were recorded at temperatures less than about 300^{o}C. Furthermore, for BO, MO and RE fly ashes an exothermic peak was recorded at 400^{o}C and associated with carbon oxidation. For FO, MO and RE fly ashes an endothermic peak was detected at 600^{o}C and related to siderite ($FeCO_3$) decomposition. For BO and FO fly ashes an endothermic peak was also recorded at about 700^{o}C and identified with calcite decomposition.

Aineto et al. observed that the fly ash trace depicted a first small exothermic peak seen at 540 ^{o}C due to the sulphides oxidation [36]. A large exothermic was produced by ferrous oxidation at 720 ^{o}C, temperature of hematite (Fe_2O_3)formation. A small and broad exothermic effect was detected up from 1000 ^{o}C which was caused by the crystallization of mullite, hercynite and anorthite, the main crystalline phases as assessed by XRD analysis.

Thermal behavior of zeolitic tuff was investigated by using TGA and DTA [26]. The TGA of the zeolitic tuff showed 11.5% weight loss up to 1000 ^{o}C. TGA curves were examined using the procedure outlined by Knowlton and White for the temperature ranges 25–85, 85–285 and 285–1000 ^{o}C corresponding to external, loosely bound and tightly bound water, respectively. The weight losses were found as 4.10, 4.41 and 2.99% by weight for the external, loosely and tightly bound water for the examined zeolitic tuff. The DTA pattern of the zeolitic tuff shows dehydration of zeolitic water until 600 ^{o}C and above 600 ^{o}C a broad endothermic peak was observed, which gives information on the structural breakdown.

Results of the thermal analysis (TG-DTA) indicated the thermal decomposition and combustion of organic materials in the sewage sludge at temperatures of about 290–388 ^{o}C [18]. The data indicated a thermal equilibrium at a temperature of about 700 ^{o}C.

TGA curves were obtained for sludge–clay mixes sintered at high temperatures [30]. At temperatures above 1100 °C, little substances would be vaporized from the mixes containing 0, 20, and 80% sludge content. However, significant weight loss was noticed for mixes with sludge contents of 50% and 100%. Hence, the bloating of aggregates observed at this temperature range was probably caused by the substances released from the sludge rather than the clay, as detected in the TGA test. No peak endothermic transition was observed in the clay material beyond the temperature of 900 °C, indicating no significant chemical/physical changes of materials up to 1400 °C because of the ceramic nature of the marine clay material. Industrial sludge showed a peak endothermic transition at approximately 1200 °C, indicating the occurrence of chemical reactions that release the substances.The 20% sludge mix showed signs of endothermic reactions at approximately 1280 °C and the 80 and 100% sludge mixes showed signs at approximately 1200 °C, whereas the 50% sludge mix had the lowest reaction temperature of 1160 °C, corresponding to the temperatures where the endothermic peaks occur. Porous structures that provided the lightweight property of these aggregates began to develop as the endothermic reaction occurred.

2.9. Lightweight Concretes

2.9.1. Physical and Mechanical Properties of Lightweight Concretes

Researchers [37, 38] studied the long term strength development of lightweight concrete produced by using Lytag in both the severe hot and dry and hot-coastal and salt-laden exposure conditions. The early results of the investigation suggested that the compressive strength of lightweight concrete was less sensitive to lack of initial curing. The drying shrinkage of this concrete was found to be more than 600 microstrain in the first 3 months' duration.

Some researchers investigated the effect of polypropylene and steel fibers on high strength lightweight aggregate concrete manufactured by Lytag [39, 40]. Addition of steel fibers appreciably increased the ductility of lightweight aggregate concrete but did not significantly affect the value of compressive strength. The value of the indirect tensile strength and that of the modulus of rupture of lightweight high-strength concrete could be

approximately doubled with the use of steel fiber reinforcement at 1.7% by volume of the concrete. Addition of polypropylene fibers at 0.56% by volume of concrete resulted in a 90% increase in the value of the indirect tensile strength. Polypropylene fibre reinforcement did not reduce drying shrinkage, while steel fibres did. Early shrinkage behaviour of this type of lightweight concrete was similar to normal-weight concrete.

Mangialardi [33] investigated the sintering process of municipal solid waste (MSW) fly ash in order to manufacture sintered products for reuse as concrete aggregates. A compact pressure of 28 N/mm^2, a sintering temperature of 1140 ^oC, and a sintering time of 60 min were the best operating conditions for manufacturing sintered products of washed MSW fly ash.

The results of an investigation into the size effect on flexural, splitting tensile, and torsional strengths of high-strength concrete (HSC) with normal aggregate (crushed limestone) and lightweight aggregate (sintered fly ash) were presented by Zhou et al [41]. The fracture behavior of the lightweight HSC seemed to be more brittle than that of the normal HSC. A reverse size effect was observed in the prism splitting tensile strengths of both normal and lightweight HSC. The torsional strength of the lightweight HSC appeared to have a stronger size dependency than that of the normal HSC.

Splitting tests were carried out for evaluating damage in four types of concrete [42]. The concrete contained either river gravel, phosphorous-slag aggregates and Lytag aggregates. Different failure behaviours were revealed mainly depending on the aggregate and interface characteristics.

Fly ash and auxiliary raw materials—clay, canbyite-melt sludge, coal, and paper-mill waste—were used to produce a sintered fly ash aggregate [24]. Sintered fly ash lightweight aggregate demonstrated high strength and low absorption of water. Lightweight aggregate concrete made with this aggregate may have compressive strength more than CL60, slump higher than 20 cm, 60 minutes slump loss less than 2 cm, and expansibility higher than 50 cm. Such properties meet the modern concrete requirements for high strength and pump-ability.

The researchers [43] indicated that by using fly ash (FA), furnace bottom ash (FBA) and Lytag, it is possible to manufacture lightweight concrete with density in the range of 1560-1960 kg/m^3. In terms of contribution to the compressive strength by per unit weight of concrete, FA, FBA, and Lytag can be beneficially used to manufacture medium strength concrete.

Lo and Cui presented the mechanical properties of a structural grade lightweight aggregate made with fly ash and clay [15]. The findings indicated that water absorption of the green aggregate was large but the crushing strength of the resulting concrete could be high. The 28-day cube compressive strength of the resulting lightweight aggregate concrete with density of 1590 kg/m^3 and respective strength of 34 MPa.

Researchers studied the properties of LWAC mixed using lightweight aggregates made from sintered silt dredged from reservoirs [44]. As expected, there was enhancement in compressive strength with higher aggregate density and lower w/b ratio. However, the differences in compressive strength became less significant with longer curing as evidenced by the smaller increase after 56 days of curing.

Although the lightweight aggregates are manufactured through a process of sintering, it is concluded that pelletizing may adversely contribute to producing lower strength concrete [14]. This is because of the smooth surface that the pelletizing process creates. The aggregates were crushed after sintering that did not involve pelletizing. This process is believed to have created rough surfaces that provided enhanced bond with the concrete matrix. The concrete made with FAA was 25% stronger than that made using pelletized fly ash based lightweight aggregates. Further, the strength of the lightweight concrete manufactured with FAA was higher than the traditional normal weight concrete by 20%. These results open the prospect of investigating the opportunity to be able to reduce the quantity of cement that is required to produce concrete of a specific strength. Such reduction would reduce carbon dioxide emission and hence would be beneficial to the environment. The reduction in weight of the structure may also produce an opportunity to investigate the possible reduction in the overall cost of the construction.

Typical UK Lightweight aggregates were found to attain a moisture content close to their maximum moisture capacities, under typical pumping pressures (4.5 MPa) [45]. The addition of a pumpaid to absorption water did not influence the amount of moisture absorbed by lightweight aggregates. This suggests that the use of a pumpaid could not be expected to influence the amount of absorption into lightweight aggregates in pumped concrete.

The use of sintered flyash aggregate in concrete as a partial replacement of granite aggregate was examined [46]. The concrete so produced was light in nature (up to 14% reduction in unit weight) and the development of such concrete with sintered aggregate minimised the consumption of granite rock, resulting in protection of the natural environment. M 20 and M 25 grade concretes were studied. It is observed that, with partial (20%, 30% and 40% by volume) replacement of natural granite aggregate by sintered aggregate; the important physical properties of concrete such as compressive strength and Young.s modulus of elasticity were retained. In addition to the light weight characteristics, sintered flyash aggregate concrete possessed strength and deformation characteristics similar to concrete with natural granite aggregate.

An experimental program was carried out to obtain the compressive strengths and elastic moduli of cold-bonded pelletized lightweight aggregate concretes [47]. Three types of aggregates were made with different fly ash contents. The water/binder ratio and the properties of lightweight aggregate were two important factors determining the compressive strength and elastic modulus of lightweight aggregate concrete. When aggregate volume fraction was 18%, the compressive strengths and elastic moduli of the concrete were independent of the aggregate type, being mainly controlled by the water to cement ratio of the paste.

The laboratory works covered properties of cold-bonded lightweight aggregates produced from fly ash [48, 49]. Different groups of mixtures were used: only fly ash and lime replaced fly ash and cement replaced fly ash. Lime and cement addition improved the mechanical properties of the final product. Lightweight aggregate concrete specimens were also produced and physical and mechanical properties were tested. Overall, the engineering

performance of the fly ash pellets was found to be adequate for non structural and structural applications.

Faust and König [50] investigated both components of lightweight aggregates and mortar matrix in detail in order to achieve a deeper understanding of the internal stress transfer and the failure mechanisms. Oven-dry density and compressive strength spectrum of lightweight aggregate concrete is illustrated in Figure 2.3.

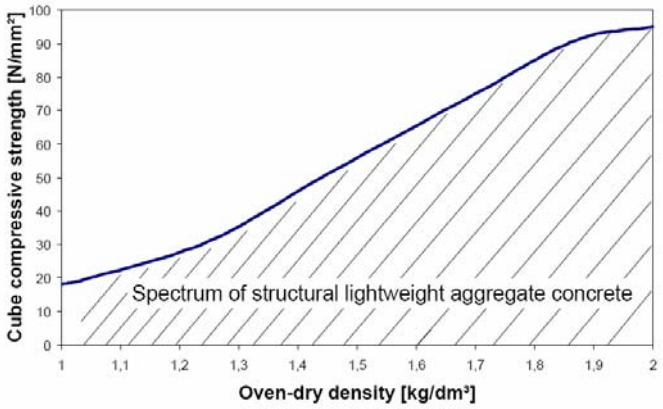

Figure 2.3. Spectrum of lightweight aggregate concrete [50]

2.9.2. Durability of Lightweight Concretes

Researchers [37, 38] reported that depth of water penetration, which was indicative of the concrete's permeability and hence durability, was found to be more sensitive to the duration of initial curing even for the specimens exposed to the high-humidity seaside ambient conditions. The water penetrability of LWACs seemed to be more sensitive to the extent of initial curing than it was for NWC. The water penetrability of LWC50 after 7 days of initial curing and subsequent exposure to the seaside was about 1/3 more than that of the NWC50 in the same exposure condition. The depth of carbonation, sulfate, and chloride penetration, and concentration in LWC50 were somewhat higher than that in NWC50 under similar exposure regimes.

Kayali and Zhu [51] prepared reinforced lightweight aggregate (Lytag) high-strength concrete slabs to determine chloride ion ingress, corrosion potentials, corrosion current density and electrical resistivity. These slabs were compared with slabs from normal

weight concrete of medium and high-strength. The results indicated that lightweight high-strength concrete slabs with fly ash in the concrete mixture showed the least amount of chloride concentration. Values of corrosion current density were very low and values of electrical resistivity were very high and indicative of extremely low corrosion current. The dense matrix of the lightweight high-strength concrete is believed to restrict continuous pores that may carry chloride ions. The effect of fly ash in lowering the chloride diffusivity further contributed to reduce harmful chloride ions. In addition, the porous sintered fly ash aggregates are believed to have acted as buffer reservoirs for the chloride laden solution and thus prevented the chloride ions from reaching the steel surface.

It is stated that the introduction of furnace bottom ash into concrete would cause detrimental effect on the permeation properties of concrete [43]. LWC incorporating FBA and Lytag resulted in an increase in the permeability; by replacing 30% of ordinary portland cement with FA, the permeability of LWC could be improved. In order to manufacture durable LWC, measures should be taken to further improve the permeation property.

A new patented lightweight aggregates is tested [14]. Lower carbonation and lower chloride penetration that were observed in lightweight concrete made from sintered and crushed fly ash aggregates are attributed to the strong bonding characteristics that develop in the interfacial zone between the aggregates and the cement paste. The interface in this concrete is therefore, no longer a site of de-bonding and crack propagation. The low carbonation depth and chloride ion penetration point to advantages in using this type of lightweight concrete in aggressive climatic zones and in off-shore structures.

In any composite material, the properties of the constituents and the interactions between them determine the behaviour of the material [52]. Concrete is a composite material with coarse and fine aggregates embedded in a cement paste matrix. As such, the aggregate and the cement paste as well as the interfacial zone between them affect the mechanical behaviour and permeability, thus durability of concrete. In concrete, it is generally not the porosity but the pore structure that is essential in establishing the permeability. In addition to that, microcracks in the matrix may contribute significantly to the permeability. Figure 2.4. shows the difference between porosity and permeability

schematically, and it indicates that the connectivity of the pore system is a prerequisite for permeability (i.e. an open pore system). A material can be porous and still perform tight as long as the pores are not interconnected (i.e. closed pore system). However, it is not clear if LWC has similar advantage over the NWC at high-strength levels as the interfacial zone of the high-strength NWC can be improved substantially by the reduction of water/cement ratio (w/c) and by the incorporation of silica fume.

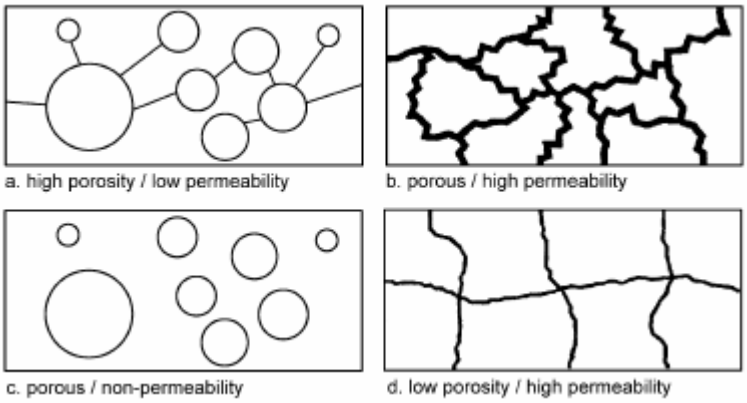

Figure 2.4. Schematic diagram showing differences between porosity and permeability [52]

3. PELLETIZATION AND SINTERING OF POWDER MATERIALS

3.1. Pelletization Theory

Agglomeration is a particle size enlargement technique which small, fine particles, such as dusts or powders, are gathered into larger masses, such as pellets [53]. Preferably, the mixture is agglomerated by pelletization, wherein fine particles dispersed in either gas or liquid are enlarged by tumbling, without other external compacting forces [7, 53]. A pelletizing rotating drum or disc may be used. The strength of the resulting pellets depends on the properties of the particles, the amount of moisture in the medium, and mechanical process parameters, such as the speed of rotation and angle of tilt of the rotating drum. The resulting pellets are nearly spherical or slightly angular, and vary in color from light to dark brown depending on the carbon and iron content in the mixes, they range in size from about 3 mm to about 40 mm. If a plastic binder is added to the mixture, coating is not needed to enhance pellet integrity or to form a coating, since the binder provides improved internal bonding. Coating is still an option, however. Drying may take place at about 110 ^{o}C in an oven. Drying is preferably provided because sintering wet pellets in a kiln may result in cracking and exploding of the pellets due to rapid temperature changes. Finer fly ash does not require any binder for achieving maximum pelletization efficiency [54].

Observations and analysis performed on these parameters with respect to mechanic and kinetic laws formed the theory of pelletization process. The essentials of the theory are as follows [55];

When a fine-grained material is moisturized, there forms a thin liquid film on the surface of the grains, which forms meniscus between the grains, structures like bridges (Figure 3.1a). In case the particles are rotated in a balling drum or disc, then they form ball shape structures with enhanced bonding forces between grains due centrifugal and gravitational forces (Figure 3.1b and c).

The strength of the pellets depends on the pelletization process parameters and finally the resultant magnitude of pressure being exerted on the pellets. Moreover, the

capillary forces (*P*, the surface tension generated by the height of liquid column) play a greater role in magnitude of coherence of the pellets. The capillary force is a function of particle diameter (*D*) and meniscus angle (β) between the particle and the liquid binder. The coherence of the structure is directly proportional with the mechanical and capillary forces exerted on the pellets (Figure 3.2).There exists three stages in pelletization process depending on the degree to which the intergranular spaces are filled with water;

- the pendular state, where the water is present at only the point of contacts of grains;
- the funicular state, where, in addition to the conditions present in pendular state, some of the pores are completely filled with water; and
- the capillary state, where all intergranular spaces are completely filled with water and no water film exists on the surface of the pellet. The most suitable state for pellet formation is capillary state, which enables the highest tension force be applied by binder between the particles.

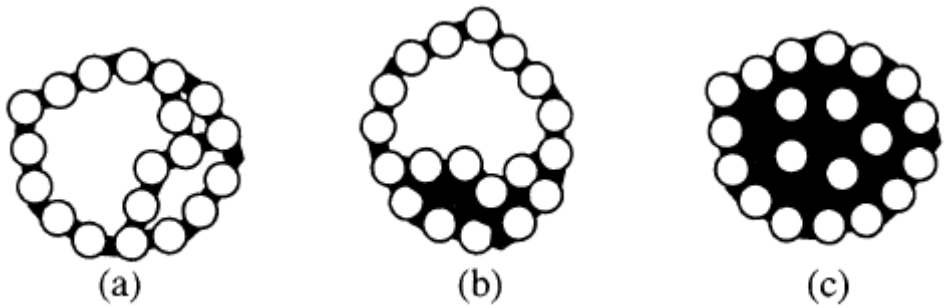

Figure 3.1. Mechanism of pellet formation [55]

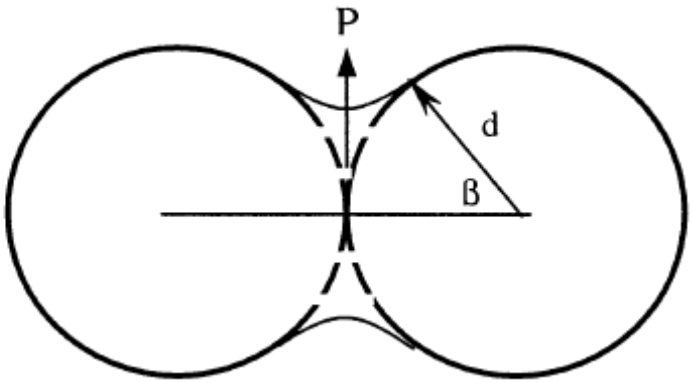

Figure 3.2. Schematic view of surface tension force created by water bridge between two particles [55]

Introducing the following assumptions and simplifications, the capillary and cohesive forces being exerted on the particles were formulized;

- all particles are spherical and have uniform diameters;
- the bonding pattern is uniform throughout the ball section;
- the particles in the ball are evenly distributed;
- effective bonding forces fluctuate around the average value.

Then, according to the above assumptions, following equation may be derived for cohesive forces in the capillary state;

$$P_c = 8*(1-\varepsilon)*\sigma/\varepsilon*D \tag{3.1}$$

where σ is the surface tension of the liquid, P_c is the cohesive force exerted on the structure in capillary state, ε is the ball porosity and D is the diameter of the spherical particle.

The theoretical studies on these parameters lead to the following equations in terms of the 'critical revolutions per min'. The term 'critical' stands to define the state where the gravitational and centrifugal forces are in equilibrium on the disc's plane;

$$m * g * \sin\beta + \mu * m * g * \cos\beta = m * R * w^2 \tag{3.2}$$

where m is the mass of the individual pellet, g is the gravitational acceleration, β is the angle of the disc's plane to normal in degrees, μ is the coefficient of friction between the pellet and the disc, R is the radius of the disc, w is the centrifugal acceleration in radians/t^2.

However, when the centrifugal acceleration and gravitational forces are in equilibrium then the normal force exerted by the pellet converges to 0 and Equation 2.8 simplifies into;

$$m * g * \sin\beta = m * R * W^2 \tag{3.3}$$

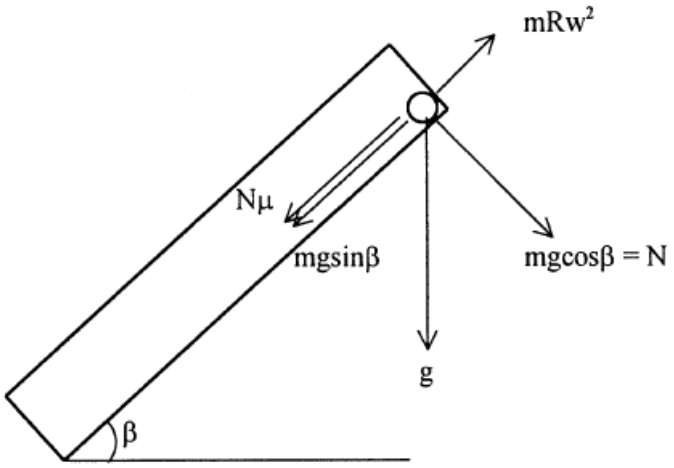

Figure 3.3. Forces acting on an individual pellet during pelletization process

and then the 'critical revolutions per min' is;

$$n_{cr} = 42.3*(\sin\alpha)^{1/2}*D^{-1/2} \quad (3.4)$$

where n_{cr} is the critical revolutions per min (rpm), D is the diameter of the disc in meters and α is the angle of disc inclination in degrees.

In the optimization studies, the parameters were: (i) speed of revolution of pelletizer disc, (ii) angle of pelletizer disc, (iii) moisture content, and (iv) duration of pelletization [55, 56]. The angle and revolution speed parameters were tried to be determined for the desired pelletization process. This was done by observing of pellet formation stages, the shape and apparent strength of pellets.

Binders play an important role in pelletizing. Binders help to (i) improve the ballability of the material, (ii) affect the green and dried strength of balls and fired strength of pellets, and (iii) adjust the chemical and mineralogical consistency and quality of fired pellets [8]. Conventional binders used in metallurgical process are bentonite, lime, cement, and some organic substances like dextrin, sulfate waste liquor, tars and alkali compounds.

3.2. Sintering of Powder Materials

3.2.1. Various Stages of Sintering

In recent years, the application of scanning electron microscopy and transmission electron microscopy with analytical capabilities to determine the microstructure and local composition of sintered products has allowed us to properly characterize the processes taking place [57]. These processes fall within the following categories. Solid state sintering that is grain growth and densification, occurs in many systems without the presence of a liquid phase during heating and at the firing temperature. Mass redistribution occurs by solid, surface and grain boundary diffusion or by a vaporization condensation process. Another class of products are made by viscous liquid sintering with a viscous liquid forming at the firing temperature allowing material redistribution and microstructure changes to occur by viscous flow. A final process is reactive liquid sintering in which a fluid liquid forms to enhance material transport and microstructure changes by processes of solution and precipitation. However, in other references [58, 59], chemical methods of ceramic powder preparation are classified as solid-state reactions, liquid-state sintering and vapour-phase reactions.

The basic model of thinking about ceramic sintering processes has been to apply phase equilibrium diagrams to determine the composition and amounts of the constituents present to apply ideas of capillary pressure as directing material transfer and grain growth and to evaluate material transfer processes such as volume diffusion, boundary diffusion, surface diffusion, viscous flow and solution-precipitation which lead to densification and microstructure changes.

Basically, sintering processes can be divided into two types [59]: solid state sintering and liquid phase sintering. Solid state sintering occurs when the powder compact is densified wholly in a solid state at the sintering temperature, while liquid phase sintering occurs when a liquid phase is present in the powder compact during sintering. Figure 3.4 illustrates the two cases in a schematic phase diagram." At temperature T_1, solid state sintering occurs in an A-B powder compact with composition X_1, while at temperature T_3, liquid phase sintering occurs in the same powder compact.

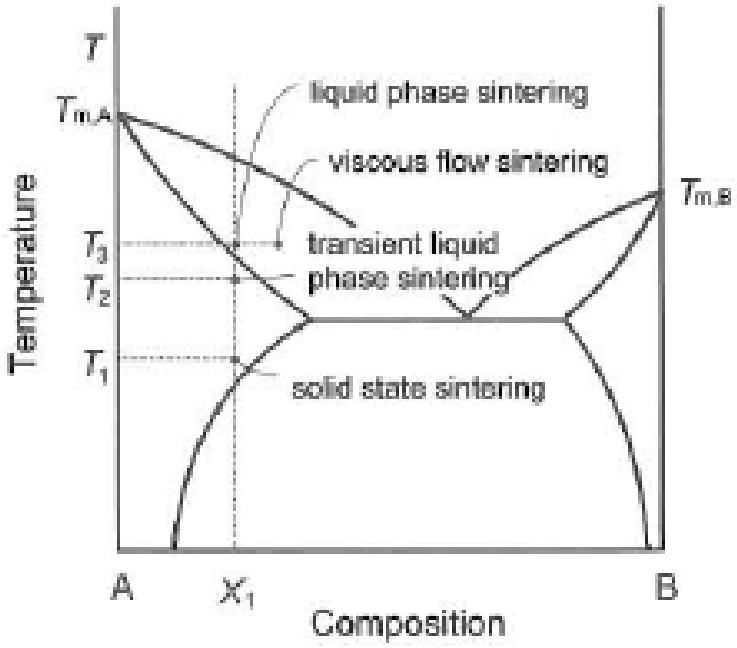

Figure 3.4. Illustration of various types of sintering [59]

Solid-state sintering: In this step, heating of the green compacts is carried out below the melting point which is generally 75 % of the absolute melting temperature [58, 60-62].When powders of metals, ionic crystals, or glasses are heated to temperatures near to their melting points, the powder particles weld together and the density of the compact changes. The process leads to a decrease in the surface area, an increase in compact strength and in many cases shrinkage in the compact. With prolonged high-temperature sintering there will be a decrease in the number of pores, the pore shape will become smooth and grain growth can be expected.

Liquid-phase and activated sintering: During liquid-phase sintering three stages-'rearrangement' or 'liquid flow', 'accommodation' or 'dissolution and reprecipitation' and 'coalescence' or 'solid phase bonding'-take place [58, 62]. These stages follow in the approximate order of their occurrence, but there may be significant overlapping for any specific system. Figure 3.5 shows the densification stages during liquid-phase sintering. With progress in liquid-phase sintering the densification kinetics is lowered. Increasing the liquid content up to approximately 35 vol. % aids initial densification. If the second stage is not effective, the melt will penetrate along the interparticle interfaces and cause particle separation, which contributes to swelling. A small dihedral angle inhibits coalescence of neighbouring particles. Activated sintering, in general, refers to process in which the

activation energy for sintering is lowered. This is mostly achieved by chemical addition to the powder.

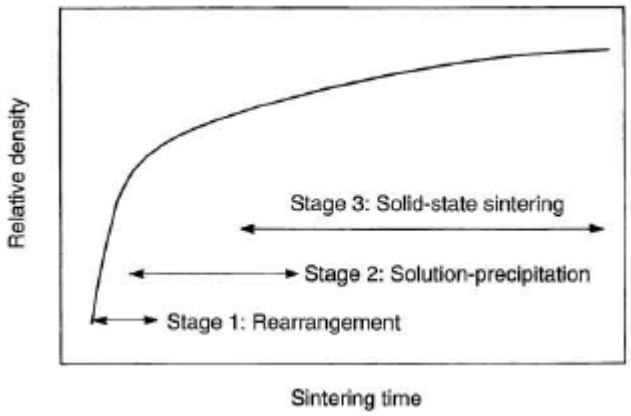

Figure 3.5. Schematic of three stages of liquid-phase sintering [58]

In addition to solid state and liquid phase sintering, other types of sintering, for example, transient liquid phase sintering and viscous flow sintering, can be utilized [59]. Viscous flow sintering occurs when the volume fraction of liquid is sufficiently high, so that the full densification of the compact can be achieved by a viscous flow of grain-liquid mixture without having any grain shape change during densification. Transient liquid phase sintering is a combination of liquid phase sintering and solid state sintering. In this sintering technique a liquid phase forms in the compact at an early stage of sintering, but the liquid disappears as sintering proceeds and densification is completed in the solid state.

3.2.2. Sintering Variables

In most cases, the sintering kinetics are determined by several parameters including pressed density, material, particle size, sintering atmosphere, temperature and even the degree of sintering [58, 62]. The major variables which determine sinterability and the sintered microstructure of a powder compact may be divided into two categories [59]: material variables and process variables. The variables related to raw materials (material variables) include chemical composition of powder compact, powder size, powder shape, powder size distribution, degree of powder agglomeration, etc. These variables influence the powder compressibility and sinterability (densification and grain growth). In particular, for compacts containing more than two kinds of powders, the homogeneity of the powder

mixture is of prime importance. To improve the homogeneity, not only mechanical milling but also chemical processing, such as sol-gel and coprecipitation processes, have been investigated and utilized. The other variables involved in sintering are mostly thermodynamic variables, such as temperature, time, atmosphere, pressure, heating and cooling rate.

Process Variables:

The most important factors involved during sintering process are temperature, time and furnace atmosphere [58, 62]. The influence of these factors on the sintering process is described below:

Sintering Temperature: Increasing the sintering temperature greatly increases the rate and magnitude of any changes occurring during sintering.

Sintering Time: Although the degree of sintering increases with increasing time the effect is small in comparison to the temperature dependence. The loss of driving force with increasing time at any temperature is one of the reasons why it is so very difficult to remove all porosity by sintering. An attempt should be made to achieve the desired properties of the sintered parts by shorter sintering times and correspondingly higher temperatures. However, the maintenance costs and energy consumption of a furnace increase when its operating temperature is raised.

Sintering Atmosphere: The main purpose for using a special sintering atmosphere is to provide protection against oxidation and reoxidation of sintered parts.

Material Variables:

The most important process before any characterization is accurate powder sampling [58]. Apart from particle appearance other important powder data required are:

- particle size and distribution
- particle shape and variations with particle size

- surface area
- interparticle friction
- flow and packing
- internal particle structure
- chemical gradients, surface films and admixed materials.

Particle Size: In terms of the basic stages of sintering, decreasing particle size leads to increased sintering [58, 62]. The smaller particle size has a greater pore/ solid interfacial area producing a greater driving force for sintering. It promotes all types of diffusion transport, e. g. greater surface area leads to more surface diffusion, small grain size promotes grain boundary diffusion and a larger interparticle contact area to volume diffusion.

Particle Shape: The factors that lead to greater intimate contact between particles and increased internal surface area promote sintering. These factors include decreasing sphericity and increasing macro- or microsurface roughness.

Particle Structure: A fine grain structure within the original particles can promote sintering because of its favourable effect on several material transport mechanisms.

Particle Composition: Alloying additions or impurities within a metal can affect the sintering kinetics. The effect can either be deleterious or beneficial depending upon the distribution and reaction of the impurity. Surface contamination, such as oxidation is usually undesirable. Dispersed phases within the matrix may promote sintering by inhibiting grain boundary motion. Reaction between impurities and either the base metal or alloying additions at the relatively high sintering temperature may be undesirable.

Green Density: A decreasing green density signifies an increasing amount of internal surface area and consequently, a greater driving force for sintering. Although the percentage change in density, increases with decreasing green density, the absolute value of the sintered density remains highest for the higher green density material.

Table 3.1 outlines some of the key processing changes and their effects [61]. No effort is made to detail all materials and processing variants, just some important principles.

Table 3.1. Sintering processing effects [61]

Change to Aid Sintering	Effects
Decrease in particle size	Faster sintering, Greater expense, Higher impurity level, Increased hazards
Increase in time	Greater expense, Grain growth and coarsening, Reduced productivity
Increase in temperature	Greater shrinkage, Grain growth, Greater expense, Less precision, Higher properties, Furnace limitations, Pore coarsening
Increase in green density	Less shrinkage, Smaller pores, Higher final density, Uniform dimensions, Density gradients
Increase in alloyingladditives	Higher strength,Homogeneity problems, Higher sintering temperatures
Use of sintering aids	Faster sintering, Lower sintering temperatures, Embrittlement, Distortion, Grain growth control

In a study [29], the researchers proved that sintering temperature had a more significant effect on aggregate characteristics than retention period. Sintering for 10 min was sufficient. However, increasing the retention period to 20 min would slightly improve the properties. In contrast, in another study [2], microstructural development increased with increasing sintering time at constant temperature.

It is notable that the alkali and alkaline content, Na_2O, K_2O, and CaO in particular, of fly ash can vary considerably. Since oxides of the alkali and alkaline metals are known to flux glass, such can greatly alter the sintering behavior of fly ash [2]. In an investigation [3], properties of different fly ash types were investigated and different results were obtained due to the difference in their physical and chemical properties. The properties of

the produced materials are dependent on the sintering conditions. The important variables in the sintering process are: The sintering temperature and time, the particle size and distribution of the powder, the composition of the system and packing pressure. Although the sintering time and packing pressure are the same for all fly ash samples during the sintering process, sintering temperature, particle size and chemical composition of the fly ash samples are different from each other. Moreover, the heating rate is a very important factor to be studied in detail as the manufacture of LWA process involves rapid sintering conditions of FA porous bodies [63].

3.2.3. Dimensional and Microstructural Changes

The fundamental process of sintering leads to a reduction in volume because of pore shrinkage and elimination [62]. Following factors in this regard may be considered:

Entrapped Gases: The expansion of gas in closed porosity has been postulated as producing compact expansion.

Chemical Reactions: Hydrogen is a common component of sintering atmospheres and can often diffuse through the metal to isolated portions of the compact where it reacts with oxygen to form water vapour. The pressure of the water vapour can lead to expansion of the entire mass. It is also possible to have reactions that lead to the loss of some element from the sinter mass to the atmosphere, such as volatilizing, and result in a shrinkage of the material.

Alloying: Alloying that may take place between two or more elemental powders very often leads to compact expansion. This effect which is due to the formation of a solid solution is often offset by shrinkage of the original porosity. Dimensional changes may also occur in a binary system where the rate of diffusion of each metal into the other is different.

Shape Changes: Green parts invariably contain variations in green density. Such variations can lead to substantial changes in shape because of the strong dependence of sintering, especially shrinkage, on green density. Low green density regions will exhibit a

greater amount of shrinkage during sintering. For example, a cylinder with a relatively high L/ D ratio compacted by a single action method would have a gradually decreasing green density from one end to the other.

Grain growth is the most important one for sintering. There is normally a large driving force for grain growth. Porosity in green compacts and in the developing sinter mass represents a very effective hindrance to grain growth. The addition of other component in the powder blend may drastically hinder bonding between adjacent particles and the formation of grain boundaries (Figure 3.6). Grain boundary grooves, may also tend to inhibit grain growth, since the movement of grain boundary away from its groove leads to an increase in grain-boundary area and energy. The control of grain growth so that grain boundaries do not pull away from pores is an essential part of sintering to zero porosity. The more nonuniform the grain structure is, particularly if it develops discontinuous grain growth, the earlier in the sintering process is the separation of pores from grain boundaries likely to occur. It is therefore important to have as uniformly sized a starting powder as possible, so as to reduce this tendency. Many times a proper additive also plays a vital role.

Many types of phase transformations may occur in the solid state during sintering at a constant temperature or during the cooling from the sintering temperature. Porosity and fine grain structure influence on the transformation.

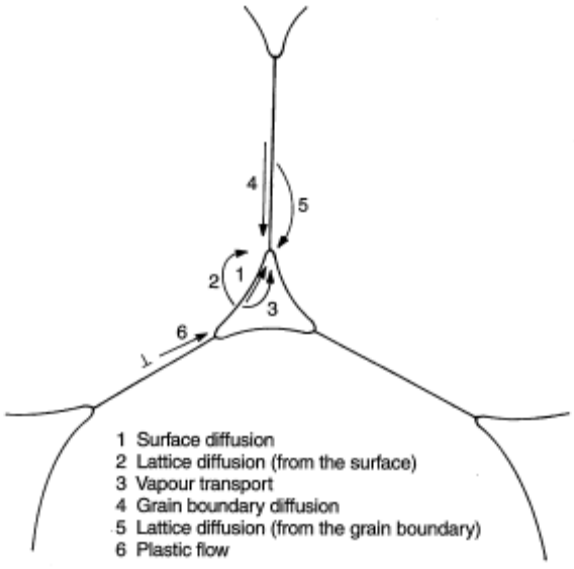

Figure 3.6. Various sintering mechanisms [58]

As material transport takes place, the geometric progression can be divided into a number of stages representative of driving forces [58, 62]:

- Initial bonding among particles
- Neck growth
- Pore channel closure
- Pore rounding
- Pore shrinkage
- Pore coarsening

The stages of sintering refer to geometric categories for analyzing the mass flow process as outlined in Table 3.2 [61].

Table 3.2. Classic stages of sintering [61]

Stage	Process	Surface Area Loss	Densification	Coarsening
Adhesion	Contact formation	Minimal unless compacted at high pressures	None	None
Initial	Neck growth	Significant up to 50% loss	Small at first	Minimal
Intermediate	Pore rounding and elongation	Near total loss of open porosity	Significant	Increase in grain size and pore size
Final	Pore closure, final densification	Negligible further loss	Slow and relatively minimal	Extensive grain and pore growth

For most cases the starting point is an assembly consisting of contacting particles [61]. Depending on the fabrication of the particle compact, the initial bonds range from point contacts to highly deformed interfaces. With sintering the contacts grow in size. and

in the initial stage there is extensive loss of surface area. As illustrated in Figure 3.7, as the pore structure becomes rounded the discrete particles are less evident and the intermediate stage of sintering occurs. This is characterized by a tubular, rounded pore structure that is open to the compact surface. Gas can permeate through the open pore space. Consequently. many sintered structures are sintered to this stage only to preserve desirable pore structures. In a crystalline solid the grain boundaries are usually attached to the open pore structure. As the pores shrink, a final stage of sintering occurs. Now as the density increases the pores spheroidize and are no longer connected to the compact surface. These are termed closed pores and any gas trapped in the pores proves difficult to remove. Since open pores are more effective in retarding grain growth, the transition to final-stage sintering gives less grain boundary pinning and usually results in rapid grain growth. As full density is approached, the compact continues to exhibit grain growth. There are many variants to this basic process, but the three stages provide a convenient definition for the morphology progression. For some structural materials all three stages are encountered, while for porous structures sintering is usually terminated in the intermediate stage.

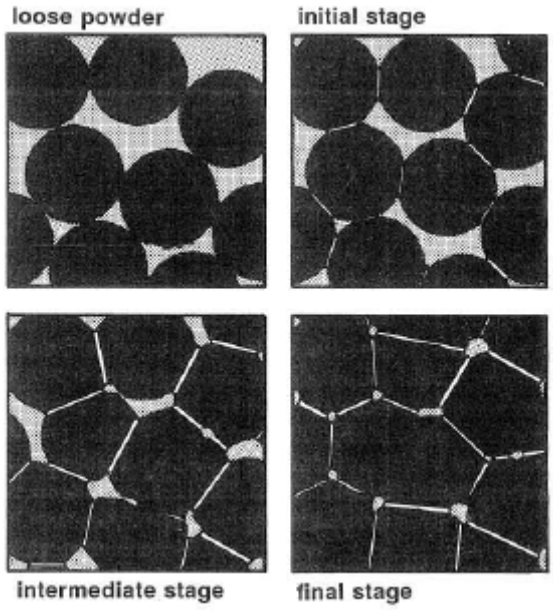

Figure 3.7. Sintering stages starting with a loose powder and subsequently being sintered in each of the three stages [61]

On a microstructural scale, sinter bonding is evident as cohesive necks grow at the particle contacts [61]. Figure 3.8 is a scanning electron micrograph of the solid-state neck

formation between sintering spheres. Particles sinter by atomic-level events that eliminate surface energy. Thus a first vision of a model for the rate of sintering would include surface energy and atomic mobility.

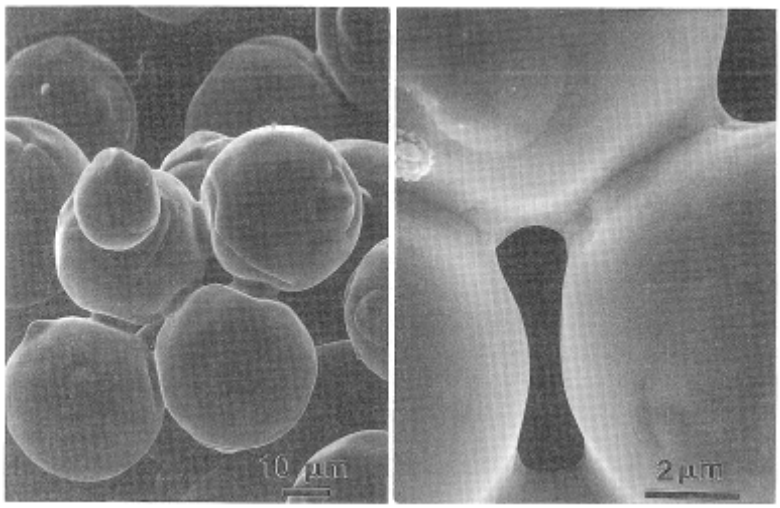

Figure 3.8. Scanning electron micrograph of sinter bonds formed between spherical particles originally in point contact [61]

During sintering the surface area *S* declines from the initial value S_o. The loss of surface area is measured by the dimensionless parameter $\Delta S/S_o$ [where $\Delta S/S_o = (S_o - S)/S_o = 1 - S/So$]. which also provides a gauge of the degree of sintering. The surface area can be measured by microscopic analysis, gas adsorption, or gas permeability techniques [61].

Another measure of sintering is the relative neck size ratio X/D, defined as the neck diameter divided by the particle diameter, as illustrated in Figure 3.9. Note that each particle is composed of atoms, usually in crystalline arrays. The neck then contains a zone of disrupted atomic bonding where the crystals meet, termed a grain boundary. Sintering depends on how atoms move to grow the neck. Thus, in addition to undergoing neck growth, a sintering compact can shrink, densify, and increase in strength. However, densification is not a necessary aspect of sintering. Interparticle neck growth, with a loss of surface area, occurs in some powder compacts without a density change. A frequent measure of sintering is the linear dimensional change, designated as a shrinkage $\Delta L/L_o$. It is the change in a compact dimension divided by the initial dimension.

Often, isotropic shrinkage is assumed in sintering, where the compact densifies from the initial green fractional density V_G to the sintered density V_s as follows:

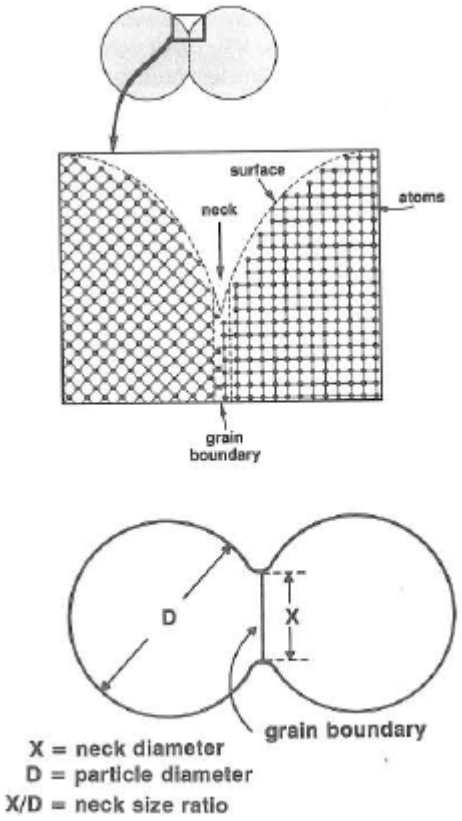

Figure 3.9. Definition of the neck size ratio X/D in terms of the two-particle sintering geometry [61]

$$V_s = V_G / (1-(\Delta L/L_o)^3 \quad (3.5)$$

Figure 3.10 plots the relation between linear shrinkage and green density as a percent of theoretical for two final density levels, 95 and 100%. A low initial packing density results in considerable dimensional change during sintering if high final densities are to be obtained. It is this dimensional change that warps many sintered structures. Thus, although a high density is desirable, there is also a benefit to a low sintering shrinkage for dimensional control. These constraints usually lead to an emphasis on a high green density. Equation can be rearranged to express shrinkage as a function of the density ratio V_s/V_G emphasizing the relative density effect on sintering shrinkage. The densification parameter ψ is the change in density due to sintering divided by the change needed to attain a pore-free solid:

$$\psi = (V_s - V_G)/(1 - V_G) \tag{3.6}$$

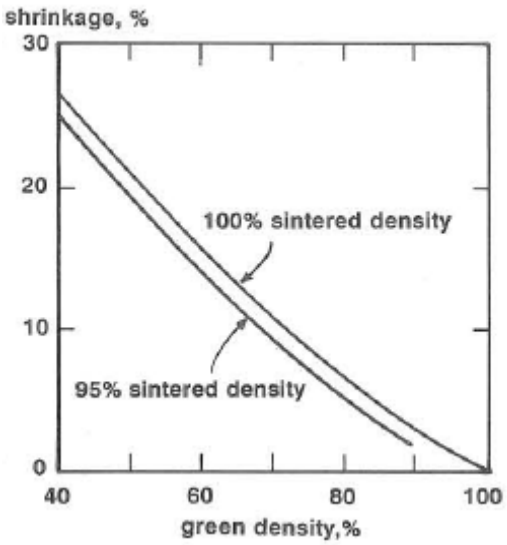

Figure 3.10. Shrinkage as a function of the green density for final density levels of 95 and 100% [61]

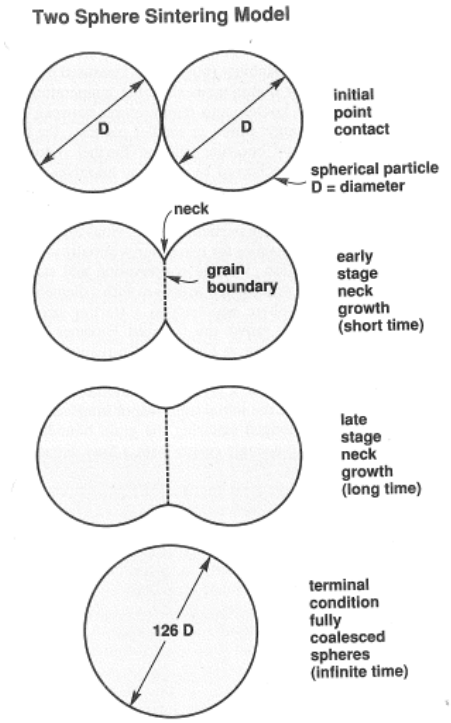

Figure 3.11. Two-sphere sintering model with the development of the interparticle bond during sintering, starting with a point contact [61]

Neck growth between contacting particles is an obvious aspect of sintering [61]. Figure 3.11 illustrates the neck profiles for two spheres initially in point contact at various levels of densification. Volume conservation and surface energy minimization dictate a final geometry of one sphere with a diameter 1.26 times the initial diameter. A two-sphere geometry is a starting point for many sintering models. As the neck grows the compact becomes stronger as a bonded network emerges, as shown in Figure 3.8.

Grains are pulled into contact by a wetting liquid, allowing coalescence at points of contact [61]. A sketch of a possible coalescence mechanism is given in Figure 3.12. Contacting grains of dissimilar size fuse into a single grain by a continuous process of directional grain growth: grain reshaping, and grain rotation. The reshaping process is by concurrent solution-reprecipitation. The grain size grows by coalescence while the number of grains decreases continuously.

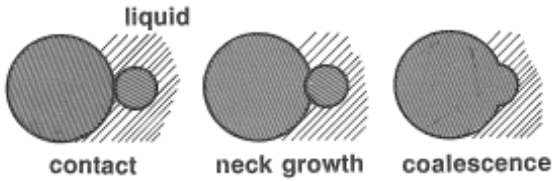

Figure 3.12. Steps leading to grain growth by coalescence of small and large grains [61]

The filling of large pores requires grain growth and grain shape accommodation. It usually begins near the component center and spreads outward when the sintered density reaches about 80% of theoretical. The higher the contact angle, the greater the difficulty in removing residual pores. As illustrated in Figure 3.13, liquid flow into the large pores depends on grain growth. A large pore remains unfilled because of preferential capillary wetting of the smaller intergrain spaces. However, during grain growth the liquid reaches a favorable condition for refilling the pore as determined by the curvature at the solid-liquid-vapor interface.

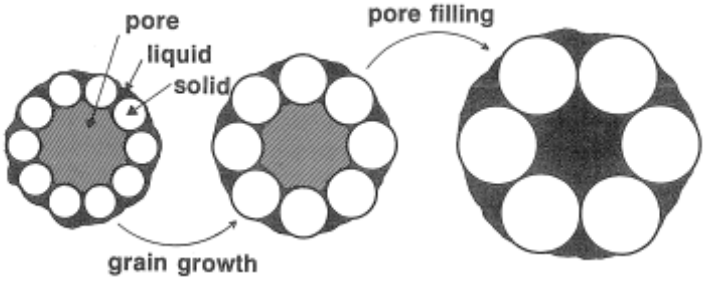

Figure 3.13. Pore filling during grain growth [61]

Figure 3.14 shows how pore structure changes with sintering [58, 61 and 62]. In the latter stage of sintering, interaction between pores and grain boundaries can take one of the following forms: the pores can retard grain growth, they can be dragged by the moving grain boundaries during grain growth or the grain boundaries can break away from the pores, leaving them isolated in the grain interior. Separation of pores from the boundaries limits the final sintered density. It is therefore important to minimize breakaway by careful temperature control during sintering. Figure 3.15 illustrates how a combination of large pore size and large grain size leads to a breakaway during grain growth. The selection of a correct isothermal sintering temperature is important in successful densification. Higher temperatures lead to faster densification, but the rate of coarsening also increases. This increased coarsening rate may lead to abnormal grain growth with pores trapped inside large grains. Thus, although densification proceeds faster, the final density may be limited. The boundary curvature between grains and phases depends on the value of the dihedral angle and on the number of surrounding grains. Since grain boundaries migrate towards their centres of curvature, grains with fewer than six sides tend to shrink, and those with more than six sides tend to ground (Figure 3.16).

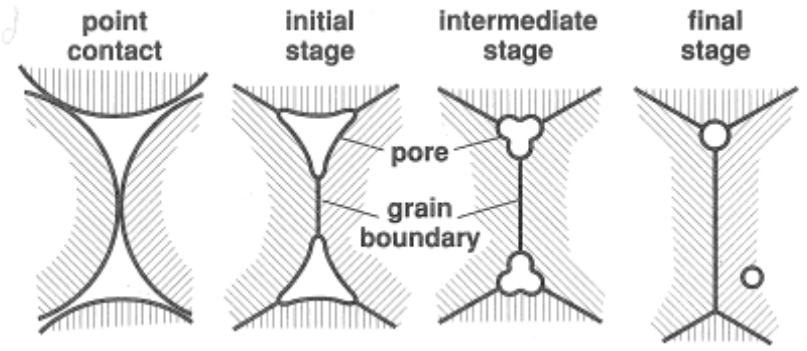

Figure 3.14. Various sintering stages [61]

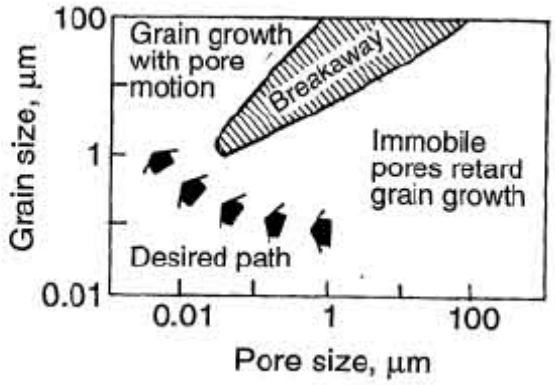

Figure 3.15. Variation of grain size versus pore size during sintering, showing the condition for breakaway from the pores [58]

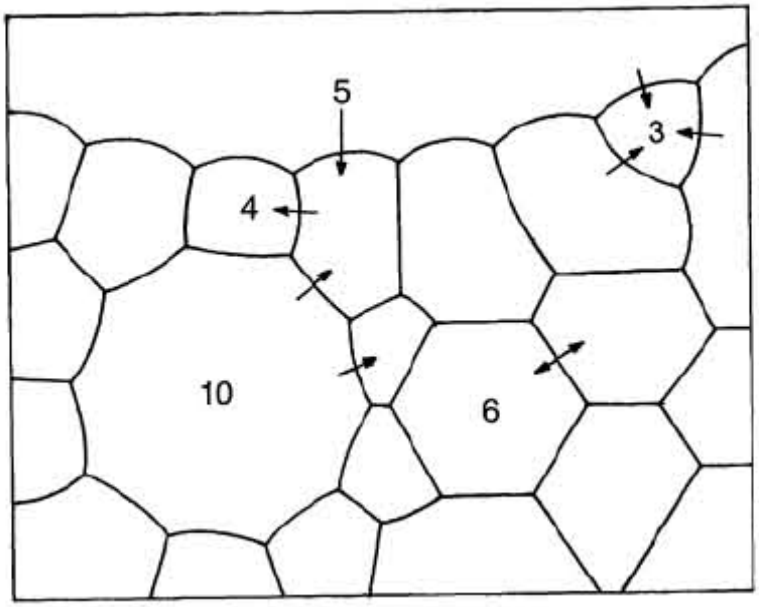

Figure 3.16. Schematic showing how the sign of curvature changes with the number of sides in a grain [58]

The surface curvature of the grains around an isolated pore is affcted by their number and the dihedral angle between them [59]. Figure 3.17 illustrates schematically the three types of surface curvature associated with various numbers of grains for a two-dimensional system and a dihedral angle of 120^{o}.

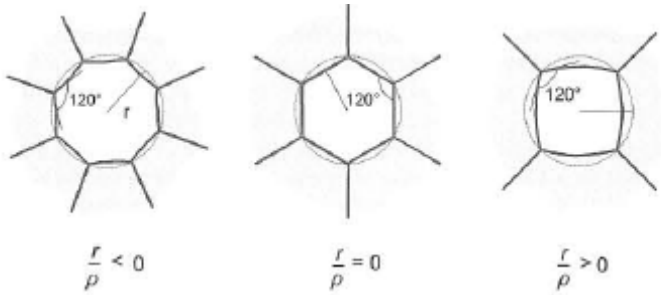

Figure 3.17. Variation of pore shape with the number of surrounding grains. Dihedral angle assumed to be 120^{o} [59]

4. EXPERIMENTAL STUDY

The study is divided into two parts; the first one is investigating the lightweight fly ash aggregate properties, the second one is about the effects of aggregate properties on the lightweight agregate concrete performance.

In the first phase of the study, the influence of different sintering binders and temperatures on the properties of lightweight fly ash aggregates was reported. Specific gravity, water absorption, porosity, thermal behaviour, crushing strength and microstructural changes (crystal structure and morphology to explain the reason of the results) of lightweight aggregates were determined. The optimal production combinations that would maximize both the porosity and strength while keeping the specific gravity minimum were found by employing Response Surface Methodology (RSM) to relate the aggregate manufacturing input parameters (temperature, sintering agent type and content) to the responses such as specific gravity, porosity, water absorption and strength. The selected aggregate types were used in concrete productions.

In the second phase of the study, the influence of different lightweight fly ash aggregates on the behaviour of concrete mixtures was discussed. The performance characteristics of the lightweight concretes and the normal weight concrete were investigated through compressive strength, modulus of elasticity, and splitting tensile strength representing the mechanical behavior; through water permeability and rapid chloride permeability representing the transport properties and through accelerated corrosion of embedded rebars and rapid freeze/thaw cycling representing the durability of concrete. In order to investigate the aggregate-cement matrix interfacial transition zone, SEM observations were performed. Regression and graphical analysis of the experimental data obtained were also performed. Analysis of variance (ANOVA) is a useful technique for analyzing experimental data. Thus, a software TableCurve 3D V4.0 was used for analyzing hardened concrete properties. The software offers a large number of graphical and numerical tools to enable the user to choose the best equation for particular needs. The validity of predicted values of different models specified by standards and literature, derived in this study and suggested by software was compared and discussed.

4.1. Properties of Materials Used in Aggregate Production

The fly ash used in this study was provided by Çatalağzı thermal power plant in Zonguldak, bentonite was supplied from Doğal Bentonit San. Tic in Çankırı, glass powder was obtained by grinding crushed window glass, portland cement (CEM I 42,5 R) was provided by Akçansa cement factory and silica fume was provided by YKS.

Chemical composition of cement, fly ash, bentonite, glass powder and silica fume are exhibited in Table 4.1. Physical properties, the results of compressive strength and pozzolanic activity tests of cement and fly ash determined according to TSE 639 are shown in Table 4.2 and Table 4.3, respectively. The compressive strength and pozzolanic activity test with Portland cement specified within TSE 639 involves replacing a portion of portland cement in a cement mortar with fly ash. Specimens are moulded and then cured as specified in TS 24. The compressive strength is then compared with standard specimens. TSE 639 specifies that the strength of test specimen must not be less than compressive strenghts of control specimens in 7 and 28 days for compressive strength test and must have a minimum of 70 % of the 28-day strength of the control for pozzolanic activity test. High-calcium fly ashes that have their own activators and are already cementitious perform better in this test than low-calcium ashes. As can be seen in Table 4.3, the results met the requirements specified in TSE 639 for both compressive strength and pozzolanic activity tests. Quantachrome-NOVA 2200e BET (Brunauer Emmett–Teller) method was used to determine specific surface area from N_2 adsorption isotherms. The BET method is commonly used on powders to obtain reliable surface area measurements (< 10% error) and was used to determine the surface areas of cement and fly ash. This technique injects liquid nitrogen into a container holding the powder sample and assumes that the gas adsorbs onto the powder in multiple uniform layers. Pressure is decreased over time and the volume of gas for each pressure change is plotted to obtain an isotherm. The isotherm represents the point at which an equal amount of gas is being absorbed and released. The intercept of the isotherm provides the volume of gas absorbed onto the sample. Surface area can be calculated by knowing the gas molecule size and number of molecules in the measured volume of gas. Fly ash used in the study conforms to Class F specified in ASTM C 618 which is shown in Table 4.4. Particle size distribution of raw materials is illustrated in Figure 4.1. Mastersizer was used to determine the grading curves of materials by laser

diffraction. Subsamples of less than 1g were taken from the powder samples using standard powder-handling techniques so that representative samples were obtained, and then run through the Mastersizer 2000 laser diffraction instrument. The Mastersizer is capable of fine particle measurements of < 1 μm diameter to 2000 μm, although data below 10 μm diameter becomes increasingly unreliable. Measurements are obtained by transporting the powder particles through a water-filled tube past a red and blue laser beam. When the laser beam encounters a particle the beam is diffracted and light is scattered at various angles and detected by a photodetector array. The light intensity depends on the scattering angle; laser diffraction by larger particles will produce low angles of scattering while diffraction by smaller particles will produce high angles of scattering. The Malvern instrument uses Mie theory to relate the amount of light energy detected to a particle diameter. Samples were run through the Mastersizer twice to obtain accurate results.

Table 4.1. Chemical composition of cement, fly ash, bentonite, glass powder and silica fume (% by weight)

Oxide (%)	CEM I 42,5R	Fly Ash	Bentonite	Glass Powder	Silica Fume
SiO_2	20,55	59,00	57,84	70,62	94,12
Al_2O_3	4,78	19,58	13,77	1,38	0,57
Fe_2O_3	3,64	7,23	6,14	0,82	0,55
CaO	63,94	0,54	3,75	8,75	0,50
MgO	1,50	4,64	3,04	3,54	1,30
SO_3	2,77	0,69	1,34	1,85	0,42
Na_2O	0,25	0,48	2,80	10,85	0,54
K_2O	0,77	5,95	2,80	1,53	1,75
Cl^-	0,0350	0,0114	0,0035	0,0025	0,0049
Loss on ignition	1,24	0,49	8,40	0,12	0,19
$CaCO_3$+$MgCO_3$	-	-	6,50	0,75	-
Insolubleresidue	1,36	-	-	-	-
Free CaO	1,25	-	-	-	-
Specific Gravity(gr/cm^3)	3,16	2,06	2,40	2,50	2,28

Table 4.2. Physical properties of cement and fly ash

		CEM I 42,5R	Fly ash
Retention on sieves (%)	45μm	12,0	45,2
	90μm	1,7	25,3
	200μm	0,1	6,5
Specific gravity (gr/cm^3)		3,16	2,06
Specific surface area (m^2/gr)		3,27	2,88
Setting time (min)	Initial	139	-
	Final	188	-

Table 4.3. Compressive strength and Pozzolanic activity tests

		Control Specimen	Compressive Strength Test	Pozzolanic Activity Test
Materials (gr)		Cement	Flyash+Cement	Flyash+Cement
Cement Content (gr)		450	450	293
Fly ash Content (gr)		-	112	104
Sand Content (gr)		1350	1233	1350
Water Content (gr)		225	225	199
Compressive Strength (N/mm^2)	2 days	26,9	28,8	-
	7 days	40,9	43,9	-
	28 days	54,0	59,8	42,6
2 –day percentage			107,06	-
7–day percentage			107,33	-
28–day percentage			110,74	78,89

It can be seen that fly ash is very coarse and glass powder is finer than fly ash, however much coarser than bentonite and cement. Bentonite and cement contain 33 % and 35 % of particles smaller than 10 μm, respectively. Glass powder and fly ash contain 21 % and 17 % of particles smaller than 10μm, respectively. It is revealed that cement is finely grained, with about 95 % of particles having sizes (d_{95}) of less than 100 μm. The fly ash is a coarse material with d_{50} values of 56 μm.

Table 4.4. Chemical properties of fly ash used and specifications

Properties	Fly ash used	ASTM C 618 (Class-F)
$SiO_2+Al_2O_3+Fe_2O_3$ (%)	85,81	70 (min)
MgO (%)	4,64	5 (max)
CaO (%)	0,54	<10
SO_3 (%)	0,69	5 (max)
Loss on ignition %	0,49	6 (max)

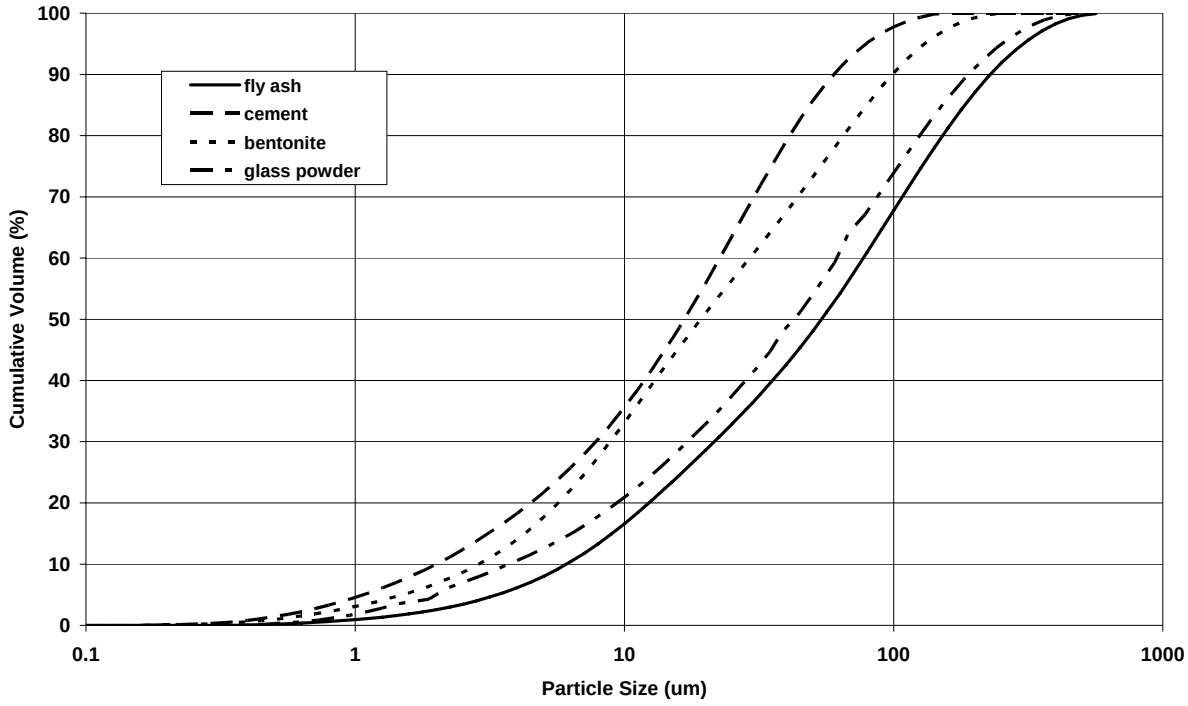

Figure 4.1. Particle size distribution of fly ash, cement, bentonite and glass powder

4.2. Preparation of Lightweight Aggregates

The pellets were produced by a pelletization disc. The angle was fixed at 43^o and speed was 45 rpm based on the findings of a previous study [48] on the optimal speed and angle of the pelletization disc used. The diameter and height of the pelletizing disc were 40 cm. and 15 cm, respectively. The different amounts of binders were mixed with fly ash for producing sintered lightweight aggregates. Binders like bentonite (B) and glass powder (G) were added as sintering agents at 5 % and 10 %, individually, by weight of fly ash (FA). Fly ash without a binder and fly ash with the combination of these two binders (B 7,5 %+G

7,5 %) were also used for making pellets. Additionally, a mixture of fly ash and 10% portland cement as replacement of fly ash, by weight, was prepared for producing lightweight aggregates through cold-bonding process. After putting the powder mixture into the pelletization disc, water was sprayed onto the powder mixtures with a quantity of 22-25 % of the total material in order to form spherical pellets (22-23 % in bentonite and bentonite-glass powder combination; 24-25 % in only fly ash, glass powder and fly ash plus cement). The amount of water to be added is related to the amount of fly ash in the mixture. When more fly ash was used, more water was required. Less water was used when bentonite was included. Addition of glass powder did not alter the water content.

Irregular particles were obtained when 15 % bentonite was added into the fly ash mixture. An increase in dosage of bentonite beyond this level resulted in sticking of pellets to each other leading to formation of muddy balls, which was attributed to high plasticity index of bentonite also indicated in another study [54]. Lesser amount of bentonite requirement may be attributed to higher expansive nature of three-layer montmorillonite structure in the bentonite. Also, pelletizing fly ash with 15 % glass powder resulted in particles with larger diameter. For these reasons, in this study, the upper limits of contents for both bentonite and glass powder were selected as 10 %. In addition, insufficient water led to difficulty in pelletization and surplus water caused bigger and irregular particles. The latter observation was also confirmed by Chiou [29]. Therefore, the amount of water needed for pelletisation was affected by the characteristics of the mixture and the pelletizing methodology.

The pelletizer pan was continued to rotate until the firm spherical pellets have been formed which took approximately 20 minutes. The pelletizing time was kept constant for each mixture. After pelletization, fly ash-cement mixture aggregates were put in plastic bags and maintained in a curing room at 25 ^{o}C temperature and 70 % R.H. for cold-bonding. The other pellets were first put in a furnace to be dried at 110 °C, drying was provided because sintering wet pellets in a kiln may result in cracking and exploding of the pellets due to rapid temperature changes and then sintered for 1 hour at three different temperatures (1100, 1150 and 1200 °C) with a heating rate of 6.7 ^{o}C/ min. Then, the aggregates were left in the furnace to cool in a slow rate. The heat increase in the furnace is

shown in Figure 4.2. The schematic illustration of aggregate production is presented in Figure 4.3.

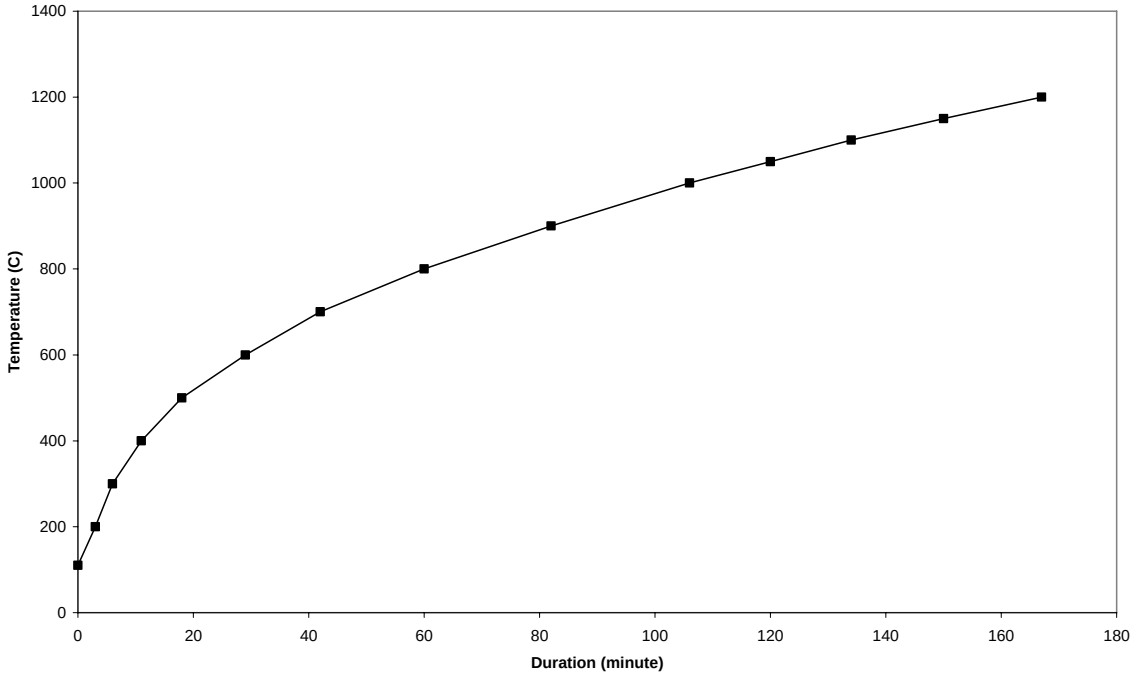

Figure 4.2. Heat increase profile in the furnace

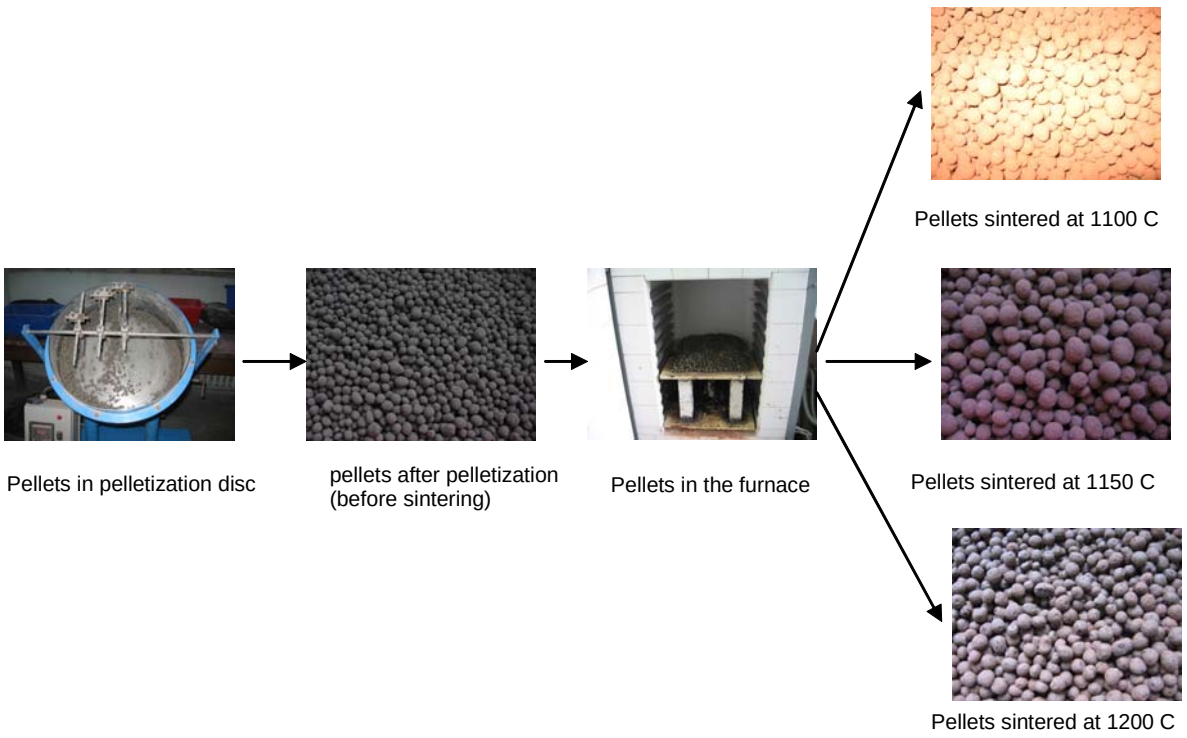

Figure 4.3. Production of lightweight fly ash aggregates

Notation (designation) for the aggregates produced is such that the letters OFA, B, G and BG indicate the type of materials used in the preparation of pellets as only fly ash, bentonite added, glass powder added and bentonite and glass powder added, respectively. The preceeding number represents the weight ratio (% by weight) of the added binders and the following number is for the sintering temperature. Also, CB represents the cold-bonded lightweight fly ash aggregates. Treatments and notations of agregates are given in Table 4.5.

Table 4.5. Treatments and notations of aggregates

Composition	Sintering Temperature (^{o}C)		
	1100	1150	1200
100% Fly Ash	OFA1100	OFA1150	OFA1200
5% Bentonite	5B1100	5B1150	5B1200
10% Bentonite	10B1100	10B1150	10B1200
5% Glass Powder	5G1100	5G1150	5G1200
10% Glass Powder	10G1100	10G1150	10G1200
7.5% Bentonite and Glass Powder	7.5BG1100	7.5BG1150	7.5BG1200
Cold Bonded (10% PC)	CB		

4.3. Tests and Analysis Performed on Lightweight Aggregates

4.3.1. Strength of Aggregates

In this study, strength of the lightweight fly ash aggregates was determined by measuring the crushing strength of the individual aggregate pellets by loading them diametrically. Also, aggregate crushing value test (ACV) was conducted on the aggregate pellets selected for the concrete production according to BS 812-110.

The individual aggregates were placed between two parallel plates and were crushed by being loaded diametrically between these parallel plates (Figure 4.4). The crushing force was measured by the load-ring with a 4.5 kN capacity.

Stress analysis shows that when spheres are compressed on diametrically opposed points the crushing strength σ is given by :

$$\sigma = \frac{2{,}8 * P}{\pi * \mathrm{X}^2} \tag{4.1}$$

where X is the distance between loading points and P is the fracture load [21, 22, 63 and 64]. Minimum 20 pellets with a diameter of approximately 10 mm were tested to calculate the average crushing strength for each aggregate type.

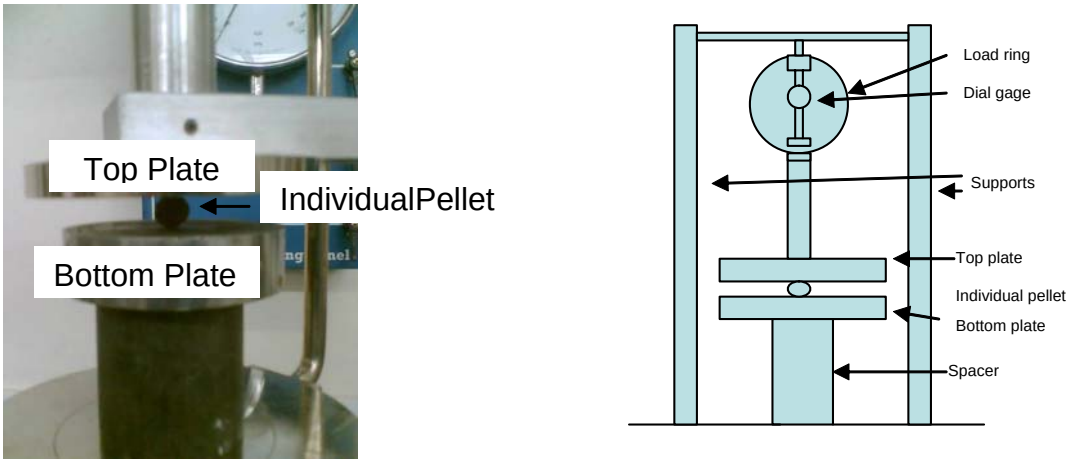

Figure 4.4. Individual pellet crushing test set up

4.3.2. Specific Gravity of Aggregates

Specific gravity is the characteristic generally used for calculating the volume occupied by the aggregate in various mixtures containing aggregate, including portland cement concrete, bituminous concrete, and other mixtures that are proportioned or analyzed on an absolute volume basis.

Specific gravity of lightweight aggregates were determined according to ASTM C 127. Specific gravity of aggregates was calculated as follows:

Specific gravity in oven dry (OD) condition;

$$\frac{m_d}{m_s - m_w} (\text{gr/cm}^3) \tag{4.2}$$

Specific gravity in saturated surface dry (SSD) condition;

$$\frac{m_s}{m_s - m_w} (\text{gr/cm}^3) \tag{4.3}$$

Apparent specific gravity;

$$\frac{m_d}{m_d - m_w} (\text{gr/cm}^3) \tag{4.4}$$

m_d = mass of oven-dry test sample in air, g,
m_s = mass of saturated-surface-dry test sample in air, g,
m_w = apparent mass of saturated test sample in water, g.

Specific gravity in the saturated surface-dry condition (SSD) is used if the aggregate is wet, that is, if its absorption has been satisfied. Conversely, the specific gravity in the oven-dry condition (OD) is used for computations when the aggregate is dry or assumed to be dry. Apparent specific gravity pertains to the solid material making up the constituent particles not including the pore space within the particles which is accessible to water.

4.3.3. Porosity of Aggregates

4.3.3.1. Open Porosity (Water Absorption) of Aggregates

Water absorption values of lightweight aggregates were determined according to ASTM C 127. The percentage of water absorption was calculated as follows;

$$\frac{m_s - m_d}{m_d} \text{x}100\ (\%) \tag{4.5}$$

m_d = mass of oven-dry test sample in air, g,
m_s = mass of saturated-surface-dry test sample in air, g,

4.3.3.2. Total Porosity (Mercury Porosimetry) of Aggregates

Pore structure (total porosity and pore size distribution) of aggregates was estimated by mercury porosimetry with a pressure applied up to 220 MPa. Mercury intrusion porosimetry (MIP) is a better measure of closed porosity of aggregates. Quantachrome-PoreMaster Mercury porosimetry was used to determine the total porosity of the lightweight fly ash aggregates.

Mercury intrusion measurements are extremely simple in principle, although a number of experimental complications need to be considered [65]. In the usual procedure, a small specimen is first dried to empty the pores of any existing fluid. It is then weighed, transferred to a chamber, which is then evacuated, and mercury is introduced to surround the specimen. Since mercury does not wet cementitious solids spontaneously, it does not intrude into empty pores unless pressure is applied. Pressure in progressive increments is then applied to the mercury, and the intrusion of mercury at each step is monitored. Assuming that the pores have a cylindrical shape, the diameters of the pores were computed according to Equation 4.6 using the pressure and intruded quantity of mercury [65-68],

$$d = -4*\gamma*\cos\theta/P \tag{4.6}$$

where d is the pore width, P is the net pressure across the mercury meniscus at the time of the cumulative intrusion measurement, γ is the surface tension, and θ is the contact angle between mercury and the pore wall. In this study, the values for γ and θ were 0.480 N/m and 141.3°, respectively

The porosity and the critical pore diameter were determined from the figures representing pore size distribution curves of each aggregate. If the pores are added to the

network one by one in order from largest to smallest, the critical diameter is the diameter of the pore that just completes the first connected pore pathway [69].

4.3.4. Differential Thermal Analysis (DTA)-Thermal Gravimetric Analysis (TGA)

Differential thermal analysis (DTA)- thermal gravimetric analysis (TGA) were used to characterize the thermal behavior such as glass transition, crystallization and melting temperatures of 20 mg of raw materials (glass powder, bentonite and fly ash) and aggregates with binders in a Pt-crucible and using Al_2O_3 as the reference material at a heating rate of 10 and 20 ^oC/min, respectively, under N_2 atmosphere with the flow rate of 40 ml/min. The instrument used was Perkin Elmer Diamond Thermogravimetric / Differential Thermal Analyzer (TG/DTA). In general, the DTA confirms and supplements the conclusions from the XRD analysis.

Thermal measurements are important in certain applications for sintered materials, but rarely are thermal properties used to follow sintering [61]. However, thermal characteristics do prove important in understanding reactions during sintering. For example, differential thermal analysis is helpful in determining the temperature of first melt formation during liquid-phase sintering. As illustrated in Figure 4.5, differential thermal analysis relies on two samples in the same thermal environment. Usually, the samples are surrounded by an inert or protective gas. One of the two crucibles holds the test powder while the other contains a standard, inert powder such as platinum or alumina. As the samples are heated, energy flows into both crucibles at the same rate and should give similar temperatures. By measuring the temperature difference between the two samples, any perturbations due to either exothermic or endothermic reactions can be detected by faster or slower heating of the sample.

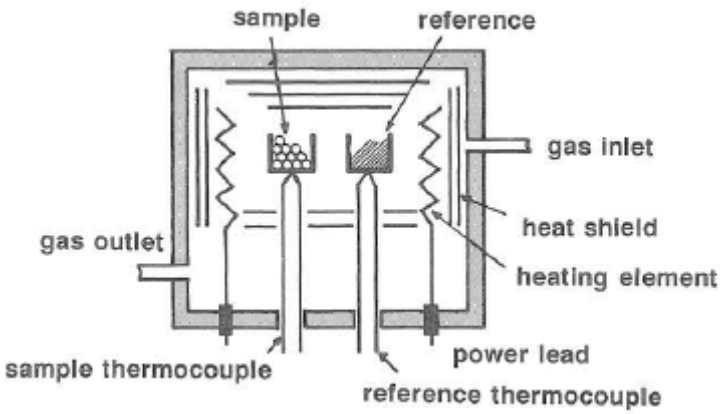

Figure 4.5. Differential thermal analysis is performed by heating the experimental powder in parallel with a reference sample [61]

Differential thermal analysis is a technique for measuring differences in heat flow in a sample [70]. A constant heating rate is used and a standard material (typically alumina) that undergoes no phase transitions in the temperature range of interest is used as the reference. The heat flow to the sample relative to the reference is recorded. When the sample goes through the glass transition temperature there is a change in heat capacity and there is an endothermic relaxation of the glass structure. As a result, the sample consumes more heat than the standard in this temperature range.

When the sample crystallizes, the atomic re-arrangement is an exothermic process, and the sample releases more heat than the standard. Glasses that do not crystallize during a DTA experiment might phase separate or simply form a homogeneous liquid when heated to $T>T_g$. A single temperature, T_g, is often used to indicate the glass transformation region. The crystallization temperature, T_x, of a glass represents the temperature at which a thermodynamically stable phase crystallizes from the melt. (Note that T_x is greater than T_g for all but very unusual systems.) Crystallization is an exothermic process than can be detected with a DTA. More than one phase can crystallize, and as such multiple crystallization exotherms can be detected for some samples. Subtle inflections in the DTA plot may indicate the presence of a diffuse exothermic peak associated with phase separation.

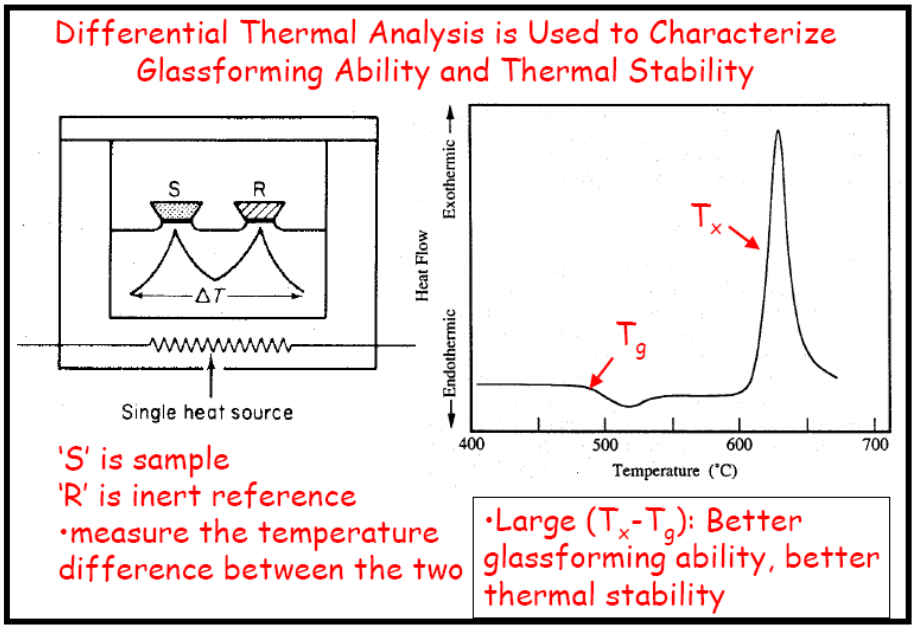

Figure 4.6. Differential Thermal Analysis [70]

4.3.5. Microstructural Analysis of Lightweight Aggregates

The X-ray diffraction (XRD) and scanning electron microscopy (SEM) tests were performed on specimens to justify and explain the experimental observations and results.

4.3.5.1. SEM Observations of Raw Materials and Lightweight Aggregates

At a basic level, SEM can be used as an adjunct to optical microscopy, for example to obtain high-magnification images of concrete fracture surfaces or to analyse material not identifiable by optical microscopy. SEM does this very well, but the full potential of SEM goes much further, especially in non-routine examinations [71].

The morphology, pore texture and pore size of aggregates and particle size distribution, shape and texture of raw materials were examined using scanning electron microscopy (SEM) installation (Philips XL30 ESEM-FEG) equipped with Backscattered Electron (BSE) and Gaseous Secondary Electron (GSE) detectors with an accelerating voltage of 20 kV. Crushed pellets were stuck onto tape placed on a stub in order to identify the micro-structural developments in the matrix and morphology of aggregates. By the

SEM images, the evident changes of the apparent shape, the porosity size and crystal structure could be observed.

4.3.5.2. X-Ray Diffraction of Raw Materials and Lightweight Aggregates

The mineral composition of aggregates was determined by XRD analysis. The pelletized and sintered aggregates were powdered by grinding to less than 150 μm in a pestle and each powder subjected to XRD analysis using a Rigaku D/MAX-Ultima+/PC X-Ray diffractometer system with Cu Kα radiation in the range of 2^o to 75^o 2Θ with increments of $0{,}02^o$ and a counting time of 2 s per step. Diffractograms were obtained in each case using the same operating conditions.

In order for a sample to diffract x-rays, several criteria must be met [70]. First, the sample must have a regular and repeating arrangement of atoms, and second the spacing between those atoms must be approximately the same length as the radiation used to probe the sample. When the X-rays used to probe the sample hit the surface, they are either scattered or they pass through to the next atomic layer. When the X-rays are scattered from planes at a regular spacing, they interact constructively. This constructive scattering only occurs at specific angles for a given inter-planar distance. In an XRD experiment, the incident x-rays are scanned at various angles (typically $2\theta = 10$ to 80^o). A comparison of those angles to known compounds will aid the identification of the crystalline phases.

XRD is especially useful in materials such as fly ash, where the individual crystals are too small to be reliably identified by other techniques [72, 73]. However, glass is effectively amorphous or non-crystalline and does not have regular arrays of atoms that produce definitive peaks in X-ray diffraction studies. Broad patterns or humps may nevertheless be seen in X-ray diffractograms derived from different types of glassy materials. Along with an overall reduction in the peak intensities derived from the crystalline components due to dilution and/or mass absorption effects, these humps provide an indication that glass is present in the fly ashes and other samples subjected to XRD analysis.

4.3.6. Optimization of Lightweight Aggregates Using Response Surface Methodology

Response surface methodology (RSM) was employed to relate the aggregate manufacturing input parameters (temperature, agent content and agent type) to the three responses (specific gravity, porosity and strength). Then, the optimal production combination that would maximize strength was found while keeping both the water absorption and the specific gravity minimum. Using Design Expert V7 software, the results were analyzed and two optimum types of lightweight fly ash aggregates having minimum specific gravity and maximum strength were achieved.

Response surface methodology was used to optimize the response of three input variables. The classical approach of changing one variable at a time and studying the effect of the variable on the response is a complicated technique, particularly in a multivariate system or if more than one response are of importance [74]. Design of experiments are statistical techniques which can be used for optimizing such multivariable systems. The optimization process involves studying the response of the statistically designed combinations, estimating the coefficients by fitting it in a mathematical model that fits best the experimental conditions, predicting the response of the fitted model and checking the adequacy of the model.

Engineers often wish to determine the values of the process input parameters at which the responses reach their optimum [75]. Design Expert software was also used for analysis of the test results in another study [76]. The optimum could be either a minimum or a maximum of a particular function in terms of the process input parameters. RSM is a set of mathematical and statistical techniques that are useful for modelling and predicting the response of interest affected by a number of input variables with the aim of optimizing this response. RSM also specifies the relationships among one or more measured responses and the essential controllable input factors. When all independent variables are measurable, controllable and continuous in the experiments, with negligible error, the response surface can be expressed by

$$y = f(x_1, x_2, \ldots\ldots, x_k) \tag{4.7}$$

where k is the number of independent variables.

To optimize the response ‘‘y’’, it is necessary to find an appropriate approximation for the true functional relationship between the independent variables and the response surface. Usually a second-order polynomial Equation is used in RSM [74, 75 and 77].

$$y = b_0 + \Sigma\, b_i\, x_i + \Sigma\, b_{ii}\, x^2_{ii} + \Sigma\, b_{ij}\, x_i\, x_j + \varepsilon \qquad (4.8)$$

where
y = response function,
b = coefficient,
x = factor,
ε = error

b_0, b_i, b_{ii}, and b_{ij} are the regression coefficients for intercept, linear, quadratic and interaction terms, respectively, and x_i, and x_j are the independent variables.

4.3.7. Desirability Approach

The desirability method is recommended due to its simplicity and availability in the software and provides flexibility in weighting and giving importance for individual response [75]. Solving such multiple response optimization problems using this technique involves using a technique for combining multiple responses into a dimensionless measure of performance called the overall desirability function. The desirability approach involves transforming each estimated response, Y_i, into a unitless utility bounded by $0<d_i<1$, where a higher d_i value indicates that response value Y_i is more desirable, if $d_i = 0$ this means a completely undesired response. In the current work, the individual desirability of each response, d_i, was calculated using Equations 4.9-4.12. The shape of the desirability function can be changed for each goal by the weight field ‘wt_i’. Weights are used to give more emphasis to the upper/lower bounds or to emphasize the target value. Weights could be ranged between 0.1 and 10; a weight greater than 1 gives more emphasis to the goal, while weights less than 1 give less emphasis. When the weight value is equal to 1, this will make the d_is vary from 0 to 1 in a linear mode. In the desirability objective function (D),

each response can be assigned an importance (r), relative to the other responses. Importance varies from the least important value of 1, indicated by (+), the most important value of 5, indicated by (+++++). If the varying degrees of importance are assigned to the different responses, the overall objective function is shown in Equation 4.13 below. Where n is the number of responses in the measure and T_i is the target value of ith response.

For goal of maximum, the desirability is defined by

$$d_i = \begin{cases} 0, & Y_i \le low_i \\ \left(\dfrac{Y_i - low_i}{high_i - low_i} \right)^{wt_i} & low_i < Y_i < high_i \\ 1, & Y_i \ge high_i \end{cases} \tag{4.9}$$

For goal of minimum, the desirability is defined by

$$d_i = \begin{cases} 1, & Y_i \le low_i \\ \left(\dfrac{Y_i - low_i}{high_i - low_i} \right)^{wt_i} & low_i < Y_i < high_i \\ 0, & Y_i \ge high_i \end{cases} \tag{4.10}$$

For goal as a target, the desirability is defined by

$$d_i = \begin{cases} \left(\dfrac{Y_i - low_i}{T_i - low_i} \right)^{wt_i}, & low_i < Y_i < T_i \\ \left(\dfrac{Y_i - low_i}{T_i - low_i} \right)^{wt_i} & T_i < Y_i < high_i \\ 0, & Otherwise \end{cases} \tag{4.11}$$

For goal within range, the desirability is defined by

$$d_i = \begin{cases} 1, & low_i < Y_i < high_i \\ 0, & otherwise \end{cases} \tag{4.12}$$

$$d_i = \left(\prod_{i=1}^{n} d_i^{r_i} \right)^{1/\Sigma r_i} \tag{4.13}$$

The optimization part in Design-Expert software V7 searches for a combination of factor levels that simultaneously satisfy the requirements placed (i.e. optimization criteria) on each one of the responses and process factors (i.e. multiple-response optimization)[78]. The numerical optimization process involves combining the goals into an overall desirability function (D). The numerical optimization feature in the design-expert package finds one point or more in the factors domain that would maximize this objective function. In a graphical optimization with multiple responses, the software defines regions where requirements simultaneously meet the proposed criteria.

4.4. Properties of Materials Used in Concrete Production

The following materials either donated by local suppliers or manufactured and used throughout the study were comprised of:

- Portland cement (CEM I 42,5R)
- Silica fume
- Artificial aggregate containing 10 % Bentonite and sintered at 1200 ^{o}C
- Artificial aggregate 10 % Glass Powder and sintered at 1200 ^{o}C
- Cold-bonded artificial aggregate
- Crushed stone
- Natural sand
- Crushed sand
- Superplasticizer
- Air-entraining agent

Some characteristics of materials (cement, silica fume and lightweight aggregates) for concrete production were summarized previously in section 4.1 in Tables 4.1-4.4 and Figure 4.1 except those of normalweight aggregates and chemical admixtures. The cement used for manufacturing of cold-bonded lightweight fly ash aggregates, was also used in concrete production.

4.5. Coarse and Fine Aggregates

Among the eighteen different sintered fly ash lightweight aggregates produced in this study, the two sintered aggregates (10B1200 and 10G1200) were selected due to their lower density and higher strength by the aid of Design Expert V7 software in order to produce lightweight high-strength concrete. It is also notable that the best results in terms of density and strength of fly ash lightweight aggregates were obtained at the same binder content and sintering temperature. Cold-bonded lightweight fly ash aggregate and normalweight calcerous crushed stone aggregate with a specific gravity of 2.7 were also used in concrete preparation for the comparison of their properties. The crushed stone coarse aggregates were obtained from Cebeci quary whereas, the natural sand and crushed sand (sandstone originated) fine aggregates used were brought from Kemerburgaz and Ayazağa, respectively. Specific gravity and water absorption of the fine aggregates were determined according to ASTM C 128. The specific gravities of natural sand and crushed sand were 2.62 and 2.63, respectively.

4.6. Tests Performed on the Aggregates Used in Concretes

4.6.1. Aggregate Crushing Value (ACV) Test

Normal and lightweight coarse aggregates utilized in concrete production, namely, two types of sintered and one type of cold-bonded fly ash lightweight aggregates and normal-weight crushed stone aggregates were tested for the aggregate crushing value (ACV) in accordance with BS 812-110 “Testing aggregates —Part 110: Methods for determination of aggregate crushing value (ACV)”. ACV is inversely proportional to aggregate strength. The aggregate crushing value (ACV) was calculated expressed as a percentage to the first decimal place, of the mass of fines formed to the total mass of the test specimen from the following equation:

$$ACV = \frac{M_2}{M_1} * 100 \tag{4.14}$$

where:

M_1 = the mass of the test specimen (in g);
M_2 = the mass of the material passing the 2.36 mm test sieve (in g).

Figure 4.7 shows the aggregate crushing value test set up and the condition of aggregates after the test and the results are presented in Table 4.6.

Figure 4.7. Aggregate crushing value test

4.6.2. Unit Weight (Bulk Density) of Coarse Aggregates

The coarse aggregates were tested in oven-dry condition utilizing the shoveling and rodding procedure to determine the unit weight (loose and rodded) according to ASTM C 29-97 "Standard Test Method for Bulk Density ("Unit Weight") and Voids in Aggregate". The unit weight test results are shown in Table 4.6.

In rodding procedure; the measure was filled one-third full and the surface was leveled with the fingers. The layer of aggregate was rodded with 25 strokes of the tamping rod evenly distributed over the surface. The measure was filled two-thirds full and again the surface was leveled and rodded as above. Finally, the measure was filled to overflowing and rodded again in the manner previously mentioned. The surface of the aggregate was levelled with the fingers. The mass of the measure plus its contents, and the mass of the measure alone were determined.

In shoveling procedure; the measure was filled to overflowing by means of a shovel, discharging the aggregate from a height not to exceed 2 in. [50 mm] above the top of the measure. The surface of the aggregate was levelled with the fingers in such a way that any slight projections of the larger pieces of the coarse aggregate approximately balanced the larger voids in the surface below the top of the measure. The mass of the measure plus its contents, and the mass of the measure alone were determined.

The bulk densities for the rodding and shoveling procedure were calculated as follows:

$$M = \frac{(G - T)}{V} \tag{4.15}$$

where:
M = bulk density of the aggregate, kg/m^3,
G = mass of the aggregate plus the measure, kg,
T = mass of the measure, kg,
V = volume of the measure,m^3

The void content in the aggregate using the bulk density determined by both the rodding and shoveling procedure, as follows:

$$\%voids = \frac{100 * [(S * W) - M]}{(S * W)} \tag{4.16}$$

where:
M = bulk density of the aggregate, kg/m^3,
S = specific gravity as determined in accordance with Test Method C 127
W = density of water, 998 kg/m^3

Table 4.6 shows the results of unit weight, crushing value and void content of aggregates. Cold- bonded had the lowest unit weight and the highest aggregate crushing value among other aggregates. It is estimated that crushing value of the artificial

aggregates was lower than that of the natural aggregates because of the artificial aggregate's porous structure [79]. Unit weight and crushing value of aggregates are in same largeness order with specific gravity and particle crushing strength results, respectively. The void volume percentages of lightweight aggregates were similar because they have a round shape and a smooth surface. However, the void volume percentage of normalweight aggregate was relatively larger than those of other lightweight aggregates, because grain shape of normalweight aggregates was more angular.

Table 4.6. The results of dry unit weight, aggregate crushing value (ACV) and voids of aggregates

Aggregates	Unit weight (kg/m^3)		ACV (%)	Voids (%)	
	Loose	Rodded		Loose	Rodded
Cold-bonded	789	842	35	39,2	35,1
B101200	933	993	28	40,1	36,2
G101200	936	999	30	41,0	37,0
Normalweight	1433	1537	23	46,8	43,0

4.6.3. Grading of Aggregates

Grading of aggregates used in concretes was determined in accordance with ASTM C 136-06 "Standard Test Method for Sieve Analysis of Fine and Coarse Aggregates". The grading of lightweight aggregate and normalweight aggregate for structural concrete conformed to the requirements given in ASTM C 330-05 "Standard Specification for Lightweight Aggregates for Structural Concrete" and ASTM C 33-03 "Standard Specification for Concrete Aggregates", respectively. The same passing percentages were selected for lightweight fly ash and normalweight aggregates considering both standards to eliminate the effect of grading difference on concrete properties. The results presented in Table 4.7 were within the limits of relevant standards.

Table 4.7. Grading of the coarse aggregates

Sieve size, mm	Passing, %	Limits of ASTM C 330	Limits of ASTM C 33
19	100	100	100
12,5	90	90-100	90-100
9,5	50	40-80	40-70
4,75	0	0-20	0-15

4.6.4. Specific Gravity and Water Absorption of Fine Aggregates

Specific gravity and water absorption of the fine aggregates were determined according to ASTM C 128. A sample of aggregate was immersed in water for 24 ± 4 h to essentially fill the pores. It was then removed from the water, the water was dried from the surface of the particles, and the mass determined. Subsequently, a portion of the sample was placed in a graduated container and the volume of the sample was determined by gravimetric method. Finally, the sample was oven-dried and the mass determined again. Using the mass values thus obtained and formulas, it is possible to calculate specific gravity and absorption as follows:

$$Specific\ gravity(OD) = \frac{A}{(B+S-C)} \tag{4.17}$$

$$Specific\ gravity(SSD) = \frac{S}{(B+S-C)} \tag{4.18}$$

$$Apparent\ specific\ gravity = \frac{A}{(B+A-C)} \tag{4.19}$$

$$Absorption, \% = \frac{100(S-A)}{A} \tag{4.20}$$

where:

A = mass of oven dry specimen, g

B = mass of pycnometer filled with water, to calibration mark, g

C = mass of pycnometer filled with specimen and water to calibration mark, g

S = mass of saturated surface-dry specimen, g

4.7. Chemical Admixtures

The superplasticizer and the air-entraining agent used in this study were Glenium 51 and Microair 200, respectively. The typical properties of admixtures are given in Table 4.8.

The superplasticizer was an admixture of a new generation based on modified polycarboxylic ether. The product has been primarily developed for the use in the concrete industry where the highest durability and performance is required. It is free of chloride and low alkali. It complies with EN 934 part 2. It is compatible with all types of cement.

Table 4.8. Typical properties of chemical admixtures

Properties	Superplasticizer	Air-entraining agent
Structure	Modified polycarboxylic ether	aliphatic alcohol and ammonium salt
Color	Brown	Yellow
pH	6.6	-
Form	Viscous liquid	Liquid
Specific gravity at 20°C (gr/cm^3)	1.095	1.00-1.02
Viscosity at 20°C	128 ± 30 cps	-
Chloride content (%) (EN 480-10)	< 0,1	< 0,1
Chlorine content (%) (EN 480-10)	< 0,1	< 0,1
Alkali content (%) (EN 480-12)	< 3	< 10

The air-entraining agent was an ultra stable air entraining admixture for use in all types of concrete based on aliphatic alcohol and ammonium salt. It has been formulated to

meet the requirements of TS EN 206-1 and relative specifications. Entrainment of optimum air content in concrete by this agent reduces segregation and bleeding and increases resistance to damage from freezing and thawing. It is compatible with other admixtures; water reducers, accelerators and retarders.

4.8. Production of Normalweight and Lightweight Concretes (Mix Design Procedure)

The weakest component determines the strength of concrete. In normal strength concretes, the interfacial zone is responsible for the strength, but in high-strength concretes, the strength of aggregate determines the strength of concrete. Due to this fact, in this study high cement dosage was used in preparation of concretes in order to obtain strong cement matrix resulting in failure through the coarse aggregates.

The concretes were coded as LWGC (Lightweight glass powder added fly ash aggregate concrete), LWBC (Lightweight bentonite added fly ash aggregate concrete), LWCC (Lightweight cold-bonded fly ash aggregate concrete) and NWC (Normalweight concrete) referring to the type of coarse aggregate used. Initial trial mixes were made to obtain a slump of 150 mm, air content of 4% and desired compressive strength and unit weight using a pan-type mixer of 50 dm^3 capacity. The cold-bonded lightweight aggregates were immersed in water for 24 hours and then kept on the sieves for the surfaces to dry before adding the aggregate into the mixer. This immersion was due to the high level of water absorption of cold-bonded lightweight aggregates affecting the slump arrangement and also as stated in a study [80, 81], the severe initial water absorption of LWA from the cement in the early age leaves a number of micro pores at the interfacial zone between aggregate particles so that micro cracks form easily under load. Moreover, the absorption of the LWA also leads to incomplete hydration of the cement paste, lowering the strength of the hardened concrete. After addition of coarse and fine aggregates, cementitious materials (cement and silica fume), the mixing water, the admixtures (superplasticizer was added first and air-entraining agent subsequently, as proposed in superplasticizer guide) with water were added and mixed for four minutes and rested for three minutes and mixed again for additional two minutes. The other aggregate types (normalweight and sintered aggregates) were added to the pan in dry condition (without previous saturation) and mixed

with fine aggregates about 1/3 of the mixing water for approximately three minutes in the pan mixer. The later stages of the mixing were same with the cold-bonded lightweight aggregates as mentioned previously. The slump, air content and unit weight of the fresh concrete were determined.

Lightweight concrete specimens were cast using ordinary Portland cement (PC 42,5), superplasticizer, air entrainig agent, water, natural sand, crushed sand and lightweight coarse aggregate with a water/binder ratio of 0.26. The density of aggregates mainly affect the density of concretes, since the volume of aggregate is significant in the mixture. Four different coarse aggregates with a volume ratio= 0.6 (volume of coarse aggregate/volume of total aggregate) were considered in the mix proportions.

Trial batches were made to obtain the desired strength, slump and air content, therefore proportions of the superplasticer and air entraining agent were adjusted. The content of these admixtures were kept constant for LWCs, but not for NWC. The amount of other constituents in NWC and LWCs were same. The only difference was the type of coarse aggregate among four concretes.

The specimens were cast in three layers and compacted in steel moulds. The specimens were cast in accordance with ASTM C192. The moulded specimens were covered with a plastic to prevent water loss from the surface of the concrete. After demoulding at 24 hours, they were labelled and cured in lime- saturated water tank at 22 ^{o}C for 28 and 56 days before testing.

The mix proportions used for all four concretes are exhibited in Table 4.9 and Table 4.10 gives the list of the tests performed on hardened concrete specimens.

Table 4.9. The proportions of the concrete mixtures (based on SSD condition) (kg/m^3)

Concretes	Cement	Silica fume	Water	Fine aggregates		Coarse aggregate	AEA[a] (%)	SP[b] (%)
				Natural sand	Crushed sand			
LWCC	551	55	158	318	318	592	1.2(0.2)	6.7(1.1)
LWBC	548	55	157	316	317	567	1.2(0.2)	6.7(1.1)
LWGC	549	55	157	317	317	580	1.2(0.2)	6.7(1.1)
NWC	551	55	158	317	319	981	1.6(0.265)	7.3(1.2)

[a]AEA: Air-entraining agent

[b]SP: Super-plasticizing admixture

Table 4.10. List of the tests conducted on hardened concrete

Tests Performed on Hardened Concretes	Standard	Specimen Size
Compression Test	ASTM C 39	100x200 mm cylinders
Modulus of elasticity	ASTM C 469	100x200 mm cylinders
Indirect Tensile Test	ASTM C 496	100x200 mm cylinders
Rapid Chloride Permeability Test	ASTM C 1202	100x200 mm cylinders
Accelerated Corrosion Test	-	100x200 mm cylinders
Water Impermeability Test	TS EN 12390-8	150 mm cubes
Rapid Freeze-Thaw Test	ASTM C 666	76x102x406 mm prisms

4.9. Tests Performed on Fresh Concretes

4.9.1. Slump Test

The slump test was performed on fresh concrete immediately after production according to ASTM C 143 “Standard Test Method for Slump of Hydraulic Cement Concrete”. A slump cone was filled with concrete in three layers. Each layer was approximately one third the volume of the cone and was rodded with 25 strokes using a tamping rod. As soon as the cone was filled with concrete, it was removed from the concrete by raising it in vertical direction. The slump was immediately measured by

determining the vertical difference between the top of the cone and the displaced original center of the top surface of the concrete.

4.9.2. Air Content and Density Tests of Fresh Concrete

The fresh density and air content test was conducted in general compliance with the standard procedure in ASTM C 138-01a, "Standard Test Method for Density (Unit Weight), Yield, and Air Content (Gravimetric) of Concrete". The density of fresh concrete was calculated by dividing the net mass of concrete by the volume of the measure. The air content of freshly mixed concrete was also determined in accordance with ASTM C 231-04, "Standard Test Method for Air Content of Freshly Mixed Concrete by the Pressure Method". The pressure procedure gave substantially the same air contents as the gravimetric method for concretes. The results of air content measured by both ASTM C 138 and ASTM C 231 were close to each other.

The net mass of the concrete in kilograms was calculated by subtracting the mass of the measure, M_m, from the mass of the measure filled with concrete, M_c. The density, D was calculated by dividing the net mass of concrete by the volume of the measure, V_m as follows:

$$D = \frac{(M_c - M_m)}{V_m} \tag{4.21}$$

The air content was calculated as follows:

$$A = \frac{(\frac{M}{V} - D)}{(\frac{M}{V})} * 100 \tag{4.22}$$

where:

A = air content (percentage of voids) in the concrete

D = density (unit weight) of concrete, kg/m^3

M = total mass of all materials batched, kg

M_c = mass of the measure filled with concrete, kg

M_m = mass of the measure, kg

V = total absolute volume of the component ingredients in the batch, m^3

V_m = volume of the measure, m^3

4.10. Tests for Determination of Physical Properties of Hardened Concrete

4.10.1. Density, Absorption and Voids in Hardened Concrete

The 100x200mm cylindrical specimens was dried in an oven at a temperature of 100 to 110 °C for not less than 24 h intervals. After removing each specimen from the oven, it was allowed to cool in dry air to a temperature of 20 to 25 °C and the mass was determined. If the specimen was comparatively dry when its mass was first determined, and the second mass closely agreed with the first, it was considered dry. If the specimen was wet when its mass was first determined, it was placed in the oven for a second drying treatment of 24 h and the mass was determined. If the third value checked the second, the specimen was considered dry. If the difference between values obtained from two successive values of mass exceeded 0.5 % of the lesser value, the specimens were returned to the oven for an additional 24-h drying period, and the procedure was repeated until the difference between any two successive values was less than 0.5 % of the lowest value obtained. This last value was designated *A*. The specimen was immersed, after final drying, cooling, and determination of mass, in water at approximately 21 °C for not less than 48 h and until two successive values of mass of the surface-dried sample at intervals of 24 h showed an increase in mass of less than 0.5 % of the larger value. The surface of the specimen was dried by removing surface moisture with a towel, and the mass was determined. The final surface-dry mass after immersion was designated *B*. The specimen was suspended after immersion by a wire and the mass in water was determined. This mass was designated *C*. By using the values for mass determined in accordance with the procedures described above, the calculations of bulk density, water absorption and voids in hardened concrete are as follows:

$$Bulk\ density(OD) = \frac{A}{B-C} \tag{4.23}$$

$$Bulk\ density(SSD) = \frac{B}{B-C} \tag{4.24}$$

$$Absorption\ (\%) = \frac{B-A}{A} * 100 \tag{4.25}$$

$$Volume\ of\ \ permeable\ voids\ (\%) = \frac{B-A}{B-C} \tag{4.26}$$

Also, where mixture quantities, aggregate moisture content, and the volume of the concrete batch were known, an oven-dry density was calculated in accordance with ASTM C 567 as follows:

$$Oc = (Mdf + Mdc + 1.2 * Mct)/ V \tag{4.27}$$

where:

Oc = calculated oven-dry density, kg/m^3 (lb/ft^3),

Mdf = mass of dry fine aggregate in batch, kg(lb),

Mdc = mass of dry coarse aggregate in batch, kg(lb),

Mct = mass of cement in batch, kg (lb),

1.2 = factor to approximate the mass of cement plus chemically combined water, and

V = volume of concrete produced by the batch m^3 (ft^3).

Using the oven-dry density determined, calculation of the approximate equilibrium density is as follows:

$$Ec = Oc + 50\ \text{kg/m}^3 \tag{4.28}$$

where:

Ec = calculated equilibrium density

4.11. Tests for Determination of Mechanical Properties of Hardened Concretes

4.11.1. Compressive Strength and Modulus of Elasticity Tests

The compressive strength and modulus of elasticity of the 100*200 mm cylinder specimens were measured according to ASTM C 39 “Standard Test Method for Compressive Strength of Cylindrical Concrete Specimens” and ASTM C 469-02 “Standard Test Method for Static Modulus of Elasticity and Poisson’s Ratio of Concrete in Compression”, respectively at the age of 28 and 56 days.

The specimens were capped using a capping compound to ensure parallel loading faces of the test specimens and constant height for all cylinders when tested. The compressive strength was calculated by dividing the maximum load to the cross sectional area of specimen. The specimen was placed with the strain-measuring equipment attached on the lower platen of testing machine. The testing head was lowered slowly to bring it in contact with the specimen. At this stage, the dial gauges were set to zero. Load was increased slowly by adjusting the lever and controlling the oil flow simultaneously. The specimen was loaded at least twice. During the first loading, which was primarily for the checking of the gages, the performance of the gages was observed and any unusual behavior was corrected prior to the second loading. The load was applied continuously and without shock. In hydraulically operated machines, the load was applied at a constant rate of 2 kN/s. Without interruption of loading, the applied load and longitudinal strain were recorded at the point (1) when the longitudinal strain was 50 millionths and (2) when the applied load was equal to 40 % of the ultimate load. Longitudinal strain was defined as the total longitudinal deformation divided by the effective gage length.

The longitudinal deformations of the specimens under loading were measured by using two linear variable differential transformers (LVDTs) connected to a data logger system. Strain could be calculated by the aid of these LVDTs.

Figure 4.8. Compressive strength and modulus of elasticity test of hardened concrete

The load and deformation was recorded. To determine the modulus of elasticity, the results were plotted, in which the slope is the modulus of elasticity. Another method is to directly calculate the modulus of elasticity by using the equation:

$$E = \frac{\sigma_2 - \sigma_1}{\varepsilon_2 - 0.000050} \tag{4.29}$$

where:

E = chord modulus of elasticity, MPa,

σ_2 = stress corresponding to 40 % of ultimate load,

σ_1 = stress corresponding to a longitudinal strain, ε_1, of 50 millionths, MPa,

ε_2 = longitudinal strain produced by stress σ_2.

Also, modulus of elasticity values of concrete specimens were calculated by the formula given by ACI 318 Building Code and BS 8110.

Calculation of modulus of elasticity using ACI 318:

$$E_c = w_c^{1,5} * 0{,}043 * \sqrt{f_c} \text{ , } 21 < f_c < 35\text{MPa}, \; 1440 < w_c < 2480 \tag{4.30}$$

Calculation of modulus of elasticity using BS 8110:

$$E_c = w_c^{2} * 0.0017 * f_c^{0.33} \text{ , } 1400 < w_c < 2320 \tag{4.31}$$

where:

E_c= modulus of elasticity

w_c = air dry density of concrete

f_c = cylinder compressive strength

Test results were compared to ACI 318 and BS 8110 equations.

4.11.2. Splitting Tensile Strength Test

Splitting tensile strength tests of concretes were performed on 100*200 mm cylinders in accordance with ASTM C 496-04 “Standard Test Method for Splitting Tensile Strength of Cylindrical Concrete Specimens”. The splitting tensile strength of concrete cylinders is a convenient relative measure of tensile strength. The test was performed by application of diametrically opposite compressive loads to a concrete cylinder laid on its side in the testing machine. Fracture or “splitting” occured along the diametral plane. The load was applied continuously and without shock, at a constant rate of 0.7 kN/s. The maximum applied load was indicated by the testing machine at failure. Calculation of the splitting tensile strength of the specimen is as follows:

$$T = \frac{2 * P}{\pi * 1 * \mathrm{d}} \tag{4.32}$$

where:

T = splitting tensile strength, MPa

P = maximum applied load indicated by the testing machine, N

l = length, mm

d = diameter, mm.

4.12. Tests for Determination of Durability of Hardened Concrete

4.12.1. Rapid Chloride Permeability Test

In this test method, the amount of charge passed through the concrete specimen, as an electrical indication of chloride permeability, was monitored during the 6 h test duration according to ASTM C 1202-05 "Standard Test Method for Electrical Indication of Concrete's Ability to Resist Chloride Ion Penetration". After 28-day and 56-day curing, the 100*200 mm concrete cylinders were cut into 50 mm thick slices from the middle portion of cylinders. The samples were coated with epoxy on ring surface. When the coating was cured, the coated specimens were vacuumed in a desiccator. After vacuumed, samples were soaked in de-aerated water for 18 h. One side of the cells was filled with sodium chloride solution (3% NaCl by mass) (negative terminal) and the other (side) filled with sodium hydroxide solution (0.3N NaOH) (positive terminal) where electrode in NaOH chamber became an anode and electrode in NaCl chamber acted as a cathode. The voltage applied to 11 Ω resistor was monitored at every 1 min by the data logging system, from which the current values of each cell could be calculated. Table 4.11 shows the chloride ion permeability rating of concretes in terms of charge passing through concrete specimen between the two cells.

Table 4.11 Chloride ion penetrability based on charge passed

Charge Passed (coulombs)	Chloride Ion Penetrability
>4000	High
2000-4000	Moderate
1000-2000	Low
100-1000	Very Low
<100	Negligible

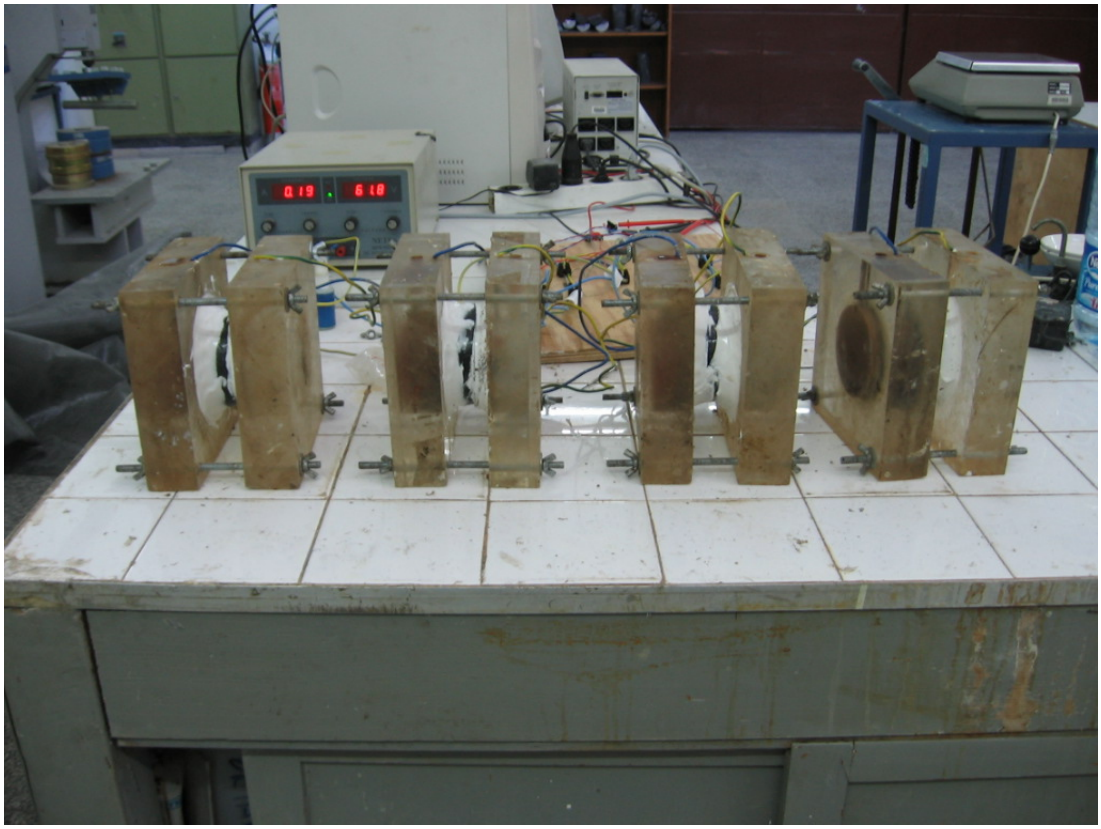

Figure 4.9. Rapid chloride permeability test

Calculation of charge passed as following:

$$Q = 900 * (I_0 + 2I_{30} + 2I_{60} + ... + 2I_{300} + 2I_{330} + 2I_{360}) \quad (4.33)$$

where:

Q = charge passed (coulombs),

I_0 = current (amperes) immediately after voltage is applied,

I_t = current (amperes) at t min after voltage is applied.

4.12.2. Accelerated Corrosion Test

The 100*200 mm cylinder specimens were used for the accelerated corrosion test. A 10 mm diameter plain steel bar was embedded into concrete. The lollipop specimens were immersed to its half height in a 15% sodium chloride (NaCl) solution at room temperature and the steel bar was connected to the positive terminal (anode) of a 20 V DC power supply while the negative terminal was connected to stainless steel plate (cathode) placed

near the specimen. The current measurements were recorded periodically. Similar test set up was arranged in a previous study [82], however in this study the steel bar was connected to a constant 20 V DC power supply instead of 12 V which was applied in the previous study. Based on the initial trial test results, it was observed that the current required to maintain an anodic potential of 12 V was very low so this value was increased in order to note an earlier corrosion initiation.

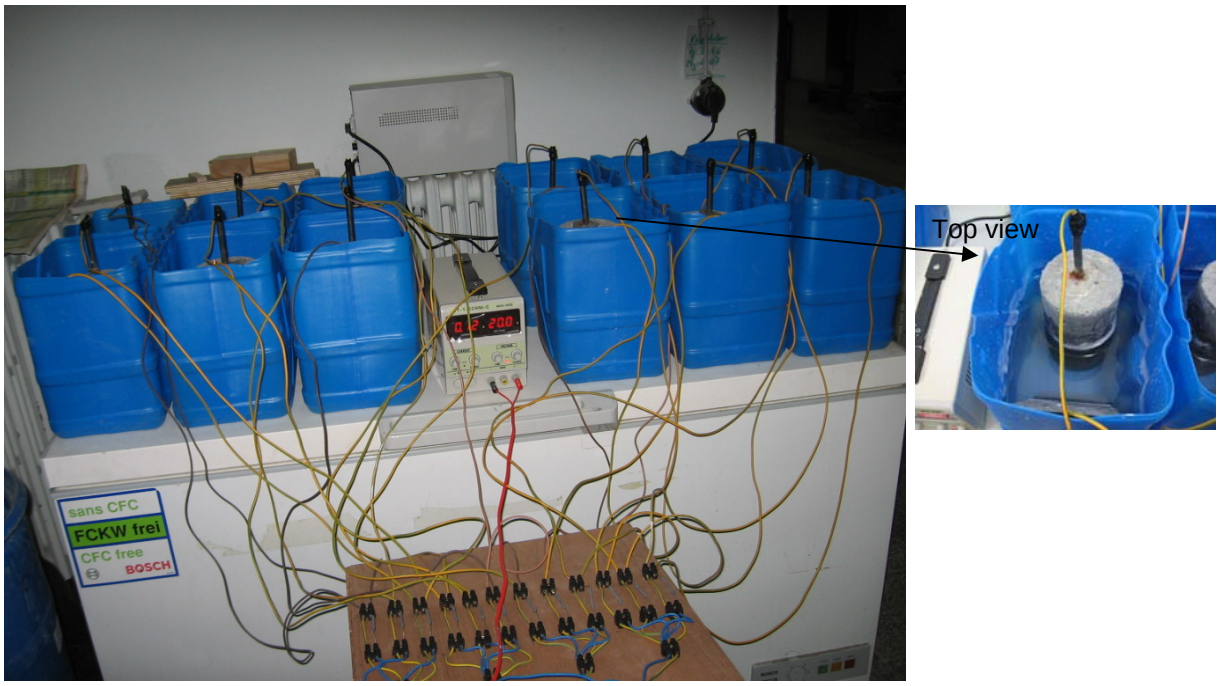

Figure 4.10. Accelerated corrosion test

4.12.3. Water Permeability Test

Water permeability test was performed in accordance with TS EN 12390-8 “Testing hardened concrete - Part 8: Depth of penetration of water under pressure”. 150 mm cubic specimens were used for water permeability test. Two different sample conditioning procedures were followed for 28-day and 56-day tests. 28-day concrete specimens were placed in the environmental chamber at a temperature of 50 ± 2°C and RH of 80±3 % for 3 days. After 3 days, the specimens were stored at 23 ± 2°C for 15 days before the start of the test. 56-day specimens were dried in an oven at a temperature of 100 to 110 °C for not less than 24 h. After removing each specimen from the oven, the masses were determined. The procedure was repeated until the difference between any two successive values was

less than 0.5 % of the lowest value obtained. Sample conditioning procedure is not indicated in TS EN 12390-8, firstly 56-day specimens were tested and they were dried in oven in order to be considered fully dry (free of water) for monitoring water penetration easily after the test. However, it was noted that the water penetration values obtained from the results were higher than the values presented in the literature. Thus, for 28-day specimens, the sample conditioning procedure given by ASTM C 1585 was adopted.

The specimen was placed in the apparatus and water was applied under pressure 500 ± 50 kPa for 72 ± 2 hours to the surface of hardened concrete. The specimen was then split in half, perpendicularly to the face on which the water pressure was applied and the depth of penetration of the water front was measured.

Figure 4.11. Water impermeability test

4.12.4. Rapid Freezing and Thawing Test

The freeze–thaw test in water was conducted on 76x102x406 mm prisms according to ASTM C 666-03 Procedure A "Standard Test Method for Resistance of Concrete to Rapid Freezing and Thawing". Freezing and thawing test was started by placing the specimens in the thawing water at the beginning of the thawing phase of the cycle. The specimens were removed from the apparatus in a thawed condition, at intervals of 25 cycles of exposure to the freezing and thawing cycles and tested for fundamental transverse frequency and weighed for the determination of mass loss. Dynamic Testing Apparatus (sonometer) was used to determine fundamental transverse frequency conforming to the requirements of Test Method ASTM C 215 "Standard Test Method for Fundamental Transverse, Longitudinal and Torsional Resonant Frequencies of Concrete Specimens''. The temperature at the center of the control specimen ranged from 4.4 ^{o}C to -17.7 ^{o}C. The specimens were returned either to random positions in the apparatus or to positions according to some predetermined rotation scheme which would ensure that each specimen tested for any length of time has been subjected to the conditions in all parts of the freezing apparatus. The test was continued until specimens were subjected to 300 cycles of freezing and thawing or until their relative dynamic modulus of elasticity fell below 60% of the initial modulus, whichever occured first.

Figure 4.12. Rapid freezing and thawing test

The numerical values of relative dynamic modulus of elasticity were calculated as follows:

$$P_c = \frac{n_1^{\,2}}{n^2} * 100 \tag{4.34}$$

where:

P_c = relative dynamic modulus of elasticity, after c cycles of freezing and thawing, percent,

n = fundamental transverse frequency at 0 cycles of freezing and thawing, and

n_1 = fundamental transverse frequency after c cycles of freezing and thawing.

The durability factor was calculated as follows:

$$DF = \frac{P * N}{M} \tag{4.35}$$

where:

DF = durability factor of the test specimen,

P = relative dynamic modulus of elasticity at N cycles, %,

N = number of cycles at which P reaches the specified minimum value for discontinuing the test or the specified number of cycles at which the exposure is to be terminated, whichever is less, and

M = specified number of cycles at which the exposure is to be terminated.

4.13. SEM Observations of Concretes

The concept that an interfacial transition zone (ITZ) or “aureole de transition” exists around sand and coarse aggregate particles in concrete has been one of the accepted tenets of concrete technology for many years [83]. A critical feature in ITZ investigations is the selection by some sampling process of the aggregate grains to be studied, since each ITZ area to be studied necessarily is associated with and surrounds some particular sand or coarse aggregate grain [84]. A single SEM specimen surface may contain hundreds of sand

grains of various sizes as well as one or more coarse aggregate grains. Some unbiased sampling procedure is necessary to select the relatively small proportion of the grains that are to be the centers of specific ITZ areas to be examined.

The field image analysis procedures commonly used are straightforward. Digital images are obtained by backscatter SEM on representative areas of polished surface specimens. Pixels corresponding to each of the components are separated by binary segmentation (i.e., thresholding) based on gray level. The percentage area of each component is determined by dividing the number of pixels of each component by the total number of pixels in the field. This percentage area is assumed to provide an appropriate estimate of the volume percent of the component. In studies of concrete, it is common to disregard the pixels corresponding to the aggregates, and express the area percentages of the different hcp components on the basis of the area of the paste, rather than the area of the concrete.

The structural characteristics of the transition zone can be obtained by the sequence of its development from the time concrete is placed [85]. These characteristics are described as follows:

- In freshly compacted concrete, water films form around the large aggregate particles. This would account for a higher water-to-cement ratio (W/C), closer to the larger aggregate than away from it (i.e., in the bulk mortar).

- As in the bulk paste, calcium, sulfate, hydroxyl and aluminate irons are produced by the dissolution of calcium sulfate and calcium aluminate compounds, and are then combined to form ettringite and calcium hydroxide (CH). Owing to the higher water-to-cement ratio, these crystalline products in the vicinity of the coarse aggregate consist of relatively larger crystals. And, therefore, they form a more porous framework than in the bulk cement paste or mortar matrix.

- With the progress of hydration, poor crystalline C–S–H and a second generation of smaller crystals of ettringite and CH start filling the empty space that exists

between the framework created by the large ettringite and CH crystals. This helps improve the density and, hence, the strength of the transition zone.

In order to examine the pore structure and interfacial transition zone (ITZ), SEM observations were performed. JEOL JSM – 7000F scanning electron microscope equipped with a backscatter electron detector SEI was used for imaging. The microscope was operated at low vacuum and 5 kV accelerating voltage with magnifications of x2000 and x4000 for ITZ and with magnification of x50 for air entrained cement mortar. The images were digitised to 1024 × 768 pixels. Each image was captured with a constant brightness and contrast settings for reproducibility. The specimens were coated with gold just before the observations were made. Micrographs were taken at the age of 28 and 56 days.

5. TEST RESULTS AND DISCUSSION

5.1. Results of Aggregate Tests

5.1.1. The Uniformity of Produced Aggregates

The uniformity of aggregates could be proved by the results of SEM analysis, crushing test and also by visual inspection for the color of the aggregates. The homogenity of aggregate properties provides consistence in concrete properties.High variability decreases the quality of the final product. Kayali reported that inconsistency in the lightweight aggregate can be manifested mainly in the water absorption capacity, hardness and particle size distribution [86]. Such variations result, as expected, in inconsistency in the final product, namely, the concrete. Since it is structural concrete that is ultimately the subject of interest, it is imperative that the produced aggregate should be of high quality and consistent characteristics. This is specially the case when such aggregates are to be used in important structures such as off-shore platforms.

In this study, pelletization and sintering processes were maintained in the same manner for all aggregate types. The speed and angle of the disc and even the content of materials added such as powders and water were all kept constant. Then, in sintering process, small amounts of pelletized aggregates were placed to the predetermined locations in the furnace to avoid inconsistency in properties of sintered aggregates. At the beginning, the furnace illustrated in the Figure 4.3 contained three shelves. All three shelves were used firstly, but the sintered aggregates from each shelf showed differences in properties among each other. For that reason, trial sintering processes were followed to obtain the optimum properties of the aggregates. Finally, it was observed that the suitable properties of highly consistent aggregates could be obtained by using only the mid-shelf, thus the other shelves were unattached to provide sufficient surrounding thermal energy from the electrical wires present at the sides of the furnace.

Color differences were observed for pellets sintered at different temperatures. The pellets were darker in color when sintered at high temperatures as compared to pellets sintered at low temperature (Figure 4.3). The changes in color due to the sintering agent content could not be monitored visually.

The color and density of outer and inner part of pellets were the same (uniform) for all agregate types due to the decreasing through combustion of carbon content with low heating rate. Some researchers [18, 27, 36 and 87] found out differences in color and density of outer and inner part of the aggregates. The different external view of aggregate was observed at different stages of heating and the difference between inner part and outer part of the aggregate (black coring: a gradient in colour from very dark in the inner part of the sample to a much lighter coloration in a thin outer layer of the pellet) were obtained in one and two step of heating or slow and rapid heating. The black coring observed in rapidly sintered fly ash samples could be due to the increase in residual unburned carbon content present in the central part of the samples. Only the thin layer close to the surface was associated with complete carbon combustion. Samples sintered using slow heating rates had a uniform light coloured cross-section without any black coring. However, black coring was also reported to be due to the formation of reduced iron species in the fly ash. In another study [2], black cores were present in some samples with the core size depending on the sample position in the furnace, the direction of air flow, and the processing time and temperature. Generally, the first sample of the ‘‘stack’’ in the direction of air flow had no or a very small blackened core, while the core size was found to increase to a maximum in the middle of the stack. This was most likely due to the unavailability of sufficient air to burnout the carbonaceous materials present in the green samples.

5.1.2. The Effects of Temperature and Type and Content of the Binder on Specific Gravity

The effects of sintering temperature, binder type and content on specific gravity are exhibited in Figures 5.1-5.6 and Table 5.1-5.3.

The principle to make lightweight aggregate by the expansion of raw materials is explained by Mun [18] as follows: A part of the raw materials is melted at a high temperature, attaining a proper viscosity, and generating a gas. The melted raw materials are expanded and then formed into a lightweight aggregate when the gas pressure is slightly higher than that required to resist the viscosity of the melted raw materials. The expansion at high temperature depends on their viscosity.

The proper viscosity could be determined from the chemical compositions of the raw materials used [18, 87 and 88]. The chemical composition of the fly ash was similar to that of the bentonite but the SiO_2 content of the fly ash was slightly higher. Generally, total CaO and MgO contents account for a sudden change in the viscosity of the raw materials at high temperatures. The fly ash did not cause a sudden change in the viscosity even at high temperature because its total CaO and MgO content was 5.18%. However, glass powder and bentonite had 12.29 and 6.79 % of total CaO and MgO content, respectively. In general, when its Al_2O_3+SiO_2 content is high, its melting point and viscosity tend to be become high. It is expected that the melting point of the fly ash would be higher than those of bentonite and glass powder because Al_2O_3+SiO_2 content was high. The contents of Al_2O_3 and SiO_2 of bentonite and glass powder were similar.

Bloating necessary for making lightweight aggregate is produced by entrapment of gases within the viscous melt at the sintering temperature used [6]. Unless there is an abundant glass formation due to the mineralogical changes by the time the upper limit of sintering is reached, any gas formed will escape through the open-pore structure. Furthermore, it was observed that if the samples were raised to bloating temperatures over a period lasting several hours, the bloating effect would be destroyed. Probably, the extensive fluxing action of carbonates contributed to the development of a sintered product of high specific gravity.

It is noted that the aggregates showed substantial changes in their physical properties with increasing concentrations of binders in the aggregate mixes. Figures 5.1 and 5.2 showed the effect of the addition of binders on specific gravity of aggregates comprising different proportions of binders to fly ash, sintered at different temperature ranges (in 50 centigrade degree increments). The highest and the lowest specific gravity values for only

fly ash (OFA) aggregates were obtained by sintering at 1200 ^{o}C and 1100 ^{o}C, respectively; whereas for aggregates with binder sintering at 1150 ^{o}C and 1200 ^{o}C mostly gave the highest and lowest specific gravities, respectively.

Specific gravity values continuously increased with increasing sintering temperature in the case of OFA aggregates. This dense structure with a higher specific gravity can be attributed to the excessive glass formation at higher temperatures as also obtained by Al-Bahar and Bogahawatta [6].

Addition of binders (disregarding binder type) increased the specific gravity values at 1100 ^{o}C and 1150 ^{o}C due to the fact that some elements retained in the pores at lower temperatures. This retaining elements closed and insulated the pores, leading to low water absorption and high specific gravity. In other words, addition of binders increased the specific gravity at lower temperatures due to the incomplete reaction causing insufficient gas evolution to form pores at low temperatures. As can be seen from the Table 4.1, specific gravities of glass powder and bentonite are 2.50 and 2.40, respectively, whereas the specific gravity of fly ash is 2.06. It is obvious that addition of binders to the fly ash increased the pellet density at low temperatures, due to the lack of sufficient heat for bloating.

At the temperatures 1100 and 1150 ^{o}C, increasing bentonite content increased the specific gravity, however increasing glass powder content caused reduction in dry basis specific gravity. In other words, specific gravity increased from 1.75 to 1.77 at 1100 ^{o}C and from 1.90 to 1.93 at 1150 ^{o}C with the rise in bentonite content. Nevertheless, in the case of glass powder, specific gravity decreased from 1.81 to 1.77 at 1100 ^{o}C and from 1.93 to 1.85 at 1150 ^{o}C. Aggregates with densities of 2.0 g/cm^3 and below are referred to as lightweight aggregates while aggregates with densities above 2.0 g/cm^3 are referred to as normal weight aggregates. All of the aggregate types produced had densities below 2.0 g/cm^3. Aggregate with bentonite had higher specific gravity values in all conditions except for 10G1150 than aggregates with glass powder. The trend of porosity variation based on the sintering temperature variation indicated that the increase of sintering temperature resulted in the formation of a viscous flow, in turn reduced the pore volume, and therefore decreased the porosity of the pellets. The specific gravity, grain size distribution and grain

shape of binders played a role in sintering, therefore in specific gravity of aggregates. Also, Wasserman and Bentur [23] revealed that the overall reduction in porosity which should lead to larger bulk density of the porous aggregate was offset by the reduction in the solid density induced by changes in the composition of the solid in the various treatments.

It can be noted that sintering temperature, binder type and content had a significant effect on the specific gravity of the sintered aggregates. The results indicated that the use of glass powder and bentonite as binders in fly ash led to a significant reduction in specific gravity in the resulting aggregate sintered at 1200 ^{o}C. The effect was more prominent in the aggregates containing higher content of binders. When 7.5 % glass powder and 7.5 % bentonite were added as binders to fly ash, a greater bloating effect was noticed as was evident from relatively low values of specific gravity of aggregate produced. The reason of this result is due to the increase in the quantity of gases evolved during sintering at that temperature. The decrease in density at high temperatures which was also reported by other researchers [18, 21, 22, 26, 33, 35, 87 and 89] was attributed to the internal sintering due to the calorification and combustion of organic materials and the accelerated expansion due to gas generation. Also, this reduction in density was attributed to internal pressure caused by the formation of CO_2 (and possibly CO) upon combustion of the carbon [2]. On the other hand, it was demonstrated that carbon was oxidised and released from the samples at temperatures below 850 ^{o}C under conventional, slow sintering conditions [90]. In another study, the researchers [8] revealed that the specific gravity increased when binders were used. Among the binders, aggregate with bentonite had a lower specific gravity compared to lime and cement. The addition of bentonite, which contained a higher amount of very fine organic matters, increased the quantity of gases evolved during sintering thereby reducing the density of the aggregates. However, Huang et al. [27] stated that the surface of the sample was not completely vitrified when gas was produced, making it possible for gas to escape. This not only increased porosity but also water absorption, thus undermining the engineering properties of the LWA thus manufactured. On the other hand, at feeding temperature of 950 ^{o}C, the water in the crystals was rapidly released in large quantity, causing the pellets to burst and thus increasing the rate of defects. As a result, all the internal gas was released before the surface became completely vitrified, thus affecting the quality of the LWA produced. In this study, the more sticky glassy materials were formed at the surface, the more gas would be wrapped up, which made the aggregates lighter. In

other words, the glassy surface texture entrapped the gas produced with the increase in internal temperature resulting in low specific gravities of aggregates with binders at 1200 ^{o}C.

Glass powder and bentonite contained high concentrations of calcium containing minerals, such as calcium oxides, carbonates, and sulfates, as well as sodium and potassium oxides and sulfates (Table 4.1). These minerals act as "fluxes." It is believed that the fluxes lower the melting point [53], causing sintering and densification at lower temperatures than if fluxes were not present. Fly ash contained lower quantities of low melting point fluxes and higher quantities of high melting point minerals than glass powder and bentonite. Density of aggregates with binders increased with temperature from 1100 ^{o}C to 1150 °C (Table 5.1-5.3 and Figure 5.1-5.6) because in this temperature range, as the aggregate sintered, the fluxing agents in the glass powder and bentonite melted to form a liquid phase that filled pores between particles through capillary action (Figures 5.33, 5.36, 5.39, 5.42 and 5.45). Density increased as pores were filled and the volume of the aggregate decreased. In addition, smaller particles in the liquid phase diffused toward the larger particles. The melted materials formed a rigid, glassy, amorphous skeleton or matrix upon hardening. As the sintering temperature increased, more of the compounds in the binders melted, substantially eliminating all the pores and forming a larger glassy, crystalline solid matrix. At the temperature of maximum densification, essentially all of the pores in the aggregate were filled. Density decreased with temperature from 1150 ^{o}C to 1200 ^{o}C because further temperature increases resulted in aggregate melting and bloating. Bloating was caused by the entrapment of gases in the melted liquid phase, resulting from volatization of certain components of the aggregate. The entrapped gases formed pores. The melting points of the aggregates were also detected by DTA curves in Figure 5.21.

Increasing temperature also reduced the volume of water accessible porosity. The pores became disconnected and larger. This result led to low water absorption and low specific gravity. Relatively larger pores occured when binders were used, leading to low specific gravity and low crushing strength at 1200 ^{o}C.

Cold-bonded fly ash lightweight aggregate had specific gravities of 1.61 and 1.30; in saturated surface dry and oven dry condition, respectively. For specific gravity in SSD

condition, its specific gravity was among the lowest ones and for OD condition it had the lowest specific gravity in oven-dry condition among other aggregate types due to its excessive internal porosity. Similar values 1.23 and 1.37 with the same cement-fly ash ratio for specific gravity in OD condition were also obtained by other researchers [32, 47] who studied on cold-bonded lightweight fly ash aggregates. It was followed by 7.5BG1200 aggregate with a specific gravity of 1.34. The reason for the low specific gravity of 7.5BG1200 aggregate was the existence of the highest amount of binders resulting in porous structure due to bloating at high temperature.

Table 5.1. Specific gravity of lightweight aggregates in OD condition

Temperature (^{o}C)	OFA	5B	10B	5G	10G	7.5BG	CB
1100	1,51	1,75	1,77	1,81	1,77	1,78	1,30
1150	1,74	1,90	1,93	1,93	1,85	1,73	
1200	1,92	1,62	1,56	1,66	1,59	1,34	

Table 5.2. Specific gravity of lightweight aggregates in SSD condition

Temperature (^{o}C)	OFA	5B	10B	5G	10G	7.5BG	CB
1100	1,79	1,89	1,88	2,02	1,91	1,86	1,61
1150	1,92	2,01	1,94	2,00	1,90	1,75	
1200	1,97	1,64	1,57	1,68	1,59	1,35	

Table 5.3. Apparent specific gravity of lightweight aggregates

Temperature (^{o}C)	OFA	5B	10B	5G	10G	7.5BG	CB
1100	2,09	2,04	2,00	2,29	2,06	1,94	1,89
1150	2,12	2,13	1,96	2,07	1,95	1,76	
1200	2,02	1,65	1,58	1,69	1,60	1,36	

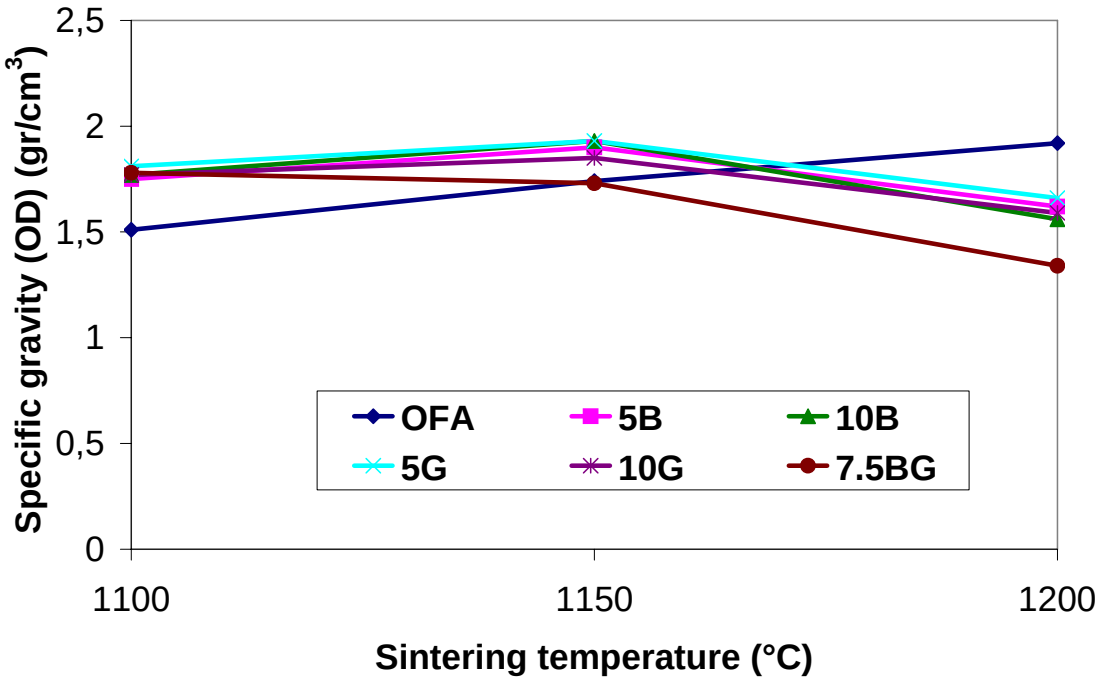

Figure 5.1. The effect of sintering temperature on specific gravity (OD)

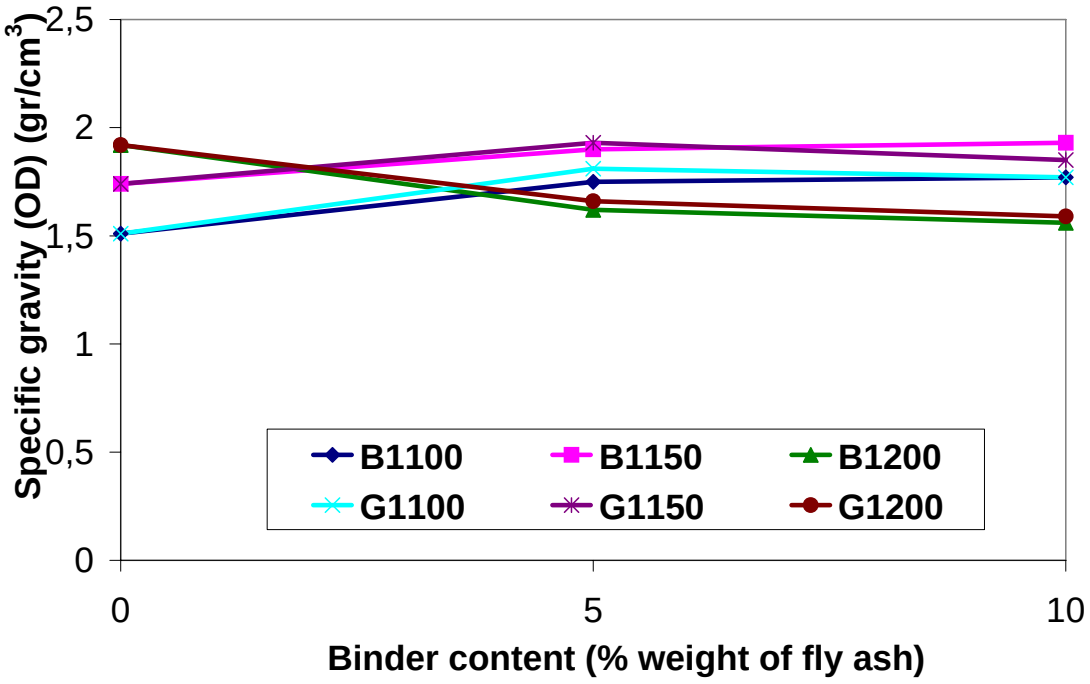

Figure 5.2. The effect of sintering agent content on specific gravity (OD)

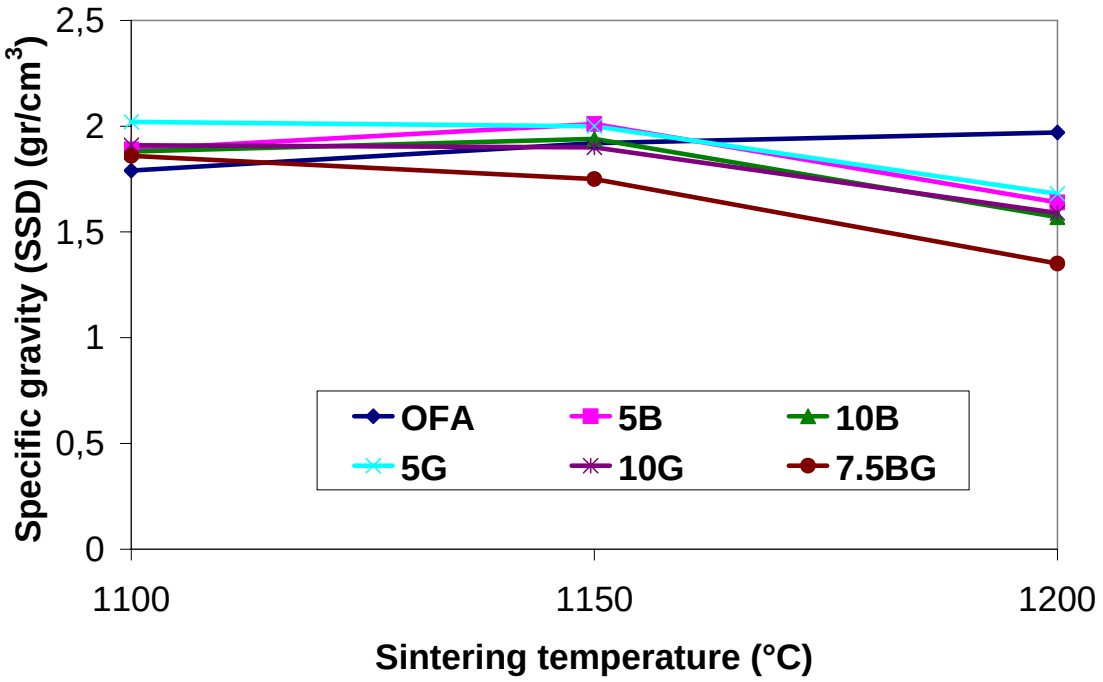

Figure 5.3. The effect of sintering temperature on specific gravity (SSD)

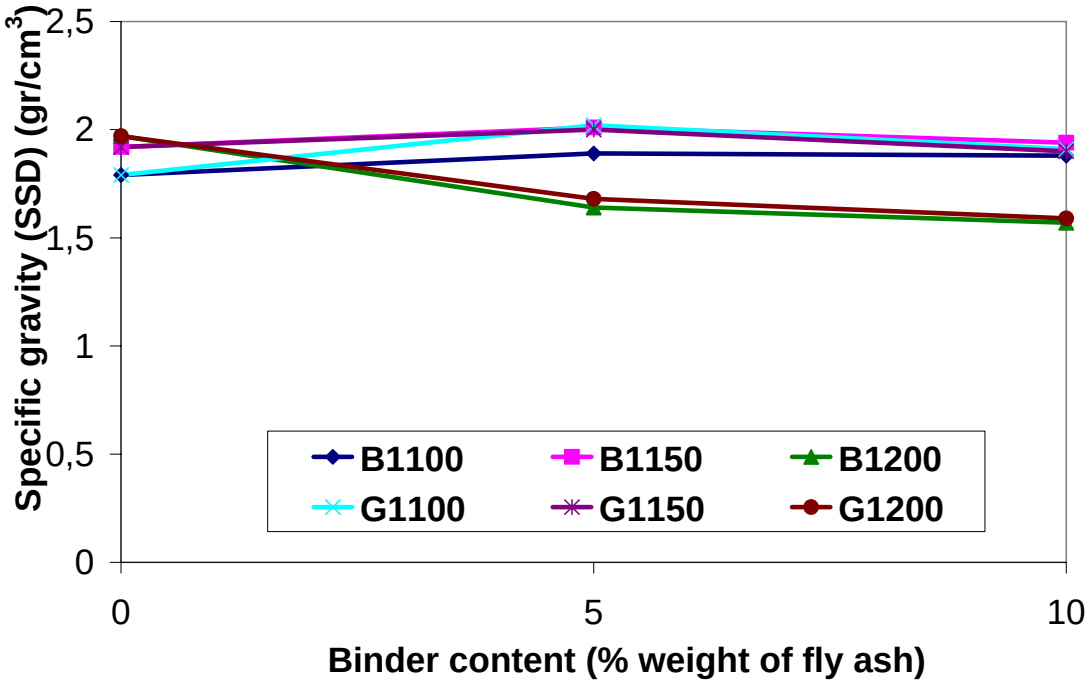

Figure 5.4. The effect of sintering agent content on specific gravity (SSD)

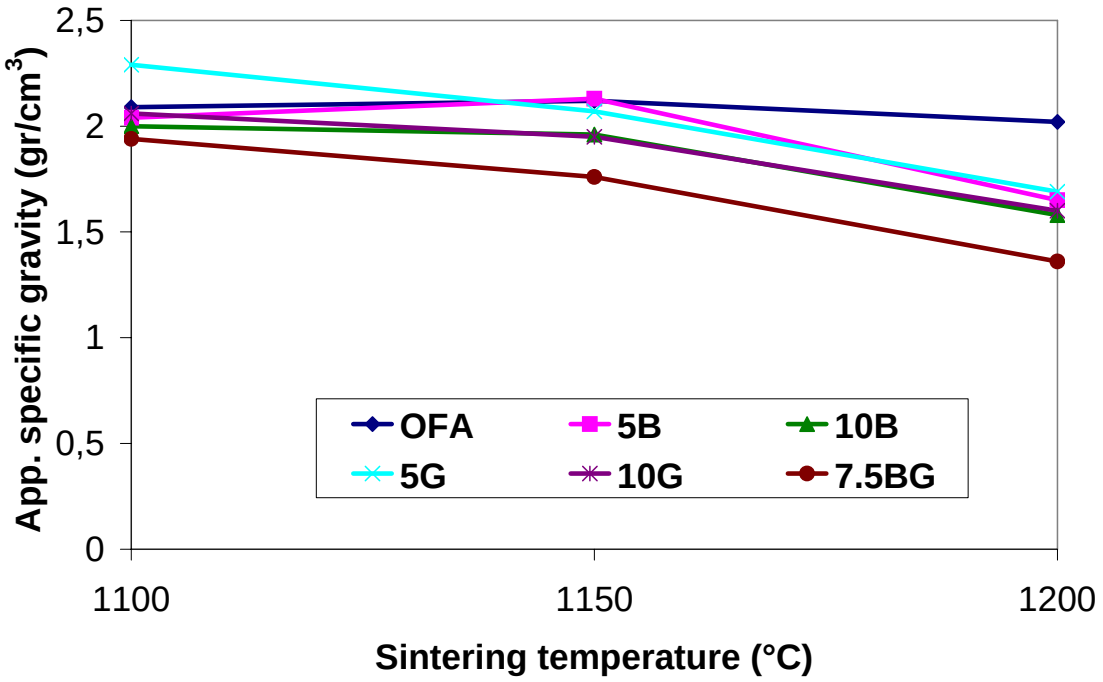

Figure 5.5. The effect of sintering temperature on apparent specific gravity

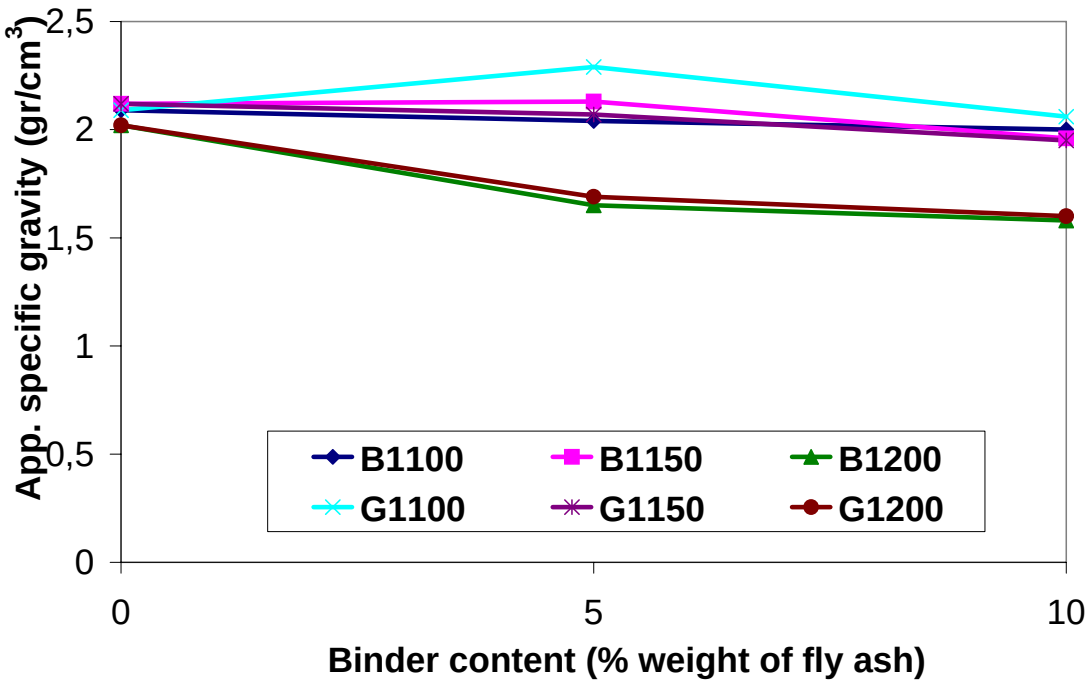

Figure 5.6. The effect of sintering agent content on apparent specific gravity

5.1.3. The Effects of Temperature and Type and Content of the Binder on Porosity

Variation in the water absorption of the lightweight aggregates with sintering agent content and temperature is shown in Table 5.4 and Figures 5.7 and 5.8.

The water absorption of all aggregate types declined with the increase in temperature. OFA aggregates showed linear decrease, however aggregates with binders exhibited a significant decrease from 1100 ^{o}C to 1150 ^{o}C, and then the drop was slight up to 1200 ^{o}C. Sintering OFA aggregates at 1100 ^{o}C led to loosely bounded fly ash particles and thus a weak porous matrix with extensive intergranular connected porosity (Figure 5.30). This is in agreement with the high water absorption obtained for this type of aggregate.

A decrease was also observed with the increase of binder content regardless of binder type. The reduction was larger in bentonite aggregates than in glass powder aggregates at 1100 ^{o}C and 1150 ^{o}C, however the reduction was same with two binder types at 1200 ^{o}C. The disconnected porosity close to surface occured at 1200 ^{o}C led to further decrease in water absorption. Also, the formation of glassy texture on the surface of aggregates at higher temperatures further prevented the increasing of water absorption of the aggregates as also revealed also in previous studies [18, 29]. The water absorption value of OFA1200 was close to the aggregates with binders sintered at 1150 ^{o}C. In other words, sintering aggregates with binders at 1150 ^{o}C showed similar or lower water absorption than OFA1200 aggregates. Increasing binder content reduced the water absorption at all temperatures.

The aggregates comprised a mixture of fly ash and binders, the agglomerate was sintered at temperatures of 1100, 1150 and 1200 ^{o}C, depending on the proportion of binder to fly ash and the desired density and other characteristics. The structure of the aggregate comprised a plurality of grains bonded to each other through a partly glassy and partly crystallized matrix, resulting from the melting or crystallization of the components with temperature as shown in XRD and DTA figures. The grains also comprised silica, alumina, and other minerals with melting points above the processing temperature. The grains fully or partially crystallized during sintering, providing an additional bond between the grains.

The aggregate sintered at high temperatures comprised a dense, continuous, relatively impermeable surface layer. Channel like internal pores and microscopic small surface pores were present in only fly ash aggregates sintered at 1100 and 1150 ^{o}C, in aggregates with binders sintered at 1100 ^{o}C and in cold-bonded aggregates. The surface pores connected with the internal pores, enabling the aggregate to absorb water. The degree of water absorption is indicative of the volume and connectivity of the pores of the aggregate.

Interconnected pores can be seen in SEM figures of aggregates sintered at low temperatures, whereas Figure 5.31, 5.37 and 5.43 are cross-sectional views of vitrified aggregates with high content binders at high temperature, which comprised a larger matrix. Vitrification resulted from sintering of the aggregates at or above the temperature of maximum densification for the particular proportions of binders to fly ash, where most of the components of the agglomerate melt. As vitrification progressed at higher temperatures, density and strength decreased due to bloating of the material.

Table 5.4. Water absorption values of lightweight aggregates

Temperature (^{o}C)	OFA	5B	10B	5G	10G	7,5BG	CB
1100	18,4	8,4	6,9	11,6	8,2	4,5	23,9
1150	10,4	2,3	0,8	3,4	2,6	0,9	
1200	2,2	1	0,7	1,1	0,7	0,8	

The water absorption of cold-bonded aggregates was 23.9 % which was the highest absorption among all aggregate types, followed by OFA1100 with a value of 18.4 %. The greater absorption value was attributed to the low sintering temperature which was not adequate for fusion of fly ash particles. The previous studies [32, 47] on cold-bonded fly ash aggregates with the same ratio of cement to fly ash (10 %) reported similar water absorption results. With an increase in this ratio, a decrease in water absorption was observed. However, increasing cement content in cold-bonded aggregate production is not suitable regarding costs. Chi et al. [47] studied three types of cold-bonded pelletized lightweight aggregates made of various ratios of cement to fly ash. Water absorption values were 34.4, 30.5 and 20.8 % for aggregates with the ratio of 10, 15 and 20 %, respectively. In another study [32], water absoption values were 21.7, 21.6 and 19.5 % for aggregates produced with the ratios of 0, 10 and 20 %, respectively.

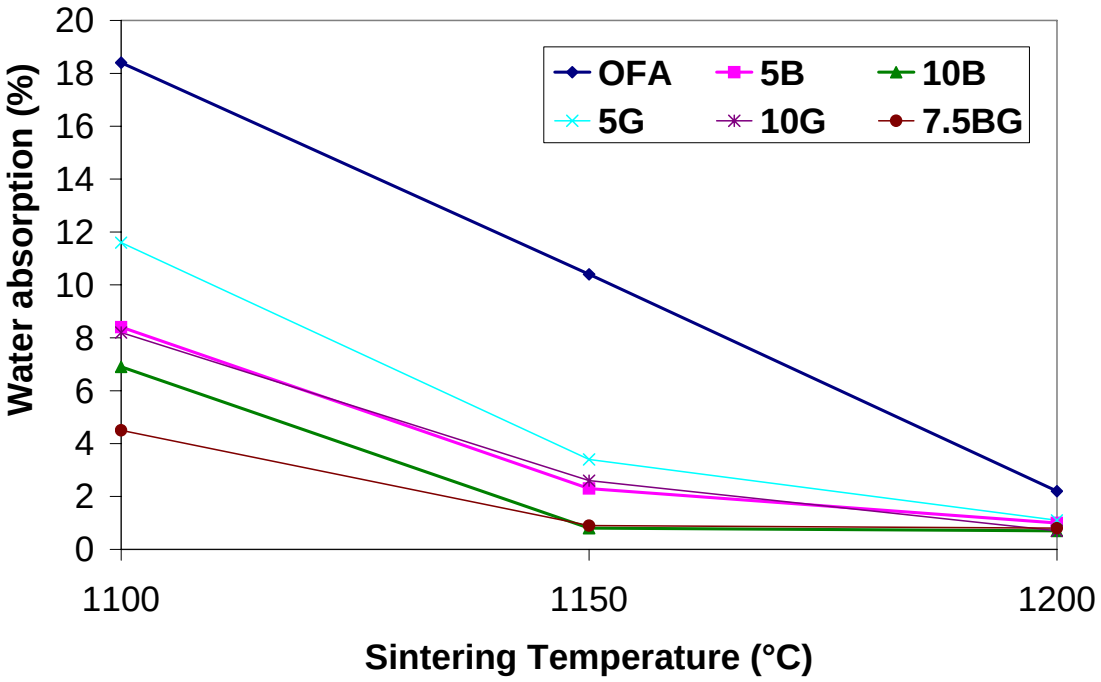

Figure 5.7. The effect of sintering temperature on water absorption

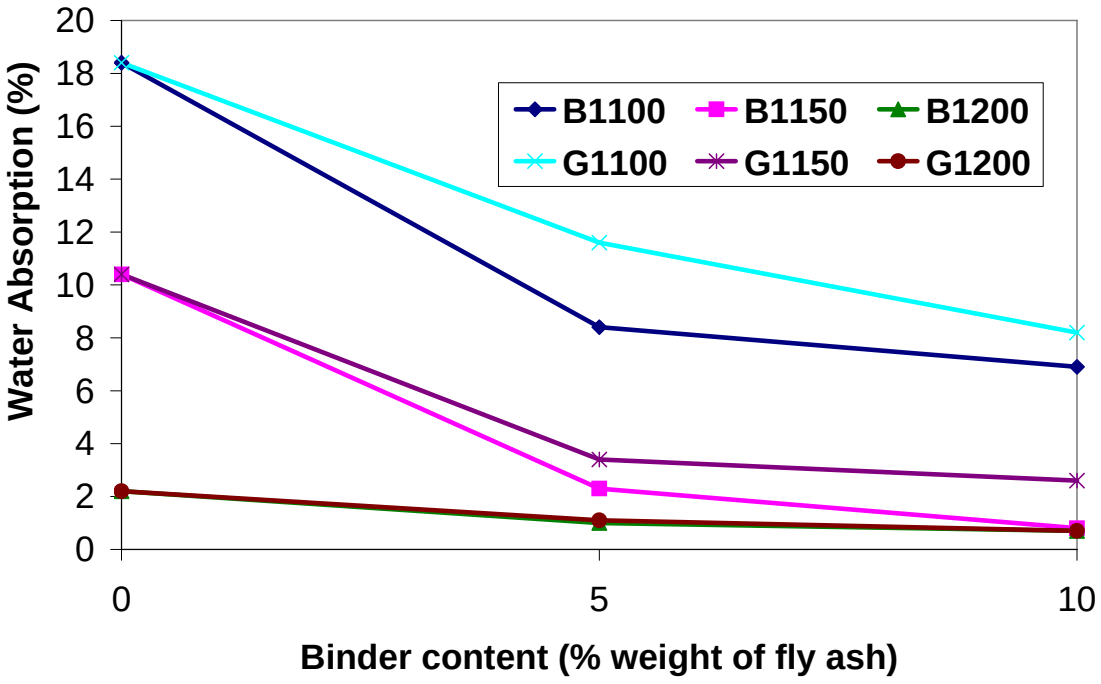

Figure 5.8. The effect of sintering agent content on water absorption

Results of total porosities measured by mercury porosimetry are presented in Table 5.5 and Figures 5.9-5.11. In all of the aggregates, the mercury porosimetry values were greater than those of the water saturation. The trend observed in this study was due to the

presence of a relatively large volume of closed pores which could not be penetrated by water but could be penetrated by mercury, due to rupture of pore walls under the high mercury pressure. Thus, it can be assumed that the mercury porosimetry reflects the total porosity in these systems, whereas the water saturation porosity is a better measure of the open porosity [23]. In terms of the physical and mechanical properties of the aggregates, one would expect that the total porosity (mercury porosimetry test data) would correlate better with the strength of the aggregates while the open porosity (water saturation data) would correlate better with the absorption characteristics of the aggregates. Both properties, strength and absorption, are of prime importance in controlling the behavior of the lightweight aggregate concrete. Furlani et al. [91] indicated that density is a function of chemical composition, but also of total porosity which is the sum of open and close porosity.

It is revealed that increase in the temperature of heat treatment should generally result in greater fusion and sintering leading to reduction in open porosity [23]. However the reduction in porosity by fusion and sintering may not be as high as expected due to increase in the volume of the solid which is a consequence of the reduction in its density.

In this study, a lower density aggregate with a microstructure of high porosity within a matrix was targetted and thus bentonite and glass powder as binders were introduced into the fly ash mix. The binders burned off during sintering, increasing the porosity of the resultant aggregates and decreasing their densities. Lightweight aggregates with densities as low as 1.34 g/cm^3 could be produced by adding binders. Aggregate production with fly ash and binders presents a further advantageous reuse application for all waste products.

Comparing the density and water absorption data clearly indicated a change in the nature of the porosity as the sintering temperature and the binder content increased. Sintering OFA aggregate at 1200 ^{o}C showed a well-formed, dense matrix material that contained a significant volume of isolated approximately spherical porosity (Figure 5.30). This behavior was also stated by some researchers [18, 21, 22 and 26] at high temperatures. These pores were in the 1–10 μm diameter range. The aggregates also had low water absorption due to the closed nature of the porosity and high strength due to the relatively small pore size and the strong matrix material. Sintering aggregates with binders

at 1200 ^{o}C caused larger isolated pores that begun to coalesce and form irregular shaped voids (Figures 5.31, 5.34, 5.37, 5.40 and 5.43). Lower water absorption values was obtained for these aggregates because the porosity remained closed, but as the larger pores bigger than 10 μm occured, crushing strength inevitably reduced. Expansion and bloating took place at this temperature due to gas evolving decomposition reactions occurring in a low viscosity glassy matrix. This behavior was also reported by other studies [18, 21, 22, 26, 28, 30, 33, 87, 89 and 90] resulting from softening of the glassy phase, together with simultaneous evolution of gas. This type of pyroplastic effect has also been observed in other materials, where gas generation is reported to be due to the decomposition of alkaline metal salts. The macro-porosity found in bloated samples is caused by gases formed at high temperature that are trapped in the microstructure forming cavities. These gases do not result from carbon combustion as this is oxidised and released from the samples at temperatures below 850 ^{o}C under conventional, slow sintering conditions [90]. This carbon combustion was also proved by DTA curves which took place at 440 ^{o}C, in this study.

In the case of total porosity of OFA aggregates, similar trend was observed as in water absorption. There was a linear reduction in porosity of OFA aggregates. The addition of binders reduced the total porosity at 1100 and 1150 ^{o}C, however the total porosity increased with the use of binders at 1200 ^{o}C. The total porosity decreased when the content of binders increased except for 7.5BG1200 aggregates. However, this result is contradictary with the results of specific gravity and crushing strength. Decrease in specific gravity denotes increase in porosity and decrease in crushing strength. The reason may be due to the formation of excessive glassy phase at 1200 ^{o}C close to the surface preventing the penetration of mercury. In the study, 220 MPa mercury pressure applied on aggregates, this pressure may be insufficient to rupture the pore walls under these circumstances. These pore walls may be so thick and gain adequate strength to resist to this pressure. In some studies [23, 30 and 67], higher pressure was applied (400 MPa) in order to determine the porosity of aggregates or concerete. Diamond [65] noted that intrudable porosity as measured in MIP was not a measure of total porosity in the system. In addition to the pore space actually intruded by mercury, finer pores undoubtedly exist in samples that require pressure for entry beyond the pressuring capacity of commercial instrumentation. Some completely isolated pores that are entirely sealed against intrusion may be present as well.

The closed porosity of OFA, 5B and 5G aggregates increased with the rise in temperature. This increase was remarkable in OFA aggregates sintered up to 1150 ^{o}C, however, a sharp increase was observed in aggregates with a content of 5 % of binder sintered to 1200 ^{o}C. The aggregates with higher content of binder showed decrease in total porosity at 1150 ^{o}C. Aggregates with 10 % bentonite exhibited a decrease from 15.1 to 2.0%, and the total porosity of aggregates with 10 % glass powder declined from 11.3 to 3.9 %. In addition, aggregates produced with both glass powder and bentonite showed a drop from 13.4 to 2.5 %. Almost the same trend was observed in specific gravity and strength. 7.5BG1200 aggregate had the highest closed porosity due to the high amount of binders resulting in occurence of insulated larger pores after sintering at high temperature. In a study [92], it was pointed out that both the total porosity and open porosity were decreased with increasing sintering temperature because of the gradual densification induced by sintering. On the other hand, the significant increase in closed porosity was due to the formation of unconnected pores in the presence of more liquid phase.

While sintered OFA1100 had higher water absorption capacity than 5B1200 and 7.5BG1200, three types of aggregates showed similar porosities, indicating the more open, water-accessible pore structure of sintered OFA1100 in comparison to 5B1200 and 7.5BG1200. For the aggregates 10B and 10G sintered at 1200 ^{o}C, the open porosity approached 0.7% and the total porosities (8.4 and 6.2%, respectively) were very close to the closed porosities (7.7 and 5.5%, respectively). This is suggested that there were only unconnected gas pores present in the sintered bodies.

The method for the preparation of the samples for the MIP test can have impact on the porosity values; for example, mechanically chipping and subsequent drying can lead to microcracks in the samples. Thus, aggregates were used as individual particles with a diameter of smaller than 8 mm for MIP tests. Mercury intrusion porosimetry provides the pore size distribution of the aggregates for relative comparison. Table 5.5 shows the min and max pore diameters, critical pore diameter in nm., total porosity and closed porosity of aggregates. Figures 5.9-5.11 illustrate the pore size distribution of aggregates. The pressures were converted to equivalent pore widths using the Washburn equation as given earlier. Minimum and maximum diameters of the pores was calculated from the largest exerted pressure value and the initial intruded pressure, respectively. The inflection point

from the curve of volume versus size of the pores (or the maximum of the dV/dp curve) was taken to be the critical pore diameter. It is suggested that this point corresponds to the smallest pore size that creates connected paths through the sample [93]. The minimum and the maximum pore sizes were about 7 nm and 10000 nm, respectively. Generally, the critical pore diameters of aggregates showed paralellism with the total porosity values. The critical diameter decreased with temperature in OFA aggregates. However, aggregates with binders showed decrease up to 1150 ^{o}C, then rise with further increase in temperature. It is generally accepted that the smaller the critical pore diameter, the finer the pore structure [94]. Some aggregates showed relatively higher critical diameter than the other types of aggregates. This result may be due to the high pressures of the mercury in the test that might have damaged the pore structure as also noted by Zhang and Zhang [93]. For example, BG1200 aggregate showed high critical diameter. This type of aggregate expanded at 1200 ^{o}C due to bloating with its high binder content. The thin pore walls could occur during expansion. This made aggregate pore structure more vulnerable to high pressures of the mercury in MIP test. Diamond [65] also stated that intrudable volume includes air voids as well as intrinsic pores, and the air void content may fluctuate depending on mixing procedure. The MIP test could be affected by many factors. According to him, conditions that must be met for MIP measurements to provide valid estimates of pore size distribution of porous solids are not satisfied in cement-based systems. He suggested that the method should not be used to measure the actual pore size distribution but only to provide threshold diameters and porosity for comparison purposes.

The total porosity of cold bonded lightweight fly ash aggregate was 31.1 %. This value was the highest value among all aggregates followed by 7.5BG1200 and OFA1100 which possessed total porosity of 21.8 and 19.1 %, respectively. The closed porosity of CB aggregate was 7.2 %. Similar values were also obtained in the case of 5B1100, 10B1200 and 5B1150 having closed porosity of 6.9, 7.7 and 7.8 %, respectively.

Table 5.5. Results of MIP tests

Aggregates	Pore diameter range (nm)		Critical pore diameter (nm)	Total porosity (%)	Closed porosity (%)
	max	min			
OFA1100	10277.72	7.02	26.92	19.1	0.7
5B1100	10277.75	7.28	32.44	15.3	6.9
5G1100	9535.24	7.01	19.90	13.6	2.0
10B1100	10277.74	6.80	38.63	15.1	8.2
10G1100	10551.59	6.70	15.94	11.3	3.1
BG1100	10840.49	7.16	34.93	13.4	8.9
OFA1150	10017.71	7.16	19.62	13.3	2.9
5B1150	10840.49	7.11	19.44	10.1	7.8
5G1150	10277.72	6.66	17.87	7.3	3.9
10B1150	10551.60	6.60	21.47	2.0	1.2
10G1150	10017.69	6.77	12.16	3.9	1.3
BG1150	9311.02	6.60	49.23	2.5	1.6
OFA1200	10840.51	6.82	16.35	6.5	4.3
5B1200	10277.77	6.88	53.38	17.6	16.6
5G1200	10840.49	6.82	21.64	16.9	15.8
10B1200	10840.46	6.82	28.03	8.4	7.7
10G1200	8159.76	7.08	12.49	6.2	5.5
BG1200	10840.49	6.68	74.91	21.8	21.0
CB	9097.12	6.75	398.4	31.1	7.2

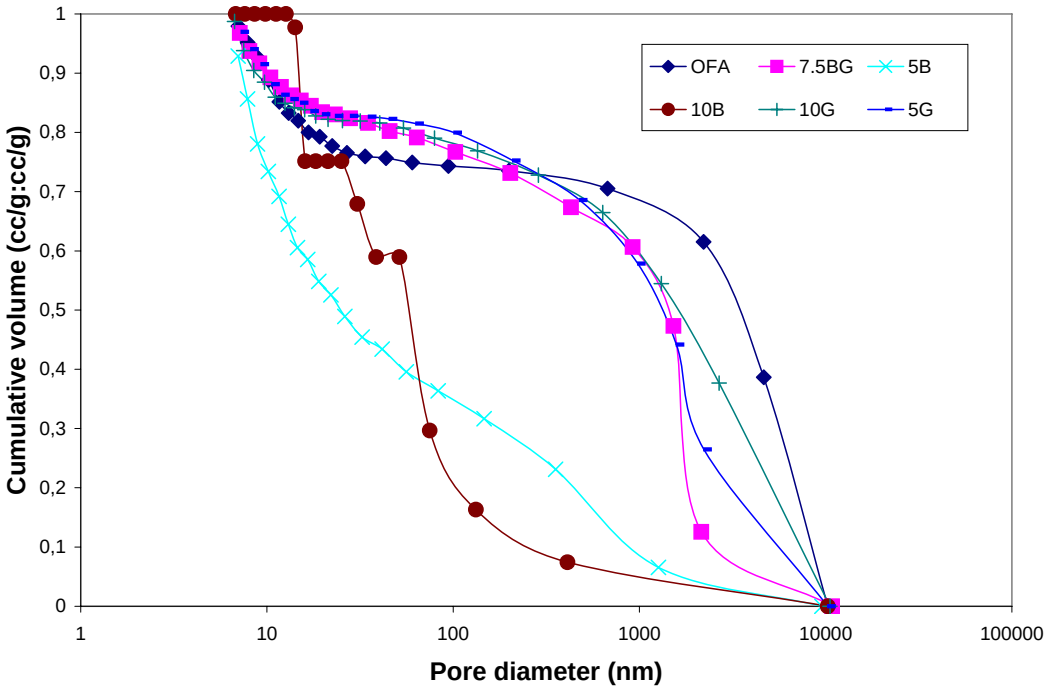

Figure 5.9. Pore size distribution of aggregates sintered at 1100 ^{o}C

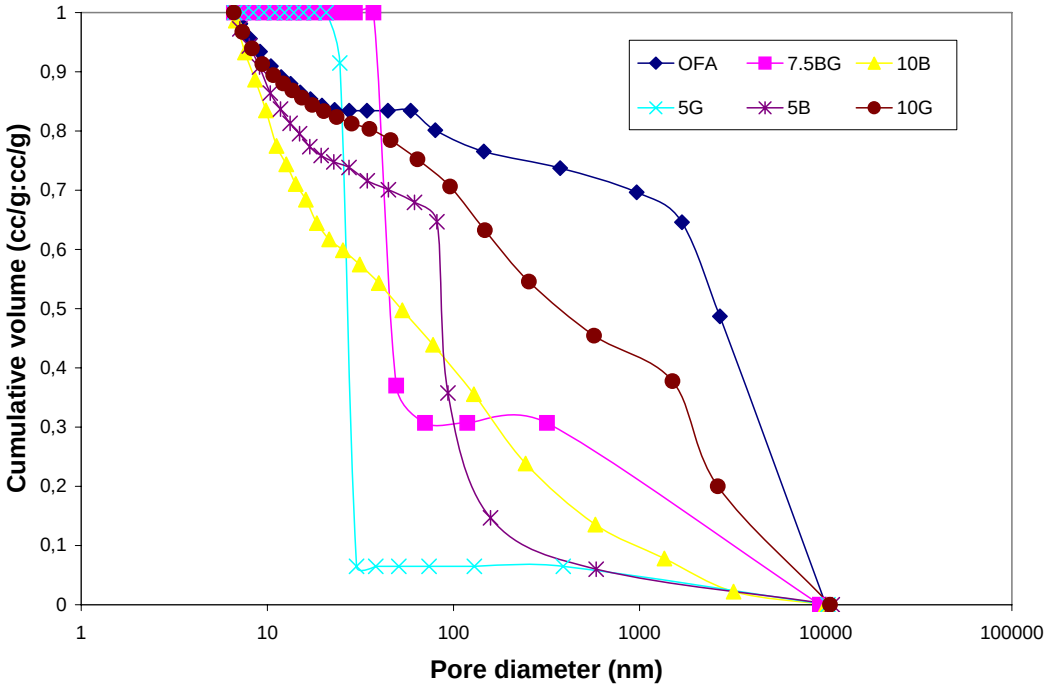

Figure 5.10. Pore size distribution of aggregates sintered at 1150 ^{o}C

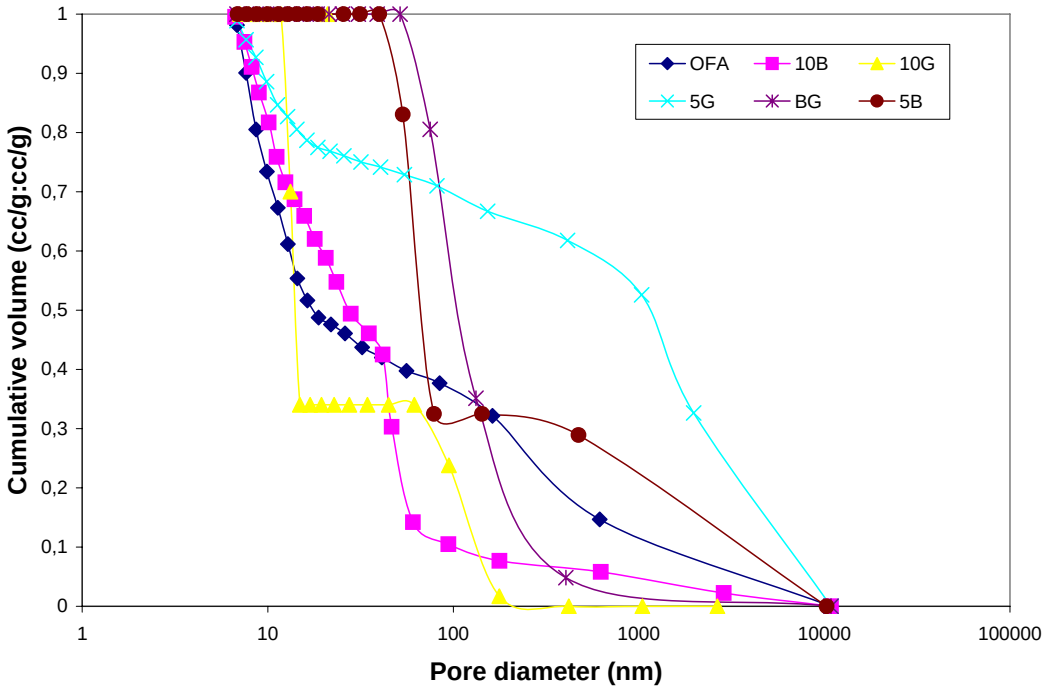

Figure 5.11. Pore size distribution of aggregates sintered at 1200 ^{o}C

5.1.4. The Effects of Temperature and Type and Content of the Binder on Crushing Strength

The effects of sintering temperature and binder type and content on crushing strength are shown in Figures 5.13, 5.14 and Table 5.6. Replotting the data in different way offers an alternative view of the data set. The complex interplay between binder type, content and temperature emerges from the data.

The aggregates with binders exhibited higher strength than the aggregates without binders (only fly ash OFA) at temperatures 1100 ^{o}C and 1150 ^{o}C. The crushing strength of aggregates with bentonite slightly increased by the content of bentonite at these mentioned temperatures, however aggregates with glass powder exhibited a slight decrease with content increase at 1150 ^{o}C. The differences in crushing strength could not be correlated only with differences in porosity as also demonstrated by another study [23]. This may be due to several influences such as change in the mineralogical composition and cracks and internal defects due to thermal stresses. Also, the difference in the strength behavior of aggregates with temperature rise can be due to the different melting points of binders as observed from DTA analysis (Figure 5.21).

The highest strength values were obtained for OFA aggregates by sintered at 1200 ^{o}C and for aggregates with binders sintered at 1150 ^{o}C. The strength of all aggregates decreased with increasing the binder content at 1200 ^{o}C. Large pores occured due to bloating at 1200 ^{o}C. In previous studies [18, 21, 22, 26, 28, 30, 34, 87, 89 and 95], sintering of different materials such as zeolitic tuff, sewage sludge ash with clay and incinerator bottom ash etc. at high temperatures caused decrease of the strength due to volume expansion. These volume expansions were observed at different temperatures depending on the difference in thermal behavior of materials investigated in those studies. In contrast to aggregates with binders, the strength of OFA aggregates increased steadily with the temperature increase due to the densification of fly ash. The expansion of only fly ash aggregates probably might take place at temperatures higher than 1200 ^{o}C, because specific gravity, water absorption and strength data of this aggregate showed similarities with the aggregates containing binders sintered at 1150 ^{o}C where they had maximum values of specific gravity, water absorption and strength. DTA curves in Figure 5.21 showed that aggregate with binders started to melt in lower temperatures than did OFA. Bloating takes place after melting started. Also, SEM images proved this result step by step as initial softening, fusing and bloating in an order from low to high temperature. Increasing binder content decreased melting points of the aggregates. Fly ash comprised more refractory minerals, such as silica and alumina, and more particularly quartz and mullite, and lesser amounts of fluxing agents, such as calcium, magnesium, potassium, and sodium oxides, than binders (Figures 5.47-5.49 and Table 4.1). Addition of binders modified the densification behavior of fly ash, resulting in a tighter temperature interval between the initial softening, sintering, and melting of the material by changing the chemical composition and mineralogy of the material. Since refractory minerals in the FA sintered and melted at higher temperatures due to their higher melting points than the fluxing agents in the binders, as the amount of binders added to the fly ash increased, the mixture sintered and melted at lower temperatures as can also be seen in SEM observations. Most researchers [18, 87 and 88] demonstrated that chemical composition strongly affected the sintering behaviour of FA, and consequently the final microstructure of sintered FA bodies. It is well known that the elemental oxide composition influences the viscosity, hence the sintering behaviour of coal ash. For instance SiO_2 acts as a network former, having a positive effect on viscosity whereas CaO or Na_2O decreases the viscosity by modifying the silicate network structure. The principal chemical compositions of fly

ash, bentonite and glass powder were SiO_2 (59.0 %, 57.84% and 70.62%), Al_2O_3 (19.58 %, 13.77 % and 1.38 %) and Flux (Fe_2O_3, CaO, MgO, Na_2O, and K_2O, 18.84 %, 18.53 % and 25.49 %), respectively. These compositions met the requirements of expansive clay (SiO_2: 48–70%, Al_2O_3: 8–25% and Flux: 4.5–31%) as stated by Riley [96]. Riley reported that two conditions were essential for the bloating of materials: The development of a glassy phase over a wide temperature range and evolution of gases from the dissociation of mineral components such as carbonates, oxides, hydrates, and sulfates present in the original material to form cellular structure in the mass. Riley proposed a composition diagram (Figure 5.12) of the major oxides (SiO_2, Al_2O_3, and fluxing oxides) showing the area in which the clays sinter to a mass viscous enough to ensure good bloating. Fly ash is enriched in glass former oxides (SiO_2+Al_2O_3 = 78.58%), whereas this content is 71.61 and 72% for bentonite and glass powder, respectively. The modifying or fluxing oxide contents of fly ash and bentonite are close to each other and lower than that of glass powder which was the main reason for the viscosity showed by the melted materials. These ranges of chemical compositions were adopted to different materials by several researchers [6, 28-30, 35 and 97]. In the light of these limitations, all materials alone could be a bloating material by itself under a sintering process. The high amounts of fluxes narrow the range of temperature, the melting process would be too rapid to have a suitable temperature for any bloating to develop. The greater possibility of better bloating could be achieved when bentonite and glass powder were mixed with fly ash at adequate proportions. The addition of glass powder increased the flux content and improved the chances of bloating in the aggregates.

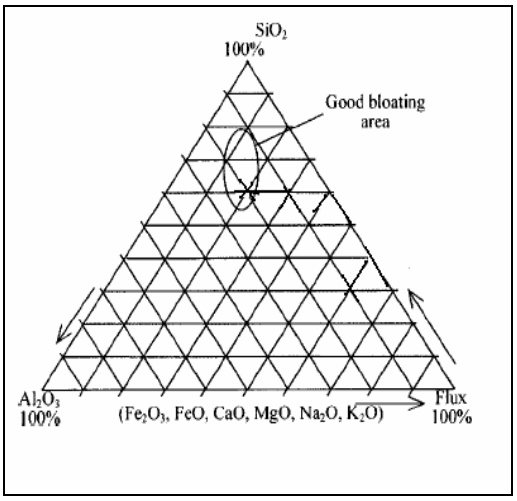

Figure 5.12. Riley's composition diagram showing good bloating area

Besides the chemical composition, other morphological characteristics of the materials such as reactivity of materials could be affected by a number of properties, including particle size, surface area and glassy phase content. Bentonite had the finest grains among the materials used and fly ash was coarser than both bentonite and glass powder. Also, bentonite and glass powder had irregular shaped particles, whereas fly ash had almost spherical particles. Differences in crystallinity were encountered as seen in XRD of raw materials. Thus the dissimilar sintering behaviour of materials could be attributed to a combined effect of crystalline structure, morphological characteristics and chemical compositions of materials used in aggregate production.

Bentonite was more effective in strength rise than glass powder especially at 1150 ^{o}C. The strength of aggregates with glass powder was lower than that of aggregates with bentonite at all temperatures. The glass powder used in the study was coarser than bentonite (Figure 4.1), resulting in larger pores during exposure to high temperatures. As can be seen in Figure 5.13, OFA aggregates became stronger by the temperature rise and showed marked increase between the temperatures 1150 and 1200 ^{o}C. Furthermore, as bentonite and/or glass powder were added, binders closed the pores by fusing, causing denser aggregates at 1100 and 1150 ^{o}C. At 1150 ^{o}C, strength gain was markedly high in aggregates with an amount of 5 % binders, especially in the case of bentonite, further increase in content, addition of 10 % binders, did not provide significant increase in strength, even aggregates with glass powder presented a slight drop.

In a study, researchers [8] indicated that further increase in fineness of fly ash can increase the strength of pellets. The use of finer fly ash has limited scope, as one should aim to utilize the available fly ash without further processing. In order to increase the strength of pellets and reduce its water absorption, the next option is to use binders, which are often used in metallurgical applications. In the same study, bentonite was observed to enhance the 10% fines value of aggregates significantly and the maximum value was obtained with 20% dosage. Beyond this dosage, there was no further enhancement in the 10% fines value of sintered aggregate. Bentonite is a clayey material consisting mainly of montmorillonite (Figure 5.48). Montomorillonite has one exceptional property, it can take up water into the interlayer space. This is connected with the typical swelling ability of

bentonite, which is important for balling because it enhances the cohesion of particles in the ball and the ball strength depends on cohesion of particles.

Among the aggregates produced with binders, B101150 had the highest and OFA1100 had the lowest strength values; 23.1 MPa and 5.1 MPa, respectively. The strengths of aggregates with binders showed the same trend of pellet densities with increasing temperature, increasing to a maximum value and then decreasing, as expected. Bentonite was finer than glass powder and aggregates made from small particle sizes showed a higher strength, which is consistent with observations obtained by several researchers [34, 88]. Since smaller particles give a larger total surface area, small ash particles may result in a larger change in the surface area during sintering, and in turn, a larger change of free energy. This implies that the sintering of smaller particles will proceed with a smaller positive of total free energy value. The densification, and thus the development of the strength is thermodynamically more likely to occur for ash with a smaller particle size. Tsai et al. [35] pointed out that in general, the strength of aggregates was affected by a number of inter-related factors, such as the porosity, the pore size and distribution, the mineral species in the powder, speciation variation during heating, densification effects by sintering, bloating of the aggregate, and even pellet surface cracking or fracturing by thermo-stress.

The crushing strength of cold-bonded lightweight aggregates was 3.7 MPa which was the lowest value among all sintered aggregates. Lightweight aggregates produced by cold bonding procedure have limited strengths due to the reaction capacity of materials used in aggregate. The crushing strengths of cold bonded lightweight aggregates present different values available in the literature which make the comparison of these values with those obtained in this study impossible. The main reasons of this result are as follows: (a) adopting different strength determination methods, even in this study, using different load ring in crushing test set up caused different load measurements although the same aggregate type was tested. Therefore, all the measurements were made with the same load ring to evaluate the results properly. (b) The difference in chemical and physical properties of materials (fly ash and cement in this case) used in aggregate production, (c) different pelletization and curing methods applied and (d) the variability in the amount of constituents such as water-powder ratio. On the other hand, it is noted that the temperature

versus density and temperature versus strength curves may vary for different furnaces used the previous studies in the literature. These curve shiftings may be attributed to the operational efficiency of a particular furnace, such as the stability of temperature profile, energy losses and location of the pellets in the furnace, besides the difference in properties of materials used.

Table 5.6. Crushing strength values of LWAs

Temperature (°C)	OFA	5B	10B	5G	10G	7,5BG	CB
1100	5,1	13,1	13,7	9,7	11,5	14,0	3,7
1150	8,6	20,4	23,1	15,6	14,7	14,2	
1200	19,3	13,4	12,0	11,8	9,6	7,1	

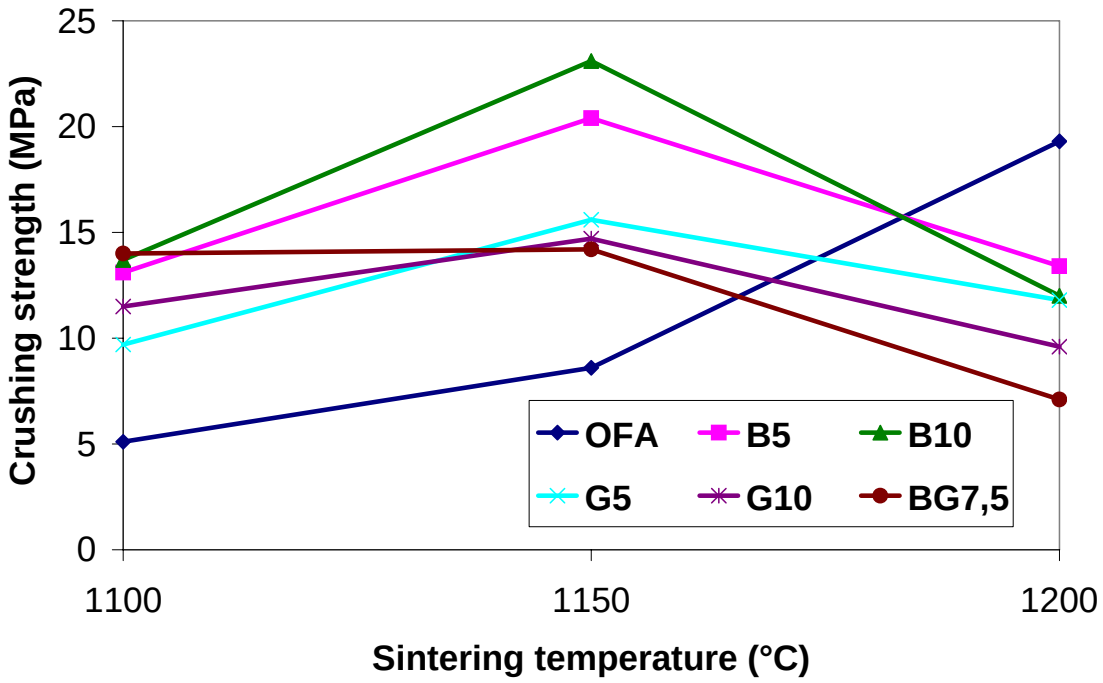

Figure 5.13. The effect of sintering temperature on crushing strength

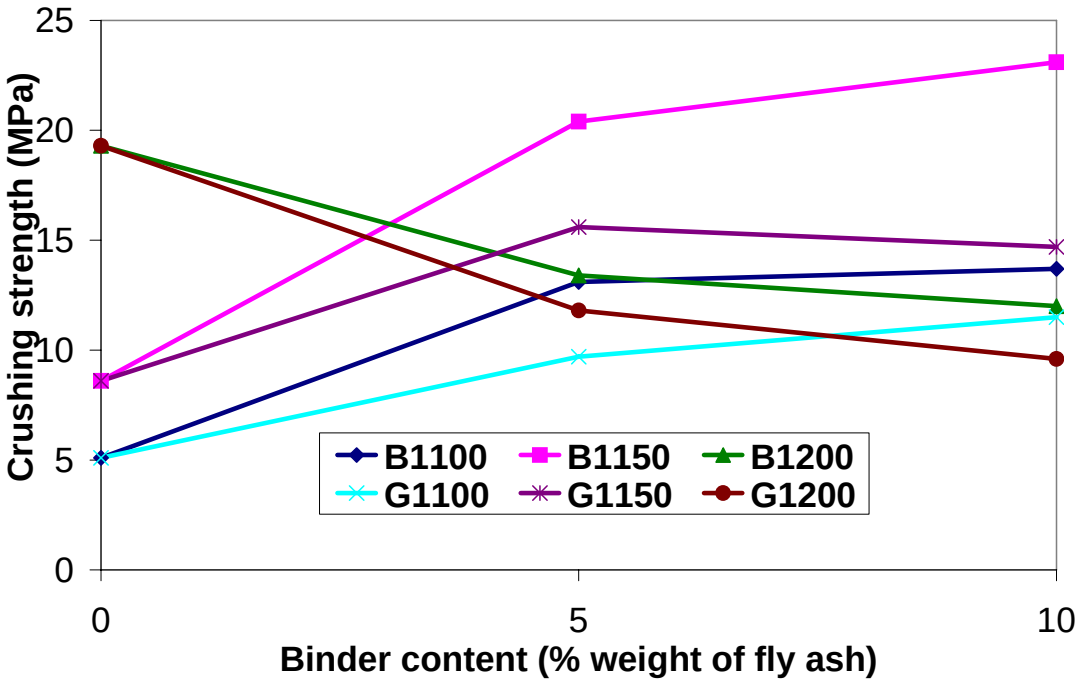

Figure 5.14. The effect of sintering agent content on crushing strength

5.1.5. Relationship between Specific Gravity (OD) and Crushing Strength of Aggregates

Crushing strength of aggregates with glass powder sintered at 1100 ^{o}C increased with the increase in binder content, and crushing strength of 7.5BG was not changed much with the increase in temperature from 1100 to 1150 ^{o}C although the specific gravities of these aggregates decreased. On the other hand, the present data indicated that strength increased linearly with density for the majority of the aggregates with the same material compositions. In other words, this stronger linearity could be observed among the aggregates with glass powder, with bentonite and only fly ash, separately. For example, 10B1150 and 5G1150 aggregates had same specific gravity of 1.93, however, crushing strengths were 23.1 and 15.6 MPa, respectively. It is obvious that decreased density does not necessarily imply decreased strength. This kind of behavior was also detected by Biernacki et al. [2] who studied the temperature and sintering time effect.

Regression analyses were performed on experimental data obtained in this study using the linear regression models for each analysis. Three different models were established with all of the aggregate types and aggregates with two different compositions.

Figures 5.15-5.17 show the relationships between the crushing strength and specific gravity of the aggregates. As it can be seen, bigger R-square values were obtained by analyzing the aggregates separately. Small R-square value of 0.60 for the whole aggregate types showed that the regression was established under poor fit. However, correlation of aggregates with bentonite and glass powder gave bigger R-square values 0.74 and 0.71, respectively showing the existence of less variation in the specific gravity and crushing strength results. The following equations and R-square values are given in an order of all aggregate types, aggregates with glass powder and aggregates with bentonite from the regression analysis results:

$$\sigma = 21{,}994*\gamma - 24{,}913,\ R = 0.77 \quad (5.1)$$

$$\sigma = 24{,}67*\gamma - 31{,}488,\ R = 0.84 \quad (5.2)$$

$$\sigma = 31{,}631*\gamma - 40{,}878,\ R = 0.86 \quad (5.3)$$

where:
σ = Crushing strength, MPa
γ = Specific gravity, gr/cm^3

It is possible to identify the mechanism responsible for the observed density–strength behavior. Using different materials in aggregates as binders resulted in different behavior due to their various chemical, physical and mineralogical properties. The phase redistribution creates a weaker composite due to precipitation of SiO_2 and Al_2O_3 crystalline phases, quartz, mullite, etc., as reported in a previous study [2]. X-ray powder diffraction characterization of sintered materials showed that the relative amounts of the primary crystalline phases, mullite and quartz were changing with processing conditions (Figures 5.51-5.55). The amount of quartz decreased with increasing temperature. It also appeared that the overall crystalline content was decreasing, indicated by decreased peak intensities with increasing temperature.

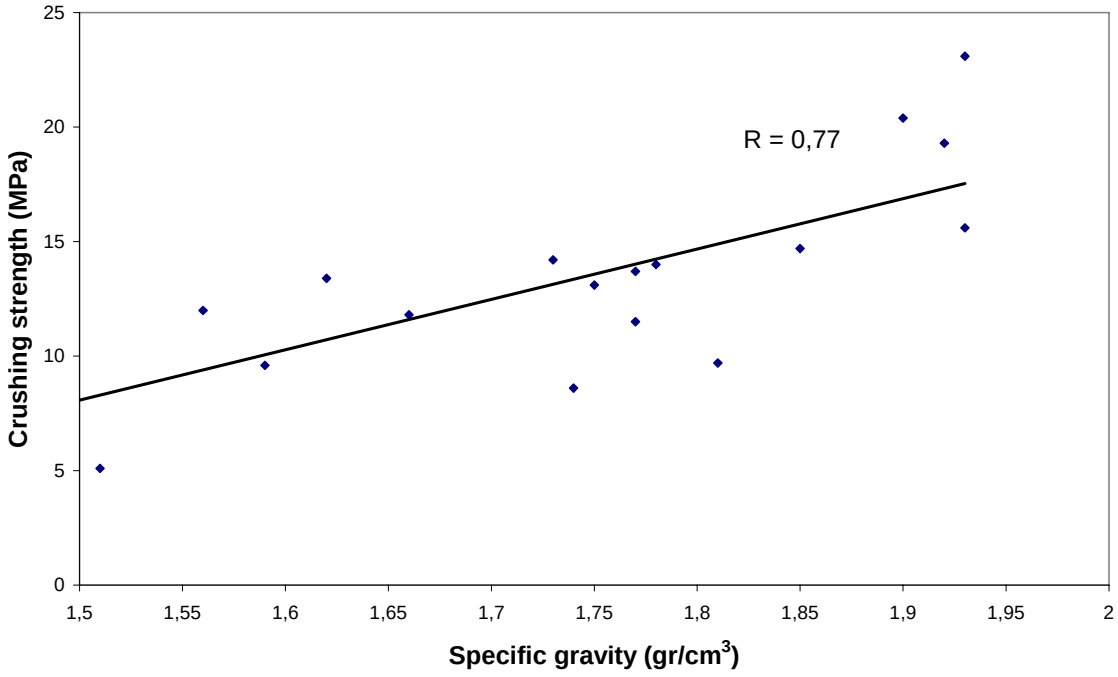

Figure 5.15. Relationship between specific gravity (OD) and crushing strength of all aggregates

The expansion at high temperature depends on viscosity of materials. The proper viscosity can be determined from the chemical compositions of the raw materials used. Generally, its CaO and MgO contents account for a sudden change in the viscosity of the raw materials at high temperatures. The melting point and viscosity are low when the ratio of Al_2O_3 to SiO_2 is low. High Al_2O_3 + SiO_2 contents led to mullite formation. It is known that high Al_2O_3 content and mullite formation improve the properties of the sintered materials. SiO_2+Al_2O_3 behave as a glass former which increases the melting temperature while the alkali oxides decrease the melting temperature [3]. Therefore, sintered material with the highest strength value probably had the highest crystallization degree with the lowest glassy phase. The occurrence of crystalline inclusions can contribute to residual stress development since crystallization in this case is accompanied by a significant change in volume, the specific gravity of the nominal glass is 2.3 while that of quartz and mullite are 2.65 and 2.8, respectively.

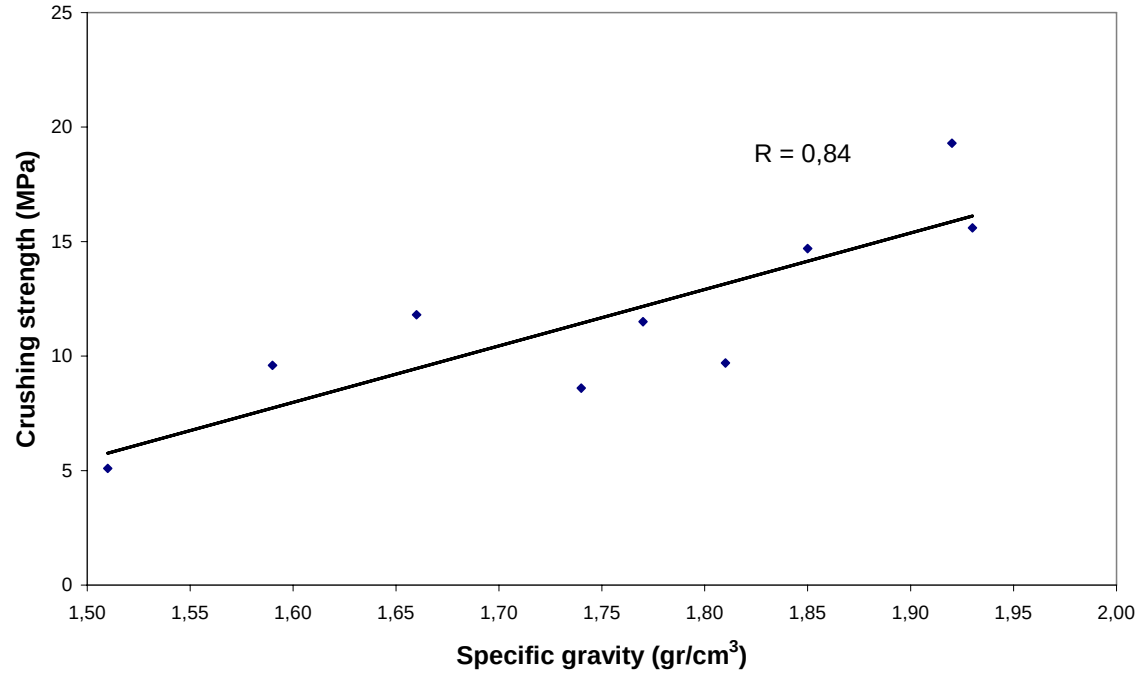

Figure 5.16. Relationship between specific gravity (OD) and crushing strength of aggregates with 0, 5 and 10 % of glass powder

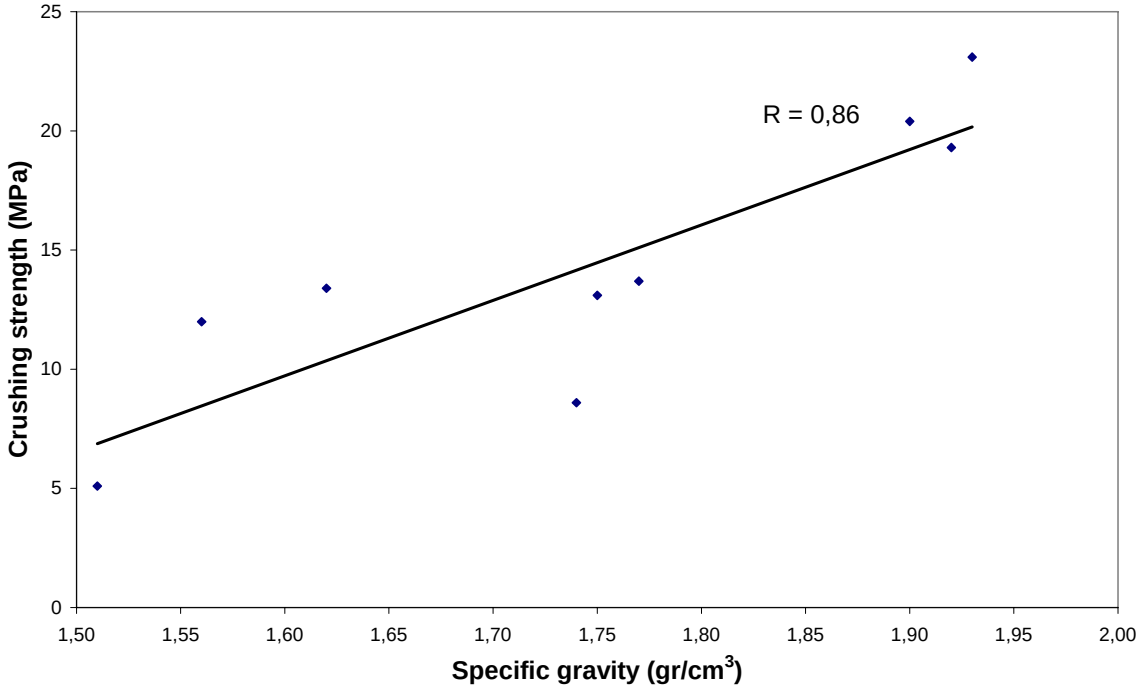

Figure 5.17. Relationship between specific gravity (OD) and crushing strength of aggregates with 0, 5 and 10 % of bentonite

5.1.6. Thermal Behavior (DTA-TG) of Powders Used in Aggregate Production

Thermal properties of raw materials and aggregate compositions were examined by using DTA-TG analysis, in platinum crucible using calcined powdered aluminium oxide as reference. Materials of about 20 mg were analysed in powder. DTA-TGA curves with the heating rate of 10 and 20 ^{o}C/min. are shown in Figures 5.18-5.21. Using higher heating rate such as 20 ^{o}C/min was because of increasing the possibility of observation of more clear DTA curves. Li et al. [97] indicated that with the decrease of heating rate, the endothermic peaks of polymorphic transformations in the corresponding curves weakened gradually, and could not be measured at 5 ^{o}C/min. The reason is that when the heating rate is too low, the heat effect from the reaction is transferred into the ambient environment and the difference of heat flow cannot be detected by the analyzer. Also, Öveçoğlu et al. [98] reported that both the Tg and Tp temperatures shifted to higher values with increasing rate.

The TGA of the glass powder showed 1.6 % weight loss up to 1053 ^{o}C (Figure 5.18). The TGA of the bentonite and fly ash exhibited 11.4 and 2.3 % weight loss up to 1160 ^{o}C, respectively (Figures 5.19 and 5.20). These results obtained from TGA were similar with the loss on ignition values of the materials. The reason of heating glass powder up to a lower temperature was the adherence of melted powder to the platinum crucible (sample holder). The weight loss value of 2.3 % reflected the weight of unburned carbon, sulfide, hydrate, carbonate and oxide that was present in the fly ash. According to the literature data [99] in the temperature range between 500-750 ^{o}C, in the inert atmosphere, degredation of carbonate can take place, just one process influence on the weight loss. In the same temperature range but in the oxidizing atmosphere unburned carbon can oxidize into carbondioxide at the same time with the degredation carbonate, both process influences on the weight loss. The weight loss can also be due to the loss of external, loosely bound and tightly bound water. Loss on ignition values of fly ash, bentonite and glass powder were 0.49, 8.40 and 0.12 %, respectively (Table 4.1). Loss on ignition values of materials showed consistency with the weight loss in the TGA. Also, $CaCO_3$+$MgCO_3$ content of bentonite and glass powder were 6.50 and 0.75 %, respectively. Glass powder exhibited a linear increase in weight loss, however bentonite showed a markedly rise in weight loss between 400 ^{o}C-650 ^{o}C. The slope of weight loss curve of fly ash increased

between 950-1160 ^{o}C. These weight loss characteristics of three materials also could be observed in TGA of aggregate compositions.

In the DTA thermogram of the fly ash (Figure 5.20), one endothermic peak was recorded at 440 ^{o}C, due to the glass transition and formation of CO_2 from carbon compounds, followed by one exhotermic peak at 623 ^{o}C due to the ferrous and sulphides oxidation and combustion of organic materials. A small exothermic effect was detected approximately at 1100 ^{o}C corresponding to the crystallization of mullite and anorthite, detected also in the study [87], the main crystalline phases as assessed by XRD. Although the melting of fly ash could not be detected clearly due to heating up to 1160 ^{o}C, it could be stated that the melting started at approximately 1150 ^{o}C proved by experimental results such as density, porosity and strength and SEM micrographs. Dong et al. [92] suggested that the impurities in fly ash, as glassy modifiers, lowered the melting temperature of the silica-rich glassy phase. As a result, the densification process was enhanced by the liquid phase at a relatively low temperature.

In the DTA thermogram of the bentonite (Figure 5.19), first and second endothermic peaks appeared at 430 ^{o}C and 656 ^{o}C due to the release of water from crystals and dehydroxylation (the loss of structural hydroxyl groups). The endothermic peak confirmed the presence of montmorillonites appearing between 600 and 700 ^{o}C and the exothermic peak at 1130 ^{o}C was observed due to the collapse of the crystal structure. Some studies [5, 100] were also reported same behaviors.

In the DTA curve of the glass powder (Figure 5.18), one endothermic and one exothermic peaks appeared at 440 ºC and 740 ºC. The first one was attributed to the glass transition and the second one was to the glass crystallization. Same behaviors were also obtained by other studies [101-103].

Figure 5.21 shows the DTA curves of the aggregates scanned between 50 and 1160 ^{o}C. Endothermic and exhotermic peaks were detected at 440 and 623 ^{o}C as pronounced above in the DTA of the fly ash. However, although endotermic peaks were observed for all aggregates, exhotermic peaks began to disappear by increase in binder content. Also, endothermic peaks approximately at 1000 ^{o}C (10G, 7.5BG), 1100 ^{o}C (5G), 1050 ^{o}C (5B)

and 980 ^{o}C (10B) due to the occurence of liquid phase were observed in the DTA curves of aggregates with binders. One of the reason of melting formation in an earlier stage could be due to the finer grains of bentonite than both glass powder and fly ash besides other reasons such as chemical compositions of materials. The endothermic peaks due to the formation of melting were also observed in some previous investigations [33, 97, 101-104]. Also, Show et al. [30] pointed out that porous structures that provided the lightweight property of the aggregates began to develop as the endothermic reaction occurred. DTA curves of aggregates reflected the thermal properties of raw materials.

In trial production treatments, when fly ash lightweight pellets were sintered below 1100 ^{o}C, the aggregates contained loosely bounded particles and weak matrix. Sintering at 1200 ^{o}C led to agglomeration of 7.5BG pellets in the furnace. However, this agglomeration could not be observed at sintering below 1200 ^{o}C. 7.5BG pellets contained 15 % total binder content (7.5% glass powder plus 7.5% bentonite). The reason of this result is due to the sintering of excessive binder content above their melting points.

The DTA data also enable us to determine the energy uptake of the samples [30]. With the same sample mass of 20 mg and a heating rate of 20°C/min the energy requirements of the materials could be determined. Less energy was needed for heating each gram of unburned aggregates that contain 10 % glass powder accompanied by 10% bentonite and 7.5 % bentonite and glass powder.

The good bloating area in the composition diagram of oxides given by Riley [96] mentioned previously in this study may not apply to all materials. Determination of substances released through analysis of TGA and peaks of endothermic transitions and exothermic crystallization of DTA gave a more reliable indication of lightweight effect in sintered aggregates.

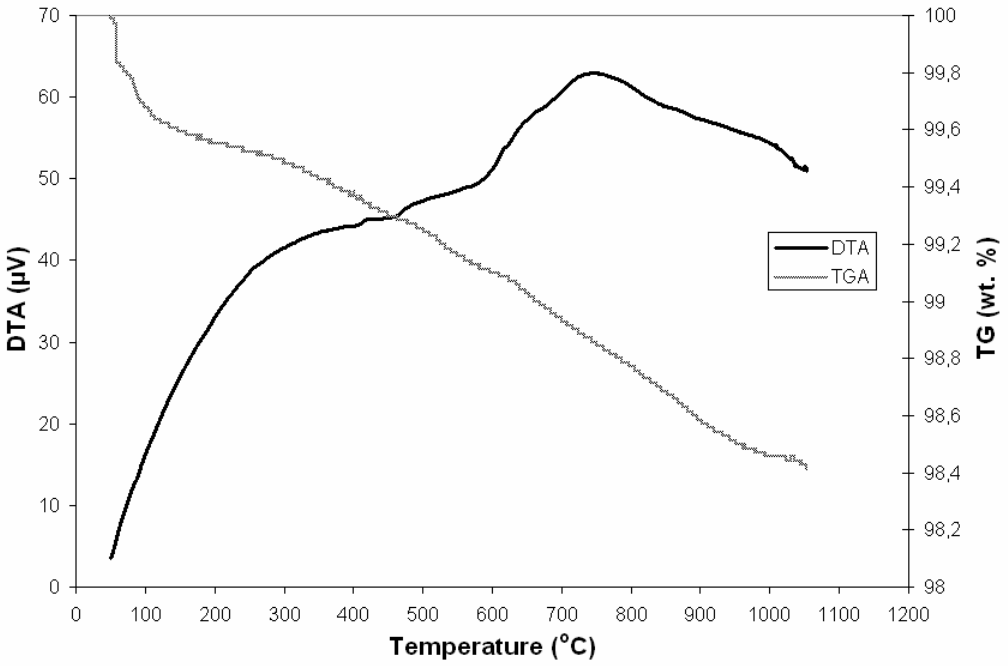

Figure 5.18. DTA/TGA curves of glass powder

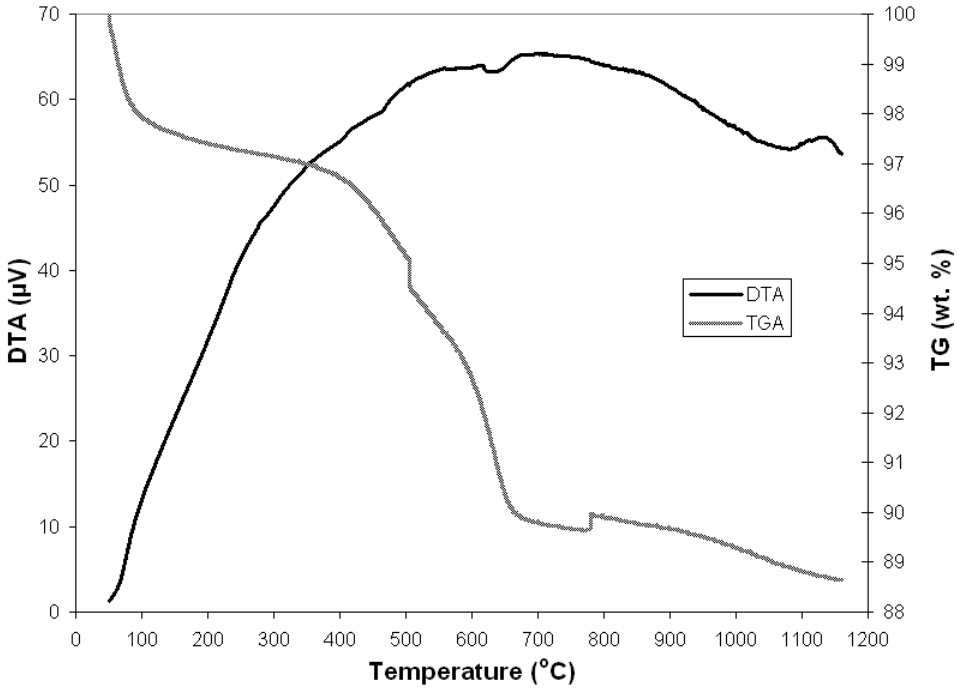

Figure 5.19. DTA/TGA curves of bentonite

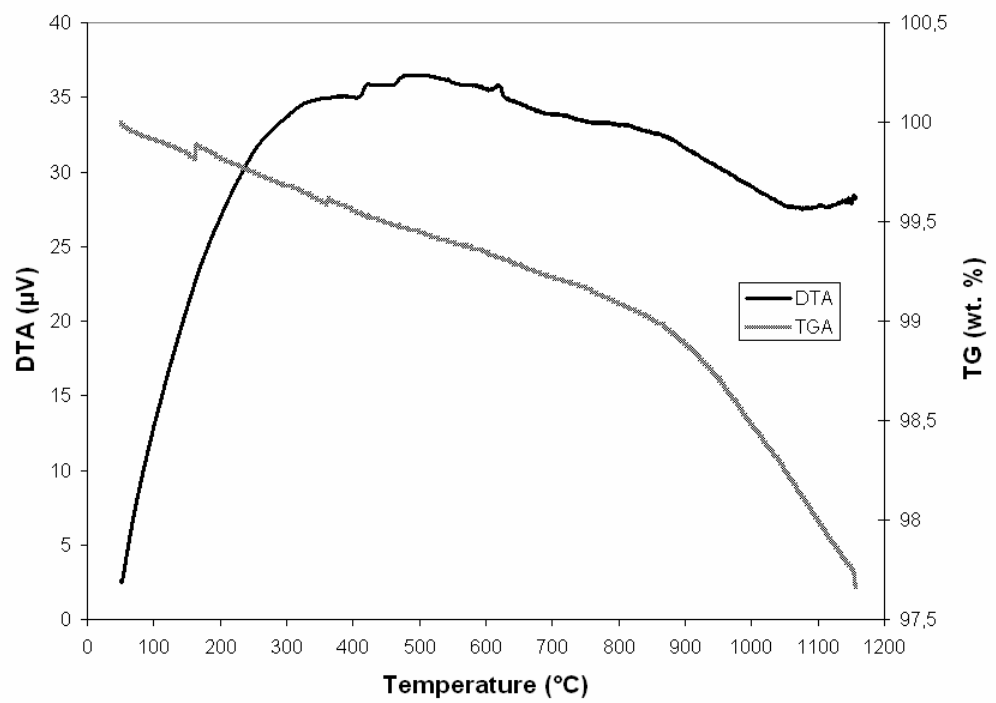

Figure 5.20. DTA/TGA curves of fly ash

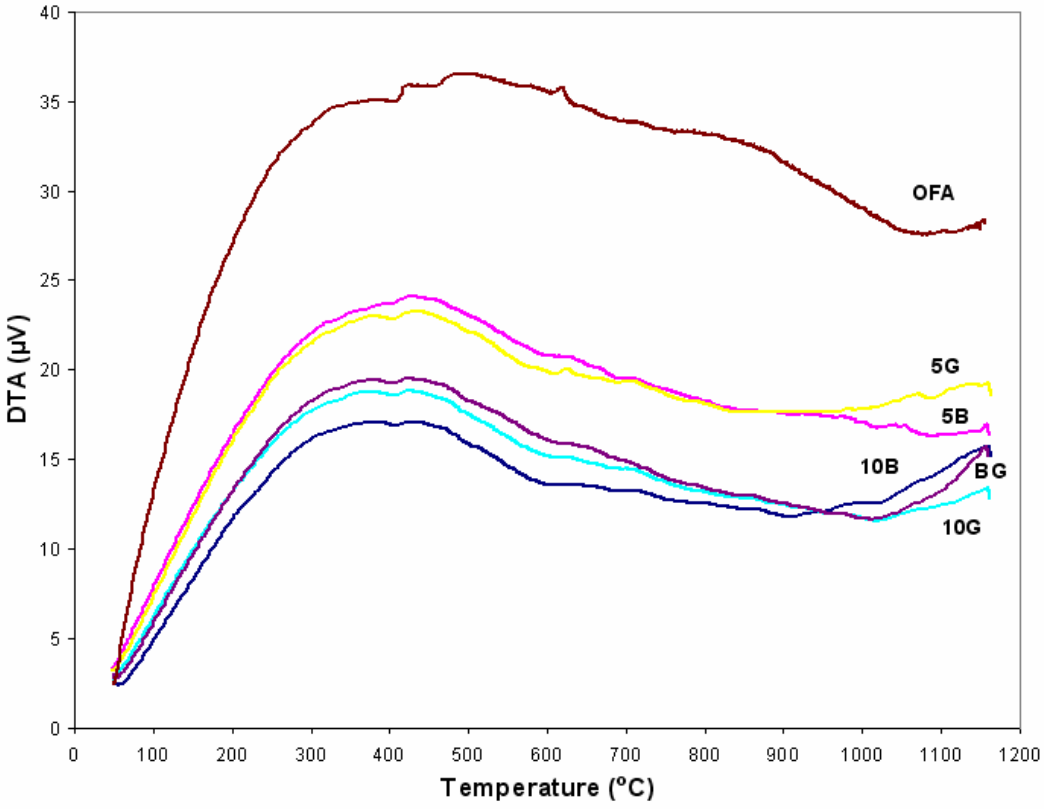

Figure 5.21. DTA/TGA curves of aggregates with binders and with fly ash only

5.1.7. Microstructural Studies on Lightweight Aggregates

5.1.7.1. SEM Observations of Raw Materials and Lightweight Aggregates

SEM observations of raw materials are shown in Figures 5.22-5.24. In contrast to fly ash which was consisted of spherical particles, glass powder and bentonite had irregular, flaky and angular particles. Hollow non-opaque cenospheres and plerospheres, filled with other smaller spherical particles or microspheres, normally dominate the morphology in finer fractions of fly ash [95]. Larger particles may be irregular and contain variable amounts of bubbles and higher contents of crystalline minerals. According to SEM results, glass powder was coarser than bentonite. SEM observations also confirmed the gradation of raw materials as presented previously in Table 4.2 and Figure 4.1.

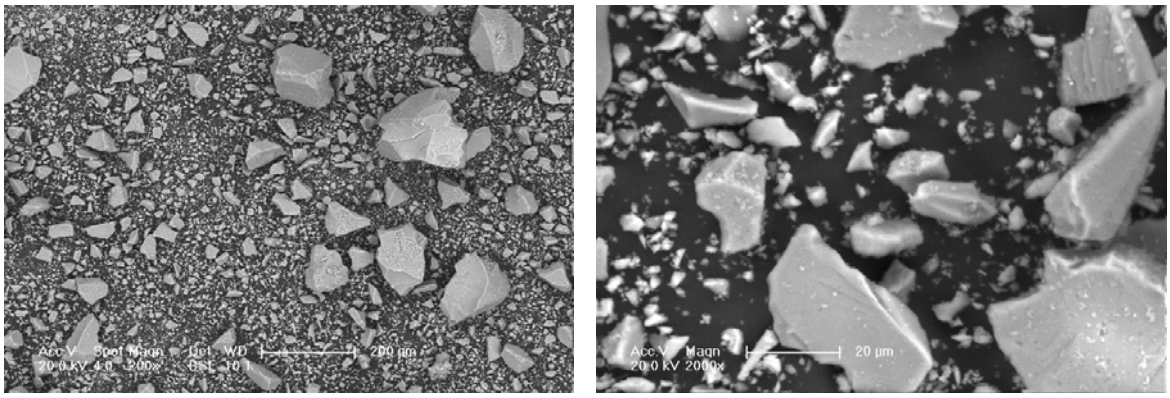

Figure 5.22. SEM observations of glass powder

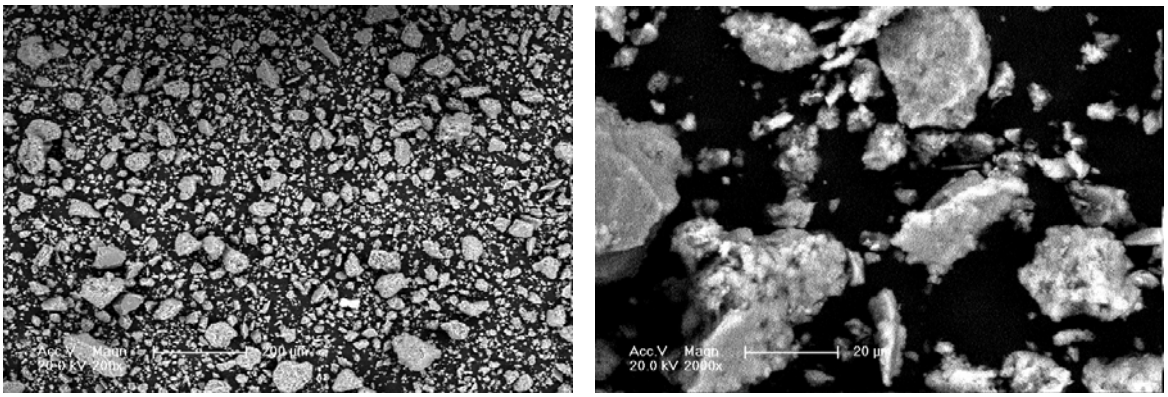

Figure 5.23. SEM observations of bentonite

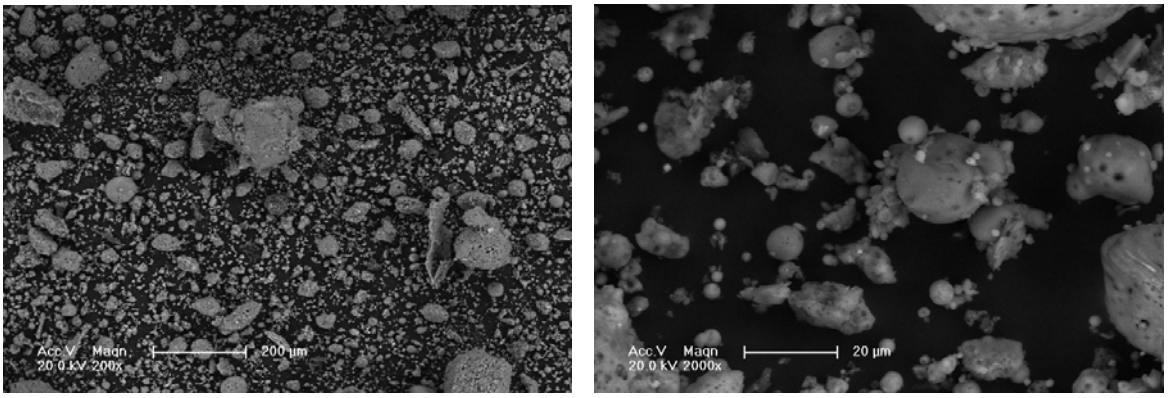

Figure 5.24. SEM observations of fly ash

There was no difference between the inner and outer part of the pellets in the case of coloration and density owing to the slow heating rate (Figure 5.25). Figures 5.26 and 5.27 show the fragments of crushed 10G1200 and 10B1200 pellets in the fractured concrete. The uniformity of color of pellets can be easily detected from these figures.

Some researchers [18, 36, 53 and 89] observed that a thin layer on the outer part of rapidly or one step sintered pellets exhibited a higher density microstructure in comparison to the inner part of the pellet. Mun [18] also reported that during the expansion of the spherically formed lightweight aggregate in the sintering process, thin layers with dense microstructures were formed on the surfaces of the aggregate, which prevented the adhesion. The thickness of the layers tended to decrease with the increase in the sewage sludge content. The decomposition of organic materials in the sewage sludge caused calorification and gas generation in the formed mixtures. These generations led to a decrease in the melted ingredient viscosity and an increase in the gas pressure due to the increased inner temperature. The thickness of the thin layers formed on the lightweight aggregate and the diameters of the pores inside them depended on the balance of the melted ingredient viscosity and gas pressure. Increasing the inner temperature and the excessive generation of the melted ingredients in the formed mixtures effectively accelerated the formation of a glass phase.

This difference in microstructure between the surface and the central region was not observed in conventionally or two step sintered pellets. It is believed that the primary cause of black coring was the insufficient oxidation of carbon due to rapid sintering rate. Oxygen from the atmosphere reacted with the carbon but the products of combustion were slow to

escape. Carbon monoxide filled the pores in the material and reduced the iron to the ferrous state, giving rise to black coring.

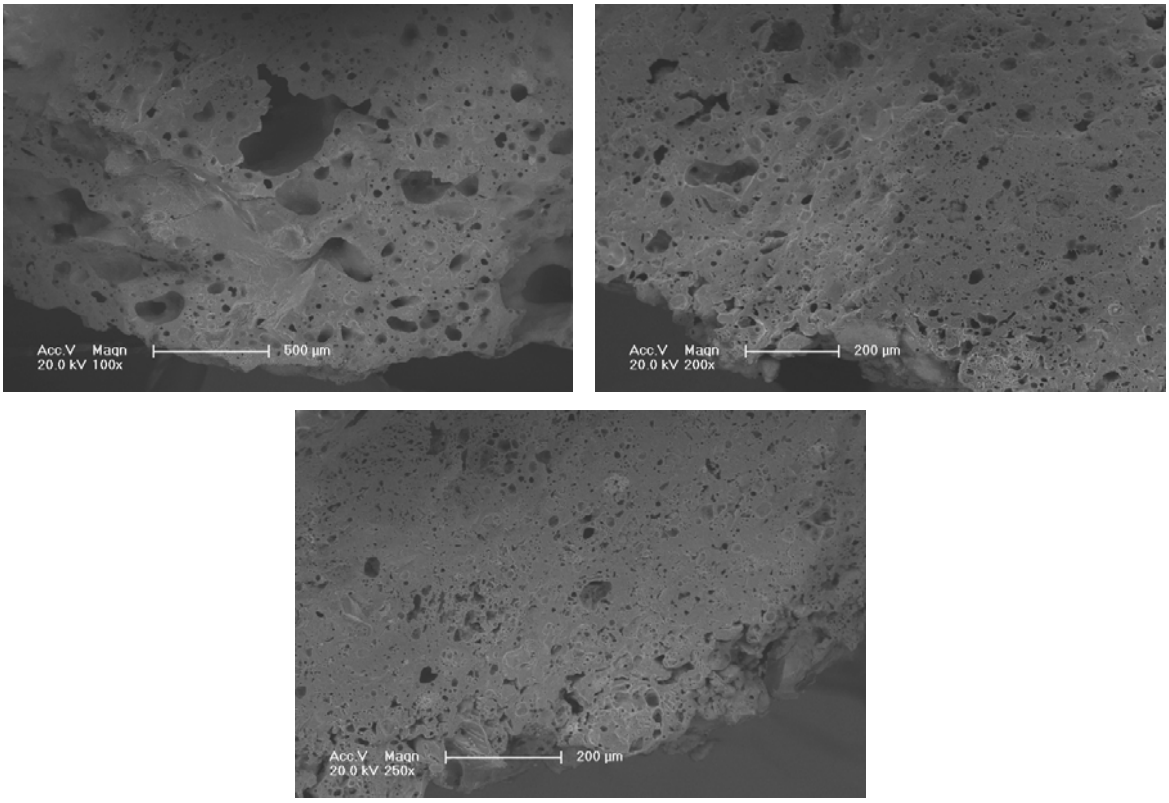

Figure 5.25. SEM micrographs representing both inner and outer part of aggregates

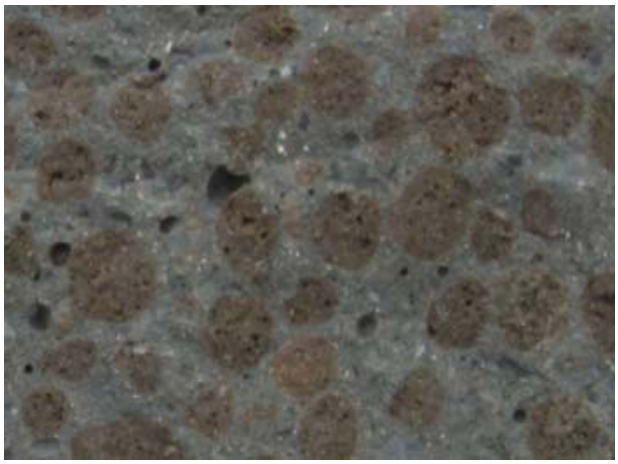

Figure 5.26. The fragments of crushed 10G1200 pellets in the fractured concrete

Figure 5.27. The fragments of crushed 10B1200 pellets in the fractured concrete

Figures 5.28-5.46 present SEM images at magnifications of 250x and 1000x of cross-sections of sintered aggregates and at magnifications of 1000x and 3000x of cross sections of cold bonded aggregate.

Relatively high water absorption, low specific gravity and low strength at 1100 ^{o}C were due to the open and connected porosity. Aggregates produced at lower temperatures than the temperature of maximum densification typically had open, porous microstructures. As maximum densification was approached, the size and number of the pores gradually decreased, because the pores are filled with melted material (Figures 5.32, 5.35, 5.38, 5.41 and 5.44). Aggregates containing high amounts of binders exhibited a rapid reduction in water absorption with temperature, whereas OFA agregates showed a gradual reduction in water absorption reduction with temperature. OFA aggregates sintered at 1200 ^{o}C and aggregates with binders sintered at 1150 ^{o}C were relatively non-porous due to the high densities attained. Sintering results in increased strength and density of formerly loosely bound particles through the formation of interparticle bonds. Aggregates with low water absorption and high strength can be attributed to the discontinuous porosity, dense structure and small pore size at 1150 °C. Nevertheless, the water absorption, specific gravity and strength values were low for aggregates containing binders at 1200 °C. It can be stated that besides closed porosity, larger pores could be responsible for this result. Enlargement of pores attributed to the entrapment of gas generated due to the decomposition of unstable materials. Although the larger pores inside the lightweight aggregate were formed by increasing binder content, in a previous study it was stated that

the formation of the glass phase was found to prevent the decrease in the strength and the increase in water absorption [18]. In another study [26], it was concluded that the first possible reason for the formation of porous structure could be due to entrapment of vapor derived from the volatilization. The second possible reason could be due to the decomposition of any thermally unstable material and/or the water vapor present in the material. The derived vapor partially trapped by viscous body might have caused the formation of pores, which led to the decrease in density and the deformation of pellets. The pores were closed and distributed homogeneously. Further increase in sintering temperature caused an increase in the size and number of the pores. The microstructure resulted from extensive liquid phase sintering with partial softening of the glassy phase, together with some decomposition reactions producing internal pore pressure that caused the finely bubbled microstructure containing approximately spherical pores, typically 5–10 μm in diameter [21]. In the process of sintering lightweight aggregates, weight loss occurred probably because of water evaporation, high temperature oxidization of organic matters, decomposition of inorganic salts or emission of volatile heavy metals [29]. The emission and decomposition of the before-mentioned substances affected the macro properties and microstructure of the lightweight aggregates. As can be seen from above, similar conclusions were derived on the expansion of different materials at high temperatures investigated.

OFA aggregates sintered at 1100 ^{o}C exhibited poorly sintered structure with very few necks between the particles, resulting in poor mechanical properties, low density and high water absorption. With increasing temperature, fly ash particles coalesce forming necks among the particles and resulting in higher density and under some conditions good mechanical properties starting at 1150 ^{o}C. With the addition of binders, the neck growth rate and neck size increased greatly starting at 1100 ^{o}C. Observations of the aggregates clearly showed the particulate nature of the fly ash particles in the aggregates sintered at low temperature whereas in high temperatures they became more fused together. However, fusion were also observed with the use of binders even in low temperature. As can be seen from the SEM images, in the case of OFA aggregates, fusing of particles occured at 1150 ^{o}C (Figure 5.29). However, addition of binders caused particles to fuse at 1100 ^{o}C, but open porosity was still present (Figures 5.33, 5.36, 5.39, 5.42 and 5.45). The fusing and bloating effect could be markedly observed owing to the high amount of binders in 7.5BG

aggregates at that temperature (Figure 5.45). In other words, binders markedly reduced the temperature needed for fusing and bloating. This reduction lowers the cost and energy consumption. It is indicated that the actual sintering temperature depends on low-melting impurities (alkalis, alkaline earth, Fe_2O_3, etc.) or specifically applied sintering agents (clays or fluxes) [105]. In a study [8], it is reported that in the structure of sintered fly ash aggregate without binders, the shapes of pores in general were irregular, spherical, and discrete, while others were elongated and interconnected. There were a few relatively large voids. Lack of binding among the grains could hence be the reason for the lower strength of fly ash aggregate. Relatively smaller pores distributed uniformly in these aggregates indicated that cement and lime improved the binding ability. But still the presence of some large voids resulted in higher water absorption and lower strength of these aggregates. The dosage of bentonite affected the microstructure. With 10% bentonite, the presences of large voids were reduced. The use of 20% bentonite resulted in minute pores distributed uniformly as compared to all other cases. This corroborated well with strength and water absorption characteristics of aggregates. Further increase in bentonite content to 30% was observed to affect the pore size and its distribution. Bentonite helped in the refinement of pores in the aggregates and finer distribution of closed pores on the entire body and thus reduced the specific gravity.

The expansion at high temperature depends on viscosity of materials [18]. The proper viscosity can be determined from the chemical compositions of the raw materials used. Generally, its CaO and MgO contents account for a sudden change in the viscosity of the raw materials at high temperatures. In general, when the ratio of Al_2O_3 to SiO_2 is high, the melting point and viscosity tend to be become high. SiO_2+Al_2O_3 behave as a glass former which increase the melting temperature while the alkali oxides decrease the melting temperature [3].

The pore size and shapes were different in glass powder aggregates compared to bentonite aggregates. The larger pores were obtained in glass powder aggregates. This can be due to the coarser particle size of glass powder than that of the bentonite. It was also noticed that the glass powder particles tended to coalesce with the water sprayed during pelletization, this situation proved that the glass powder particles became coarser than they were before pelletization.

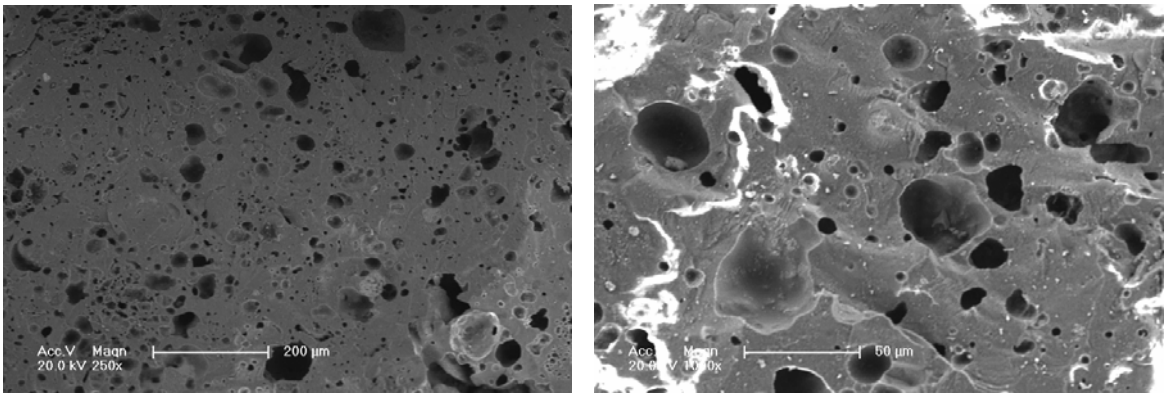

Figure 5.28. SEM observations of OFA1200

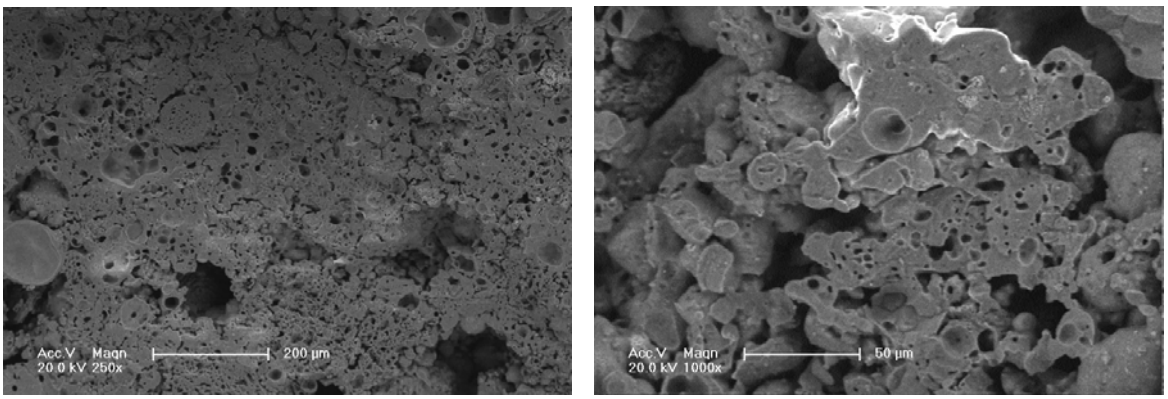

Figure 5.29. SEM observations of OFA1150

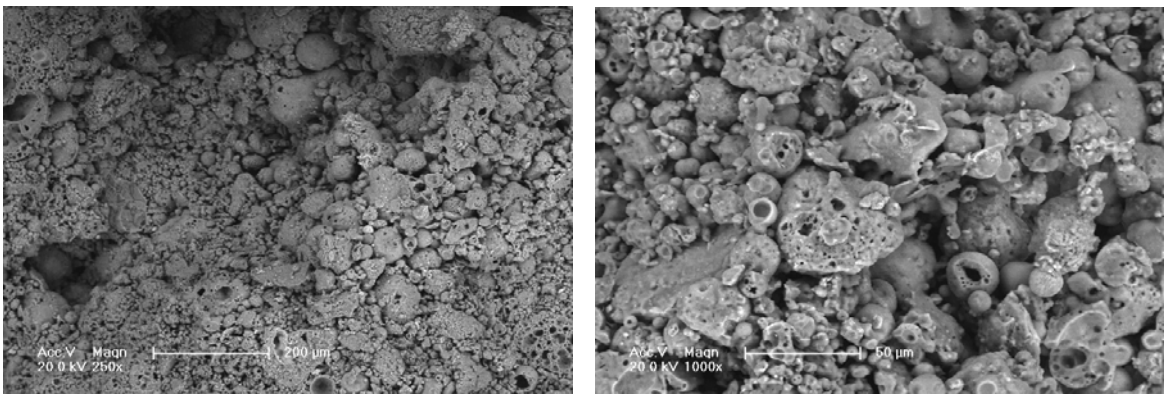

Figure 5.30. SEM observations of OFA1100

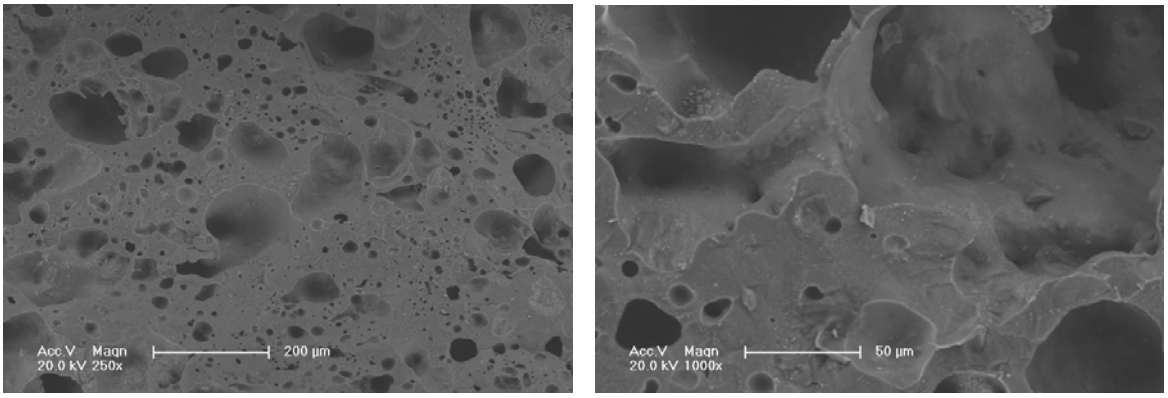

Figure 5.31. SEM observations of 10G1200

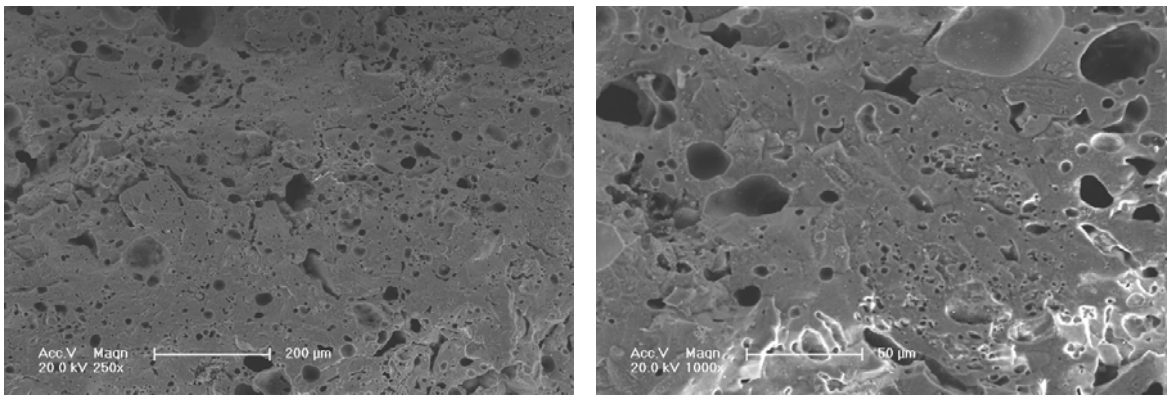

Figure 5.32. SEM observations of 10G1150

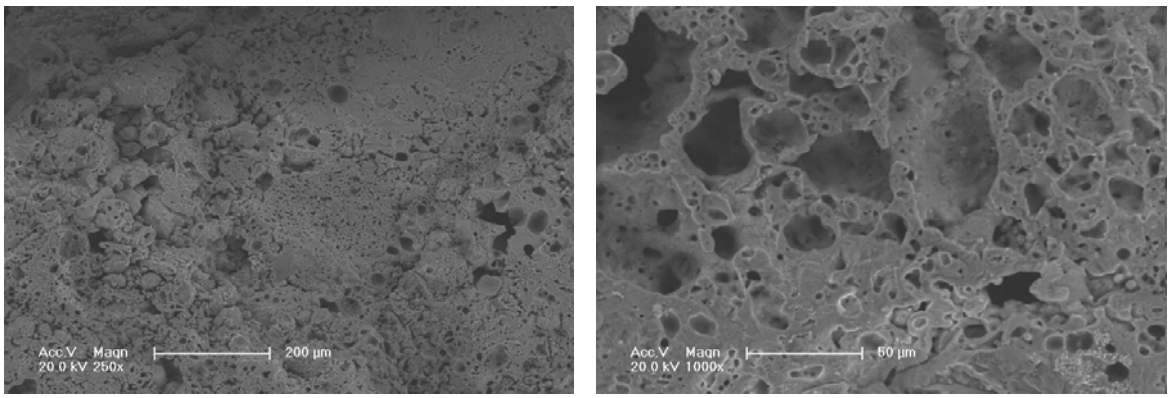

Figure 5.33. SEM observations of 10G1100

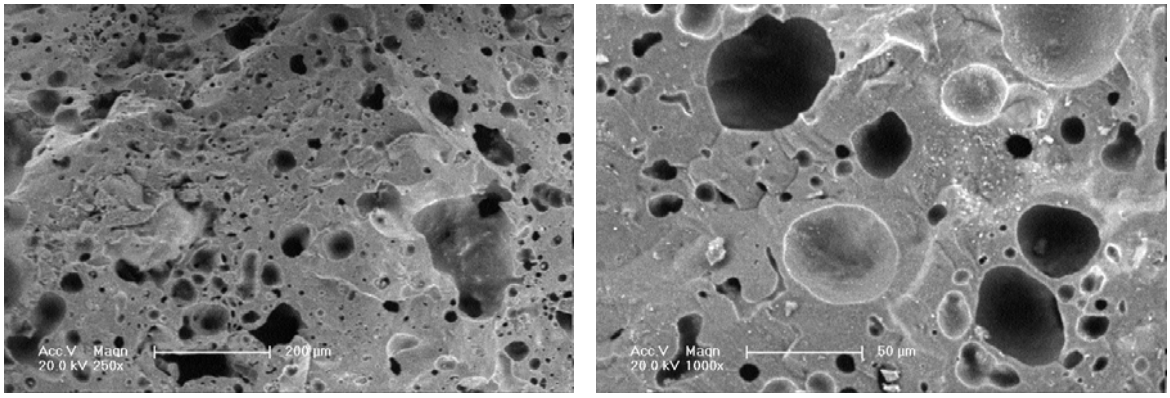

Figure 5.34. SEM observations of 5G1200

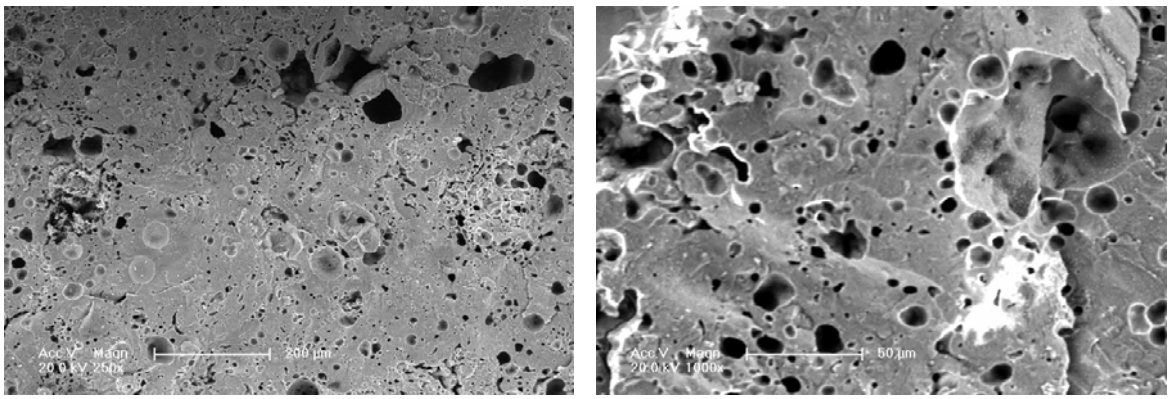

Figure 5.35. SEM observations of 5G1150

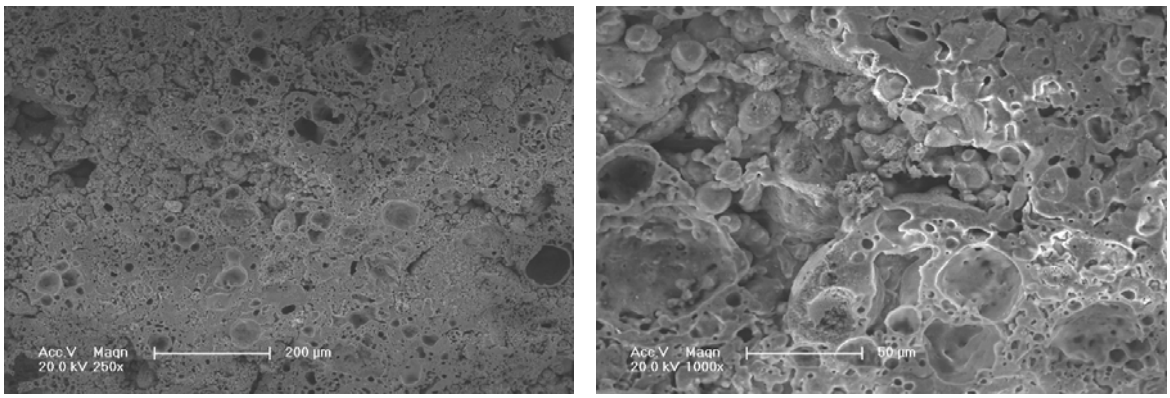

Figure 5.36. SEM observations of 5G1100

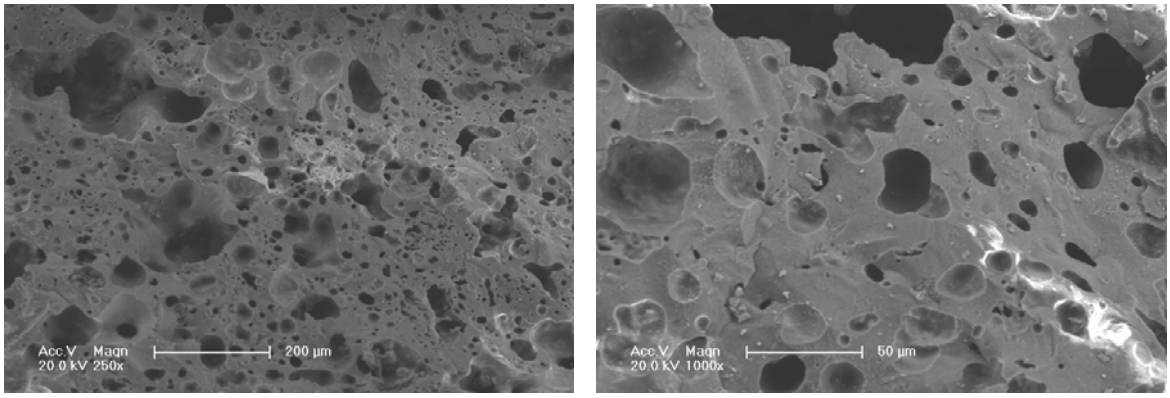

Figure 5.37. SEM observations of 10B1200

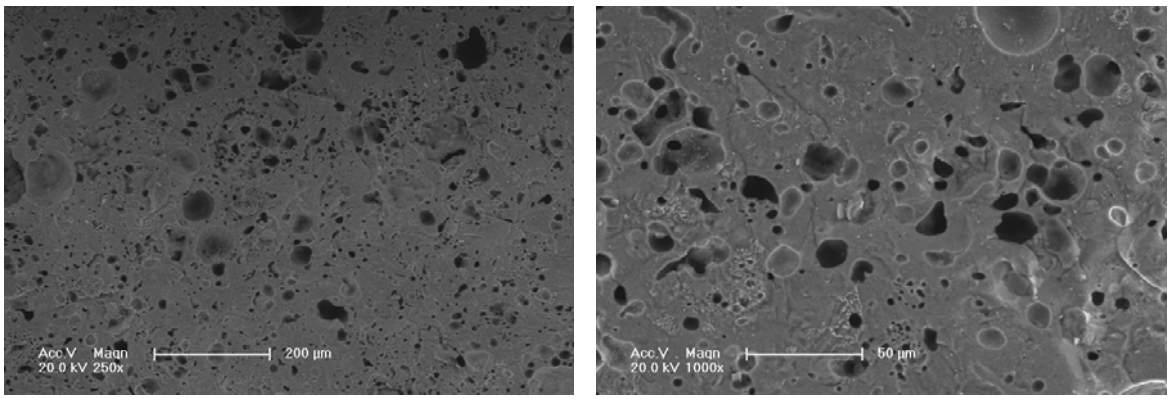

Figure 5.38. SEM observations of 10B1150

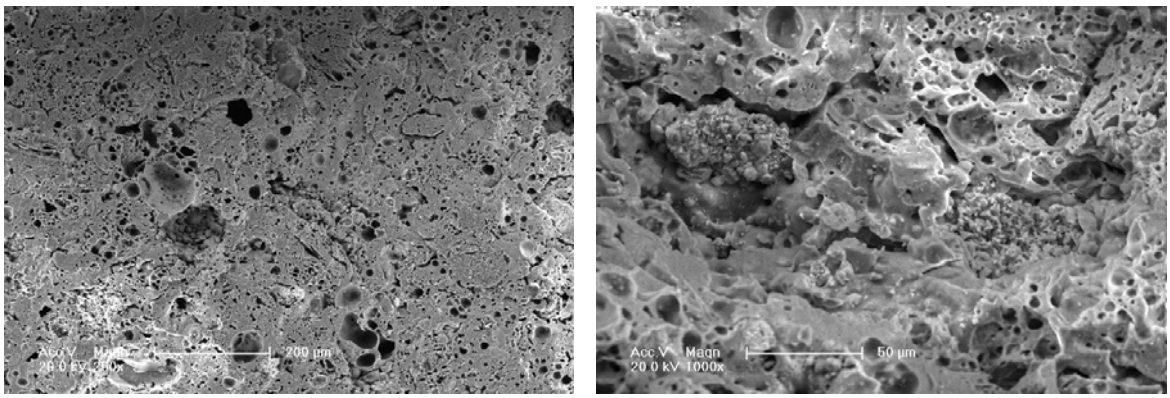

Figure 5.39. SEM observations of 10B1100

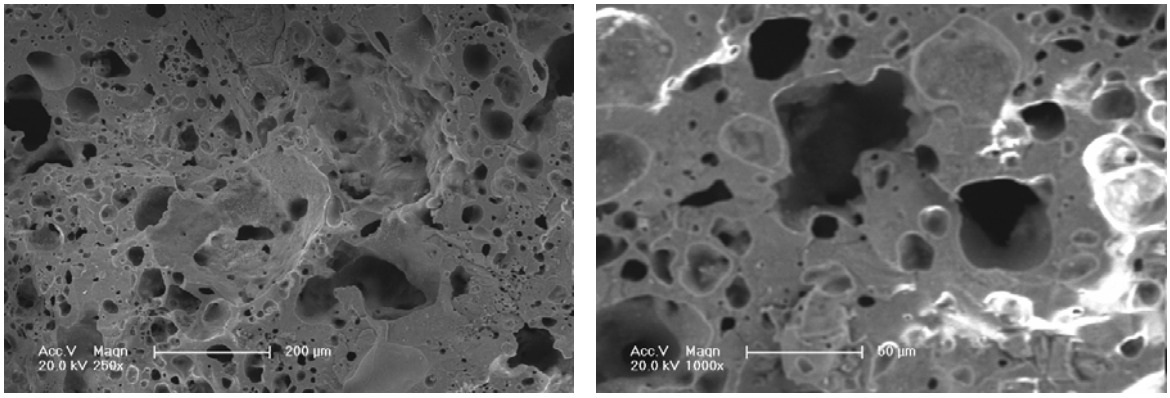

Figure 5.40. SEM observations of 5B1200

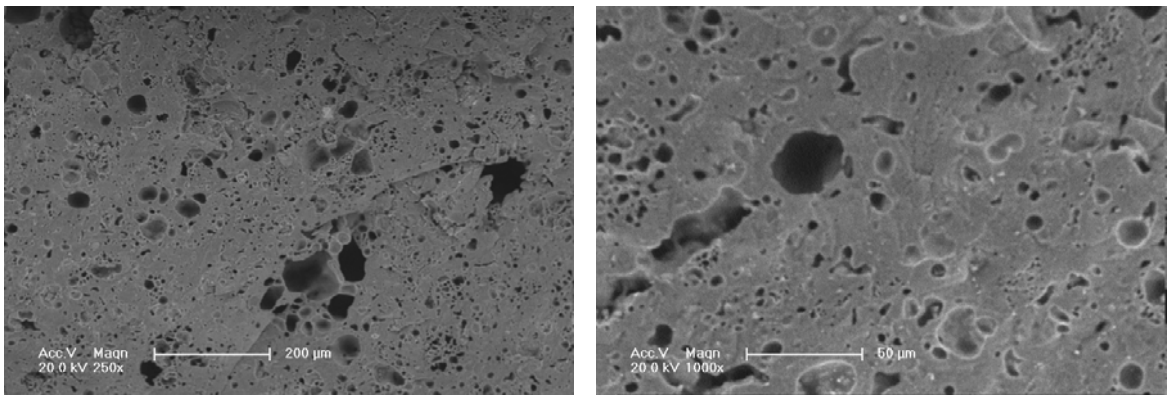

Figure 5.41. SEM observations of 5B1150

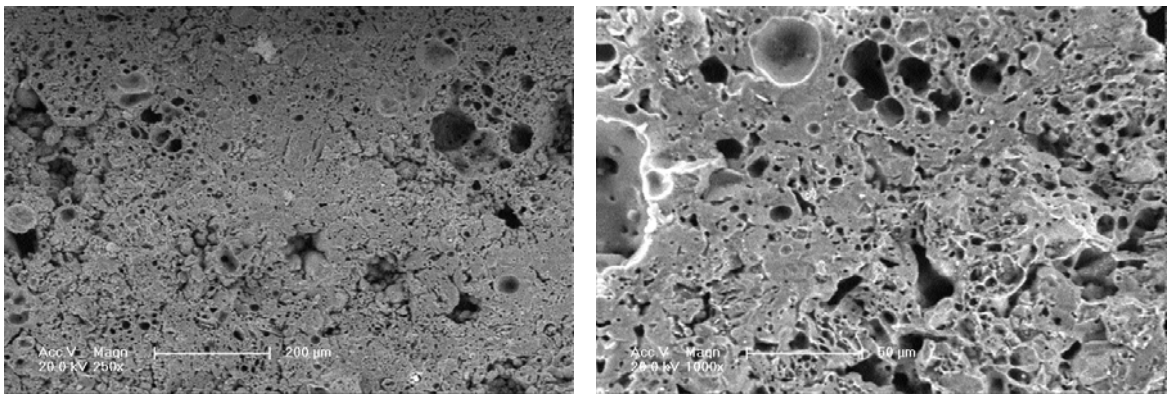

Figure 5.42. SEM observations of 5B1100

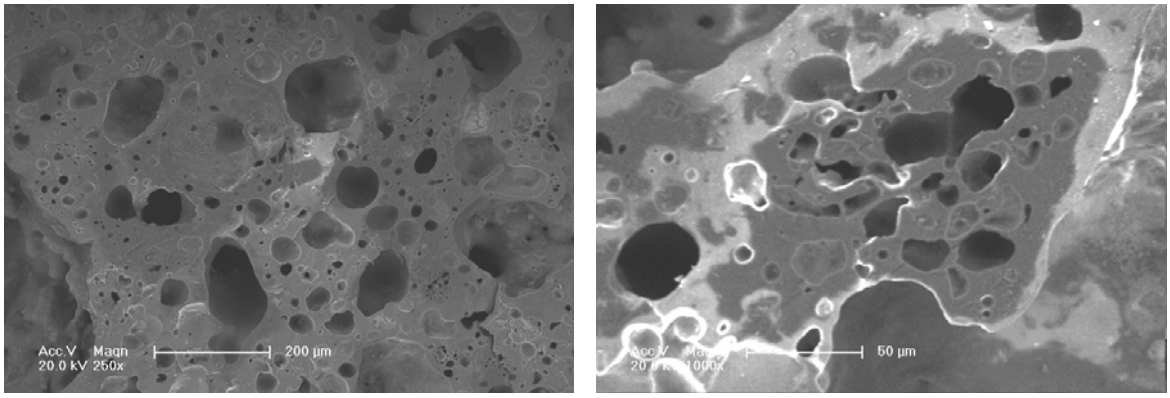

Figure 5.43. SEM observations of 7.5BG1200

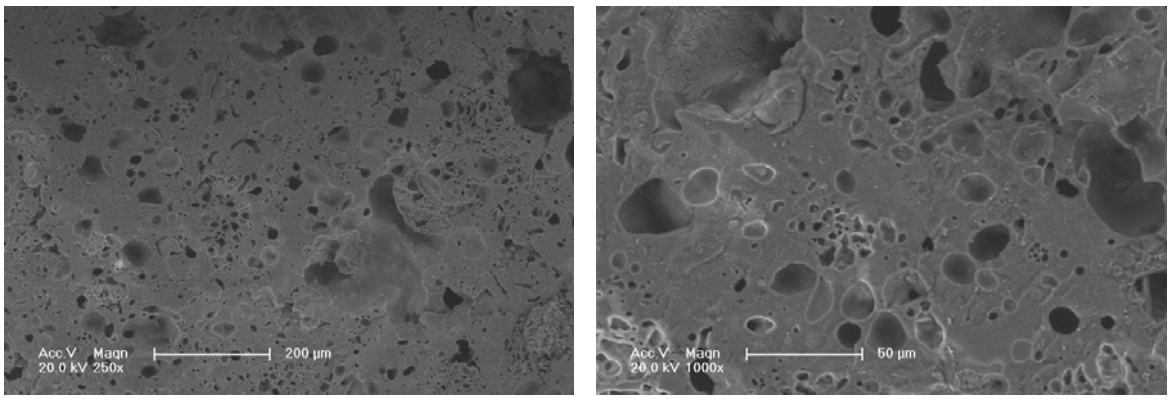

Figure 5.44. SEM observations of 7.5BG1150

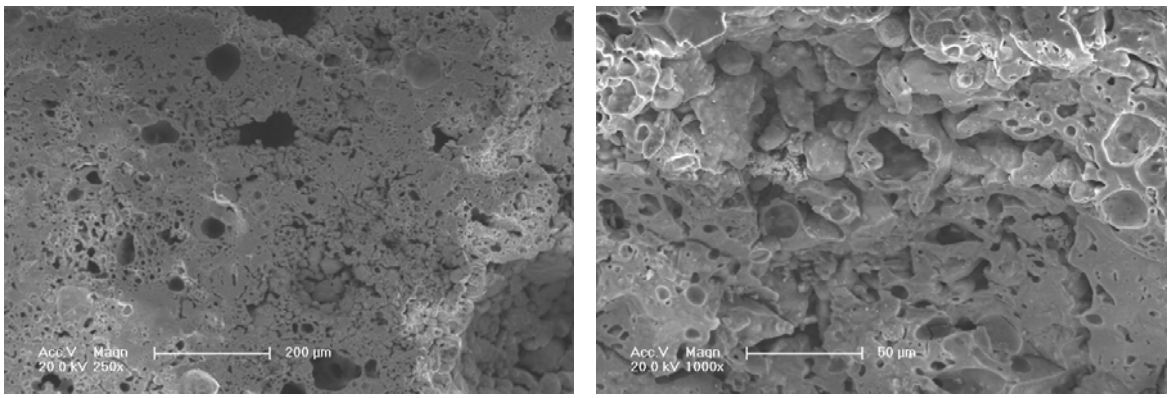

Figure 5.45. SEM observations of 7.5BG1100

The SEM test was also performed to visually examine the resulting hydration products of cold bonded aggregates (Figure 5.46). It is remarkable to observe the hydration of cement with fly ash in cold-bonded aggregates. This type of hydration product with the presence of calcite was also observed in another study [104]. The general aspect of the CSH gel formed after the hydration. The XRD diffractions also proved the calcite formation (Figure 5.56). The SEM micrographs showed the evidence of crystal formation in the matrix aggregates. The hardened cold bonded aggregates composed of fly ash and cement are mostly $Na_2O–Al_2O_3–SiO_2$, and contain small amounts of CaO, MgO, and FeO_2. Finally, $Na_2O–Al_2O_3–SiO_2$ is bonded with another hydrolysis product of fly ash such as silica gel and gives the hardened paste a high strength [79]. Generally, fly ash is found in an amorphous phase, which is etched by NaOH. When SiO_2 or Al_2O_3 undergoes a pozzolanic reaction, they were attacked by OH^- ion, which is attached to Si or network structure atom. The oxygen atoms get separated by OH^- ions, and through this reaction, the hydration reaction progresses as silicate, or another oxy anion is taken from the original structure. These experimental observations are consistent with the XRD trends.

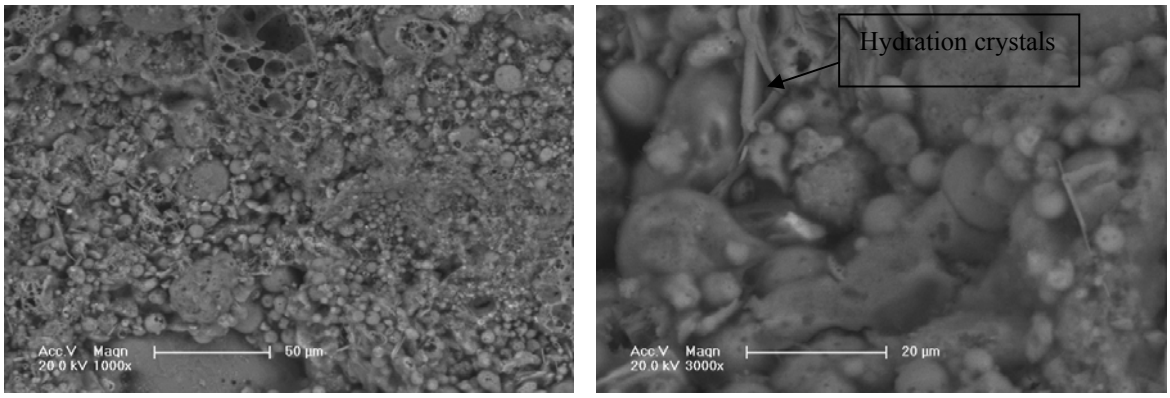

Figure 5.46. SEM observations of CB

5.1.7.2. X-Ray Diffraction of Raw Materials and Lightweight Aggregates

The main crystalline phases in the as-received fly ash were mullite and quartz (Figure 5.47). Some researchers [88, 89 and 92] also demonstrated that XRD data of fly ash samples all contained quartz and mullite as the only crystalline phases detected, however others [46, 95, 104 and 107] pointed out additional crystalline phases. Dong et al. [90] revealed that the mullite existing in the fly ash belonged to primary mullite, which was formed from aluminosilicate clay minerals during the combustion process of raw coal.

Quartz, anorthite and montmorillonite were detected as the main crystalline phases in the XRD of as-received bentonite (Figure 5.48). The accessory minerals were stratlingite and revdite. The XRD patterns of glass powder indicated its amorphous phase (Figure 5.49). No diffraction peaks were detected in the glass powder. These results are consistent with previously reported data on the mineralogy of glass materials [102, 108].

Fly ash and other sintered aggregates presented a crystalline formation and amorphous phase. The broad hump was observed due to the glass content, present in the diffraction spectrum at around 23^{o}. This broad hump showing the presence of amorphous (glass) phase was also detected in other studies [73, 92 and 99].

Increasing the binder concentration in the mixes resulted in a tighter temperature interval between the initial softening, sintering, maximum densification (vitrification), and complete or near complete melting of the samples, due to the modification of the chemical composition and mineralogy of the fly ash with increasing amounts of binders.

OFA aggregates presented peaks of spinel ($MgAl_2O_4$) and anorthite ($CaAl_2Si_2O_8$) in addition to mullite and quartz (Figure 5.50). High Al_2O_3 + SiO_2 contents causes mullite formation. As seen from the X-ray diffraction diagram, the intensity of the anorthite and spinel peaks was lower than the intensity of the mullite and quartz peaks. The presence of anorthite is generally associated with the substitution of Ca ion into the SiO_2–Al_2O_3 couple at high temperatures. Therefore, anorthite phase with a relatively small intensity occurred in the sintered OFA aggregate. The crystalline phases present in the as-received PFA (mullite and quartz) remained in the sintered samples. However, there was a reduction in the quartz peaks and formation of spinel and anorthite was observed. The formation of anorthite also occured at different sintering temperatures in a study conducted by Adell et al. [89] depending on the sintering method. In the mentioned study, for slow sintered samples, anorthite appeared at 1100 ^{o}C, while rapid sintering resulted in anorthite formation at 1050 ^{o}C. The anorthite peaks reduced at high sintering temperatures and could not be detected at or above 1250 ^{o}C for slow sintered FA and 1300 ^{o}C for rapid sintered FA. However, it is notable that fly ash used in different studies can vary considerably. Since oxides of the alkali and alkaline metals are known to flux glass, such can greatly alter the sintering behavior of fly ash. It is obvious that conclusions drawn for this

particular ash, may not hold for other fly ashes with varying alkali and alkaline contents also noted in a study [2]. In another study [3], properties of different fly ash types were investigated and different results were obtained due to the difference in their physical and chemical properties. Also, mentioned temperatures in other studies can not hold as the exact values in comparison with the temperatures in our study due to the different sintering process. Using different furnaces with different sizes can alter the temperature effect on aggregates, thus aggregates sintered at pronounced temperatures can vary from one study to another.

As deduced from X-ray diffraction spectrum of bentonite aggregates, formations of spinel ($MgAl_2O_4$) and albite ($NaAlSi_3O_8$) were observed (Figures 5.51 and 5.52). The reduction in quartz was more significant in 10B aggregates than 5B aggregates sintered at 1200 ^oC. The increase in bentonite content decreased quartz formation by decreasing the fly ash content in aggregate at that temperature. The intensity of other peaks remained unaltered, indicating that there were no major variation, in the mineralogical composition of the aggregates and no new compounds were formed. However, the XRD pattern of sintered aggregates with bentonite showed no peaks for anorthite, montmorillonite, stratlingite and revdite (predominant crystalline phases in raw bentonite), thus indicating an almost complete volatilisation of such compounds (Ca ions) during sintering. This was consistent with the TGA-DTA thermograms of bentonite and aggregates with bentonite. Addition of bentonite resulted in albite formation instead of anorthite which was slightly available in OFA aggregates.

In the case of 5G aggregates (Figure 5.54), quartz and mullite were predominant minerals present as usual in the case of other aggregates, followed by tridymite (SiO_2), spinel ($MgAl_2O_4$) and albite ($NaAlSi_3O_8$) peaks. Increasing content of glass powder in aggregates (10G aggregates) led to formation of diopside ($Ca(Mg,Al)(Si,Al)_2O_6$) instead of albite ($NaAlSi_3O_8$) (Figure 5.53). The formation of diopside can be explained by the high CaO content of glass powder. The XRD patterns of glass powder aggregates indicate the decrease in tridymite peaks (a poorly crystallised form of silica) as the temperature increased. Also, 10G aggregates showed large amounts of tridymite. Cheng and Chen [102] examined the quenched glass which was amorphous. After heat treatment at 850, 900, 950, 1000 and 1050 ^oC, respectively, the glass had a crystallised phase. In our study, it

is obvious that sintering of glass powder which was totally amorphous caused new compound formations as seen in Figure 5.49. Diopside, albite and tridymite were the new crystalline forms other than OFA aggregates had resulting from the sintering of aggregates with glass powder. These crystallizations were also confirmed by DTA. In a study [109], when the spherical silica gel particles were sintered at 700 ^{o}C, the peaks characteristic of diopside appared at 29.9 and 35.5^{o}. Moreover, the intensity of peaks assigned to diopside crystal increased with temperature up to 900 ^{o}C and heat treatments at temperatures above 900 ^{o}C produced negligible change in the intensity of the peaks. In our study, the diopside peaks appeared at same degrees observed in previous study, also in addition of these, lower intensity of diopside crystal peak appeared at 44^{o}. After increasing the glass content, the diopside mineral peaks appeared. The reason could be that when glass content increased, the magnesium hydroxide was decomposed with the temperature increase, therefore, free magnesia and silica could react and re-crystallize to form diopside. The diopside formation due to heat increase with the same behavior was also reported in another study [110].

The XRD patterns of 7.5BG aggregates presented the presence of quartz, mullite peaks, followed by tridymite, muscovite and albite peaks (Figure 5.55). It is clear that new compounds were formed by addition of glass powder and bentonite. Albite and tridymite were also observed in sintered aggregates with bentonite and aggregates with glass powder, separately. However, muscovite was not detected previously in other types of aggregates. The relative peak intensities of quartz were lower in especially 10G and 10B aggregates than in OFA at same temperatures due to a phase transformation of quartz. However, this intensity loss in quartz was not observed in 7.5BG aggregates.

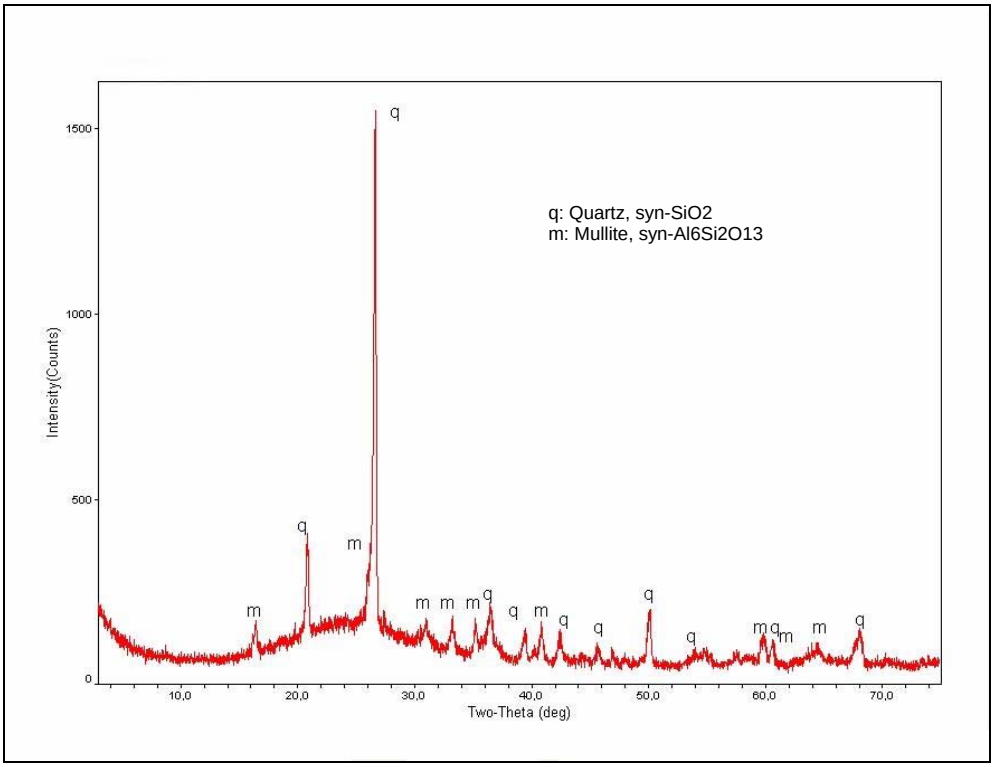

Figure 5.47. X-ray diffraction spectrum of fly ash as received

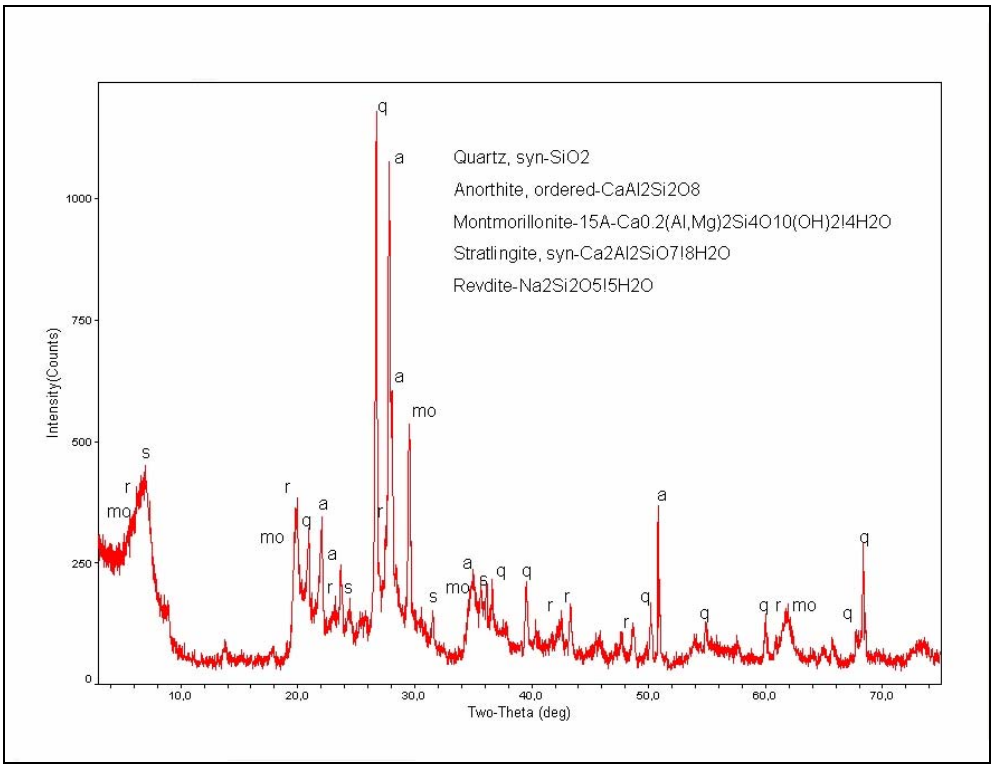

Figure 5.48. X-ray diffraction spectrum of bentonite

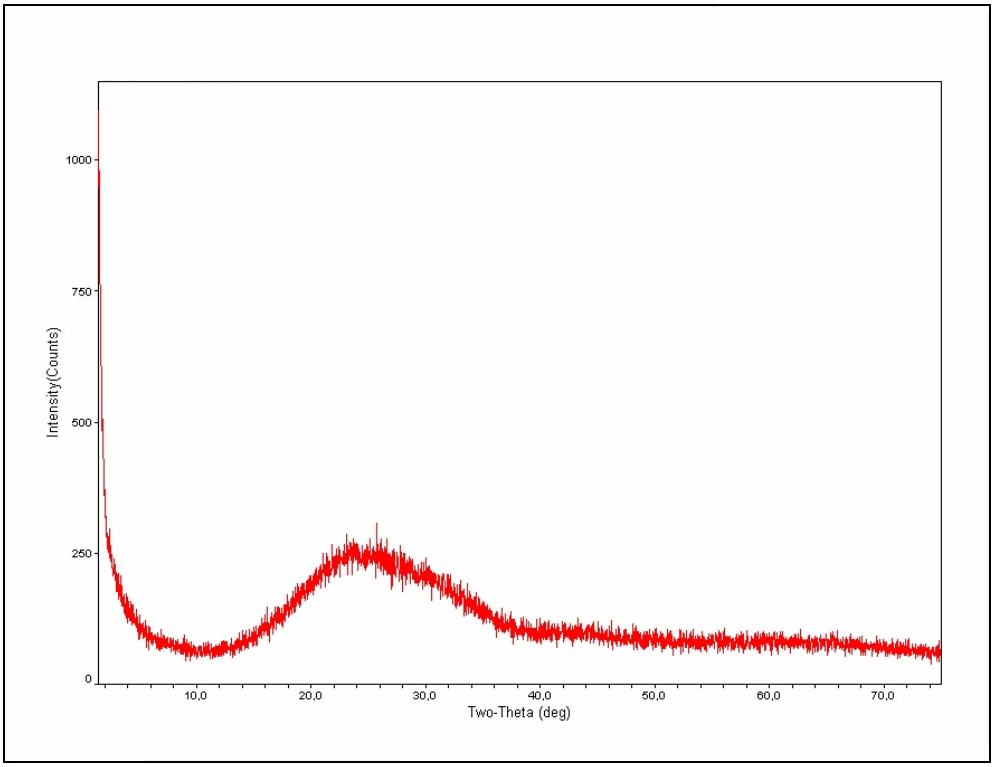

Figure 5.49. X-ray diffraction spectrum of glass powder

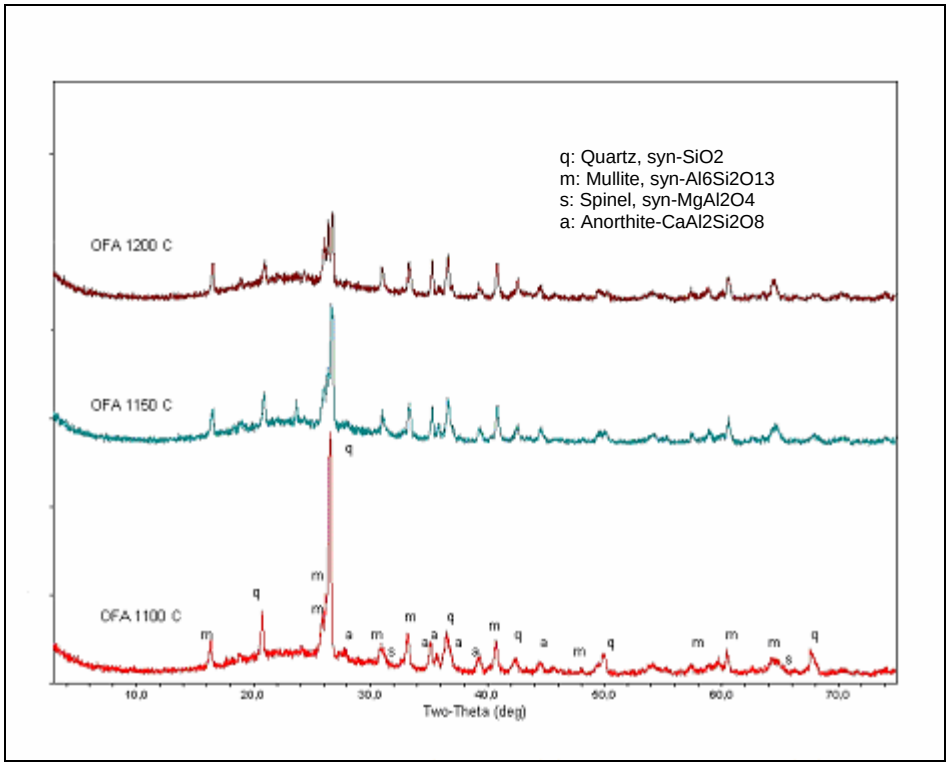

Figure 5.50. X-ray diffractogram of OFA pellets heated at 1100; 1150 and 1200 ^{o}C

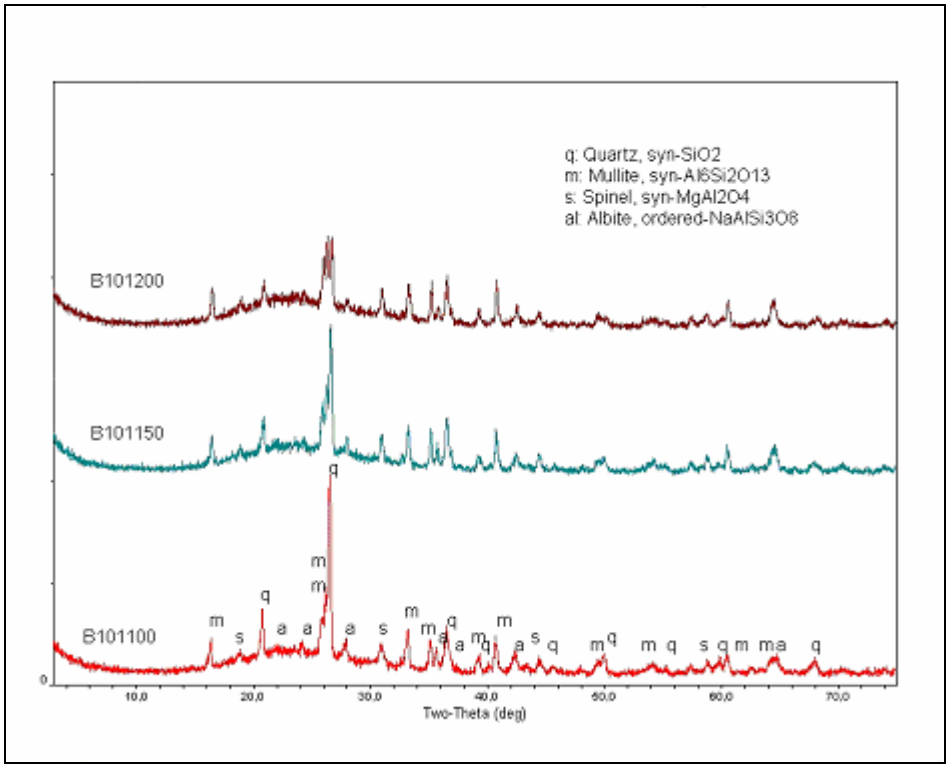

Figure 5.51. XRD spectrum of 10B aggregates heated at 1100; 1150 and 1200 ^{o}C

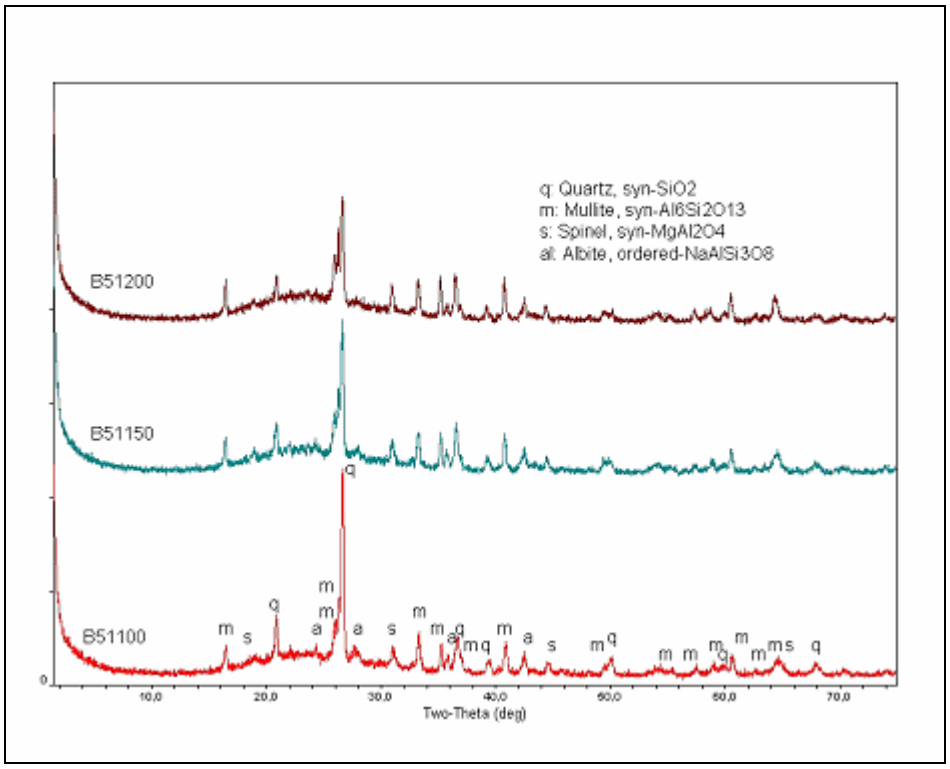

Figure 5.52. XRD spectrum of 5B aggregates heated at 1100; 1150 and 1200 ^{o}C

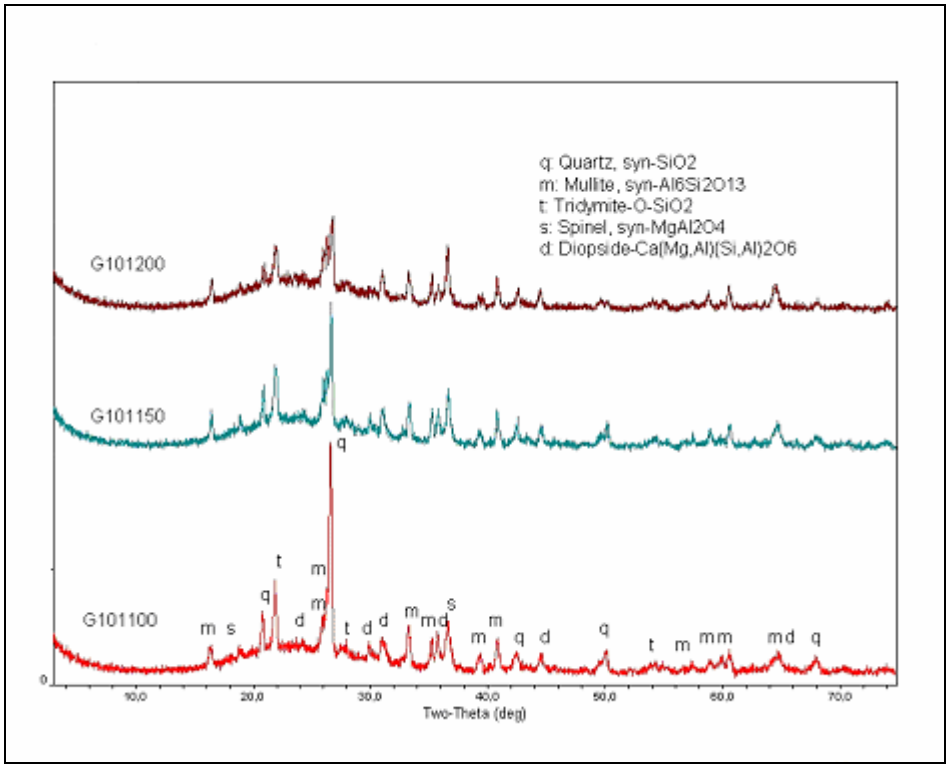

Figure 5.53. XRD spectrum of 10G aggregates heated at 1100; 1150 and 1200 °C

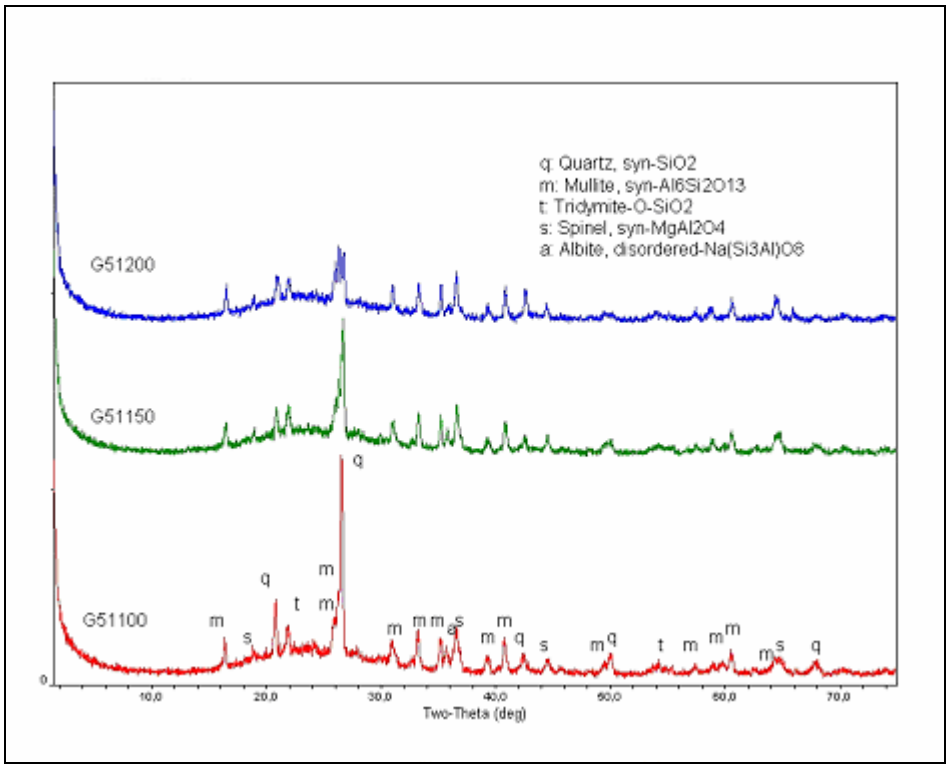

Figure 5.54. XRD spectrum of 5G aggregates heated at 1100; 1150 and 1200 °C

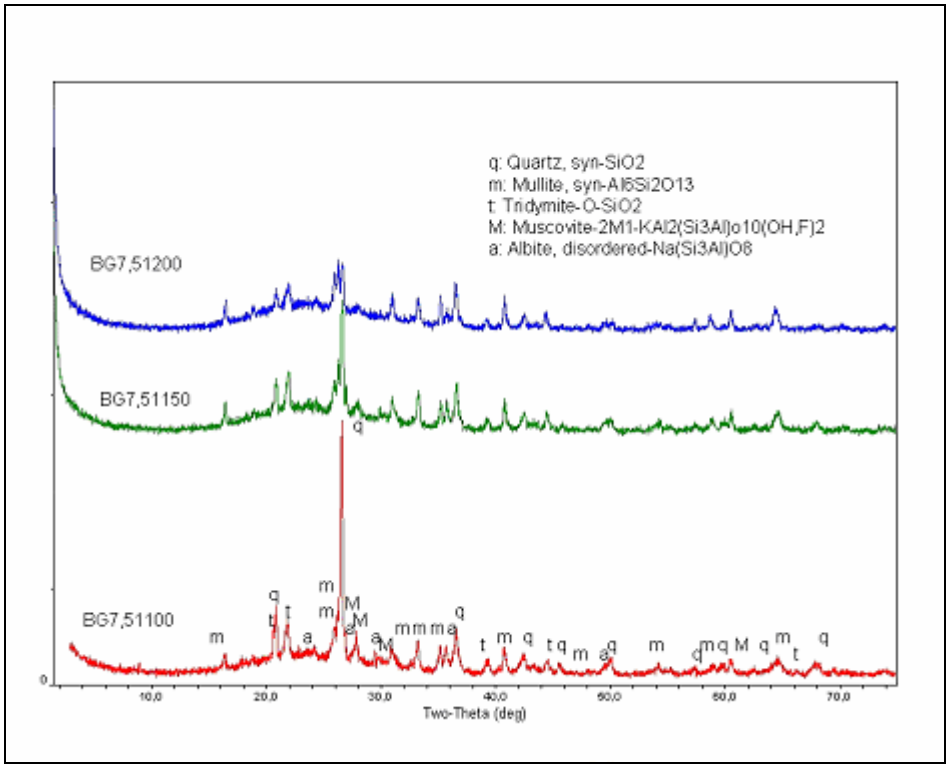

Figure 5.55. XRD spectrum of 7.5BG aggregates heated at 1100; 1150 and 1200 ^{o}C

The reduction of quartz peaks was observed for all aggregate types with temperature increase. This result confirms the previous studies [2, 3, 21-23, 89, 92 and 95]. These results obviously showed that sintering produced new crystalline phases not found in the raw materials (fly ash, bentonite and glass powder). The crystallisation was also detected in DTA. Aggregates sintered at higher temperatures had also increased XRD background levels compared to the aggregates sintered at low temperature, indicating that they contained more amorphous silicate glass. The peak intensities decreased with increasing the heat treatment temperature. The heat treatment at 1100 ^{o}C, the crystal growth rate increased substantially, and thus produced a better crystalline. However, with heat treatment temperature increased to higher temperatures, the crystal growth rate were decreased, therefore the peak intensities decreased. The quantity of quartz being reduced was greater than that consumed in the formation of other crystalline phases also observed by Wasserman and Bentur [23]. This implies that the part of the reduction in quartz content was accompanied by formation of additional glassy phase.

Quartz, mullite and calcite ($CaCO_3$) were detected as the main crystalline phases in the XRD of cold-bonded aggregates (Figure 5.56). Monkman and Shao [111] also

observed some acicular or flaky products identified as calcium carbonates in SEM. The EDS of carbonated cement shows that the products are a mixture of calcium, oxygen, and carbon supporting their identification as calcite.

The carbonation of calcium-carrying materials forms thermodynamically stable calcium carbonates. Calcium silicate compounds can be carbonated according to the following reactions:

$$3CaO \cdot SiO_2 + 3CO_2 + \mu H_2O \rightarrow SiO_2 \cdot \mu H_2O + 3CaCO_3 \quad (5.4)$$

$$2CaO \cdot SiO_2 + 2CO_2 + \mu H_2O \rightarrow SiO_2 \cdot \mu H_2O + 2CaCO_3 \quad (5.5)$$

Calcium hydroxide will also carbonate according to the following reaction:

$$Ca(OH)_2 + CO_2 + H_2O \rightarrow CaCO_3 + 2H_2O \quad (5.6)$$

Equations suggest that carbonation curing is a CO_2 consuming process. In general, carbon dioxide can be sequestered into almost all compounds of calcium and converted to stable calcium carbonates.

It is indicated that inherent crystalline constituents of fly ashes, such as lime and quartz, appear also in the patterns of their hydrated blended pastes, whilst the presence of calcite in all systems could be attributed also to possible carbonation during handling [112]. The presence of calcite in both fly ash and cement was also pronounced in other studies [113-115].

The experimental observations are consistent with the SEM images and XRD trends.

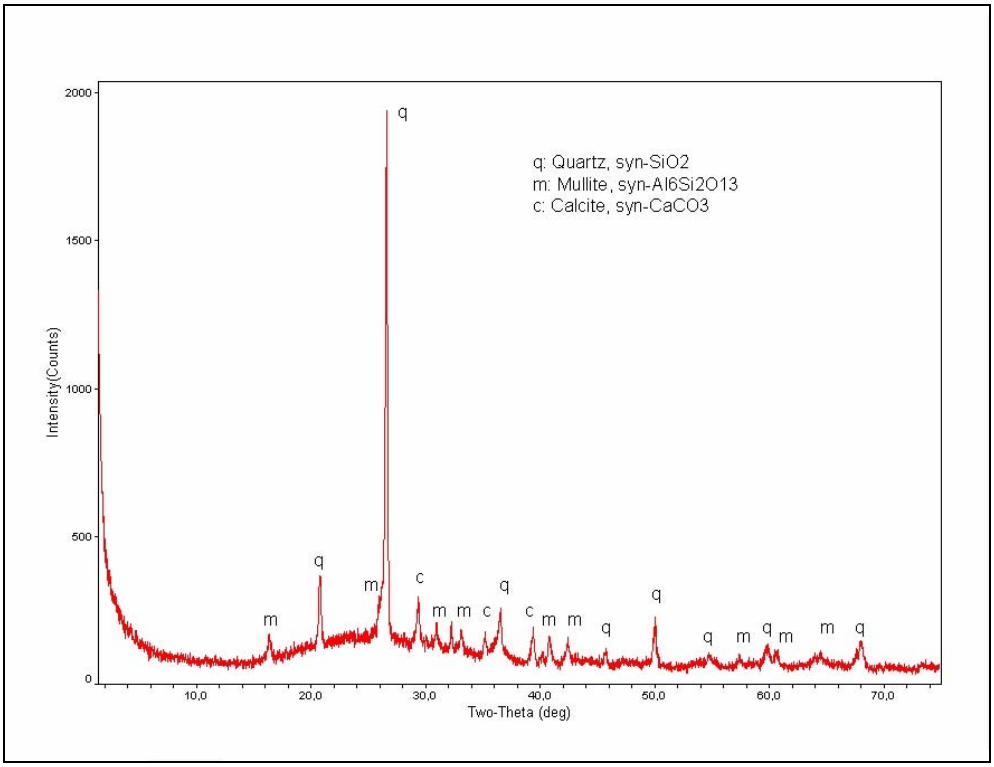

Figure 5.56. X-ray diffraction spectrum of CB

5.2. Optimization of Properties of Lightweight Fly Ash Aggregates for Suitability in High-Strength Lightweight Fly Ash Concrete Production Using Response Surface Methodology

Response surface methodology comprises a group of statistical techniques for model building and model exploitation [74, 116 and 117]. By careful design and analysis of experiments, it seeks to relate a response or output variable to the levels of a number of predictors or input variables that affect it. It allows calculations to be made of the response at intermediate levels which were not experimentally studied and shows the direction in which to move if we wish to change the input levels so as to decrease or increase the response. Response surface methodology using Design Expert V7 software was used to optimize the responses of three input variables. Using design of experiments based on response surface methodology, the aggregate properties having minimum specific gravity and maximum strength can be arrived with minimum number of experiments without the need for studying all possible combinations experimentally. Further the input levels of the different variables for a particular level of response can also be determined.

However, in this study, two different designs were applied:

- D-Optimal Design
- Historical Data Design

The main challenge for the manufacturer is how to choose the process input parameters that would produce a high strength lightweight concrete. The three variables chosen for the study were namely, sintering temperature, binder content and binder type, designated as A, B, C whereas the predicted responses, namely, specific gravity, porosity and crushing strength, were each designated as Y. Table 5.7. shows the process variables, their coded and actual values. The mathematical relationship between the variables and the responses can be approximated by the second order polynomial.

The factors with their low and high levels (-1 level and +1 level) were entered to run the software and to obtain the design points by using response surface methodology. However, aggregates with 7.5 % bentonite and 7.5 % glass powder were not included due to the usefulness of this type of aggregate in concrete production. As previously stated, this aggregate types were stuck in the furnace during sintering at 1200 ^{o}C. This production difficulties made this aggregate type undesirable. Temperature and binder content were numeric factors, binder type was a categoric factor.

Table 5.7. Independent process variables and experimental design levels used

Variables	Code	Unit	-1	0	+1
Temperature	^{o}C	A	1100	1150	1200
Binder content	%	B	0	5	10
Binder type	-	C	G	-	B

5.2.1. D-Optimal Design

D-Optimal design under Response Surface Methodology was used to analyze the interactive effect of temperature, binder content and binder type and to arrive at an optimum. This method helps to optimize the effective parameters with a minimum number

of experiments, as well as to analyze the interaction effect between those parameters. By selecting the model proposed by the software (quadratic is default), the 19 runs (9 model points, 5 to estimate lack of fits and 5 replicates) were given. Table 5.8 shows the experimental design employed.

Table 5.8. Design matrix

Run	Factor 1	Factor 2	Factor 3
	A: Temperature	B: Binder content	C: Binder type
1	1100	0	G
2	1100	0	G
3	1100	0	B
4	1100	5	G
5	1100	5	B
6	1100	10	G
7	1100	10	G
8	1100	10	B
9	1150	0	G
10	1150	0	B
11	1150	5	G
12	1150	10	B
13	1150	10	B
14	1200	0	B
15	1200	0	G
16	1200	5	B
17	1200	5	B
18	1200	10	G
19	1200	10	G

Using Design Expert software, the experimentally obtained specific gravity, water absorption and crushing strength values were analyzed and the coefficients of the parameters in the second order polynomial were arrived at and given by the regression equation (which gives the predicted values). According to the obtained results the

developed models are statistically accurate and can be used for further analysis. The final models in terms of coded and actual factors are shown below:

Final equations in terms of coded factors:

$$\text{Specific gravity} = +1.89+0.018*A+0.013*B+0.012*C-0.15*A*B+0.024*A*C-0.012*B*C-0.16*A^2-0.043*B^2 \quad (5.7)$$

$$\text{Water absorption} =+3.66-5.45*A-3.48*B+0.25*C+2.15*A*B-0.47*A*C+0.33*B*C+1.58*A^2+2.08*B^2 \quad (5.8)$$

$$\text{Crushing strength}=+12.90+2.62*A+2.03*B-1.58*C-3.39*A*B+0.067*A*C-2.16*B*C \quad (5.9)$$

And the final models in terms of actual factors for agent B are shown below:

$$\text{Specific gravity}=-85.91840+0.14969*t+0.71039*c-5.98286E-004*t*c-6.38371E-005*t^2-1.72078E-003*c^2 \quad (5.10)$$

$$\text{Water absorption}=+1008.86900-1.59581*t-11.47587*c+8.59369E-003*t*c+6.31841E-004*t^2+0.083139*c^2 \quad (5.11)$$

$$\text{Crushing strength}=-126.39198+0.11885*t+16.44372*c-0.013570*t*c \quad (5.12)$$

The final models in terms of actual factors for agent G;

$$\text{Specific gravity}=-86.99323+0.15067*t+0.70542*c-5.98286E-004*t*c-6.38371E-005*t^2-1.72078E-003*c^2 \quad (5.13)$$

$$\text{Water absorption}=+1030.28786-1.61458*t-11.34444*c+8.59369E-003*t*c+6.31841E-004*t^2+0.083139*c^2 \quad (5.14)$$

$$\text{Crushing strength}=-128.31845+0.12155*t+15.57819*c-0.013570*t*c \quad (5.15)$$

The above equations are based on the quadratic models for specific gravity and water absorption and 2 factor interactions (2FI) for crushing strength suggested by the software against other models such as linear and cubic since these models fitted well with the experimental data.

Analysis of variance (ANOVA) are given in Table 5.9-5.11. Lack of fit test compares the residual error to the pure error from replication and gives F values for all the models. F value must be lower if a particular model is to be significant. From the F test, it was found that the calculated F value was more than the tabulated F value for the corresponding degrees of freedom thus rejecting the null hypothesis of ‘‘significant lack of fit’’ for linear, 2FI and quadratic models indicating that the lack of fit is insignificant. Quadratic being the higher order polynomial was selected among them for specific gravity and water absorption and 2FI model for crushing strength. For the cubic model, the calculated F value was less than the tabulated F value for corresponding degrees of freedom, thus accepting the null hypothesis, indicating that the lack of fit is significant thereby making this model aliased and hence was disqualified.

ANOVA for response surface quadratic model gives the sum of squares and degrees of freedom for the model terms from which mean square of the model terms are calculated. F value of the models and individual model terms helps in finding their significance. The model F values of 4.51, 57.89 and 5.30 imply that the models are significant. Values of ‘‘Prob > F ’’ less than 0.0500 indicate significant model terms.

Among the different models studied, for specific gravity and water absorption, only the quadratic models were found to fit the experimental data best with standard deviations of 0.096 and 1.24 and with correlation coefficient (R^2 value) of 0.78 and 0.98, respectively, indicating that the fitnesses of the selected models is good and the models could be used for further navigation. However, for crushing strength, 2 factor interactions (2FI) was

found to fit the experimental data best with a standard deviation of 3.57 and with a correlation coefficient (R^2 value) of 0.73 indicating that the fitnesses of the selected model is good. The results demonstrated that the models developed are quite accurate as the percentages of error in prediction were in a good agreement. However, the percentages of error values are high for water absorption. This is due to the relatively low values obtained.

The statistical significance of the terms in each regression equation was examined using the sequential F-test, lack-of-fit test and other adequacy measures using the same software to obtain the best fit. The fit summary tab in the design-expert software suggests the highest order polynomial where the additional terms are significant and the model is not aliased. Selecting the step-wise regression method eliminates the insignificant model terms automatically. The sequential F-test for significance of both the regression model and the individual models terms along with the lack of fit test were carried out using Design-Expert V7 software. The ANOVA for the reduced quadratic models summarize the analysis of each response and show the significant model terms.

As can be seen from the ANOVA results for the specific gravity, water absorption and crushing strength, all the adequacy measures are in logical agreement and indicate significant relationships. The adequate precision ratios in all cases are greater than 4 which indicate adequate models discrimination.

The analysis of variance result for the specific gravity model shows that the quadratic effect of the temperature along with the interaction effect of the temperature and binder content are significant model terms.

For the water absorption model the results indicate that the main effect of the temperature and binder content and the quadratic effect of the temperature and binder content along with the interaction effect of the temperature and binder content are significant model terms. However, the temperature and binder content are the factors most associated with the water absorption. However, the binder type is the factor that has insignificant effect on specific gravity and water absorption.

In crushing strength model, the analysis of variance results demonstrated that the main effect of the temperature along with the interaction effects of the temperature and binder type with binder type and binder content are significant model terms.

Table 5.9. ANOVA for specific gravity response surface quadratic model

Source	Sum of Squares	df	Mean Square	F Value	p-value Prob > F
Model	3,33E-01	8	4,16E-02	4,51	0.0149
A-t	4,29E-03	1	4,29E-03	0,47	0.5107
B-c	2,27E-03	1	2,27E-03	0,25	0.6303
C-a	2,34E-03	1	2,34E-03	0,25	0.6251
AB	2,01E-01	1	2,01E-01	21,74	0.0009
AC	6,96E-03	1	6,96E-03	0,75	0.4054
BC	1,88E-03	1	1,88E-03	0,20	0.6611
A^2	8,20E-02	1	8,20E-02	8,89	0.0138
B^2	6,13E-03	1	6,13E-03	0,66	0.4340

Table 5.10. ANOVA for water absorption response surface quadratic model

Source	Sum of Squares	df	Mean Square	F Value	p-value Prob > F
Model	714,69	8	89,34	57,89	< 0.0001
A-t	381,28	1	381,28	247,08	< 0.0001
B-c	154,52	1	154,52	100,13	< 0.0001
C-a	1,03	1	1,03	0,67	0.4333
AB	41,37	1	41,37	26,81	0.0004
AC	2,57	1	2,57	1,66	0.2260
BC	1,31	1	1,31	0,85	0.3777
A^2	8,03	1	8,03	5,21	0.0457
B^2	14,31	1	14,31	9,27	0.0124

Table 5.11. ANOVA for crushing strength response surface 2FI model

Source	Sum of Squares	df	Mean Square	F Value	p-value Prob > F
Model	404,90	6	67,48	5,30	0.0069
A-t	89,78	1	89,78	7,06	0.0209
B-c	52,81	1	52,81	4,15	0.0643
C-a	44,52	1	44,52	3,50	0.0860
AB	103,91	1	103,91	8,17	0.0144
AC	0,06	1	0,06	4,45E-03	0.9479
BC	62,67	1	62,67	4,93	0.0465

Figures 5.57 and 5.58 are 3D view graphs showing the effect of the temperature and binder content for B and G on the specific gravity and Figures 5.63 and 5.64 show the interaction effect of the input parameters for B and G on the specific gravity. It is evident from figures that both the temperature and the binder content have strong effect on the specific gravity of aggregates. While, in the case of the binder content, the results demonstrate that increasing the binder content until it reaches its centre value would result in increasing the specific gravity, the specific gravity then starts to drop as the content tends to increase above the centre limit. Such behaviour could be attributed to the following reasons. Firstly, fusing and densification take place that make the specific gravity to increase. Secondly, it could be due to the fact that the expansion and bloating occur by the entrapment of gases in the melted liquid phase, resulting from volatization of certain components of the aggregate and this would result in reducing the specific gravity as stated previously in experimental results. In terms of the interaction effect between the temperature and binder content, it is evident that by using low binder content and high temperature, specific gravity tends to increase, as mentioned previously. When using high temperature and high binder content this would reduce the specific gravity as discussed earlier. On the other hand, sintering with low temperature and low binder content would also reduce the specific gravity of the aggregates due to the lack of fusing of grains.

The result demonstrates that all the input parameters have a significant effect on the water absorption of the aggregates. No significant interaction effect was found in the case of the water absorption. From Figures 5.59 and 5.60, it can be noticed that the water

absorption decreases as the temperature increase. This is because the high temperature would lead to isolated, impermeable and disconnected pores which would improve their permeability characteristics. The reduction was observed for both upper and lower limits for binder contents. However, 3D views showed an increase in absorption with increase in binder content at 1200 ^{o}C. Finally, the water absorption decreased as the temperature increased due to the relatively impermeable pores obtained as a result of the melted liquid phase. Figures 5.65 and 5.66 show the effect of the binder content and temperature on the water absorption of aggregates with bentonite and glass powder. Generally speaking, the results indicate that as the temperature increases, the water absorption of aggregates would be reduced. This is important in the optimization of the aggregate characteristics.

Temperature and binder content variables were found to have their own effect on the crushing strength regarding the binder types. As the temperature increased from -1 to +1 in coded values, the crushing strength increased in aggregates with bentonite (Figures 5.61, 5.62, 5.67 and 5.68). This shows that bentonite contributes significantly in increasing the crushing strength. However, a little drop was observed in aggregates with 10 % bentonite at 1200 ^{o}C. Unlikely, considering the aggregates with glass powder as the temperature increased from -1 to +1 in coded values, the crushing strength increases with the content increase at 1100 ^{o}C, thereafter started to decrease. This shows the different behavior between the bentonite and glass powder binders. This difference was also proved by the relationship between density and strength of aggregates produced with two different binders disscussed previously in Figures 5.16 and 5.17. The 3D contour plots of the effect of two significant variables A and B on the crushing strength are shown in Figures 5.61 and 5.62. In relation to the interaction effect between the temperature and binder content, the results indicated that using high content of binder decreased crushing strength with increase in temperature . On the other hand, applying low bentonite content increased crushing strength with increase in temperature.

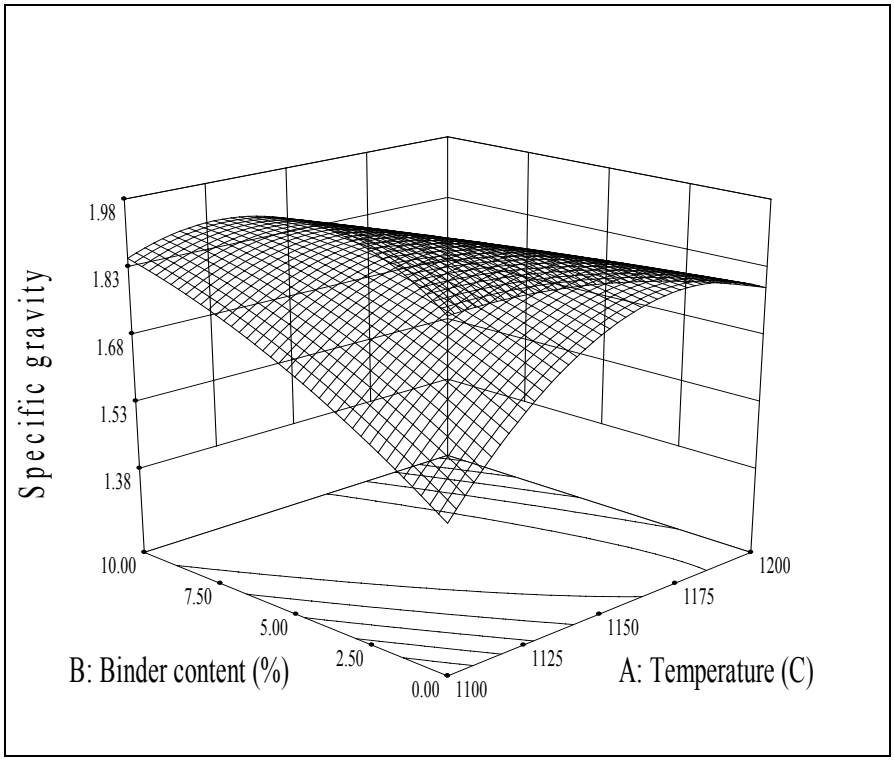

Figure 5.57. 3D diagram showing the contour plots for A and B on the specific gravity of bentonite aggregates

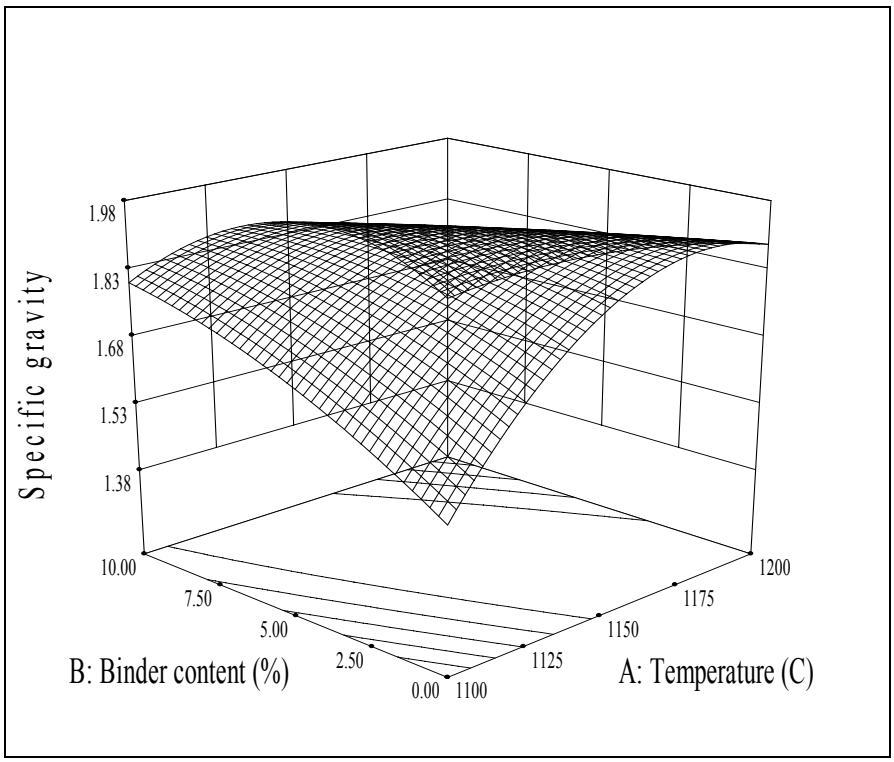

Figure 5.58. 3D diagram showing the contour plots for A and B on the specific gravity of glass powder aggregates

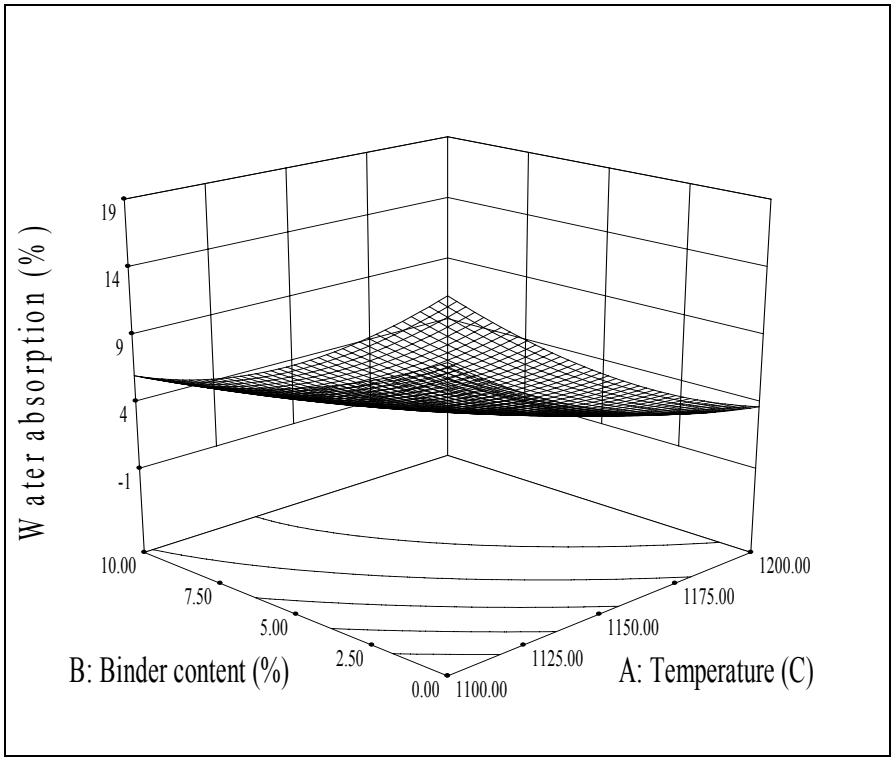

Figure 5.59. 3D diagram showing the contour plots for A and B on the water absorption of bentonite aggregates

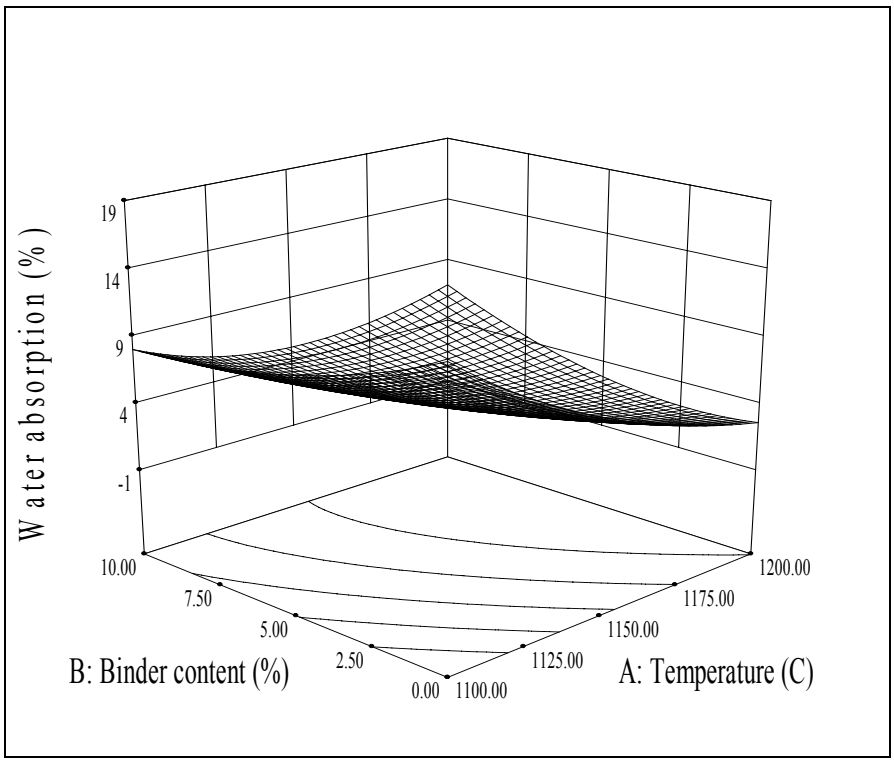

Figure 5.60. 3D diagram showing the contour plots for A and B on the water absorption of glass powder aggregates

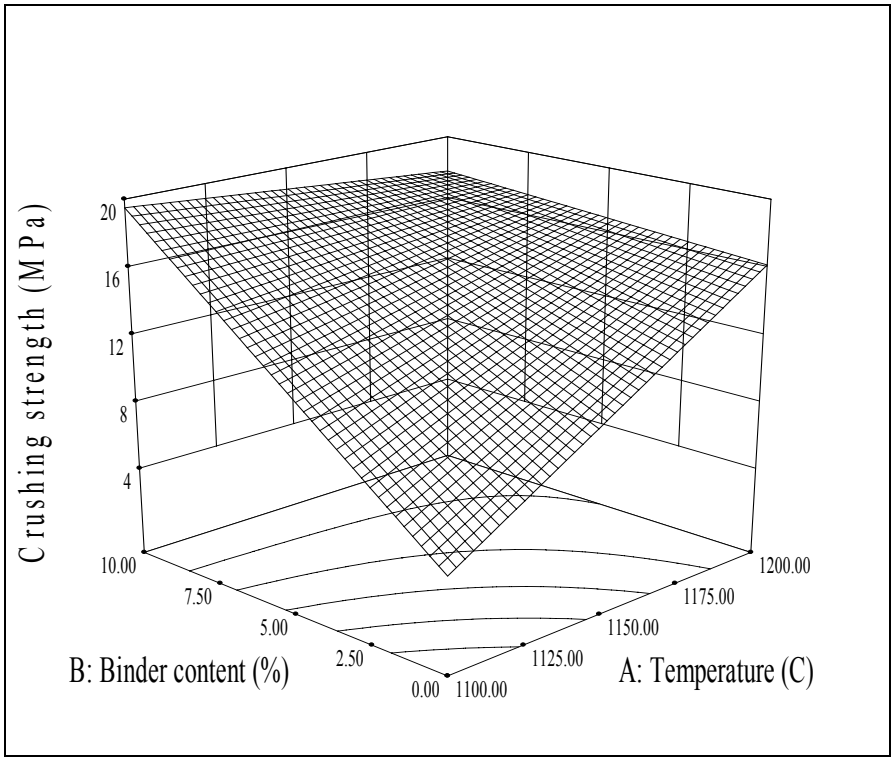

Figure 5.61. 3D diagram showing the contour plots for A and B on the crushing strength of bentonite aggregates

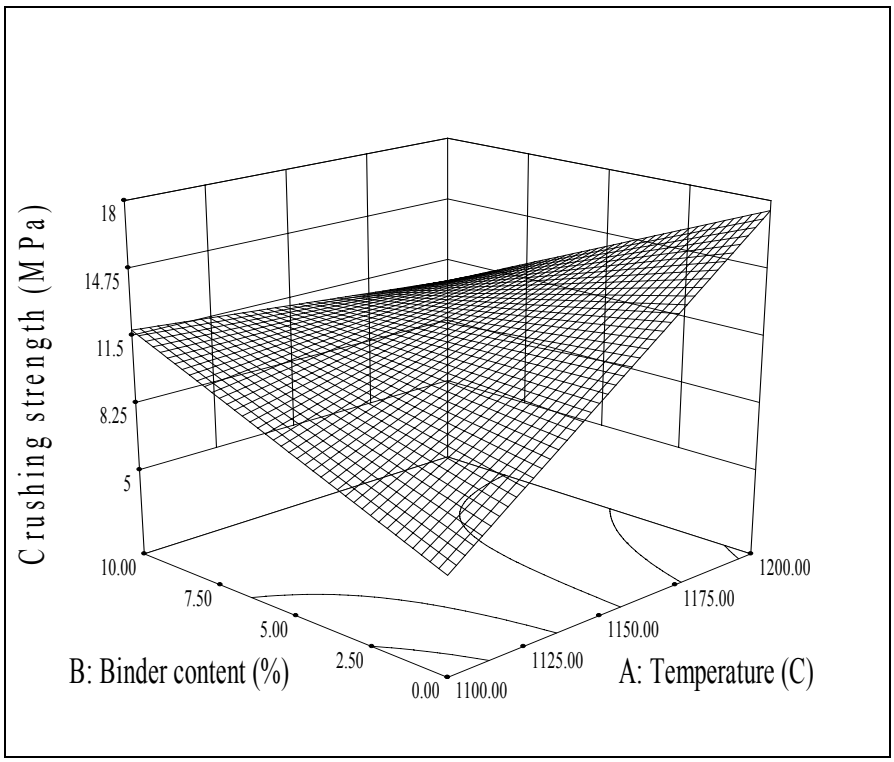

Figure 5.62. 3D diagram showing the contour plots for A and B on the crushing strength of glass powder aggregates

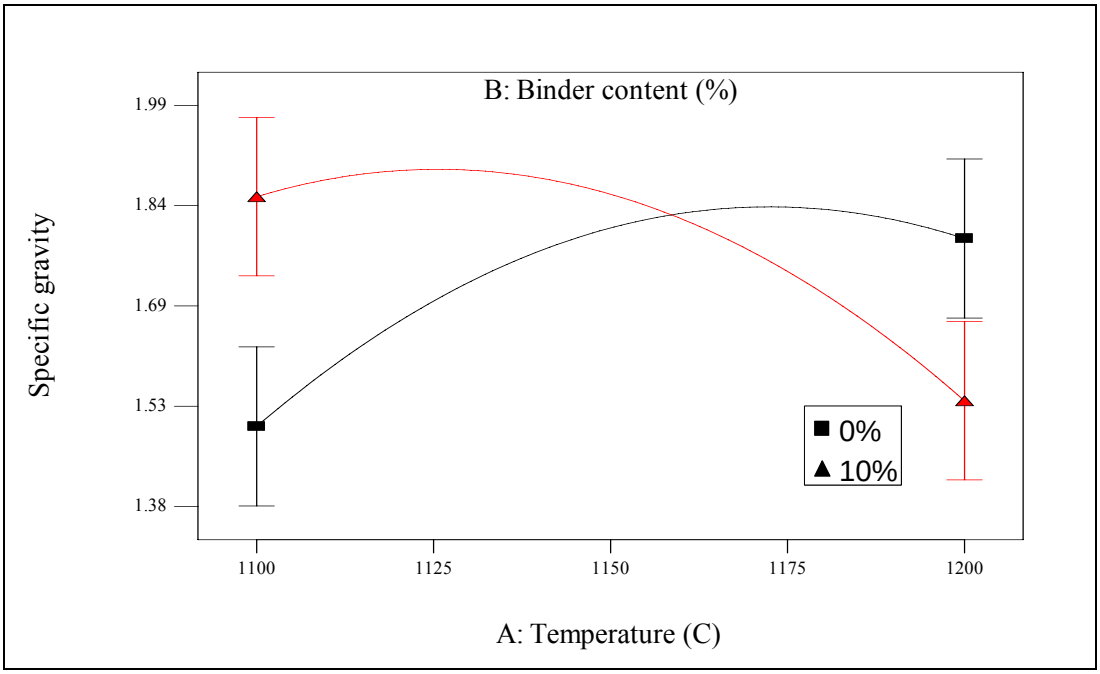

Figure 5.63. Interaction effect between A and B on the specific gravity of bentonite aggregates

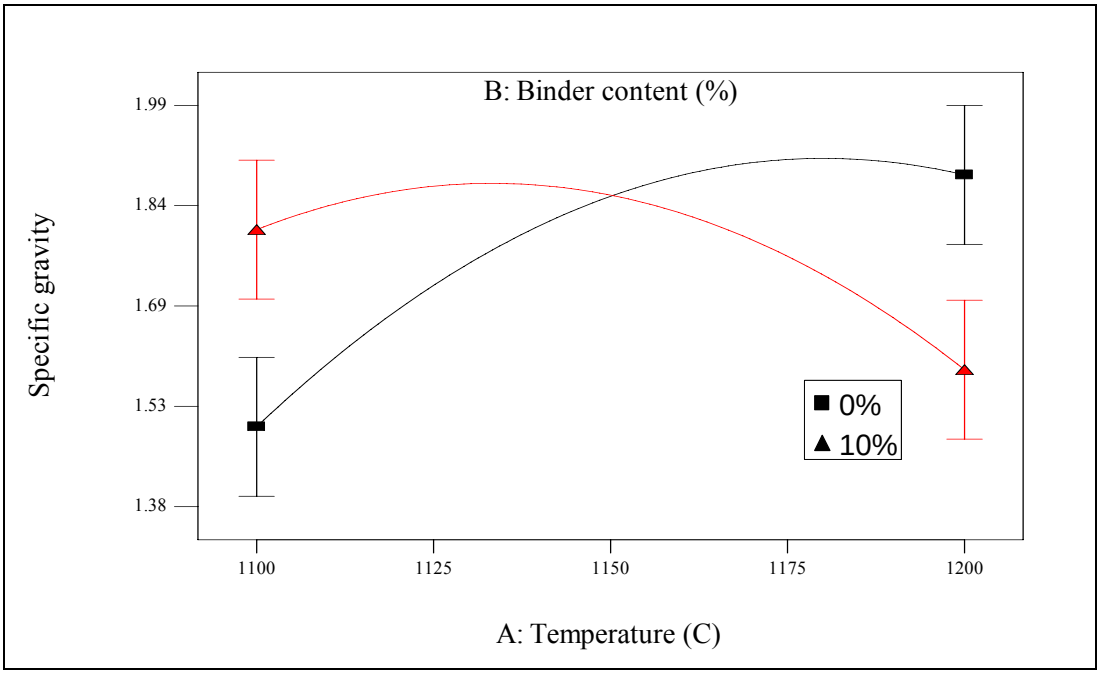

Figure 5.64. Interaction effect between A and B on the specific gravity of glass powder aggregates

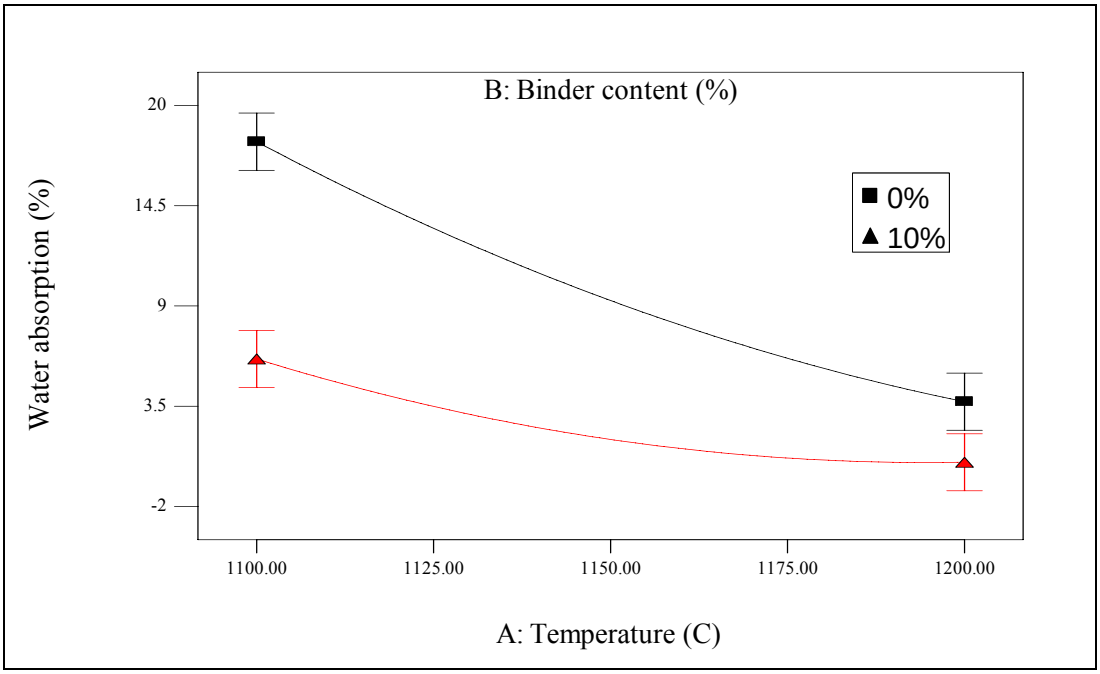

Figure 5.65. Interaction effect between A and B on the water absorption of bentonite aggregates

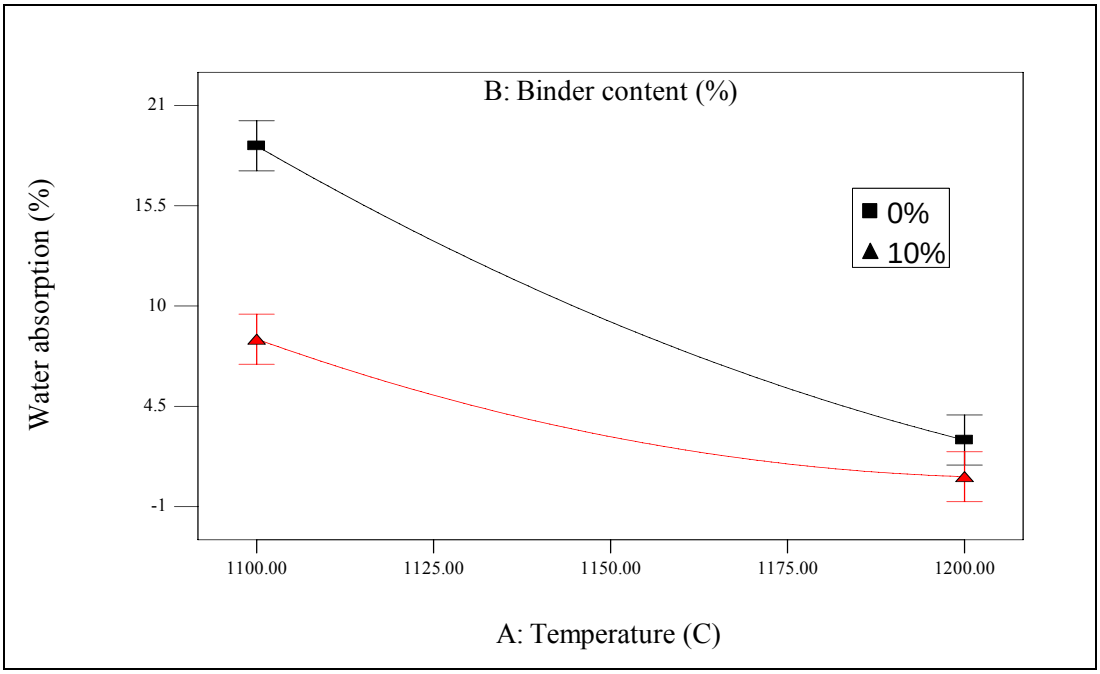

Figure 5.66. Interaction effect between A and B on the water absorption of glass powder aggregates

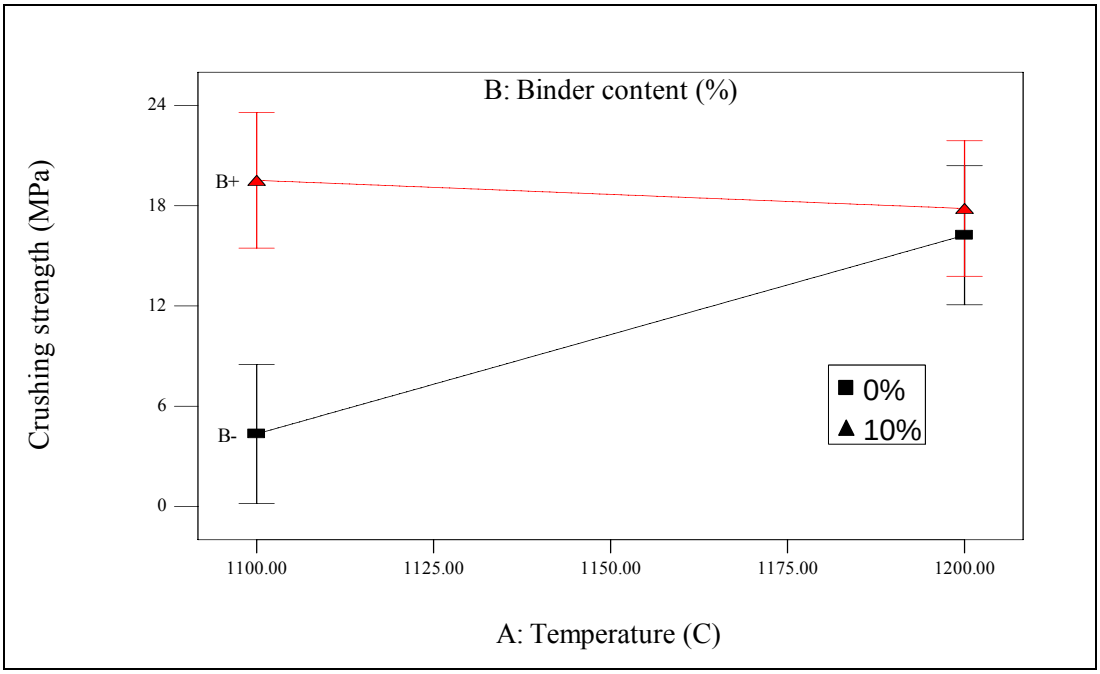

Figure 5.67. Interaction effect between A and B on the crushing strength of bentonite aggregates

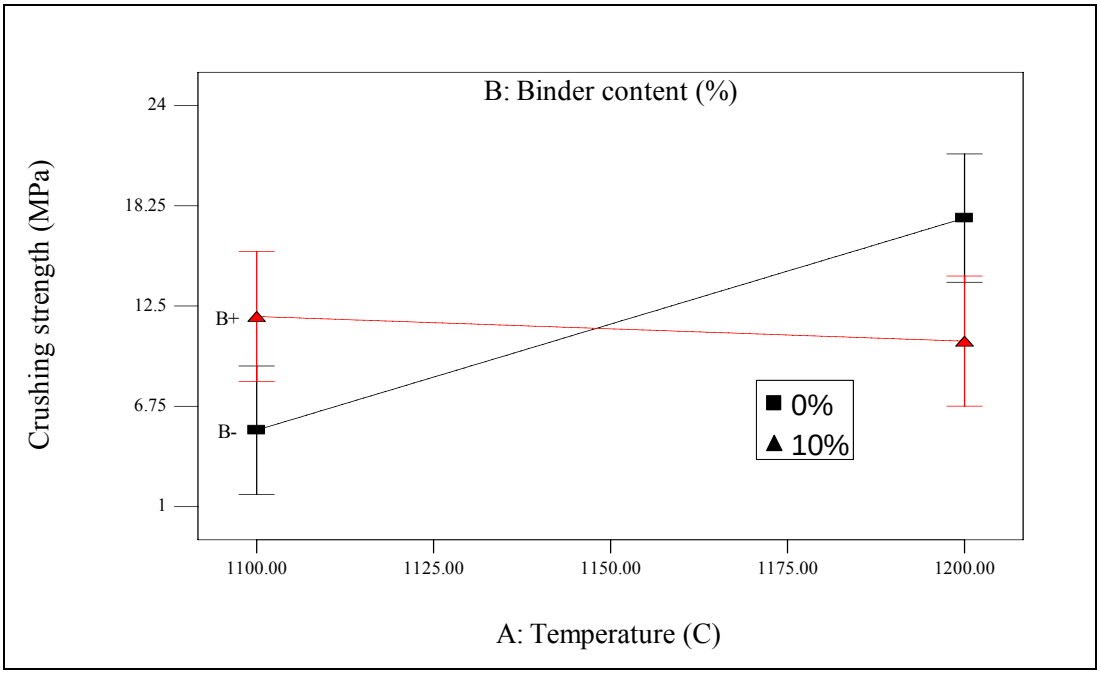

Figure 5.68. Interaction effect between A and B on the crushing strength of glass powder aggregates

As any increase in the specific gravity is usually reflected in increasing the crushing strength, as a consequence both strength and specific gravity are usually studied together.

On balance, and based on the above discussion, it is better to run an optimization study to find out the optimal aggregate properties at which the desirable mechanical and physical properties of the aggregates can be achieved. In fact, once the models have been developed and checked for adequacy, the optimization criteria can be set to find out the optimum aggregate characteristics. In this investigation, three criteria were implemented to achieve high strength lightweight concrete. The first criterion was to reach the maximum strength and the minimum specific gravity with no limitation on the process parameters. While, in the second criterion, the goal was to reach the maximum strength as well as the minimum specific gravity and water absorption. The third criterion was applied to minimize both specific gravity and water absorption and to maximize the crushing strength with a greater importance. However, Tables 5.12 and 5.13 summarize these three criteria. Also, Tables 5.14-5.16 present the optimal solution based on the three optimization criteria as determined by design-expert software. The optimization results clearly demonstrate that, whatever the optimization criteria, 10B1200 and 10G1200 aggregates have the highest desirabilities among all aggregates that would lead to minimum specific gravity and maximum strength of 1.54 and 17.83 MPa for bentonite and 1.59 and 10.48 for glass powder, respectively. Figures 5.69 and 5.70 present the 3D view of desirability for lightweight aggregates with bentonite and glass powder based on the first criterion. It is obvious that the graphical optimization allows visual selection of the optimum aggregate properties according to certain criterion. If the water absorption is taken into account, the desirability values increase for both aggregate types. In this case, the water absorption values of bentonite and glass powder would be 0.43 and 0.64 %, respectively, while specific gravity and strength values remain the same, as can be seen in Tables 5.14-5.16. These type of desirability plots are extremely practical for quick technical use in the workshop to choose the values of the parameters that would achieve certain response value for these types of aggregates. The desirability decreases with decrease in temperature and binder content.

Table 5.12. Optimization criteria used in this study

Name	Limits		First importance	Second importance	First goal	Second goal
	Lower	Upper				
Temperature	1100	1200	3	3	is in range	is in range
Content	0	10	3	3	is in range	is in range
Type	bn	gp	3	3	is in range	is in range
Specific gravity	1,49	1,94	5	5	minimize	minimize
Water absorption	0,6	18,8	none	3	none	minimize
Crushing strength	4,8	24	3	3	maximize	maximize

Table 5.13. The third criterion of numerical optimization

Name	Limits		Third importance	Third goal
	Lower	Upper		
Temperature	1100	1200	3	is in range
Content	0	10	3	is in range
Type	bn	gp	3	is in range
Specific gravity	1,49	1,94	5	minimize
Water absorption	0,6	18,8	3	minimize
Crushing strength	4,8	24	4	maximize

Table 5.14. Optimal solution as obtained by design-expert based on the first criterion

Number	Temperature	Content	Type	Specific gravity	Crushing Strength	Desirability
1	1200,0	10,00	bn	1,54	17,83	0,801461
2	1200,0	10,00	gp	1,59	10,48	0,542378
3	1100,0	4,23	bn	1,69	10,76	0,443798
4	1100,0	4,05	gp	1,67	8,02	0,376276
5	1100,0	4,00	gp	1,66	7,99	0,376268
6	1116,4	0,00	gp	1,65	7,38	0,355986

Table 5.15. Optimal solution as obtained by design-expert based on the second criterion

Number	Temperature	Content	Type	Specific gravity	Water absorption	Crushing Strength	Desirability
1	1200	10,00	bn	1,54	0,43	17,83	0,851327
2	1200	9,82	bn	1,55	0,34	17,80	0,843305
3	1200	10,00	gp	1,59	0,64	10,48	0,640466
4	1100	5,93	bn	1,75	8,93	13,34	0,456599
5	1100	6,00	bn	1,75	8,86	13,45	0,456581
6	1100	7,10	gp	1,75	9,54	10,01	0,392882
7	1100	7,17	gp	1,75	9,49	10,06	0,392875
8	1100	7,00	gp	1,75	9,62	9,94	0,39286
9	1100	7,95	gp	1,77	9,00	10,56	0,391755
10	1100	6,03	gp	1,72	10,40	9,31	0,390463

Table 5.16. Optimal solution as obtained by design-expert based on the third criterion

Number	Temperature	Content	Type	Specific gravity	Water absorption	Crushing Strength	Desirability
1	1200	10,00	bn	1,54	0,43	17,83	0,83539
2	1200	10,00	gp	1,59	0,64	10,48	0,600576
3	1100	6,68	bn	1,77	8,20	14,48	0,45809
4	1100	8,58	gp	1,78	8,67	10,98	0,383578
5	1100	8,34	gp	1,78	8,79	10,81	0,383511
6	1100	8,00	gp	1,77	8,97	10,59	0,383226
7	1100	7,68	gp	1,76	9,16	10,39	0,382704

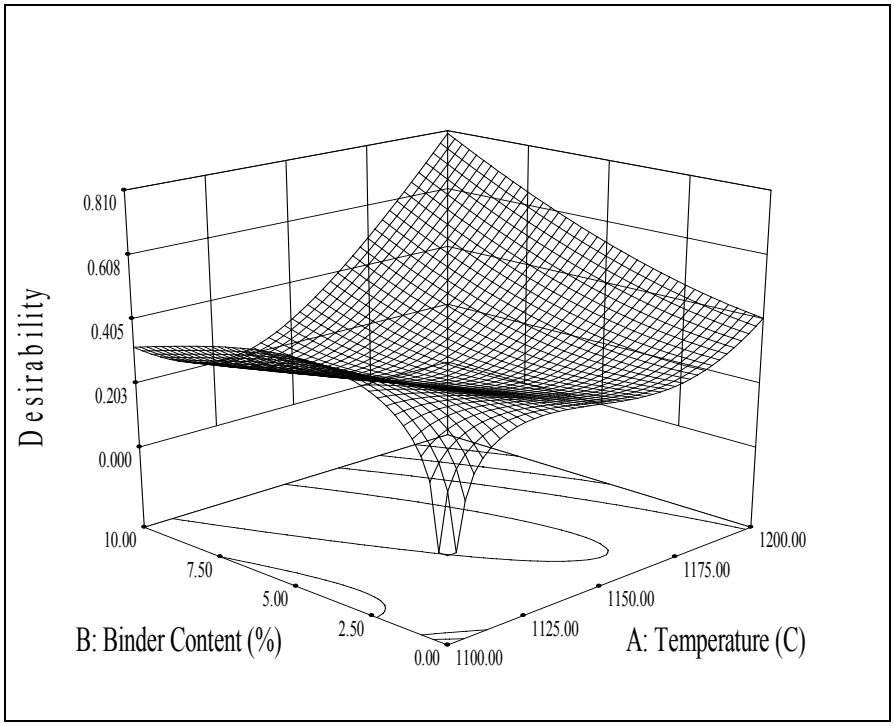

Figure 5.69. Desirability for bentonite aggregate based on the first criterion

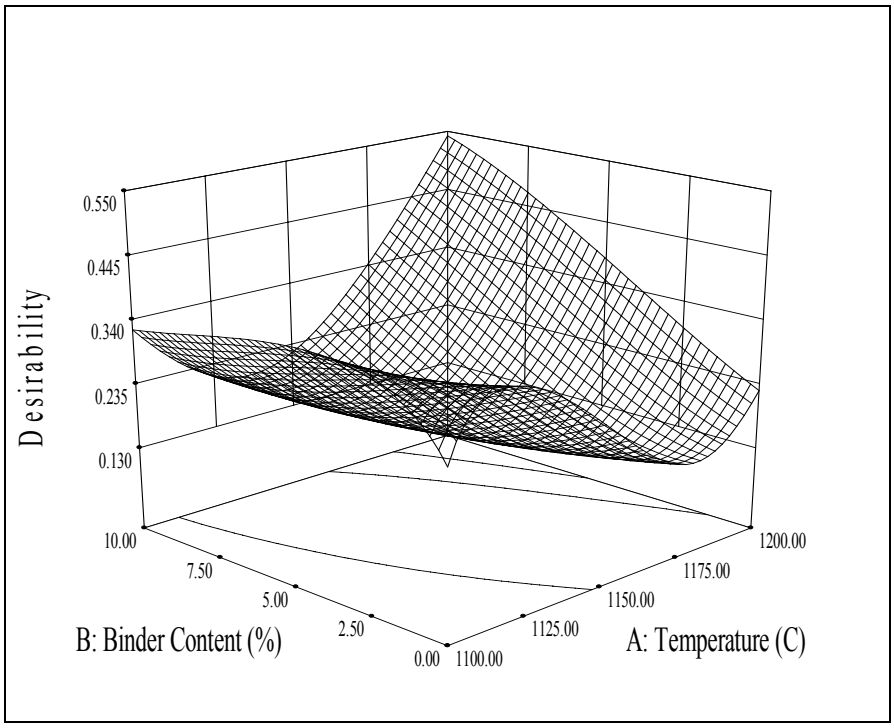

Figure 5.70. Desirability for glass powder aggregate based on the first criterion

5.2.2. Historical Data Design

In Design Expert software, historical data design is also used for importing data that already exists. Table 5.17 shows the imported data design matrix. Any set of numeric or categoric data can be imported and analyzed via the Historical Data design interface on the Response Surface tab. Here are the basic instructions:

- Specify the number of numeric and categoric factors.
- Enter the minimum and maximum values for each numeric factor.
- Set the number of experiments to equal the number of observations in your data file.
- Specify the levels for any categoric factors – these levels must match the imported data exactly – it is case sensitive.
- Enter the response names.
- Once you have the blank design layout, you can Copy the data from your file and Paste it into the design layout screen. Remember that the number of columns and rows must be the same. You can adjust the number of rows by right-clicking on a gray square to the left of any row and adding or deleting rows as needed.
- Continue with analysis –recommended checking Design Evaluation to determine if there is any aliasing and how much correlation there is between factors.

In general, efficiency of the sintering process is influenced by multiple parameters such as sintering temperature, binder content and type, among others, and their effects may be either independent or interactive. The influence of sintering variables such as temperature, binder content and type on the aggregate properties has not yet been reported clearly. RSM has shown to be a powerful tool in optimizing experimental conditions to maximize or minimize various responses. Sintering temperature (t), binder content (c) and binder type (a) were the three parameters investigated. According to range of each variable, the independent variables are coded to the (-1, 1) interval. The low and high levels are coded -1 and +1, respectively. The three factors and lower, middle and upper design points for RSM in coded and uncoded values are shown in Table 5.7. In RSM, natural variables are transformed into coded variables that have been defined as dimensionless with a mean zero and the same spread or standard deviation. Multiple

regression equations were generated relating response variable to coded levels of the independent variables. Analysis of variance (ANOVA) shows that the selected models adequately represented the data obtained (Tables 5.18-5.23).

Table 5.17. Design matrix (Imported data)

Run	Factor 1 A: Temperature	Factor 2 B: Binder content	Factor 3 C: Binder type
1	1100	0	G
2	1100	5	G
3	1100	10	G
4	1150	0	G
5	1150	5	G
6	1150	10	G
7	1200	0	G
8	1200	5	G
9	1200	10	G
10	1100	0	B
11	1100	5	B
12	1100	10	B
13	1150	0	B
14	1150	5	B
15	1150	10	B
16	1200	0	B
17	1200	5	B
18	1200	10	B

The design matrix of the variables in the coded units is shown in Tables 5.24-5.29, along with the predicted and experimental values of responses and percentages of error. The predicted values of responses were obtained from models fitting techniques using the software Design Expert. The statistical model was developed by applying multiple

regression analysis methods on using the experimental data for aggregates in the treatment. The final mathematical models in terms of coded and actual factors are listed below:

Final equation in terms of coded factor:

$$\text{Specific gravity (od)} = +1.88+0.012 * A+0.011 * B-4.444E-003 * C-0.15 * A * B -8.333E-004 * A * C+4.167E-003 * B * C-0.15 * A^2-0.044 * B^2 \quad (5.16)$$

$$\text{Specific gravity (ssd)} = +1.97-0.071 * A-0.047 * B-0.010 * C-0.12 * A * B +7.500E-003 * A * C-1.667E-003 * B * C-0.14 * A^2-0.027 * B^2 \quad (5.17)$$

$$\text{Apparent specific gravity} = +2.07-0.17 * A-0.11 * B-0.017 * C-0.092 * A * B +0.021 * A * C-5.833E-003 * B * C-0.13 * A^2-0.011 * B^2 \quad (5.18)$$

$$\text{Water absorption} = +3.52-5.33 * A-3.51 * B-0.42 * C+2.34 * A * B+0.37 * A * C -0.26 * B * C+1.67 * A^2+2.19 * B^2 \quad (5.19)$$

$$\text{Porosity} = +10.37-2.62 * A-2.58 * B+0.52 * C+1.68 * A * B-0.22 * A * C +0.34 * B * C+4.65 * A2-3.08 * B2 \quad (5.20)$$

$$\text{Crushing strength} = +13.03+2.27 * A+1.55 * B+1.27 * C-4.00 * A * B -0.13 * A * C+1.08 * B * C \quad (5.21)$$

Final equation in terms of actual factors:

For agent G;

$$\text{Specific gravity(od)} = -80.86319+0.14053 * t+0.71475 * c-6.05000E-004 * t * c -5.96667E-005 * t^2-1.76667E-003 * c^2 \quad (5.22)$$

$$\text{Specific gravity(ssd)} = -72.64056 + 0.12892 * t + 0.56517 * c - 4.90000E\text{-}004 * t * c - 5.56667E\text{-}005 * t^2 - 1.06667E\text{-}003 * c^2 \quad (5.23)$$

$$\text{Apparent specific gravity} = -64.83194 + 0.11845 * t + 0.40917 * c - 3.70000E\text{-}004 * t * c - 5.23333E\text{-}005 * t^2 - 4.33333E\text{-}004 * c^2 \quad (5.24)$$

$$\text{Water absorption} = +1075.90972 - 1.69408 * t - 12.27917 * c + 9.35000E\text{-}003 * t * c + 6.66667E\text{-}004 * t^2 + 0.087667 * c^2 \quad (5.25)$$

$$\text{Porosity} = +2563.26667 - 4.35950 * t - 7.05833 * c + 6.70000E\text{-}003 * t * c + 1.86000E\text{-}003 * t^2 - 0.12300 * c^2 \quad (5.26)$$

$$\text{Crushing strength} = -135.90000 + 0.12800 * t + 18.49333 * c - 0.016000 * t * c \quad (5.27)$$

For agent B;

$$\text{Specific gravity(od)} = -80.84208 + 0.14049 * t + 0.71642 * c - 6.05000E\text{-}004 * t * c - 5.96667E\text{-}005 * t^2 - 1.76667E\text{-}003 * c^2 \quad (5.28)$$

$$\text{Specific gravity(ssd)} = -73.00222 + 0.12922 * t + 0.56450 * c - 4.90000E\text{-}004 * t * c - 5.56667E\text{-}005 * t^2 - 1.06667E\text{-}003 * c^2 \quad (5.29)$$

$$\text{Specific gravity} = -65.81194 + 0.11928 * t + 0.40683 * c - 3.70000E\text{-}004 * t * c - 5.23333E\text{-}005 * t^2 - 4.33333E\text{-}004 * c^2 \quad (5.30)$$

$$\text{Water absorption} = +1058.72639 - 1.67942 * t - 12.38250 * c + 9.35000E\text{-}003 * t * c + 6.66667E\text{-}004 * t^2 + 0.087667 * c^2 \quad (5.31)$$

$$\text{Porosity} = +2573.58333 - 4.36817 * t - 6.92167 * c + 6.70000E\text{-}003 * t * c + 1.86000E\text{-}003 * t^2 - 0.12300 * c^2 \quad (5.32)$$

$$\text{Crushing strength} = -129.4000 + 0.12267 * t + 18.92667 * c - 0.016000 * t * c \quad (5.33)$$

Model summary statistics gives several comparative measures for model selection. Ignoring the aliased model, the quadratic model for specific gravity, water absorption and porosity and 2 factor interactions (2FI) model for crushing strength come out the best: low standard deviation and high R squared statistics. Among the different models studied, for specific gravity (OD), specific gravity (SSD), apparent specific gravity, water absorption and porosity, only the quadratic models were found to fit the experimental data best with standard deviations of 0.093, 0.084, 0.09, 1.22 and 4.22 and with correlation coefficients (R^2 value) of 0.78, 0.82, 0.90, 0.98 and 0.66, respectively, indicating that the fitnesses of the selected models are good and the models could be used for further navigation. However, for crushing strength, 2 factor interactions (2FI) was found to fit the experimental data best with a standard deviation of 3.99 and with a correlation coefficient (R^2 value) of 0.60 indicating that the fitnesses of the proposed model is good.

ANOVA of the regression parameters of the predicted response surface models are summarized in Tables 5.18-5.23. Values of "Prob>F'' less than 0.0500 indicate that model terms are significant. The results demonstrated that the quadratic effect of temperature and interaction between temperature and binder content were significant for specific gravity (OD). However, linear effects of variables did not produce a significant effect in this case. The linear and quadratic effects of temperature and interaction effect between temperature and binder content were significant for specific gravity (SSD). The results indicated that linear effects of temperature and binder content, quadratic effect of temperature and interaction effect between temperature and content were highly significant ($p < 0.001$ or $p < 0.05$) for apparent specific gravity. The linear and quadratic effects of temperature and binder content and interaction effect between temperature and binder content were significant for water absorption. The variables demonstrated no significant effect on the total porosity. The interaction effect between temperature and binder content on crushing strength was observed.

For the model fitted, software generates model coefficients, R^2-values, F-values and significant probabilities and hence one can justify the significance of each experimental variable. From statistical point of view, three tests are required to evaluate the model: test of significance of factors and interactions, R-squared test and the lack-of-fit test. Test of significance of factors and interactions determines which factors must be included in

model and which factors must be excluded. Tables 5.18-5.23 show the results of the test of significance of factors and interactions for the responses. When p-value (probability value) of one term is more than 0.05, this indicates that this is insignificant at the 95% confidence level. R-squared is a statistical measure of how well a model approximate real data points. The test of lack-of-fit is used to determine whether discrepancies between measured and expected values can be attributed to random or systematic errors. The lack-of-fit test compares the residual error to pure error from replicated design points. If p-value for lack-of-fit is less than 0.05, there is statistically significant lack-of-fit at the 95% confidence level. Plots of experimental and theoretical values indicated an excellent fit for specific gravity in OD and SSD, apparent specific gravity and water absorption, however slightly poor fit was observed for porosity and crushing strength. RSM demonstrated that experimental values were reasonably close to the predicted values confirming the validity and adequacy of the predicted models. The goodness of the model can be checked by the determination coefficient R^2. The regression models were highly significant ($p < 0.001$ or $p < 0.05$) for specific gravity in od and ssd, apparent specific gravity and water absorption with satisfactory coefficient of determination (R^2) that varied from 0.78 to 0.98.

Table 5.18. ANOVA for specific gravity (OD) response surface quadratic model

Source	Sum of Squares	df	Mean Square	F Value	p-value Prob > F
Model	0,283674	8	0,035459	4,096479	0.0251
A-t	0,001875	1	0,001875	0,216612	0.6527
B-c	0,001408	1	0,001408	0,1627	0.6961
C-a	0,000356	1	0,000356	0,041076	0.8439
AB	0,183013	1	0,183013	21,1428	0.0013
AC	8,33E-06	1	8,33E-06	0,000963	0.9759
BC	0,000208	1	0,000208	0,024068	0.8801
A^2	0,089003	1	0,089003	10,28218	0.0107
B^2	0,007803	1	0,007803	0,901428	0.3672

Table 5.19. ANOVA for specific gravity (SSD) response surface quadratic model

Source	Sum of Squares	df	Mean Square	F Value	p-value Prob > F
Model	0,289214	8	0,036152	5,113355	0.0125
A-t	0,060208	1	0,060208	8,515956	0.0171
B-c	0,026133	1	0,026133	3,696337	0.0867
C-a	0,0018	1	0,0018	0,254595	0.6260
AB	0,12005	1	0,12005	16,98005	0.0026
AC	0,000675	1	0,000675	0,095473	0.7644
BC	3,33E-05	1	3,33E-05	0,004715	0.9468
A^2	0,077469	1	0,077469	10,95739	0.0091
B^2	0,002844	1	0,002844	0,402322	0.5417

Table 5.20. ANOVA for apparent specific gravity response surface quadratic model

Source	Sum of Squares	df	Mean Square	F Value	p-value Prob > F
Model	0,627689	8	0,078461	9,635158	0.0013
A-t	0,336675	1	0,336675	41,34426	0.0001
B-c	0,143008	1	0,143008	17,56167	0.0023
C-a	0,005	1	0,005	0,614008	0.4534
AB	0,06845	1	0,06845	8,405776	0.0176
AC	0,005208	1	0,005208	0,639592	0.4445
BC	0,000408	1	0,000408	0,050144	0.8278
A^2	0,068469	1	0,068469	8,408164	0.0176
B^2	0,000469	1	0,000469	0,057649	0.8156

Table 5.21. ANOVA for water absorption response surface quadratic model

Source	Sum of Squares	df	Mean Square	F Value	p-value Prob > F
Model	568,6093	8	71,07616	47,88015	< 0.0001
A-t	341,3333	1	341,3333	229,9377	< 0.0001
B-c	147,7008	1	147,7008	99,49803	< 0.0001
C-a	3,125	1	3,125	2,105143	0.1807
AB	43,71125	1	43,71125	29,4459	0.0004
AC	1,613333	1	1,613333	1,086815	0.3244
BC	0,800833	1	0,800833	0,539478	0.4813
A^2	11,11111	1	11,11111	7,484952	0.0230
B^2	19,21361	1	19,21361	12,94317	0.0058

Table 5.22. ANOVA for porosity response surface quadratic model

Source	Sum of Squares	df	Mean Square	F Value	p-value Prob > F
Model	315,2575	8	39,40719	2,21	0.1289
A-t	82,16333	1	82,16333	4,62	0.0602
B-c	79,5675	1	79,5675	4,47	0.0636
C-a	4,805	1	4,805	0,27	0.6158
AB	22,445	1	22,445	1,26	0.2905
AC	0,563333	1	0,563333	0,03	0.8627
BC	1,400833	1	1,400833	0,08	0.7854
A^2	86,49	1	86,49	4,86	0.0549
B^2	37,8225	1	37,8225	2,13	0.1789

The fitted response surface plot was generated by statistically significant above model by Design Expert program to understand the interaction of the parameters required for optimum response. The plots are shown in Figs 5.71-5.94. Equations were then used to facilitate plotting of three-dimensional surface plots. Two parameters of each model were plotted on the X and Y axes with the response in Z axis.

Table 5.23. ANOVA for crushing strength response surface 2FI model

Source	Sum of Squares	df	Mean Square	F Value	p-value Prob > F
Model	261,66	6	43,61	2,734013	0.0706
A-t	61,65333	1	61,65333	3,865192	0.0750
B-c	28,83	1	28,83	1,80742	0.2059
C-a	28,88	1	28,88	1,810555	0.2055
AB	128	1	128	8,024621	0.0163
AC	0,213333	1	0,213333	0,013374	0.9100
BC	14,08333	1	14,08333	0,882917	0.3676

The regression models allowed the prediction of the effects of the three parameters on responses. The relationships between variables are illustrated in three dimensional (3D) representation of the response surfaces and interaction effects between temperature and binder content for both aggregates with bentonite and aggregates with glass powder plots generated by the models (Figures 5.71-5.82). Moreover, the response and interaction plots generated for specific gravities showed that at lower and upper levels of binder content, the temperature influenced the responses in a quadratic manner and hence specific gravities increased with increasing temperature to a certain level, but decreased with further increase (Figure 5.83-5.94). Further, at lower and upper levels of binder content, as the temperature increased the water absorption also displayed an decrease.

The effect of variables on responses showed that the responses behaved more as a quadratic function except crushing strength which behaved more as a 2FI function. 3-dimensional plot of responses model for aggregates with bentonite and glass powder shows the influence of temperature and binder content on the responses. Specific gravity increases by increasing temperature. But when temperature goes beyond a certain limit, the specific gravity decreases. In other words, the specific gravity (OD) started to increase with increased temperature and reached a maximum followed by a decrease with further increase in the temperature. A similar trend was observed for all three types of specific gravities employed. Specific gravity towards the upper design point of the variables produced a greater response compared to that produced at the lower design point. The

binder content increase led to increase in specific gravity at 1100 ^{o}C, however increase in binder content reduced the specific gravity at 1200 ^{o}C.

Temperature and binder content had a significant influence on the water absorption of aggregates. The water absorption of aggregates decreased with increasing binder content and temperature. However, total porosity decreased with increase in binder content and temperature and then began to decline a little with their further increase for two binder types.

The crushing strength of aggregates with bentonite increased with binder content at 1100 ^{o}C and decreased with increase in binder content at 1200 ^{o}C. However, the rate of decrease of strength in aggregates with glass powder was larger than in the aggregates with bentonite.

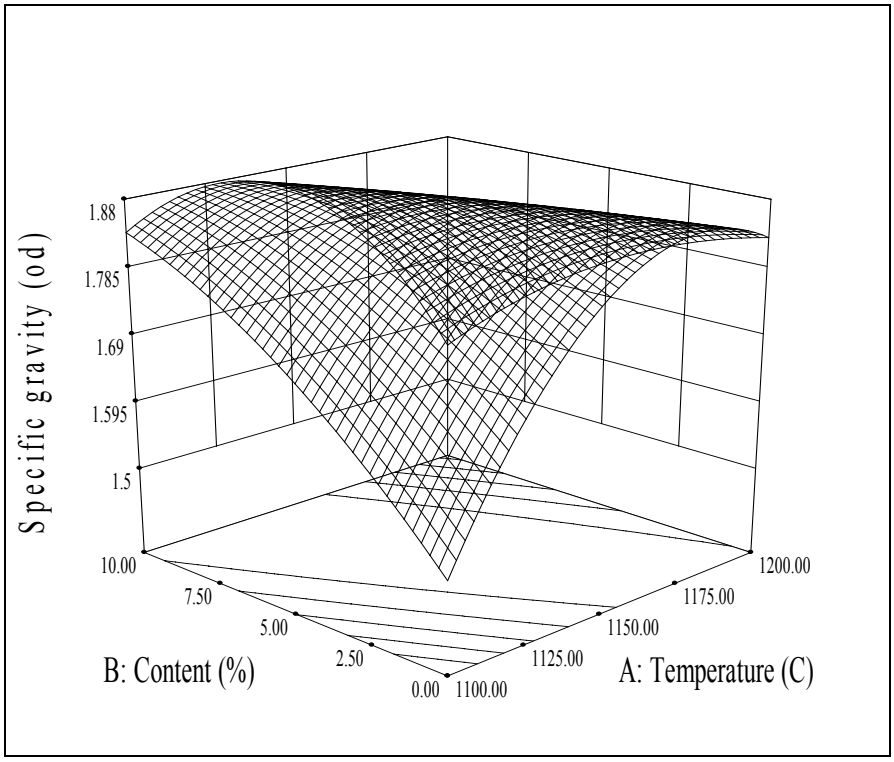

Figure 5.71. 3D diagram showing the contour plots for grades A and B on the specific gravity (OD) of bentonite aggregates

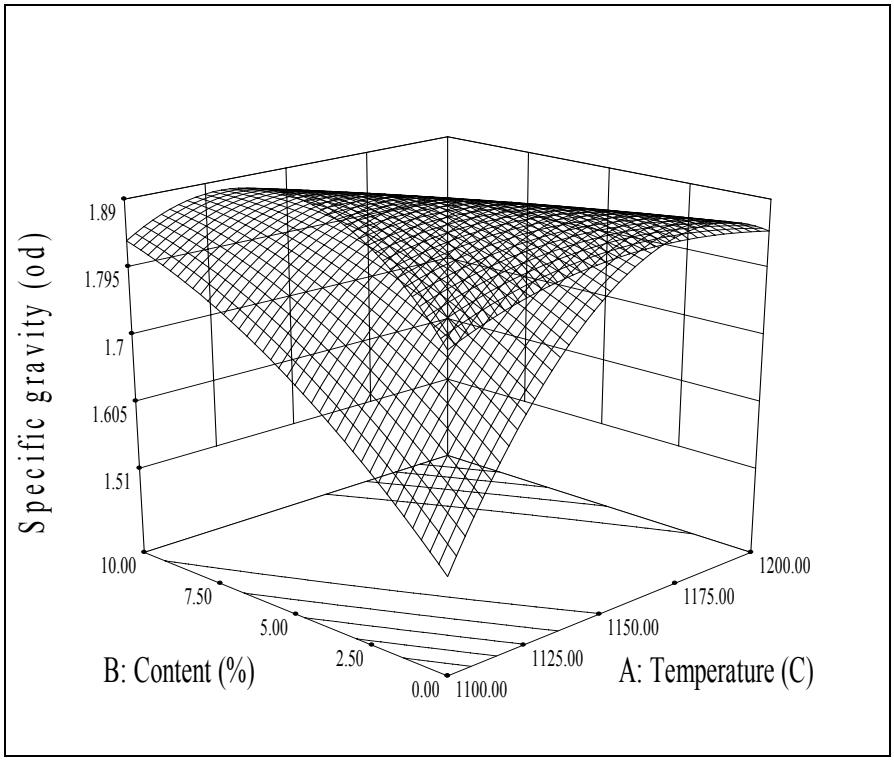

Figure 5.72. 3D diagram showing the contour plots for grades A and B on the specific gravity (OD) of glass powder aggregates

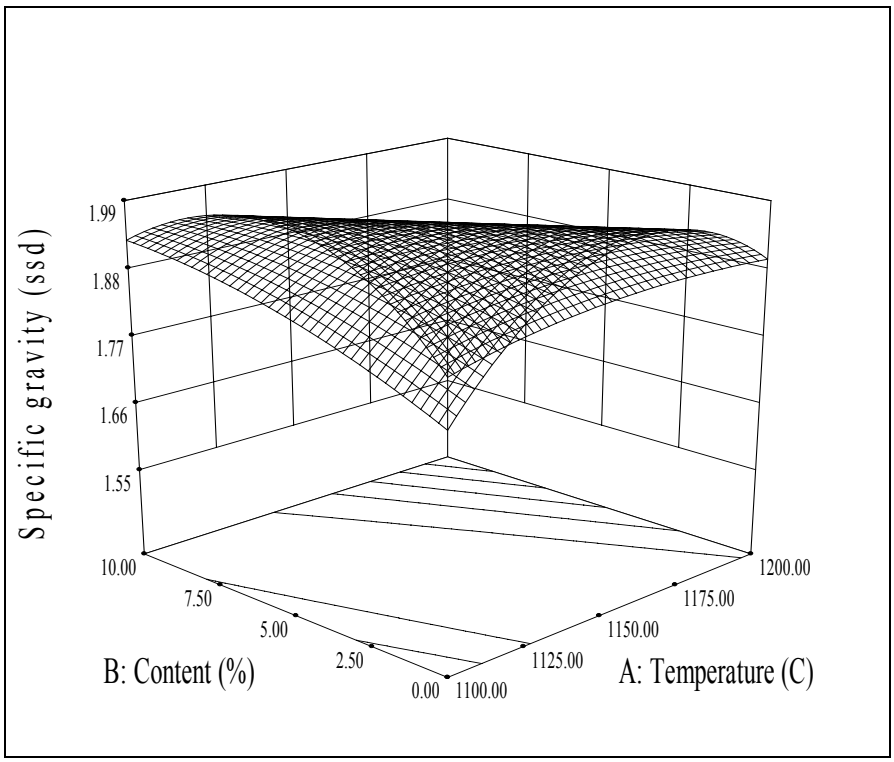

Figure 5.73. 3D diagram showing the contour plots for grades A and B on the specific gravity(SSD) of bentonite aggregates

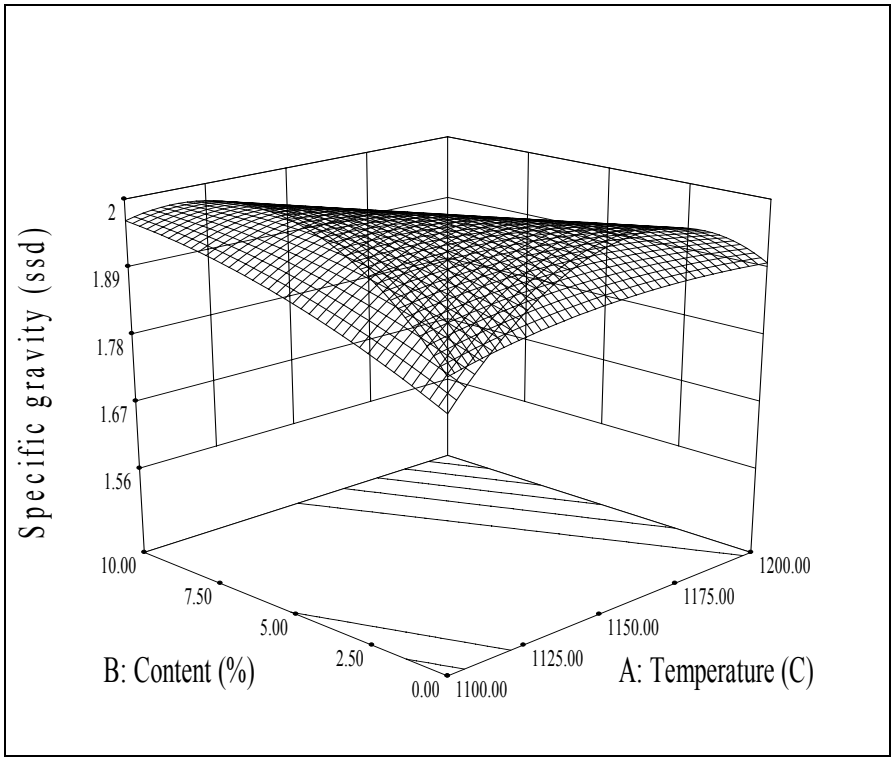

Figure 5.74. 3D diagram showing the contour plots for grades A and B on the specific gravity(SSD) of glass powder aggregates

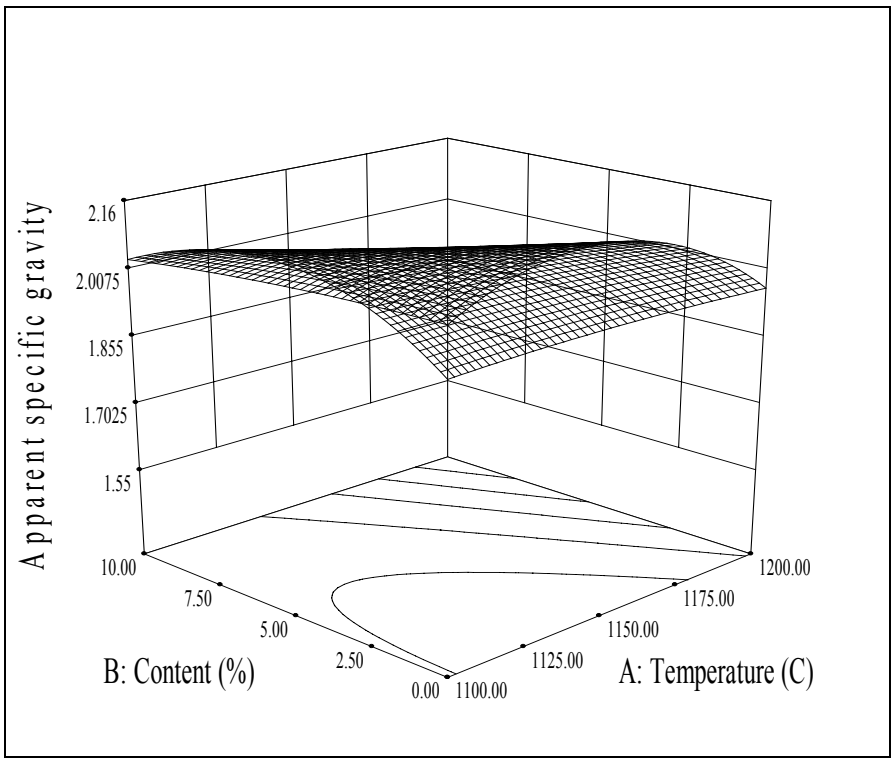

Figure 5.75. 3D diagram showing the contour plots for grades A and B on the apparent specific gravity of bentonite aggregates

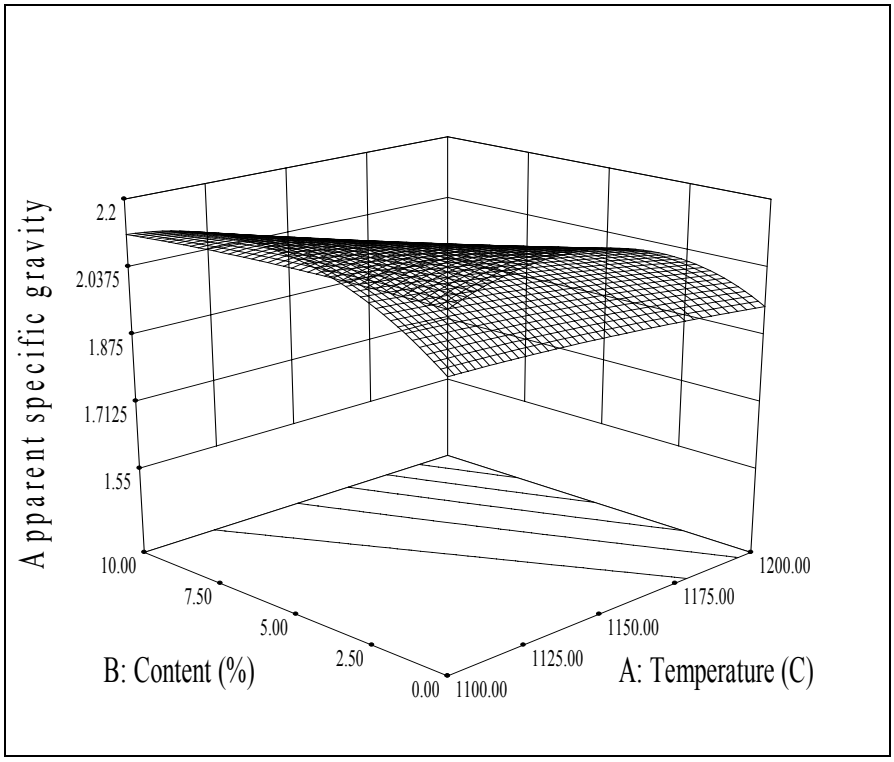

Figure 5.76. 3D diagram showing the contour plots for grades A and B on the apparent specific gravity of glass powder aggregates

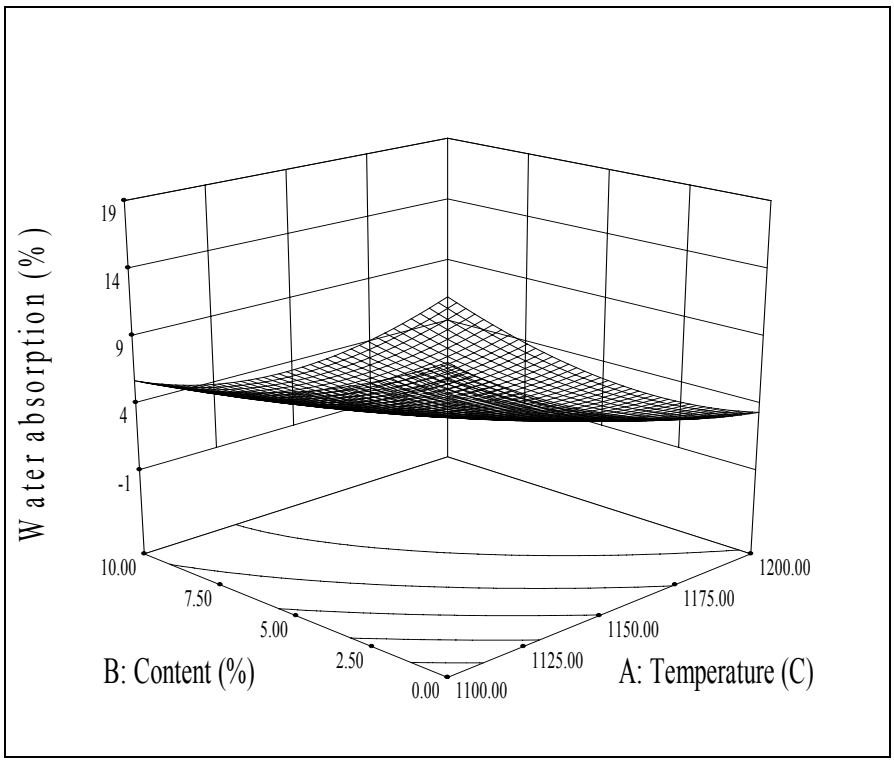

Figure 5.77. 3D diagram showing the contour plots for grades A and B on the water absorption of bentonite aggregates

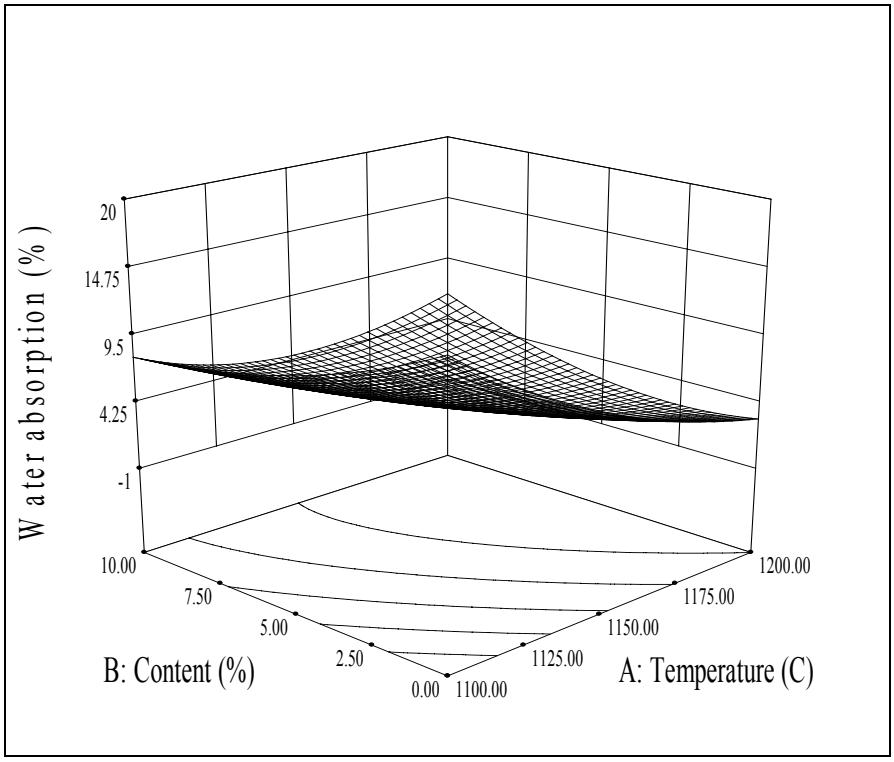

Figure 5.78. 3D diagram showing the contour plots for grades A and B on the water absorption of glass powder aggregates

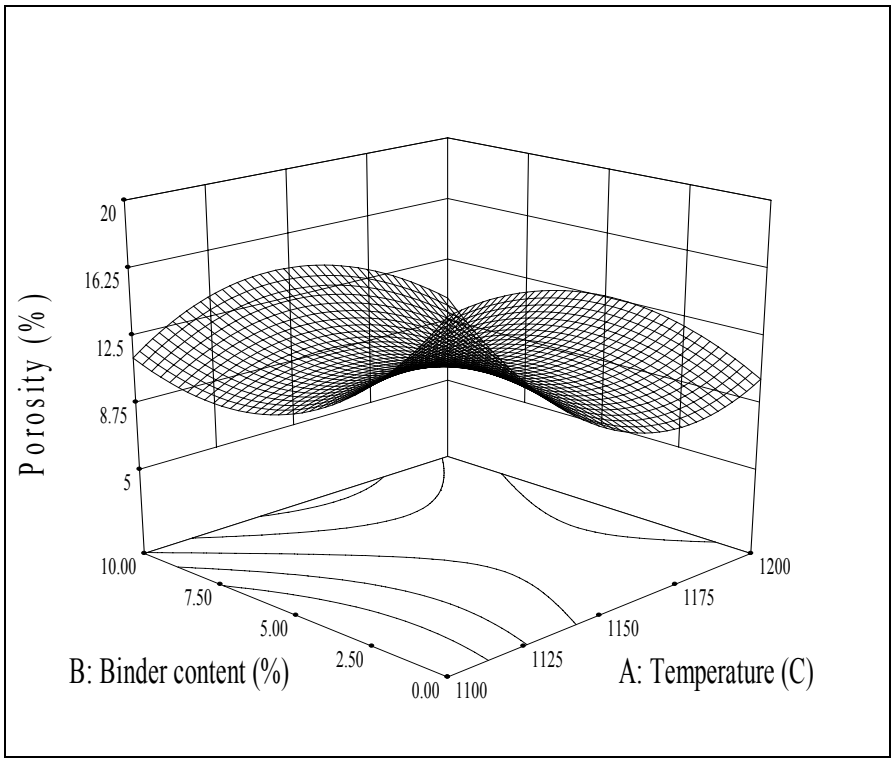

Figure 5.79. 3D diagram showing the contour plots for grades A and B on the porosity of bentonite aggregates

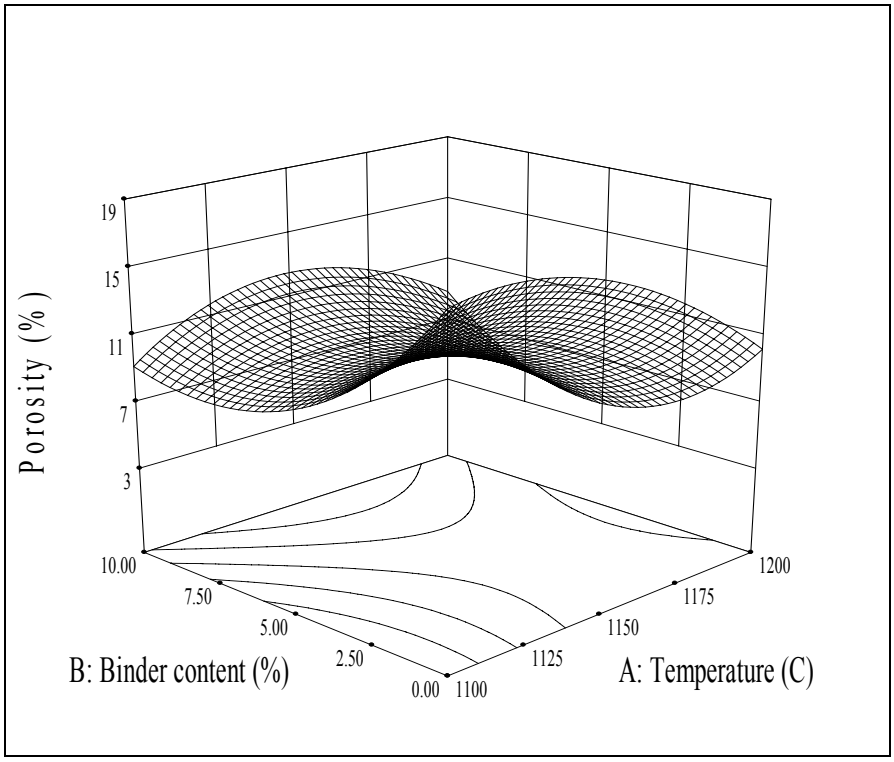

Figure 5.80. 3D diagram showing the contour plots for grades A and B on the porosity of glass powder aggregates

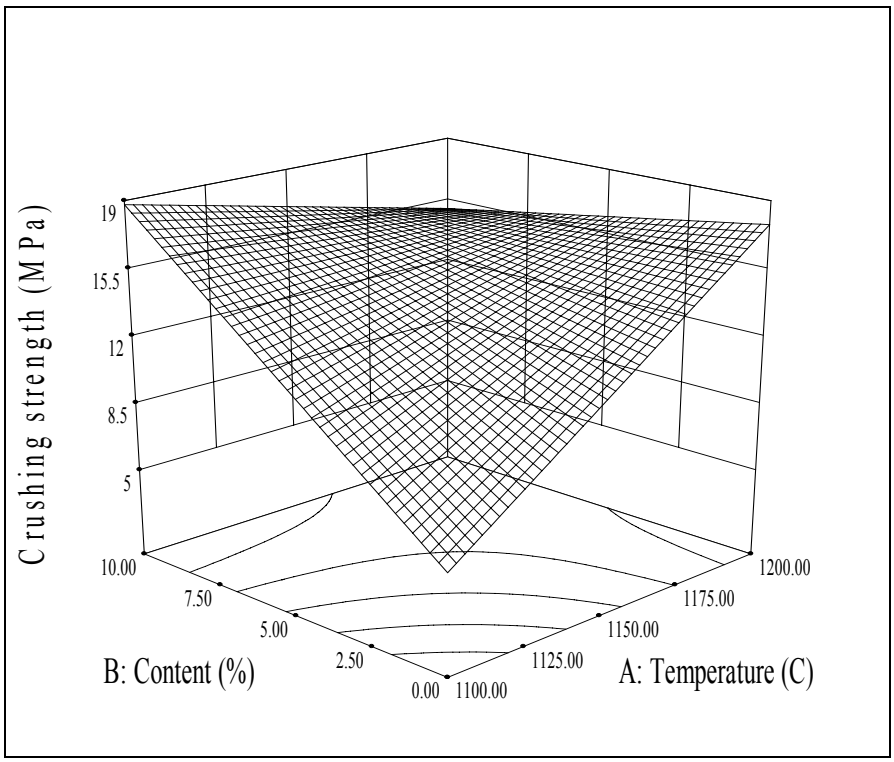

Figure 5.81. 3D diagram showing the contour plots for grades A and B on the crushing strength of bentonite aggregates

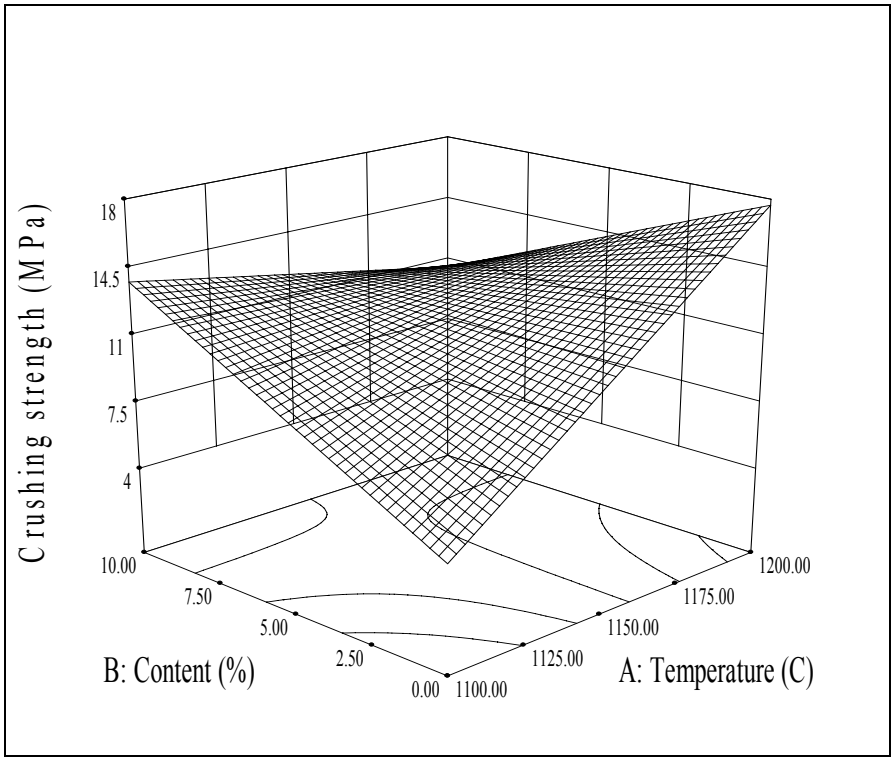

Figure 5.82. 3D diagram showing the contour plots for grades A and B on the crushing strength of glass powder aggregates

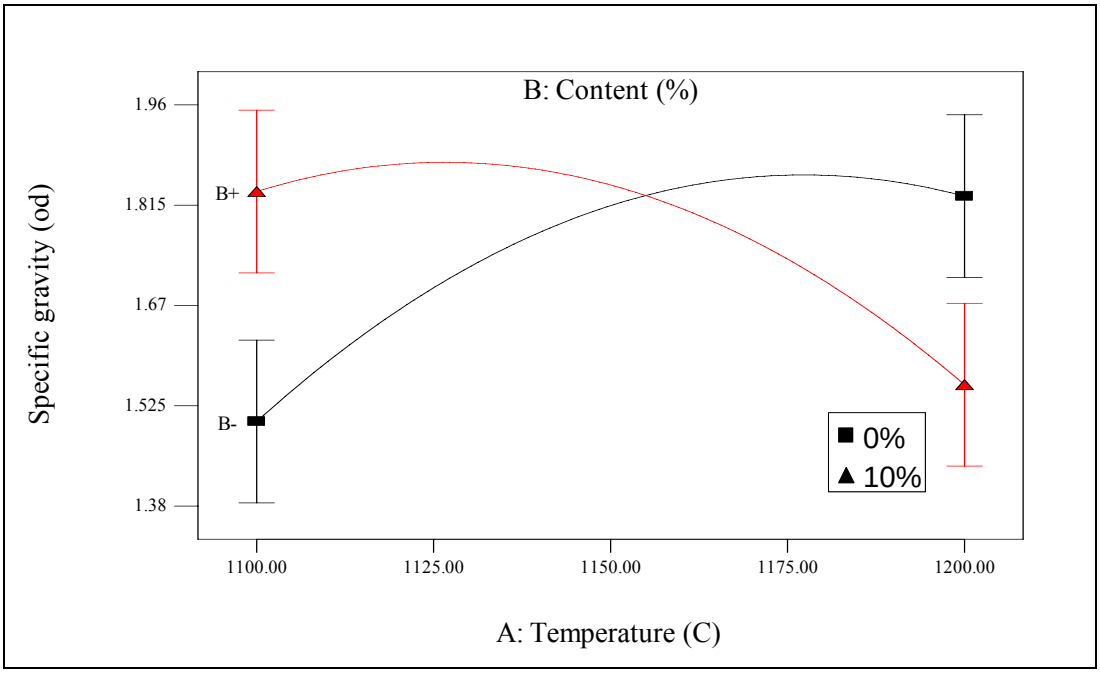

Figure 5.83. Interaction effect between A and B on the specific gravity (OD) of bentonite aggregates

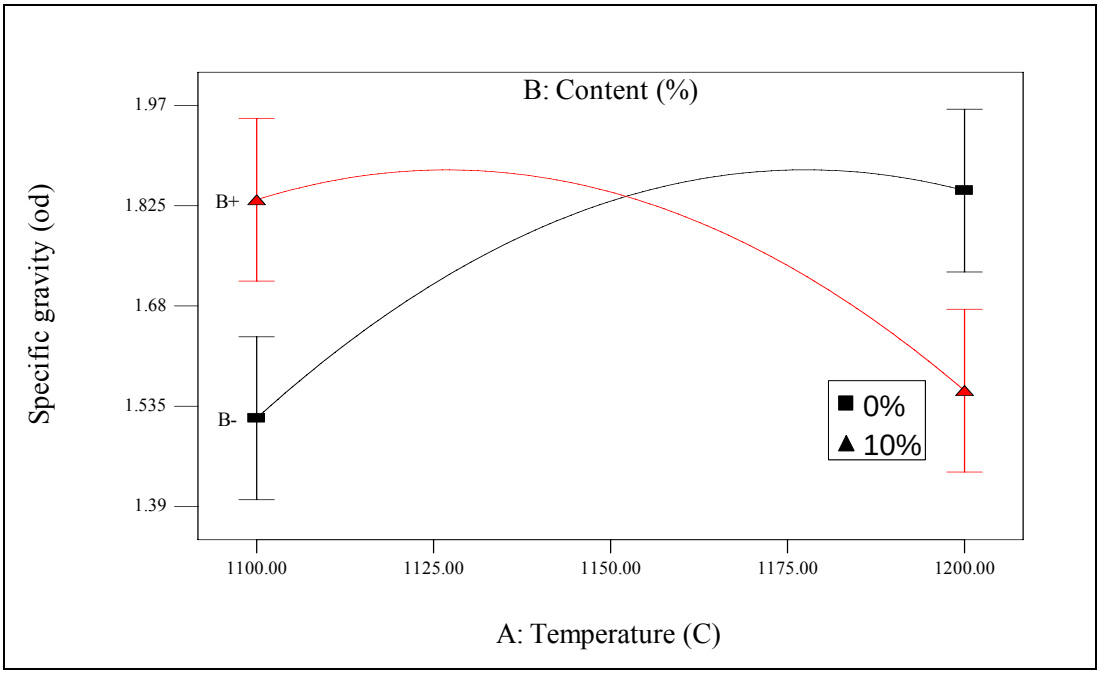

Figure 5.84. Interaction effect between A and B on the specific gravity (OD) of glass powder aggregates

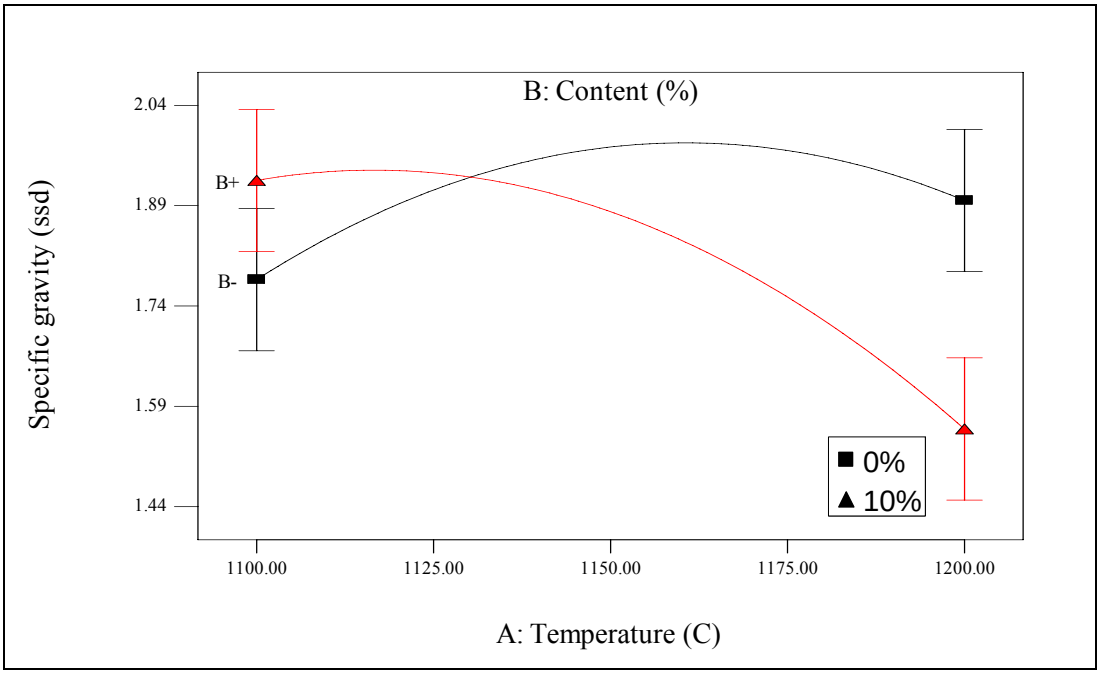

Figure 5.85. Interaction effect between A and B on the specific gravity (SSD) of bentonite aggregates

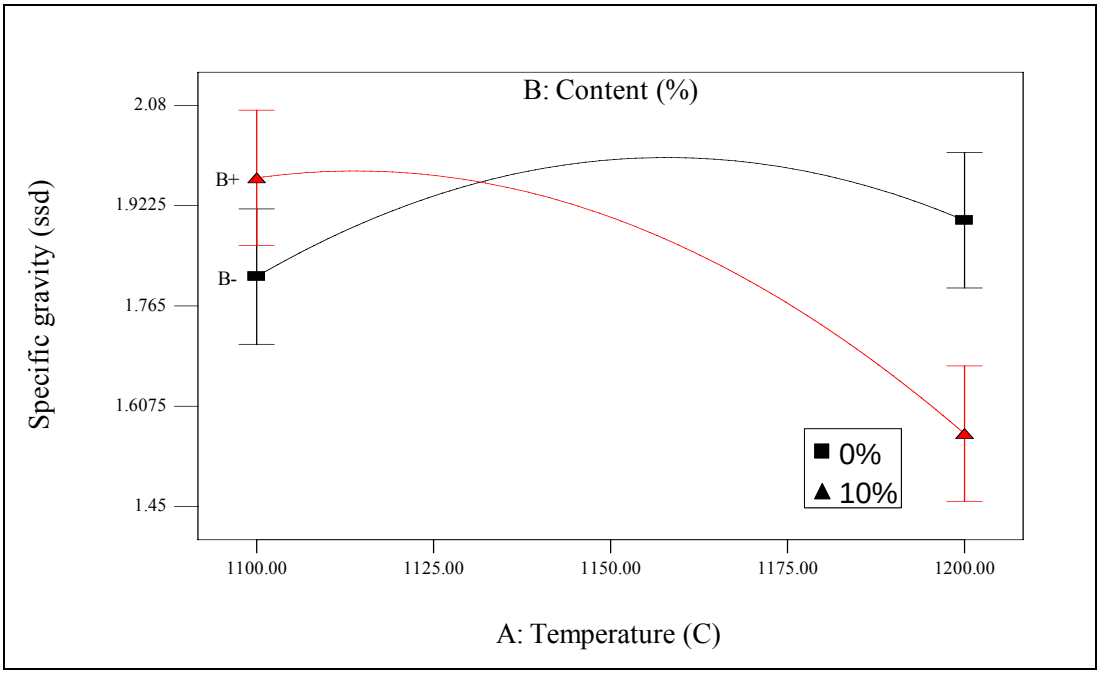

Figure 5.86. Interaction effect between A and B on the specific gravity(SSD) of glass powder aggregates

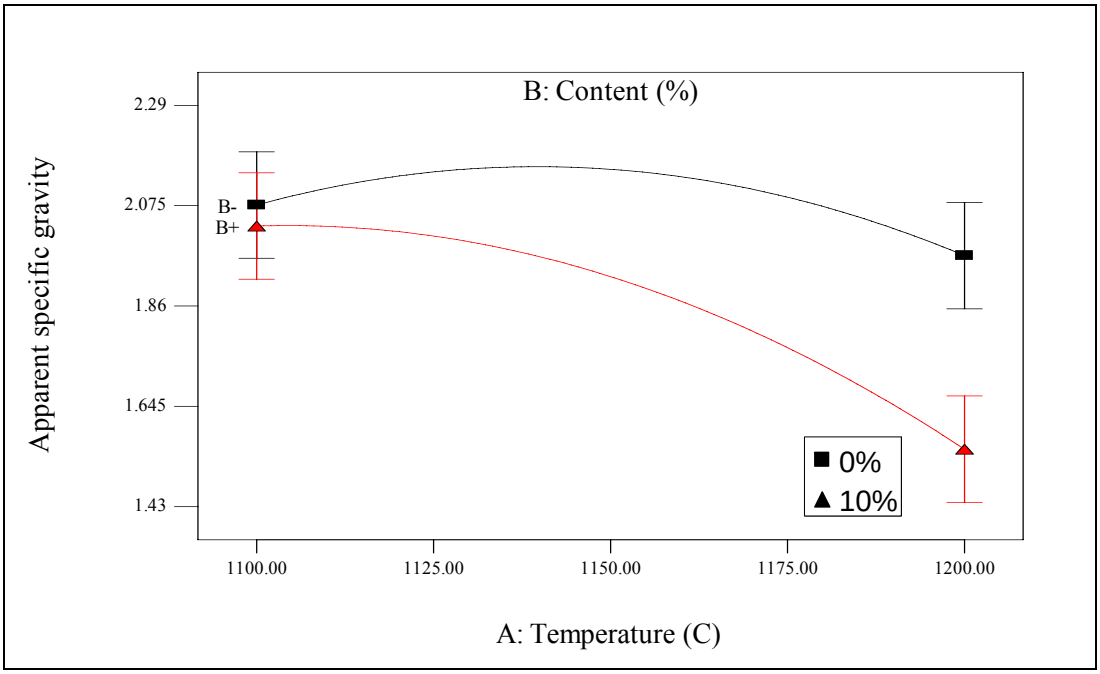

Figure 5.87. Interaction effect between A and B on the apparent specific gravity of bentonite aggregates

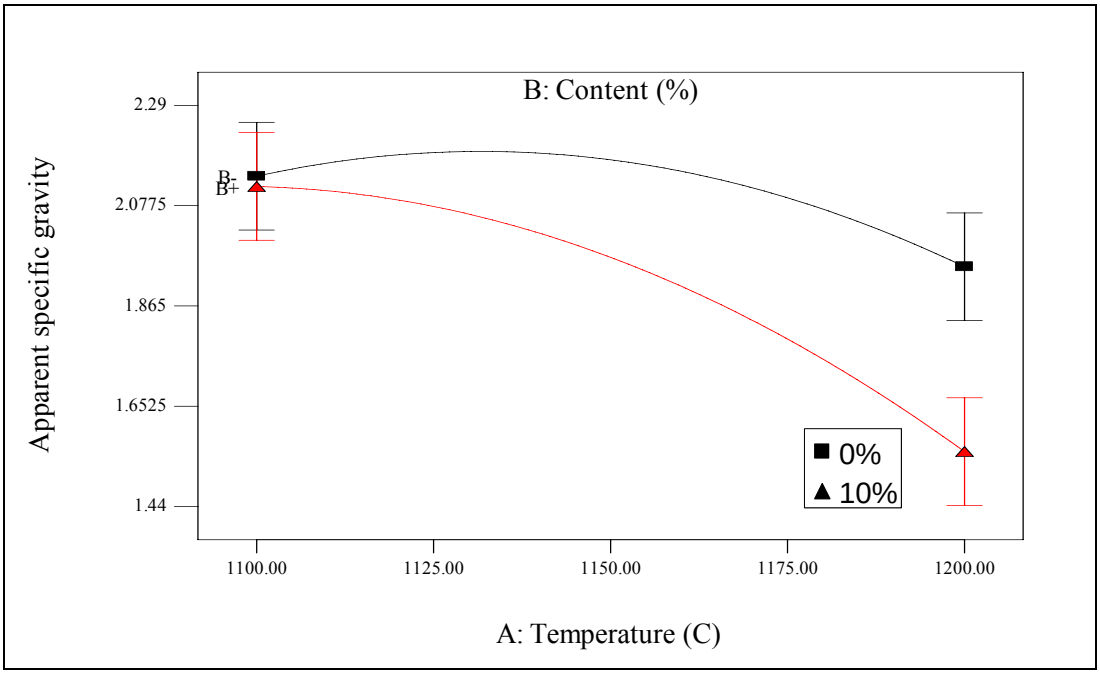

Figure 5.88. Interaction effect between A and B on the apparent specific gravity of glass powder aggregates

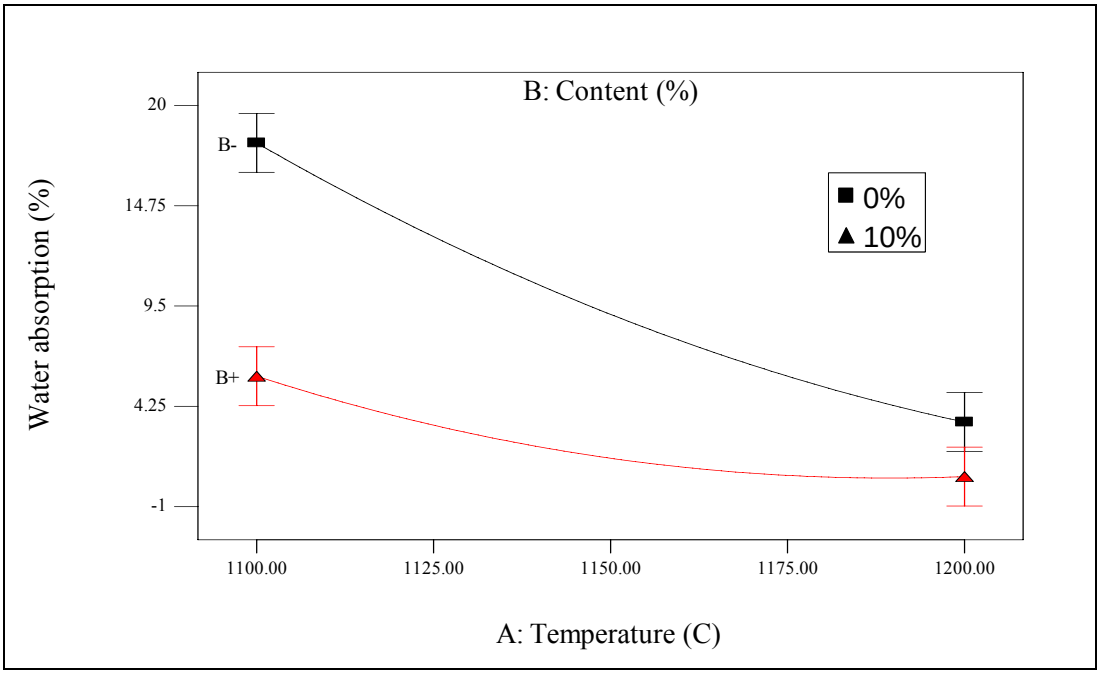

Figure 5.89. Interaction effect between A and B on the water absorption of bentonite aggregates

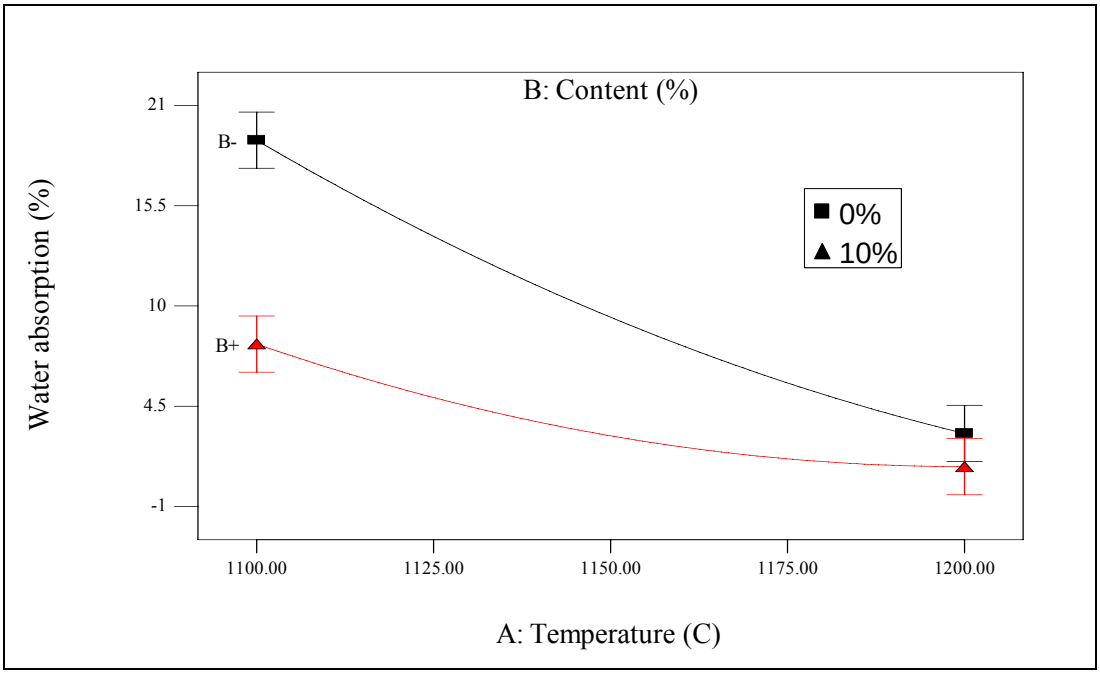

Figure 5.90. Interaction effect between A and B on the water absorption of glass powder aggregates

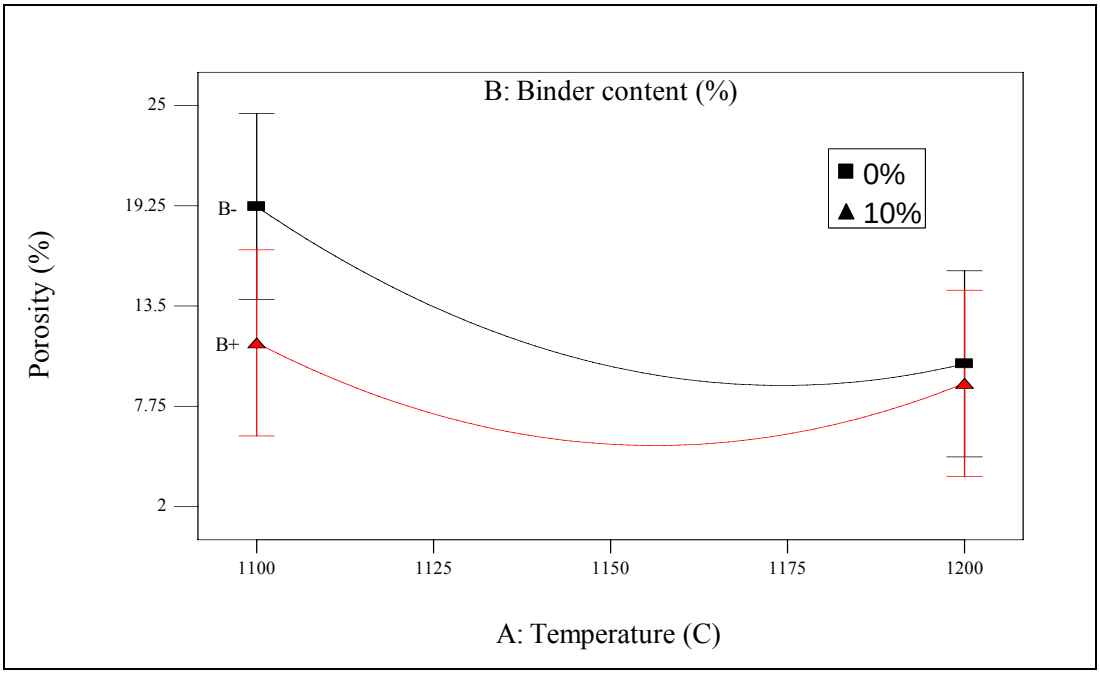

Figure 5.91. Interaction effect between A and B on the porosity of bentonite aggregates

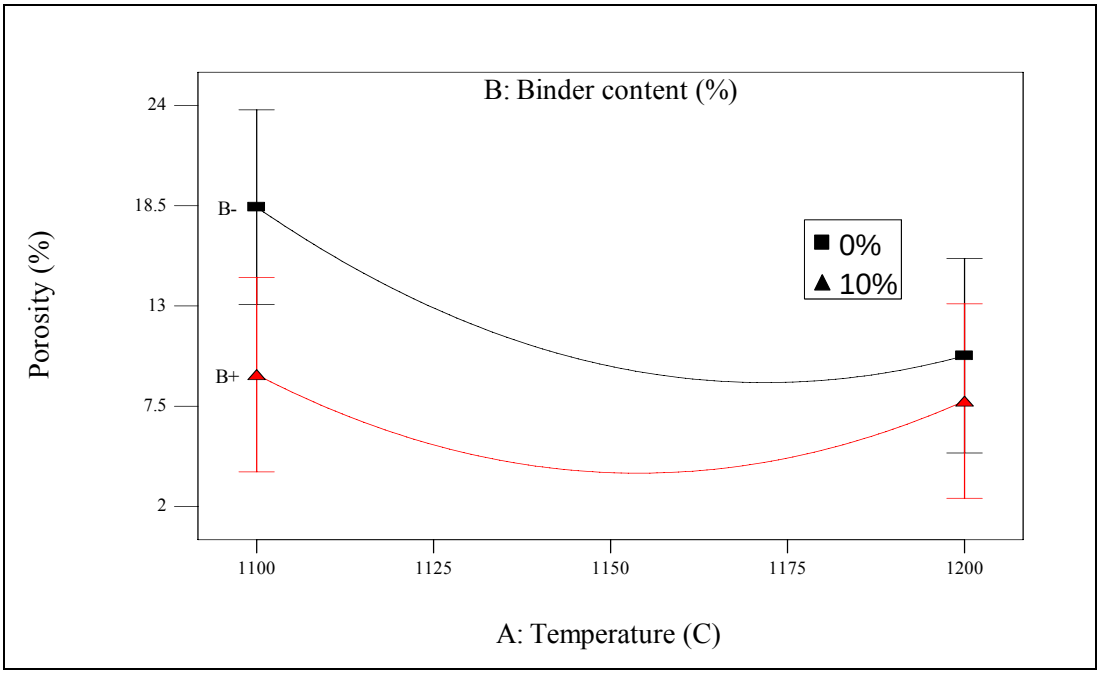

Figure 5.92. Interaction effect between A and B on the specific gravity of glass powder aggregates

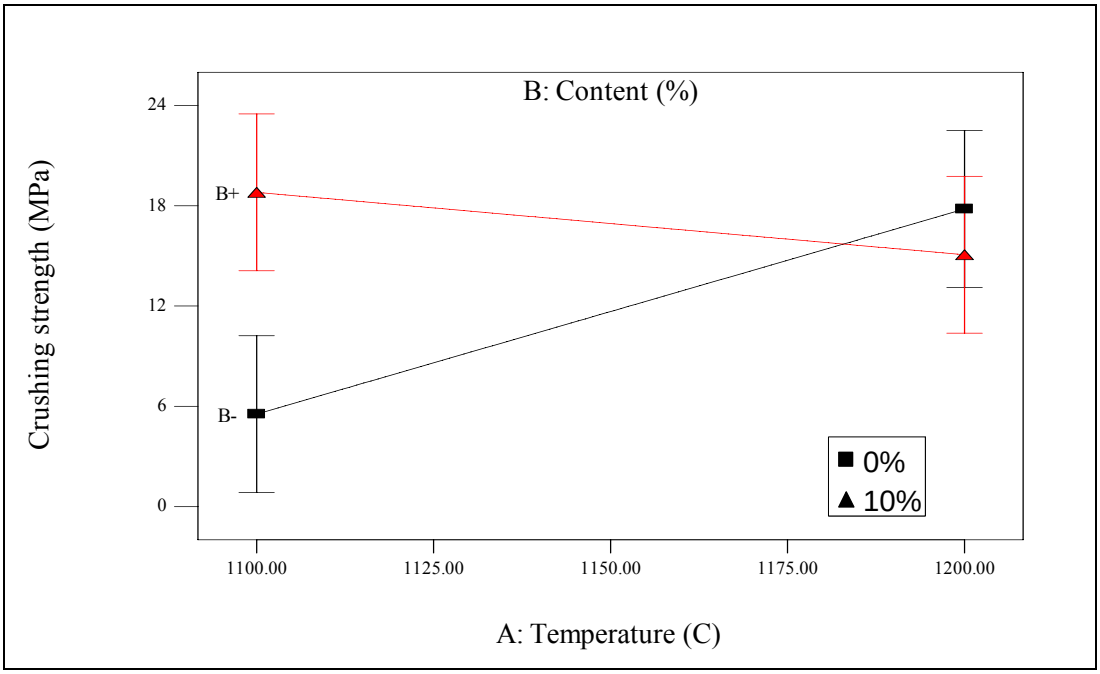

Figure 5.93. Interaction effect between A and B on the crushing strength of bentonite aggregates

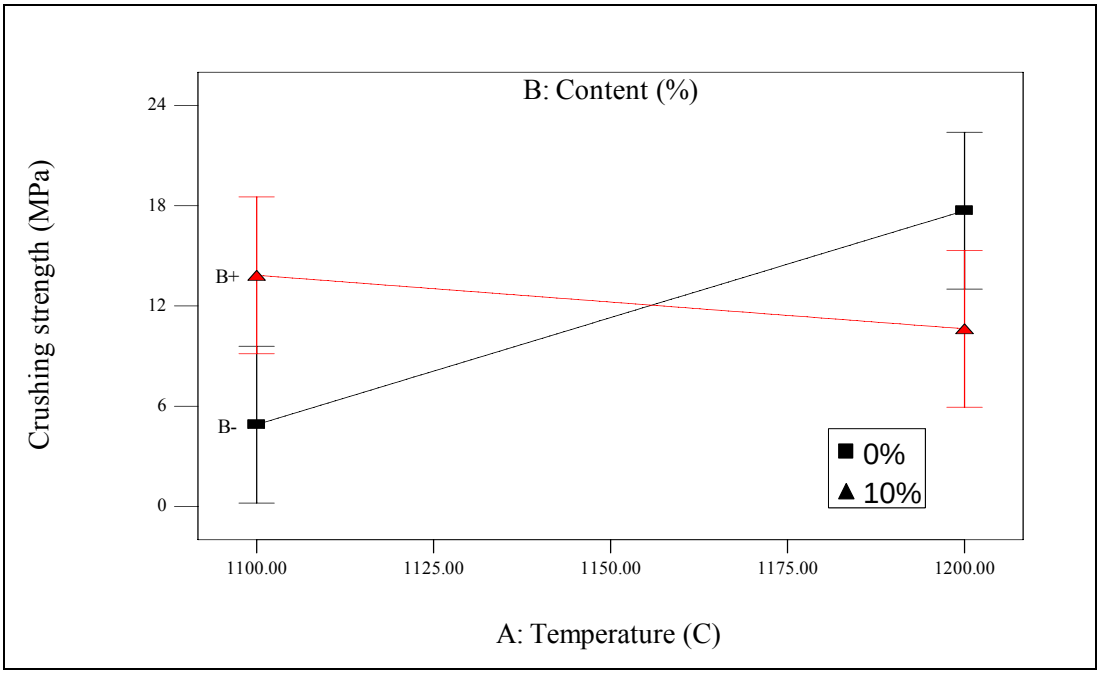

Figure 5.94. Interaction effect between A and B on the crushing strength of glass powder aggregates

The optimization module in design-expert searches for a combination of factor levels that simultaneously satisfy the requirements placed (optimization criteria) on each of the responses and process factors (multiple response optimization). Numerical and graphical optimization methods were used by choosing the desired goals for each factor and response. The optimization process involved combining the goals into an overall desirability function. The numerical optimization finds a point or more that maximize this function. While, in the graphical optimization with multiple responses you need to define regions where requirements simultaneously meet the proposed criteria. The graphical optimization results allow visual inspection to choose the optimum sintering parameters.

Three criteria were introduced in this numerical optimization. Tables 5.24 and 5.25 illustrate the goal, lower and upper limits as well as the importance for each response and factor in the first and second and third criteria, respectively. The first criterion is to reach an aggregate type with low specific gravity and high strength and to minimize the specific gravity and maximize the strength. While in the second criterion, the goal was to reach an aggregate with also low water absorption and to minimize the specific gravity and water absorption and maximize strength. In the third criterion, in addition to second criterion, the importance of strength is increased.

The optimization results demonstrated that, whatever the optimization criteria, 10B1200 and 10G1200 aggregates have the highest desirabilities among all aggregates that would lead to minimum specific gravity and water absorption and maximum strength, as also obtained previously by D-optimal design (Tables 5.26 and 5.28). The 3D view of desirability for bentonite and glass powder based on the first criterion are illustrated in Figures 5.95 and 5.96. It is obvious that the graphical optimization allows visual selection of the optimum aggregate properties according to certain criterion. If the water absorption is taken into account, the desirability values increase for both aggregate types. The desirability decreased with decrease in temperature and binder content as can be seen in Tables 5.26-5.28 and Figures 5.95 and 5.96.

Table 5.24. Optimization criteria used in this study

Name	Limits		First importance	Second importance	First goal	Second goal
	Lower	Upper				
Temperature	1100	1200	3	3	is in range	is in range
Content	0	10	3	3	is in range	is in range
Type	gp	bn	3	3	is in range	is in range
Specific gravity(OD)	1,51	1,93	5	5	minimize	minimize
Specific gravity(SSD)	1,57	2,02	5	5	minimize	minimize
Apparent specific gravity	1,58	2,29	5	5	minimize	minimize
Water absorption	0,7	18,4	none	3	none	minimize
Crushing strength	5.1	23.1	3	3	maximize	maximize

As a result, two different sintered aggregates were selected in order to use in concrete production due to their low density and water absorption and high crushing strength proposed by the Design Expert software. Also, initial trial mixes were performed with the other sintered aggregates to determine concrete densities with a specified constituent contents in Table 5.38, however, it was not possible to obtain a concrete with the aggregates other than the selected ones having high cement content and low water-cement ratio with a density below 2000 kg/m^3. 7.5BG aggregates were not analyzed in the

software because sintering of this type of aggregate at 1200 ^{o}C led to sticking of pellets in the furnace probably due to its high binder content.

Table 5.25. The third criterion of numerical optimization

Name	Limits		Third importance	Third goal
	Lower	Upper		
Temperature	1100	1200	3	is in range
Content	0	10	3	is in range
Type	gp	bn	3	is in range
Specific gravity(OD)	1,51	1,93	5	minimize
Specific gravity(SSD)	1,57	2,02	5	minimize
Apparent specific gravity	1,58	2,29	5	minimize
Water absorption	0,7	18,4	3	minimize
Crushing strength	5.1	23.1	4	maximize

Table 5.26. Optimal solution as obtained by design-expert based on the first criterion

Number	Temperature	Content	Type	Sg(OD)	Sg(SSD)	Apparent Sg	Crushing Strength	Desirability
1	1200,00	10,00	bn	1,56	1,56	1,55	15,07	0,877823
2	1197,62	10,00	bn	1,58	1,58	1,58	15,16	0,861189
3	1200,00	10,00	gp	1,56	1,56	1,56	10,63	0,794503
4	1100,00	2,24	bn	1,61	1,83	2,07	8,51	0,397592
5	1100,00	1,45	bn	1,57	1,81	2,08	7,46	0,393478
6	1100,00	2,42	gp	1,63	1,87	2,14	7,06	0,301845
7	1100,00	2,28	gp	1,62	1,87	2,14	6,94	0,301729
8	1100,00	1,75	gp	1,60	1,85	2,14	6,46	0,298776

Table 5.27. Optimal solution as obtained by design-expert based on the second criterion

Number	Temperature	Content	Type	Sg(OD)	Sg(SSD)	Apparent Sg	Water Absor.	Crushing Strength	Desirability
1	1200	10,00	bn	1,56	1,56	1,55	0,57	15,07	0,894318
2	1200	10,00	gp	1,56	1,56	1,56	1,18	10,63	0,817796
3	1100	4,21	bn	1,69	1,87	2,07	10,76	11,12	0,390621
4	1100	4,11	gp	1,69	1,90	2,14	12,37	8,57	0,298021
5	1100	4,07	gp	1,69	1,90	2,14	12,42	8,53	0,298016
6	1100	4,49	gp	1,70	1,91	2,14	11,90	8,91	0,297597

Table 5.28. Optimal solution as obtained by design-expert based on the third criterion

Number	Temperature	Content	Type	Sg(OD)	Sg(SSD)	Apparent Sg	Water Absor.	Crushing Strength	Desirability
1	1200,00	10,00	bn	1,56	1,56	1,55	0,57	15,07	0,875039
2	1200,00	9,81	bn	1,56	1,56	1,56	0,46	15,12	0,871411
3	1200,00	9,96	gp	1,56	1,57	1,56	1,16	10,66	0,782227
4	1200,00	9,91	gp	1,56	1,57	1,56	1,12	10,70	0,782222
5	1199,29	10,00	gp	1,56	1,57	1,56	1,19	10,66	0,779342
6	1192,90	10,00	gp	1,62	1,63	1,63	1,22	10,86	0,721101
7	1100,00	4,91	bn	1,71	1,88	2,07	9,85	12,05	0,38919
8	1100,00	5,00	bn	1,71	1,88	2,06	9,74	12,17	0,389175
9	1100,00	5,43	bn	1,73	1,89	2,06	9,23	12,73	0,388617
10	1100,00	4,25	bn	1,69	1,87	2,07	10,70	11,17	0,388021
11	1100,00	4,69	gp	1,71	1,91	2,14	11,66	9,09	0,293136
12	1100,00	4,62	gp	1,71	1,91	2,14	11,75	9,02	0,293121

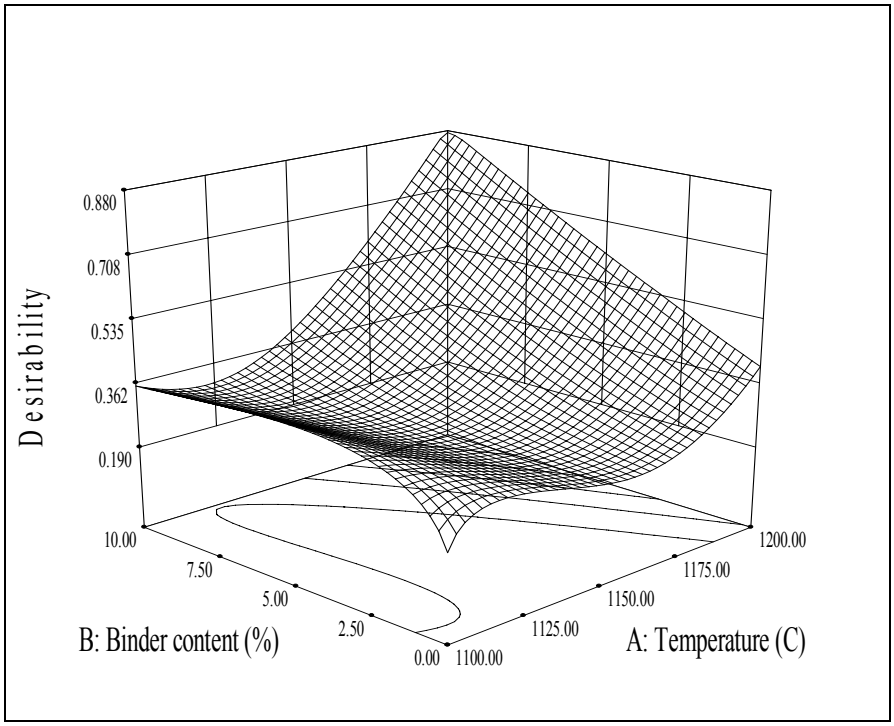

Figure 5.95. Desirability for bentonite based on the first criterion

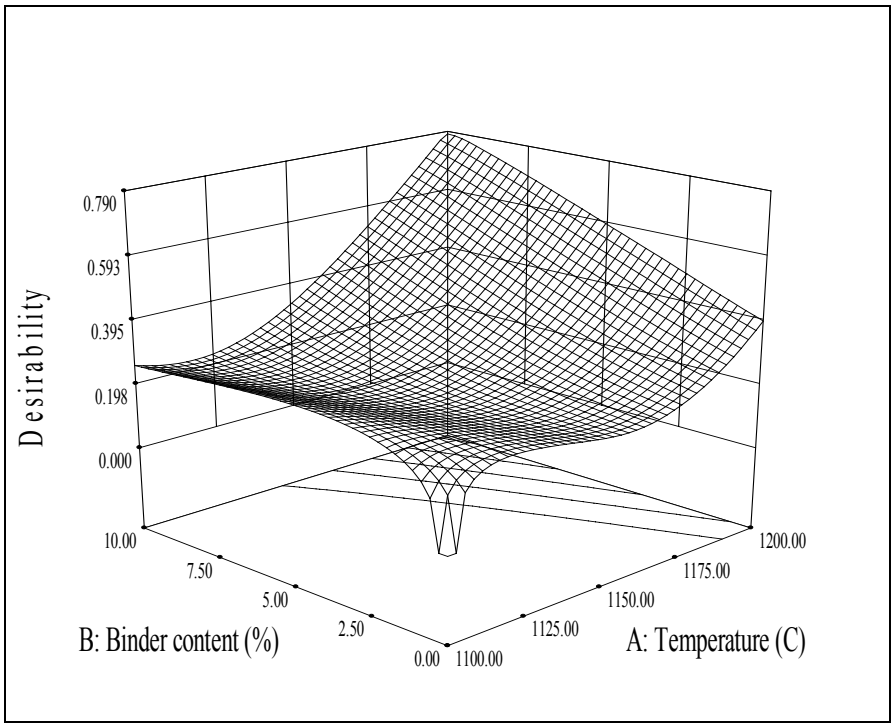

Figure 5.96. Desirability for glass powder based on the first criterion

Lightweight porous aggregates, with adequate strengths, with densities less than 1.60 (in this case) can be made for use in high-strength lightweight concrete according to both trial mixes and optimization results obtained from Design Expert software. This suggests that the low density of these aggregates is beneficial to produce lightweight high strength concrete. Aggregates with relatively high densities, that are impermeable to water ingress, with high strengths, can be made for use as replacement aggregates in conventional (normal weight) concrete.

5.3. Results of Concrete Tests

5.3.1. Slump, Air Content and Density of Concrete Specimens

As can be seen in Table 5.38, the slump and air content values for all concrete types were 16±1 cm and 4±0,3 %, respectively. It is clear that in order to obtain similar slump and air content value for lightweight concretes as compared to normal weight concrete, a lower amount of superplasticizer and air entraining agent was needed (Table 4.9). This could be due to the spherical particle shape of lightweight aggregates compared to the angular particles of crushed stone, resulting in decrease of the water demand of the fresh concrete. Also, in a study [43], it is reported that when lightweight aggregate were used to replace natural sand and basalt, respectively, the water demand of the concrete decreased. This was attributable to the similar result discussed and to the spherical/round particle shape having a “ball-bearing effect”. In order to reach target slump and air content, using less amount of chemical admixtures in lightweight concretes than in normal weight concrete contributes to reduction in production cost. Also, it is stated that air entrainment in lightweight concrete, as in normal weight concrete, improves durability [16]. The recommended ranges of total air contents for lightweight concrete are given as 4-8 % for 19 mm maximum size of aggregate which are consistent with this study. Moreover in concretes made with some lightweight aggregates, it is a particularly effective means of improving workability of otherwise harsh mixtures. The mixing water requirement is then lowered while maintaining the same slump, thereby reducing bleeding and segregation. However, in a study [118], it is demonstrated that the lighter the mix, the less was the slump values. The reason for this was that the work done by gravity was lower in the case

of lighter aggregate. Due to lower aggregate density, structural low-density concrete did not slump as much as normal density concrete with the same workability.

The concretes were workable and cohesive and segregation was not observed. It can be seen that when natural coarse aggregate was replaced with lightweight ones, there was a significant reduction in the density of fresh and hardened concrete (Table 5.29). All of the lightweight concretes had a fresh and oven-dry density lower than 2000 kg/m^3. Although LWCC had a greater fresh density than the other lightweight concretes, its oven dry density was lower than the others because the cold-bonded aggregates had much higher water absorption due to their high volume of open pores. The 28-day density in oven dry condition varied from 1860 to 1943 kg/m^3 among lightweight concretes. A reduction in the self-weight in oven dry condition between 19 % and 25 % was obtained with the replacement of normal aggregates with aggregate with 10 % glass powder and cold bonded fly ash aggregate, respectively. In the case of fresh density and density in SSD condition, the maximum reductions in the selfweight were 21.5 % and 20.6 %, respectively, with concrete made from aggregates with 10 % bentonite. This suggested that the low densities of both cold bonded and sintered fly ash aggregates was beneficial to produce lightweight concrete. In this study, the 28-day od density in the range of 1860-1943 kg/m^3 was achieved. As expected, 56-day density (OD) values were relatively higher than the 28-day density (OD) values owing to the formation of hydration products in progressive aspect. The density classes of lightweight concretes based on oven-dry density according to BS EN 12390–7 is given in Table 5.30. Lightweight concrete density class LC 2.0 is achieved with the high strength values. Much lighter concretes could be obtained by partial or total replacement of fine aggregate as well as full replacement of coarse aggregate by using combined fine and coarse lightweight aggregate following the grading requirement suggested by ASTM C 330. In this study, only the normalweight coarse aggregates were replaced fully with the lightweight coarse aggregates. However, it is obvious that replacement of fine aggregates would further reduce the compressive strength of concretes.

Table 5.29. The properties of the fresh and hardened concretes

Concretes	Slump, (cm)	Fresh Density, (kg/m^3)	Air content, (%)	28-day density (SSD), (kg/m^3)	28-day density (OD), (kg/m^3)	56-day density (OD), (kg/m^3)	Calculated Density (OD), (kg/m^3)	Calculated Equilibrium Density (OD), (kg/m^3)
LWCC	15	1991	3,9	2025	1860	1868	1826	1876
LWBC	15,5	1960	4,3	1979	1915	1922	1919	1969
LWGC	16,5	1975	4,1	1997	1943	1963	1924	1974
NWC	17	2381	3,8	2387	2316	2323	2327	2377

Table 5.30. Lightweight concrete density classes

Density class	Range of oven-dry densities, kg/m^3
LC 1.0	> 800 and < 1000
LC 1.2	> 1000 and < 1200
LC 1.4	> 1200 and < 1400
LC 1.6	> 1400 and < 1600
LC 1.8	> 1600 and < 1800
LC 2.0	> 1800 and < 2000

5.3.2. Compressive Strength and Modulus of Elasticity

The values of compressive strength and modulus of elasticity of concretes are shown in Tables 5.32 and 5.35 and Figures 5.98 and 5.102, respectively. As it was expected, the lightweight aggregate concretes had lower compressive strength and modulus of elasticity values than the normal weight concrete due to the higher porosity and lower strength of the lightweight aggregates included in these concretes. LWCC, on the other hand, had lower compressive strength and modulus of elasticity compared to LWBC and LWGC which had comparable strength and modulus values. Lower density and crushing strength of cold bonded fly ash aggregates are most probably responsible for this. In addition, cold bonded aggregates stored a high amount of water due to presaturation process before mixing. Their uniform distribution in the cement paste and the continous transport of water from the

aggregate to its environment converts each grain of aggregate to a water supply for the concrete surrounding it [37, 119]. The water transport in concrete is depending on the microstructure of the concrete and on the existent humidity gradient. As soon as hardening of concrete occurs, in the cement paste a system of pores develops. Concrete with silica fume shows a refined pore structure with smaller radii than in the normal concrete. The radii of these pores are smaller than in the cold bonded aggregates, so that the requirement for water transport is the existence of a humidity gradient. The capillary forces of the cement paste are high enough to absorp water from the aggregate grain. This transport stops when the relative humidity in the cold-bonded aggregate and in the hardened cement paste are in equilibrium. As explained above, this water transport from cold bonded aggregate to the cement paste could increase the water-cement ratio of concrete resulting in lower strength. The replacement of the normal aggregate in high strength concrete with the lightweight aggregate resulted in a 13 %, 18 % and 49 % reduction in the 28-day compressive strength for LWGC, LWBC and LWCC, respectively. This reduction ratios decreased in 56-day strength as 9 %, 11% and 48 %, respectively. The highest strength gain from 28 days to 56 days (11.2 %) of LWBC could be attributed to the higher pozzolanic activity of 10B1200 aggregates, while NWC showed the lowest strength gain (4.9 %). However, considering the 28-day strengths of LWBC and LWGC, although 10B1200 aggregate had higher crushing strength, the concrete prepared by 10G1200 aggregate exhibited higher compressive strength. Wasserman and Bentur [23] also noted that higher strength aggregate does not necessarily lead to higher, or proportionally higher strength concrete. Therefore there is reason to suggest that the mechanical properties of lightweight aggregate concrete can not be predicted accurately only on the basis of the strength of the aggregate and the effective w/c ratio (strength) of the paste matrix. In their study, they revealed that at early age lower strength was obtained with aggregates of smaller absorption and the closure of the gap in strength at later age between the concrete from untreated aggregate and the heat treated aggregates might be attributed to the higher pozzolanic activity of the latter. However, in our study, water absorptions of aggregates were same for sintered aggregates used in concrete. Also, the closure of the gap in strength was observed between LWBC and LWGC at 56 days. Nevertheless, as can be seen in Table 5.38, this relatively higher compressive strength of LWGC as compared to LWBC attributed to the difference in density between these two concretes having similar air content, 4.3 % for LWBC and 4.1 % for LWGC. The 28-day compressive strength and the

dry concrete density of lightweight concretes varied from 42.3 to 55.8 MPa and from 1860 to 1943 kg/m^3, respectively. LWGC was heavier than LWBB. Heavier concrete resulted in stronger concrete. Nemes and Jozsa [120] indicated that the achieved maximum compressive strength depended on the particle density of LWA. This result was also confirmed by Figures 5.99 and 5.100 which exhibit the relationship between the compressive strength and the oven-dry density. However, there is no general relationship between density and strength classes for different types of lightweight aggregates. In this study, regression analysis was performed on the compressive strength and density among the lightweight aggregates using polynomial, power and linear regression models which gave the best fits against other regression models shown in Table 5.31.

The linear model showed the linearity between the compressive strength and density. The compressive strength was directly proportional to the OD density of hardened concrete. The positive sign of the equations showed that the compressive strength increased with increasing density, where this result was not valid in the case of fresh density and density in ssd condition for LWC in 28 days. Large R values of 0.96 for polynomial, 0.94 for power and 0.94 for linear model showed that the regression was established under good fit, which means that there was no remarkable variation in the compressive strength and density of concrete results. However, this regression analysis did not include normalweight concrete test results (Figures 5.99 and 5.100). The reason is the different failure mechanisms of ligtweight and normalweight concretes. The influence of different lightweight aggregates on concrete strength is greater than that of common concrete [121]. The strength of aggregate of common concrete is 1.5–2.0 times higher than the strength of concrete by itself, while the strength of lightweight aggregate is far lower than that of the concrete, so they have different destructive forms if compressed. When the values of normalweight concrete were imported, the R values decreased. Also, separately 28-day values showed larger R values than both 56-day and 28 and 56-day values. 56-day values with the smallest R values indicated the worst fit among others. In addition, relationship between compressive strength and density in OD condition exhibited larger R values than both in fresh density and density in SSD condition. Strength of lightweight concrete was closely associated with the density. An increase in compressive strength was observed with the increase in oven dry density. Lo et al. [122] also demonstrated that the compressive strength increased with increasing concrete density. The slight scattering of

strength results indicated a minor variation in the quality of the lightweight aggregate. The particle strength and stiffness of a lightweight aggregate depends on pore-size distribution, shape, and the total volume of pores in the individual particles; large, irregularly shaped cavities will weaken the aggregate particles leading to weaker strength in the LWAC. Indeed, lightweight aggregate concrete offers considerable weight advantages over the other form of concrete for both structural and non-structural applications. It was observed that lightweight concrete showed a more brittle behavior than normalweight aggregate concrete under compression load. Table 5.97 shows the view of concrete specimen after compression test. As known, high strength concrete acts more brittle than normal strength concrete. In addition to this fact, when the high strength concrete was also lightweight, this markedly observed brittleness could be clearly observed in high strength lightweight concretes. The relative brittleness of lightweight concrete is usually explained by the weakness of lightweight aggregate particles which causes a limited crack arresting capacity [42]. In other words, subsequent failure in lightweight concrete is rapid because the aggregates do not act as crack arrestors as in normal weight concrete [39]. The sudden failure observed in high-strength concrete is also attributed to the reduced ability to redistribute the stresses in the matrix that has much fewer microcracks.

Figure 5.97. The view of concrete specimen after compression test

Table 5.31. Relationship between compressive strength and density at specific situations

Equations	R value	Sub data
$\sigma = -0{,}0014\gamma^2 + 5{,}3909\gamma - 5257{,}1$ (Poly)	0,96	LWC in 28 and 56 days
$\sigma = -0{,}0015\ \gamma^{2} + 5{,}7294\ \gamma - 5550{,}3$	1	LWC in 28 days
$\sigma = -0{,}0027\ \gamma^{2} + 10{,}408\ \gamma - 10069$	1	LWC in 56 days
$\sigma = -0{,}0003\ \gamma^{2} + 1{,}429\ \gamma - 1468{,}3$	0,99	LWC and NWC in 28 days
$\sigma = -0{,}0004\ \gamma^{2} + 1{,}5705\ \gamma - 1617$	0,96	LWC and NWC in 56 days
$\sigma = -0{,}0004\ \gamma^{2} + 1{,}5377\ \gamma - 1582{,}3$	0,96	LWC and NWC in 28 and 56 days
$\sigma = -0{,}0322\ \gamma^{2} + 126{,}72\ \gamma - 124754$	1	LWC in 28 days (Fresh density)
$\sigma = 0{,}001\ \gamma^{2} - 4{,}1726\ \gamma + 4527{,}7$	0,90	LWC and NWC in 28 days (Fresh)
$\sigma = -0{,}0133\ \gamma^{2} + 52{,}846\ \gamma - 52600$	1	LWC in 28 days (SSD)
$\sigma = 0{,}0008\ \gamma^{2} - 3{,}313\ \gamma + 3626{,}1$	0,92	LWC and NWC in 28 days (SSD)
$\sigma = 1E\text{-}20\ \gamma^{6{,}6123}$ (Power)	0,94	LWC in 28 and 56 days
$\sigma = 1E\text{-}20\ \gamma^{6{,}5912}$	0,98	LWC in 28 days
$\sigma = 8E\text{-}20\ \gamma^{6{,}34}$	0,92	LWC in 56 days
$\sigma = 0{,}002\ \gamma^{1{,}3416}$	0,80	LWC and NWC in 28 days
$\sigma = 0{,}0045\ \gamma^{1{,}2432}$	0,71	LWC and NWC in 56 days
$\sigma = 0{,}0027\ \gamma^{1{,}3047}$	0,74	LWC and NWC in 28 and 56 days
$\sigma = 4E+51\ \gamma^{-15{,}157}$	0,80	LWC in 28 days (Fresh density)
$\sigma = 0{,}0092\ \gamma^{1{,}1339}$	0,64	LWC and NWC in 28 days (Fresh)
$\sigma = 1E+38\ \gamma^{-11{,}038}$	0,85	LWC in 28 days (SSD)
$\sigma = 0{,}0087\ \gamma^{1{,}14}$	0,61	LWC and NWC in 28 days (SSD)
$\sigma = 0{,}1752\ \gamma - 282{,}34$ (Linear)	0,94	LWC in 28 and 56 days
$\sigma = 0{,}1683\ \gamma - 270{,}32$	0,98	LWC in 28 days
$\sigma = 0{,}172\ \gamma - 274{,}94$	0,92	LWC in 56 days
$\sigma = 0{,}0339\ \gamma - 14{,}505$	0,82	LWC and NWC in 28 days
$\sigma = 0{,}0327\ \gamma - 8{,}3597$	0,73	LWC and NWC in 56 days
$\sigma = 0{,}0336\ \gamma - 12{,}038$	0,76	LWC and NWC in 28 and 56 days
$\sigma = -0{,}3666\ \gamma + 774{,}78$	0,79	LWC in 28 days (Fresh density)
$\sigma = 0{,}0289\ \gamma - 6{,}4849$	0,69	LWC and NWC in 28 days (Fresh)
$\sigma = -0{,}2642\ \gamma + 579{,}03$	0,85	LWC in 28 days (SSD)
$\sigma = 0{,}0292\ \gamma - 7{,}5468$	0,66	LWC and NWC in 28 days (SSD)

where:

σ = Compressive strength of concrete

γ = Density of concrete

Table 5.32. Results of compressive strength

Concretes	Compressive strength, (MPa)	
	28 day	56 day
LWCC	42,3	44,6
LWBC	53,5	59,5
LWGC	55,8	60,4
NWC	62,9	66,0

Compressive strength classes for lightweight concretes according to BS EN 206-1 is presented in Table 5.33.

Table 5.33. Compressive strength classes for lightweight concretes

Compressive strength class	f_{ck}, cylinder, MPa	f_{ck}, cube, MPa
LC 8/9	8	9
LC 12/13	12	13
LC 16/18	16	18
LC 20/22	20	22
LC 25/28	25	28
LC 30/33	30	33
LC 35/38	35	38
LC 40/44	40	44
LC 45/50	45	50
LC 50/55	50	55
LC55/60	55	60
LC 60/66	60	66
LC 70/77	70	77
LC 80/88	80	88

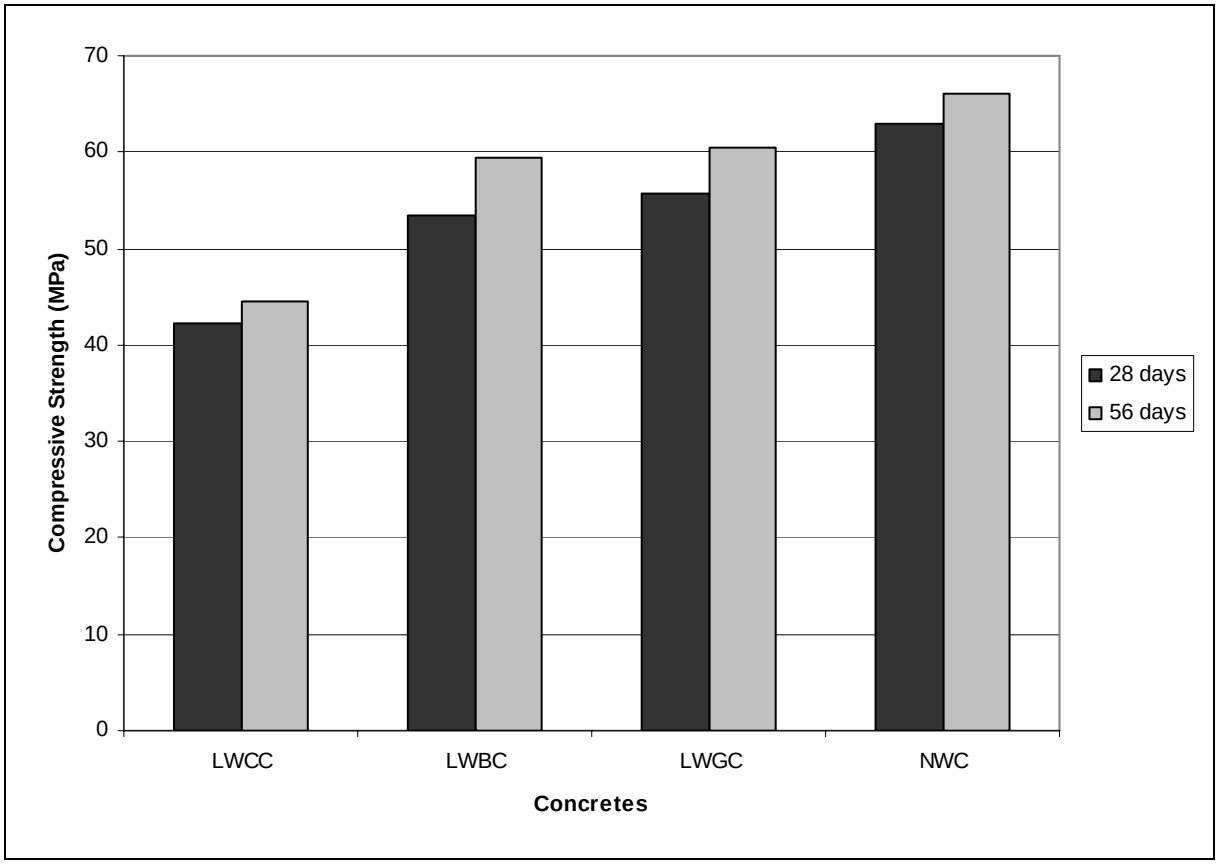

Figure 5.98.The compressive strength values of 28-day and 56-day concrete specimens

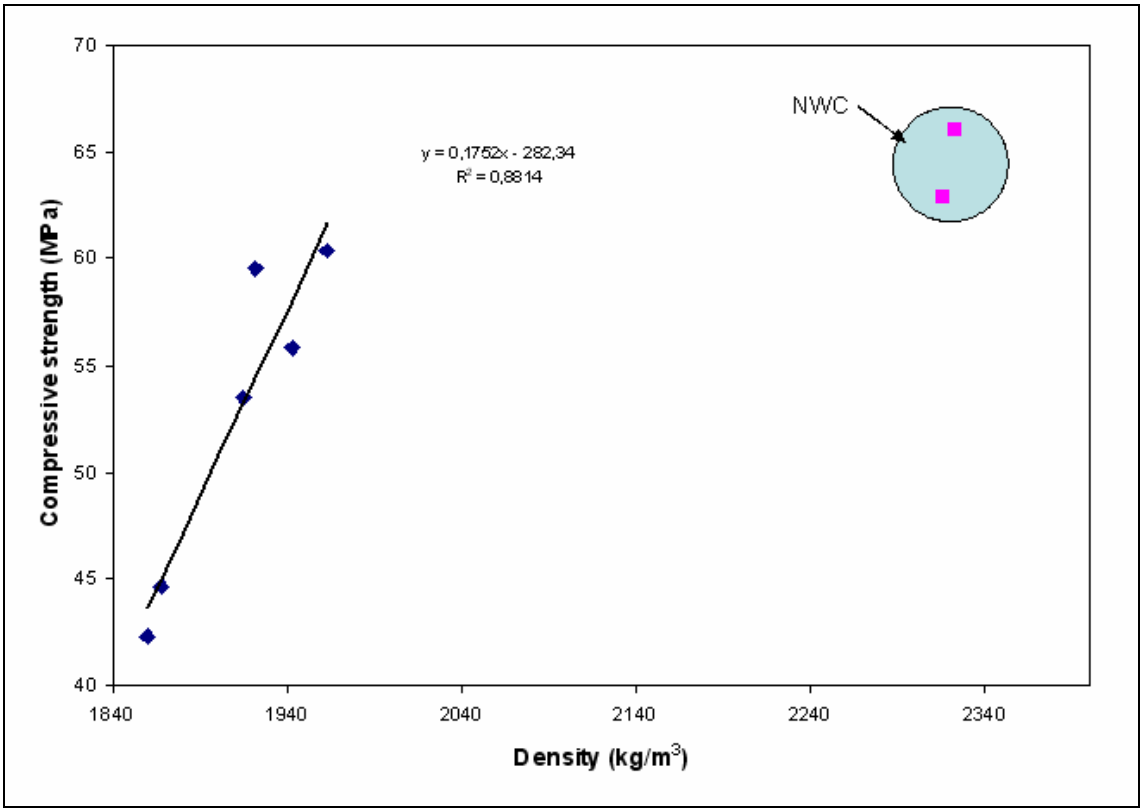

Figure 5.99. Compressive strength vs density (linear model)

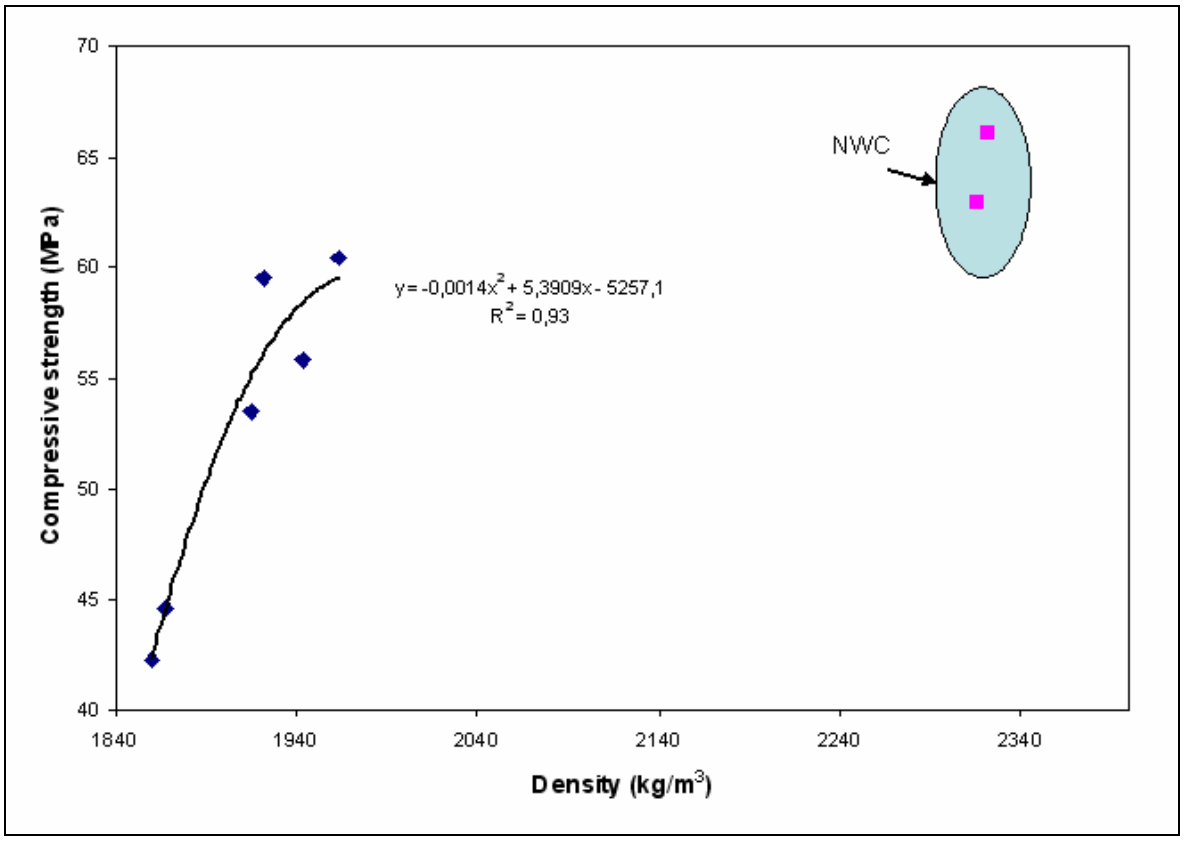

Figure 5.100. Compressive strength vs density (polynomial model)

Analysis of variance is a useful technique for analyzing experimental data. When several sources of variation are acting simultaneously on a set of observations, the variance of the observations is the sum of the variances of the independent sources [47]. Thus, a software TableCurve 3D V4.0 was used for regression and graphical analysis of the data obtained. TableCurve 3D combines a powerful surface fitter with the ability to find the ideal equation to describe three dimensional empirical data. In TableCurve 3D, the dependent variable is Z. All equations express Z as a function of the two independent variables X and Y. For all built-in equations, X and Y are interchangeable. In some manner, an individual vector of X, Y, and Z values must be specified in order to define an XYZ data table. The first step in using TableCurve 3D is to set up an XYZ data table. In a parametric model, the main emphasis is upon solving for the parameters that are intimately associated with features within the data. Unlike approximating functions intended only for interpolations and extrapolations, a parametric model is very sensitive to parameter count and to interactions between the parameters. Often a parametric model is used not for describing an underlying theoretical model but rather for characterizing the unique features within a data set. TableCurve 3D gives scientists and engineers the power to find the ideal

model for even the most complex data, including equations that might never have been considered. TableCurve 3D's built-in equation set includes a wide array of linear and nonlinear models for any application. TableCurve 3D also has state-of-the art surface fitting capabilities.

Once XYZ data have been fit, TableCurve 3D automatically sorts and plots the fitted equations by the statistical criteria selected (r^2, DOF adjusted r^2, Fit Standard Error or the F Statistic). A 3D residuals graph as well as parameter output are generated for each fitted equation. Viewing a surface fit from all angles is imperative in determining whether or not a given fit is accurate.

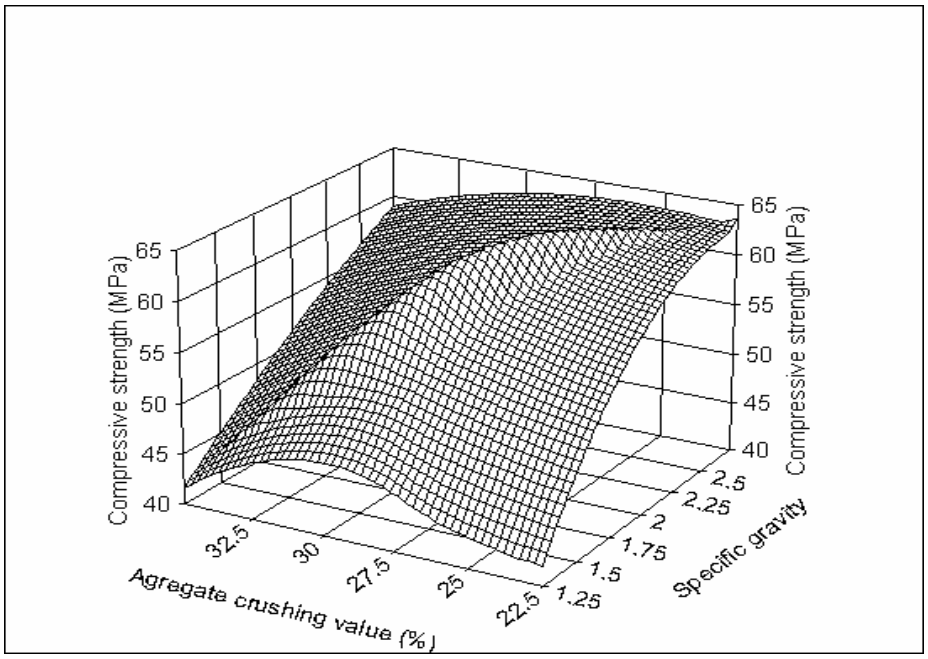

Figure 5.101. 3D view of experimental results of LWC and NWC

There are several equations of compressive strength of lightweight aggregate concrete calculated [121]. In these equations, the parameters affecting the compressive strength of lightweight concrete are effective water–cement ratio of lightweight aggregate concrete, dry apparent specific gravity of lightweight coarse aggregate, actual consumption of lightweight aggregate, actual strength of cement and strength of lightweight aggregate. Also, in another study [118], it is concluded that the concrete strength depends on the strength, stiffness and density of the coarse aggregates. In the current study, effective

water–cement ratio of lightweight aggregate concrete, actual consumption of lightweight aggregate and actual strength of cement were same for all concrete types. However, the remaining parameters are the specific gravity and the strength of aggregates.

From relations between compressive strength of concrete and specific gravity of aggregate and aggregate crushing value, equations could be derived as below:

$$\sigma = -1{,}6392\mu + 101{,}16,\ R = 0{,}95 \tag{5.34}$$

$$\sigma = 11{,}699\delta + 32{,}713,\ R = 0{,}85 \tag{5.35}$$

where:
σ = compressive strength of concrete MPa
δ = aggregate crushing value %
μ= specific gravity

In this study, the modulus of elasticity for LWAC ranged from 22.4 to 28.6 GPa which was comparatively less than that for normal-weight concrete with similar strength as 38.0 and 38.9 GPa for 28 and 56 days, respectively. The modulus of elasticity is affected by the compressive strength of concrete, stiffness and volume of the LWA used, interfacial zone between the aggregates and paste and the elastic properties of the constituent materials [118]. In this sudy, only the aggregate types were different as stated previously. Using the law of mixtures approach, in its simplest models, this law as applied to the case of modulus of elasticity may be expressed as follows:

$$E = E_1V_1 + E_2V_2 \tag{5.36}$$

where E is the modulus of elasticity of the mixture, while E_i and V_i refer to the modulus of elasticity and volume fraction of the mixture constituents, respectively. This law may apply to concrete where cement paste may be considered constituent 1, while the aggregates are constituent 2.

In high-strength concrete, the modulus of elasticity of the hardened cement paste is high and the difference between the modulus of elasticity of the aggregates and the hardened paste becomes small enough to result in higher bond strength and monolithic behaviour [39]. In other words, lightweight aggregate concrete is expected to manifest a clearer monolithic behaviour than normal weight aggregate concrete. This is due to the lower modulus of elasticity of the aggregate, resulting in a smaller difference between its value and that of the hardened cement paste, and to the increased aggregate–paste bond due to the rough and porous surfaces of the lightweight aggregates. LWGC showed slightly lower modulus of elasticity than LWBC, whereas LWGC had slightly higher strength. For almost similar strength values, the E value of the NWC was ~42 % higher than the E value of the LWBC and LWGC. Also, the 28-day E values of LWBC and NWC were 33 and 88 % higher than that of the LWCC. The modulus of elasticity of the aggregate depends not only on the density, but also on the pore structure and the surface texture of the ligtweight aggregate. Therefore, an aggregate with a dense structure and evenly distributed pores will give a higher modulus of elasticity and more concrete stiffness than a more porous aggregate. The three parameters, namely density, total porosity and critical pore diameter of the lightweight aggregates, supported the results of modulus of elasticity. 10G1200 and 10B1200 had close and the highest specific gravity and bulk density values and lowest total porosity and critical pore diameter while CB had the lowest specific gravity and bulk density values and highest total porosity and critical pore diameter (Table 5.34). The smaller critical pore diameter means the finer pore structure. It is clear that sintered aggregates showed its denser structure with its high density and low total porosity and exhibited its evenly distributed finer pore structure with its small critical pore diameter and pore size distribution than cold-bonded aggregates. As compared to normal weight concrete, a much lower modulus of elasticity would be expected for lightweight concrete [122]. The lower E-value of lightweight concrete absorbs energy from impact and cyclic loading, reducing the formation of micro cracking at the cement/aggregate interface. Essentially, a lower E value for lightweight concrete means that it is more flexible because stiffness is defined as the product of modulus of elasticity and moment of inertia, EI [123]. Reduced stiffness can be beneficial at times, and the use of lightweight concrete should be considered in these cases instead of normalweight concrete. In cases requiring improved impact or dynamic response, where differential foundation settlement may occur, and in

certain types or configurations of shell roofs, the property of reduced stiffness may be desirable. The modulus of elasticity increase was very small in 56 days for all concretes.

Table 5.34. Summary of aggregate characteristics used in concrete production

Characteristics	Aggregates			
	Cold-bonded	10B1200	10G1200	Normalweight
Specific gravity based on SSD condition	1,63	1,57	1,60	2,71
Apparent specific gravity	1.89	1.58	1.60	2.71
Specific gravity based on OD condition	1,30	1,56	1,59	2,70
28-hour water absorption (%)	25,5	0,7	0,7	0,8
Total porosity (%)	31,1	8,4	6,2	-
Critical pore diameter (nm)	398.4	28.03	12.49	-
Rodded bulk density (kg/m^3)	842	993	999	1537
Loose bulk density (kg/m^3)	789	933	936	1433
Voids (%) loose	39.2	40.1	41.0	46.8
Voids (%) rodded	35.1	36.2	37.0	43.0
ACV (%)	35	28	30	23
Pellet crushing strength (MPa)	3.7	12.0	9.6	-

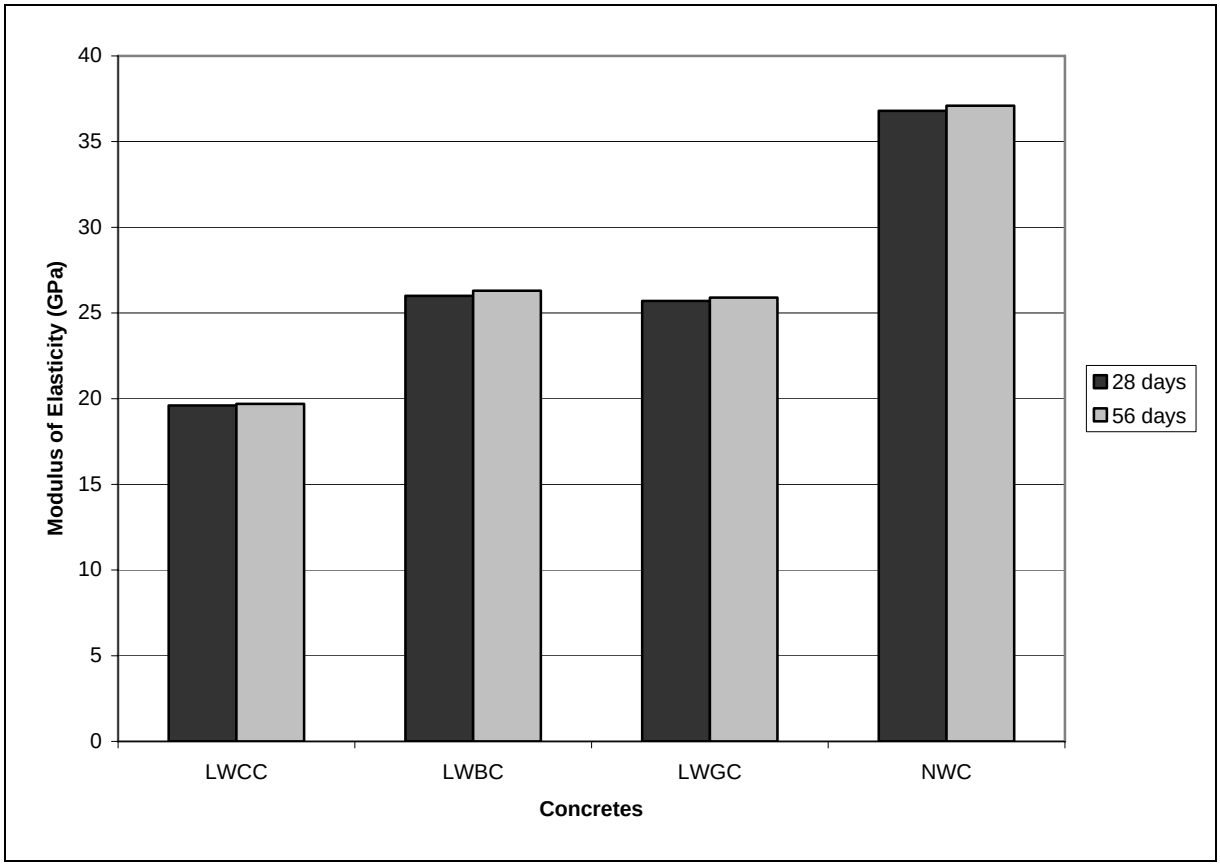

Figure 5.102. The modulus of elasticity values of 28-day and 56-day concrete specimens

The dependency between the modulus of elasticity and the compressive strength was analyzed; the best regression being obtained with an expression of the power type (Figure 5.103).

$$E = 0{,}6258\ \sigma^{0{,}9185}\ ,\ R^2 = 0{,}9114 \text{ for LWC in 28 and 56 days} \quad (5.37)$$

$$E = 0{,}3797\ \sigma^{\ 1{,}0544},\ R^2 = 0{,}9687 \text{ for LWC in 28 days} \quad (5.38)$$

$$E = 0{,}54\ \sigma^{\ 0{,}9473},\ R^2 = 0{,}9917 \text{ for LWC in 56 days} \quad (5.39)$$

$$E = 0{,}0744\ \sigma^{\ 1{,}4779},\ R^2 = 0{,}9056 \text{ for LWC and NWC in 28 days} \quad (5.40)$$

$$E = 0{,}0977\ \sigma^{\ 1{,}3861},\ R^2 = 0{,}8275 \text{ for LWC and NWC in 56 days} \quad (5.41)$$

$$E = 0{,}1155\ \sigma^{\ 1{,}3558},\ R^2 = 0{,}8237, \text{ for LWC and NWC in 28 and 56 days} \quad (5.42)$$

where the modulus of elasticity (E) being expressed in GPa and the compressive strength (σ) in MPa.

Also, regression analysis was performed on the modulus of elasticity and density (OD) among the lightweight aggregates using power regression model which gave the best fits against the other regression models with the following equations:

$$E = 3E\text{-}19\ \gamma^{6,0735},\ R^2 = 0,8091 \text{for LWC in 28 and 56 days} \quad (5.43)$$

$$E = 2E\text{-}21\ \gamma^{6,7082},\ R^2 = 0,87 \text{ for LWC in 28 days} \quad (5.44)$$

$$E = 3E\text{-}18\ \gamma^{5,7779},\ R^2 = 0,7827 \text{ for LWC in 56 days} \quad (5.45)$$

$$E = 2E\text{-}07\ \gamma^{2,4326},\ R^2 = 0,8732 \text{ for LWC and NWC in 28 days} \quad (5.46)$$

$$E = 2E\text{-}07\ \gamma^{2,4691},\ R^2 = 0,8728 \text{ for LWC and NWC in 56 days} \quad (5.47)$$

$$E = 2E\text{-}07\ \gamma^{2,4498},\ R^2 = 0,8729 \text{ for LWC and NWC in 28 and 56 days} \quad (5.48)$$

where:
E = modulus of elasticity in GPa
γ = density in od condition in kg/m^3

By multiplying Equations 5.37 and 5.43 and Equations 5.42 and 5.48, modulus of elasticity was calculated as below:

$$E = 4.33E\text{-}10 * \sigma^{0.459} * \gamma^{3.037} \text{ for LWC} \quad (5.49)$$

$$E = 4.62E\text{-}08 * \sigma^{0.678} * \gamma^{1.2249} \text{ for LWC and NWC} \quad (5.50)$$

where:
E = modulus of elasticity in GPa
σ = compressive strength in MPa

γ = density in OD condition in kg/m^3

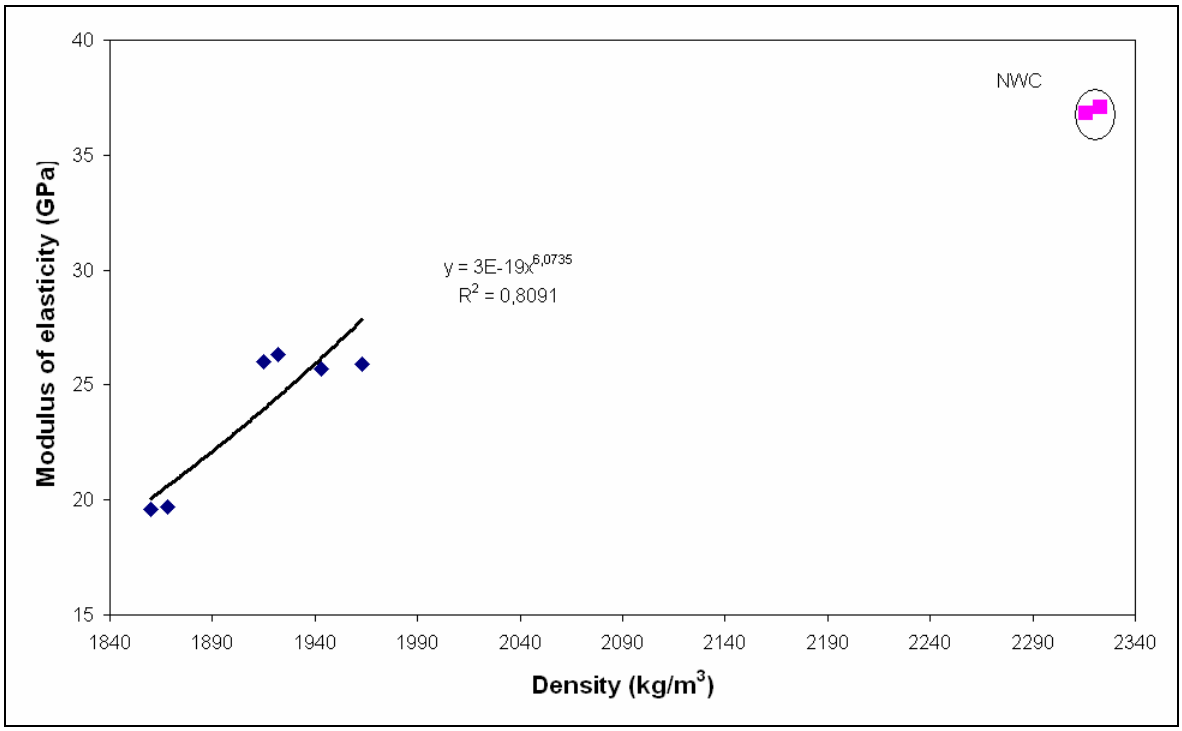

Figure 5.103. Relationship between modulus of elasticity and density

All models given by standards are also for lightweight concretes as specified earlier in Equations 4.30 and 4.31. BS 8110 and ACI 318 suggest that the modulus of elasticity could be estimated from the compressive strength and density of concretes. Table 5.35 illustrates the measured E value with those estimated. Predicted values of modulus of elasticity by ACI 318 which is for concretes having less than 41 MPa compressive strength overestimated the experimental results whereas BS 8110 underestimated the results except for LWCC. Table 5.35 shows the experimental results and estimated modulus of elasticity values by the relevant standards and Equation 5.49 suggested in this study while the relationship between experimental, predicted and calculated modulus of elasticity and compressive strength of lightweight concretes are exhibited in Figure 5.104. However, both models and equation derived in this study gave close estimated values to the experimental results. All calculated values were between the predicted values proposed by two standards. The models given by codes and standards were also reported to overestimate the modulus of elasticity value of high-strength structural lightweight concretes by a study [124]. However, for the concrete reported in a study [37] the calculated E values using code formulae were less than the observed value. In the

calculation of modulus of elasticity, w_c used was the oven dry density instead of air dry density specified in standards.

Table 5.35. Experimental, calculated and predicted results of modulus of elasticity

Concretes	Modulus of Elasticity (GPa)							
	Experimental		ACI 318		BS 8110		Calculated	
	28 day	56 day	28 day	56 day	28 day	56 day	28 day	56 day
LWCC	19,6	19,7	22,4	23,2	20,2	20,8	20,5	21,3
LWBC	26,0	26,3	26,4	27,9	23,2	24,2	25,0	26,5
LWGC	25,7	25,9	27,5	29,1	24,2	25,4	26,6	28,5
NWC	36,8	37,1	38,0	39,1	35,8	36,6	-	-

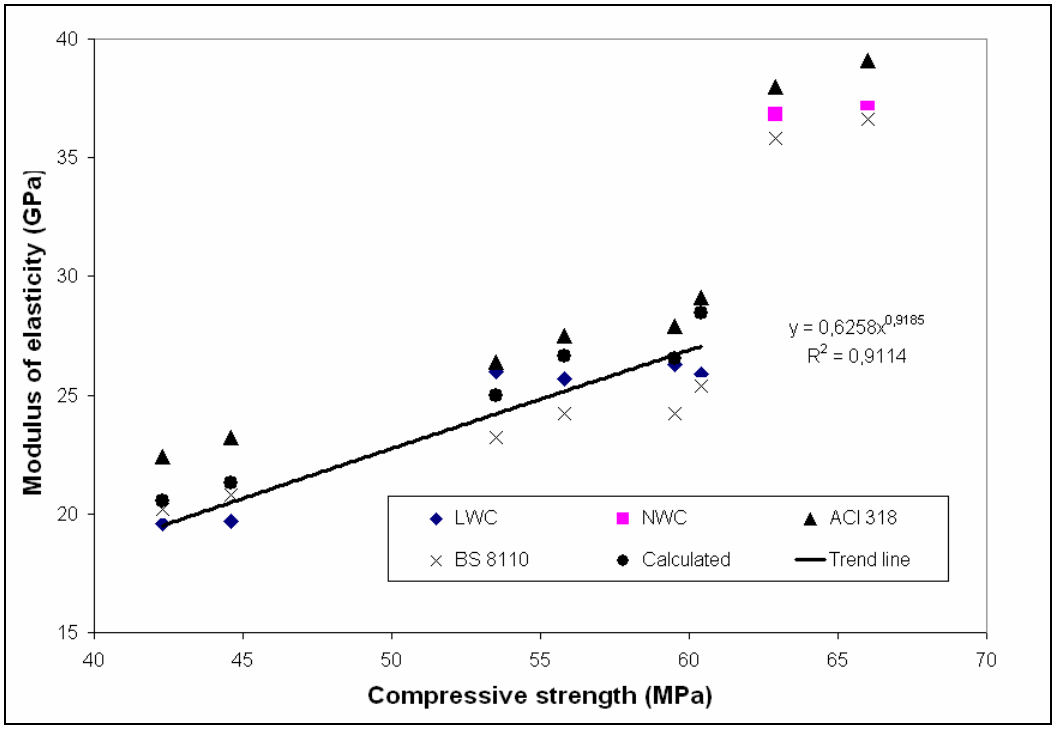

Figure 5.104. Relationship between modulus of elasticity and compressive strength

In analyzing the variations, the first step is to compute the sum of squares (SS) and then the mean squares (MS). The total variation includes two parts: the variation within the columns and the variation between the columns. Each of the variations can be reduced to the mean square when they are divided by the corresponding degree of freedom. The ratio of any two of mean squares provides basic information for the F test of significance.

Statistical method was applied to analyze the experimental data of the compressive strengths, density and elastic moduli of concretes. X represented compressive strength, Y represented density and Z represented modulus of elasticity. The test of multivariate analysis of variance with 95% confidence level (α =0.05) was applied.

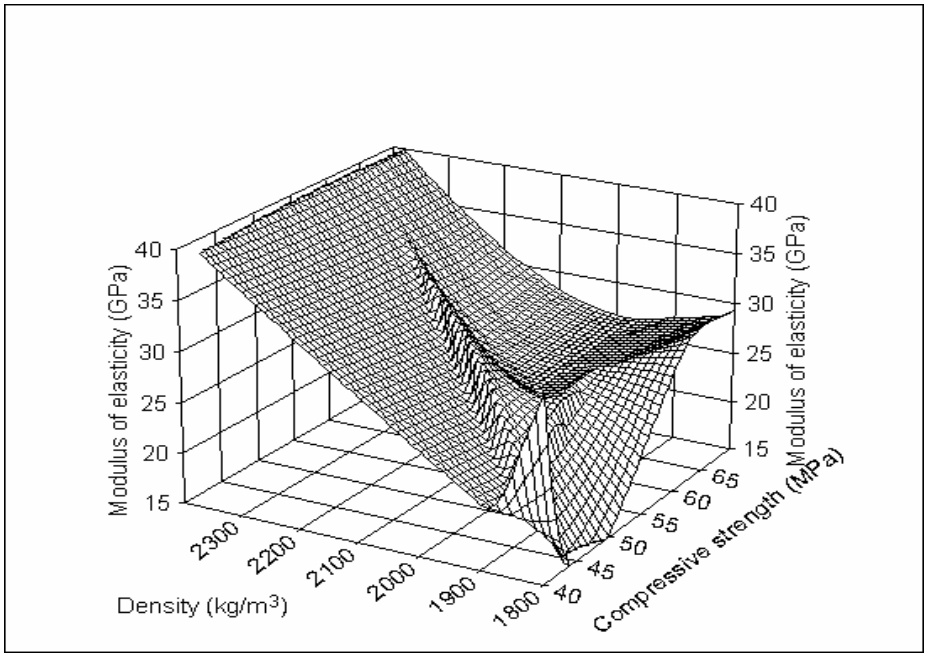

Figure 5.105. 3D view of experimental results of LWC and NWC

The application of response surface methodology yielded the following regression equation which is an empirical relationship between the modulus of elasticity (*Z*) and compressive strength (*X*) and density (*Y*).

$$E = a+b*\sigma+c*\gamma \quad (5.51)$$

The significance of each coefficient was determined by Student's t-test and p-values (Table 5.36). The larger the magnitude of the t-value and the smaller the p-value, the more significant is the corresponding coefficient. This implied that the factor most significant (t-value = 6,96856, p-value < 0.005) for elasticity was the density and the next was the compressive strength.

The results of the response surface fitting in the form of analysis of variables are shown in Table 5.37 and 5.38. The F-test with a very low probability value ($p < 0.0001$) showed a very high significance for the regression model. The value of the determination

coefficient ($R^2 = 0.98$) verifies the suitable fit of the model, thus indicating a discrepancy of 0.02 % for total variation, which is a normally accepted range of experimental error. The value of the adjusted determination coefficient (adjusted $R^2 = 0.96$) is also very high which indicates a high significance for the model. Figure 5.106 illustrated 3D view of the predicted values obtained by the software.

Table 5.36. Coefficients of the model given by software

Parm	Value	Std Error	t-value	P>|t|
a	-36,6289312	4,570959006	-8,01340182	0,00049
b	0,284671999	0,077374661	3,679137257	0,01431
c	0,023802136	0,003415647	6,968557863	0,00094

Table 5.37. ANOVA for response surface fit to the experimental results

Source	Sum of Squares	DF	Mean Square	F value	P>F
Regr	304,02988	2	152,01494	120,477	0,00006
Error	6,3088735	5	1,2617747		
Total	310,33875	7			

Table 5.38. Actual and predicted values by response surface fit for modulus of elasticity

X	Y	Z	Z Predicted	Residual	Residual %
66	2323	37,1	37,5	-0,351783	-0,948
62,9	2316	36,8	36,4	0,3973156	1,080
60,4	1963	25,9	27,3	-1,38885	-5,362
59,5	1922	26,3	26,1	0,243242	0,925
55,8	1943	25,7	25,5	0,1966835	0,765
53,5	1915	26	24,2	1,8178889	6,992
44,6	1868	19,7	20,5	-0,82983	-4,212
42,3	1860	19,6	19,7	-0,084667	-0,432

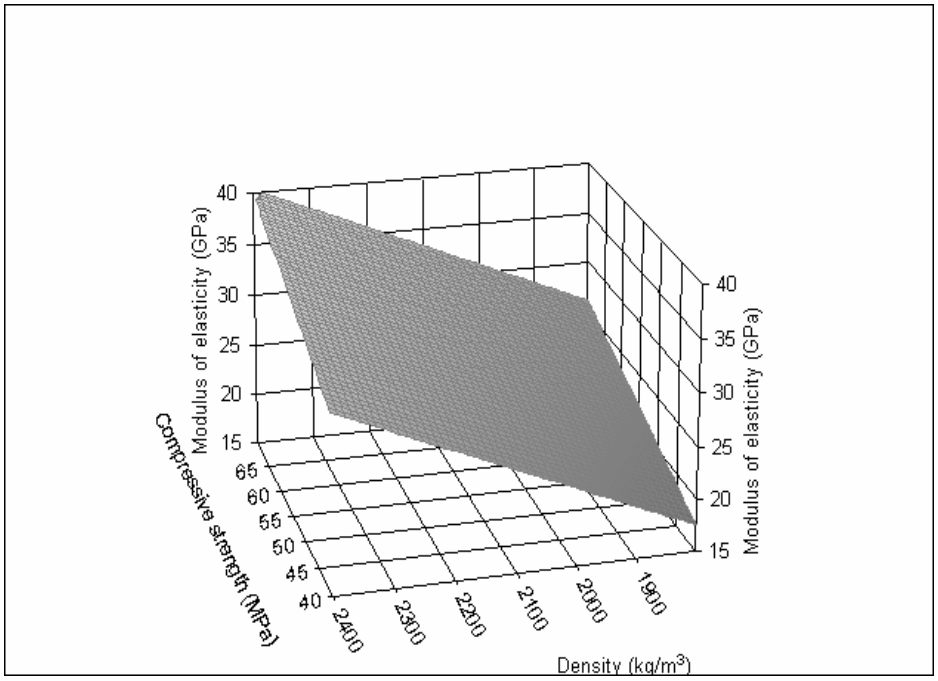

Figure 5.106. 3D view - response surface plot showing the effect of density and compressive strength on modulus of elasticity

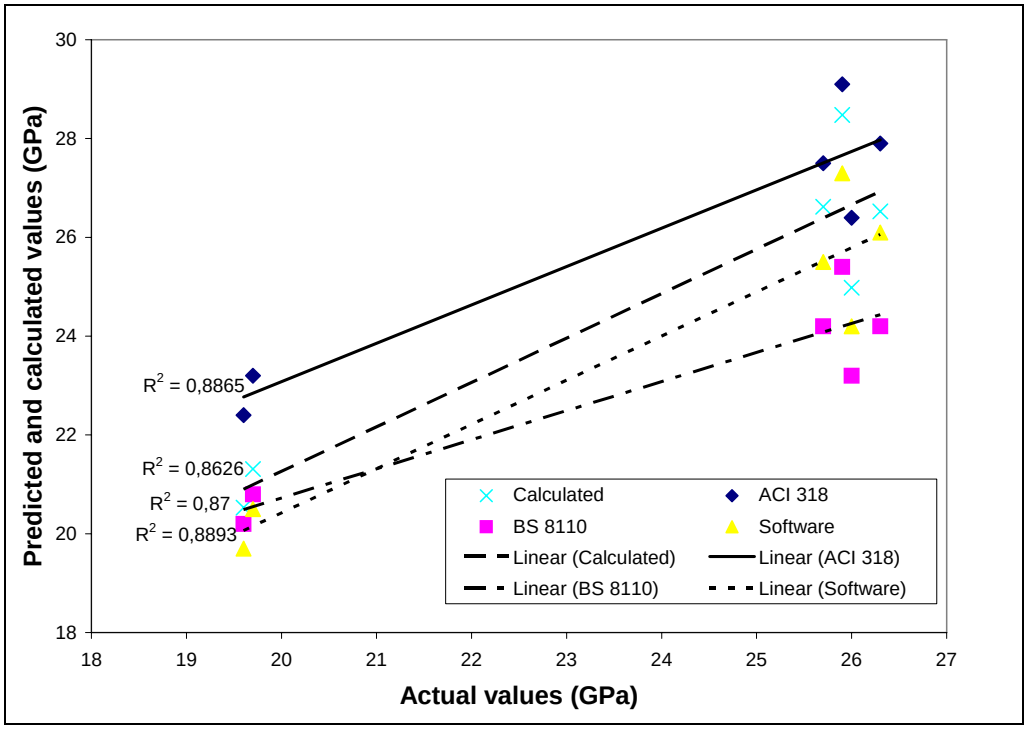

Figure 5.107. Relationships between actual values and predicted and calculated values of modulus of elasticity of lightweight concretes

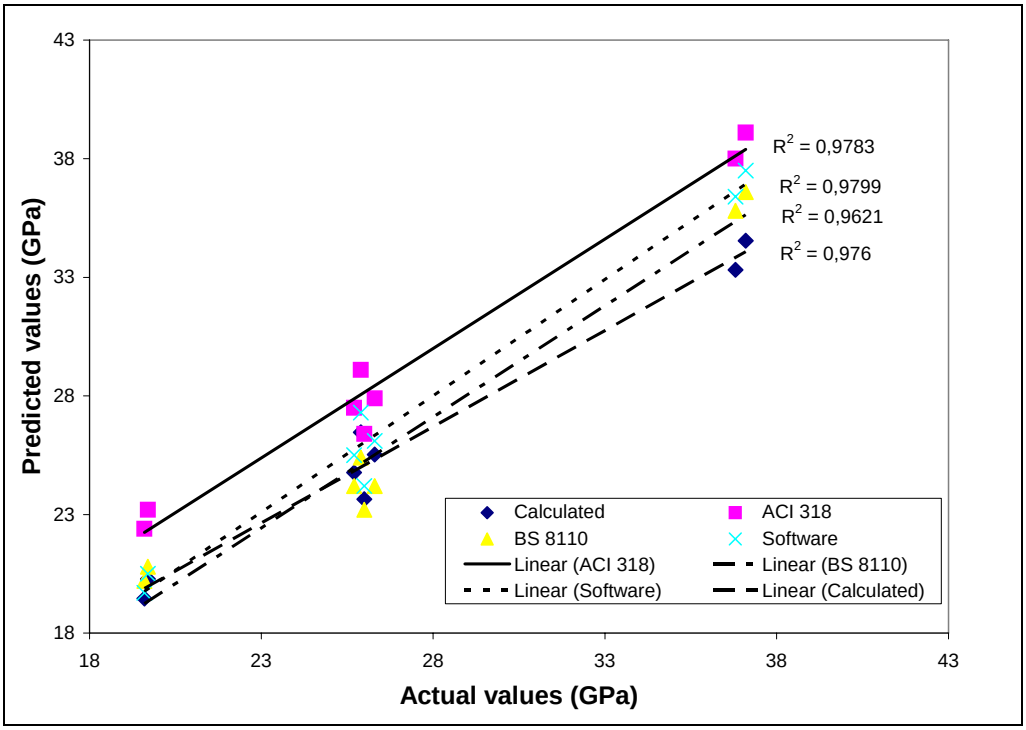

Figure 5.108. Relationships between actual values and predicted and calculated values of modulus of elasticity of lightweight and normalweight concretes

Relationships between actual values and predicted and calculated values of modulus of elasticity are shown in Figure 5.107. The large R^2 values were evidences for the good relationships which proved that there was no remarkable variations between the experimental and estimated values of modulus of elasticity of lightweight aggregates. The R-square values were 0.889, 0.887, 0.870 and 0.863 for predicted values obtained by using software, ACI 318, BS 8110 and equation derived in this study, respectively. All the estimated values were close to each other and showed small variations with the experimental results. The best fit model was proposed by software which possesed the largest R-square value of 0.889. All R^2 values of models were large enough to use in predicting modulus of elasticity of concretes. The determination of R-square values was done for lightweight aggregates. Owing to this fact, the R^2 value of software which analyzed for both lightweight and normalweight concrete, decreased from 0.98 to 0.889 when the normalweight concretes were exported. Also, Figure 5.108 illustrated the relationships between actual values and predicted and calculated values of modulus of elasticity of lightweight and normalweight concretes. Importing the normalweight concrete data into the analysis R^2 values increased as 0.9799, 0.9783, 0.976 and 0.9621 for software, ACI 318, equation in this study and BS 8110, respectively. The best fit model

was obtained again by software with a high R^2 value. All R-square values of models were extremely large enough to apply in estimating the modulus of elasticity of both lightweight and normalweight concretes.

5.3.3. Splitting Tensile Strength

The splitting test is believed to give a close representation of the true tensile strength of concrete [41]. The compressive strength of concrete is commonly considered in structural design, but for some purposes, the tensile strength is of interest for example in the design of highway and airfield slabs, shear strength and resistance to cracking [125]. Previous tests showed that diagonal tensile strengths of beams and slabs correlate closely with the concrete splitting strengths [123]. A minimum tensile-splitting strength of 2.0 MPa is a requirement for structural-grade lightweight aggregates conforming to the requirements of ASTM C 330.

Table 5.39 and Figure 5.110 present the splitting tensile strength of lightweight and normalweight concretes studied. LWCC exhibited the lowest 28-day and 56-day tensile strengths as, 3.7 MPa and 3.9 MPa, respectively, among the concretes tested. The difference in splitting tensile strengths of other concretes was small, the NWC giving the slightly higher tensile strength. Some researchers reported that compared with NWC, the elastic modulus and tensile strength are generally low for LWAC [38]. However, the 28-day tensile strength of NWC was only ~ 6 % and ~ 4% higher than those of LWBC and LWGC, respectively. In addition, the highest and lowest strength increases from 28 days to 56 days obtained with LWBC and NWC were 6.3 % and 3.9 %, respectively. This trend was also observed in the case of compressive strength, however the increase rates in splitting tensile strength were smaller than those in compressive strength.

Although in a study [41], it is concluded that the use of lightweight aggregate in high strength concrete caused a higher reduction in the splitting tensile strength and dynamic modulus of elasticity than in the compressive strength, the use of sintered lightweight aggregates in concrete led to a higher reduction in the modulus of elasticity and compressive strength than in the splitting tensile strength. The splitting tensile strengths of LWCC, LWBC and LWGC were 72.5, 94.1 and 96.1 %, respectively, of normalweight

concrete. This result also confirmed the saying “Lightweight concrete splitting tensile strengths vary from approximately 75 to 100% of normalweight concrete of equal compressive strength” [123]. The ratios of splitting tensile strength to compressive strength in 28 days and in 56 days were 8.7 %, 9.0 %, 8.8 %, 8.1 % and 8.7 %, 8.6 %, 8.4 %, 8.0 % for LWCC, LWBC, LWGC and NWC, respectively. The ratios of splitting tensile strength to compressive strength of lightweight aggregates were found to be similar to that of normalweight concrete. However, in a study [38], it was found that the tensile/compressive strength ratio appeared to be lower for high-strength LWC than that of high strength NWC.

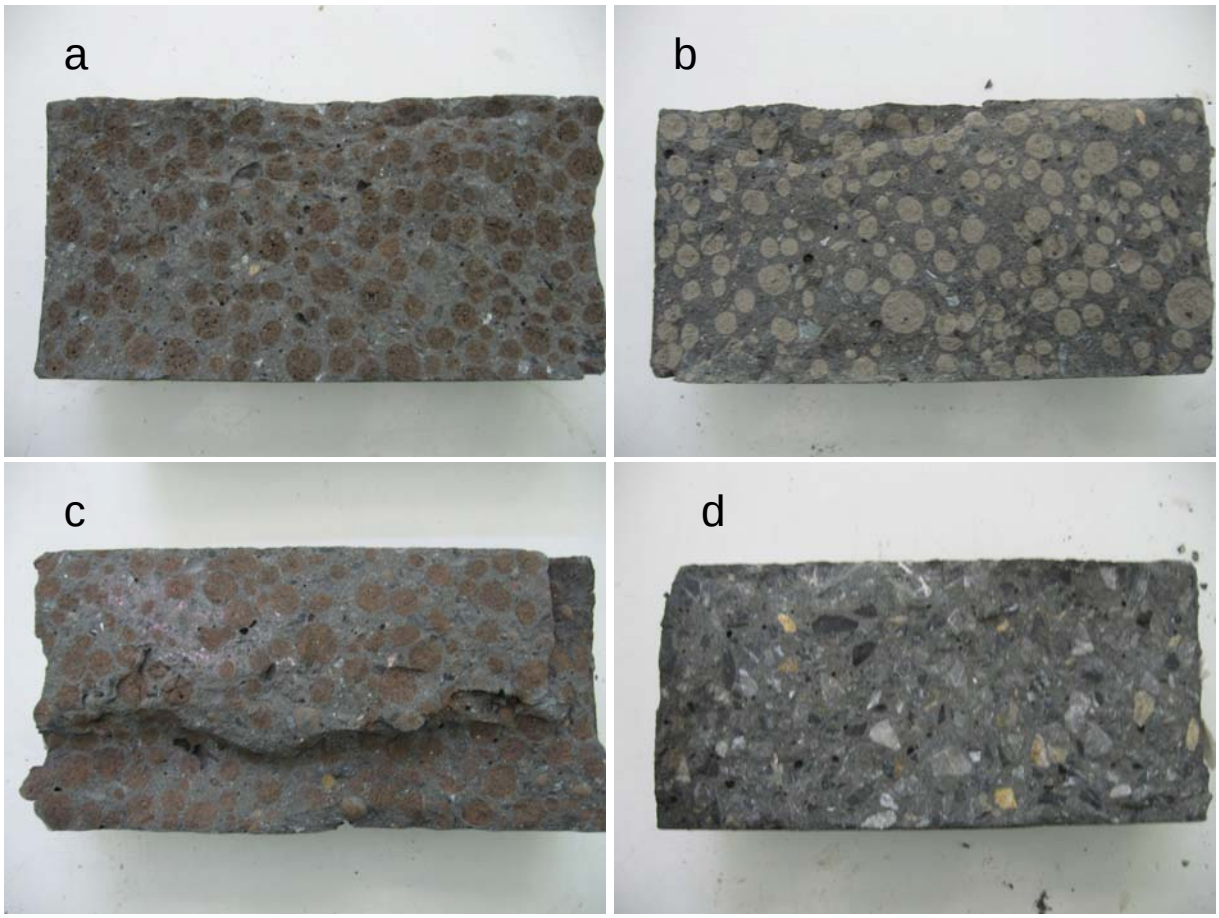

Figure 5.109. Splitted concrete specimens obtained from splitting tensile strength test a) LWGC; b) LWCC; c) LWBC; and d) NWC

The ultimate strength of concrete is mainly controlled by the strength of the lightweight aggregate itself. When fractured surfaces were inspected, it was observed that interfacial bond failure did not take place. The aggregate particles were found to split along the diameter so as to form two equal half-hemispheres for all concretes. The bonding that

occurred between the hardened cement mortar and the aggregates remained good after the tests. The fractured plane passed across all the aggregate sections (Figure 5.109). The microstructural studies on interfacial zone (Figures 5.141-5.148) showed the mechanical and chemical interlocking between the cement mortar and the aggregates.

Table 5.39. Results of splitting tensile strength

Concretes	Splitting tensile strength, (MPa)	
	28 day	56 day
LWCC	3,7	3,9
LWBC	4,8	5,1
LWGC	4,9	5,1
NWC	5,1	5,3

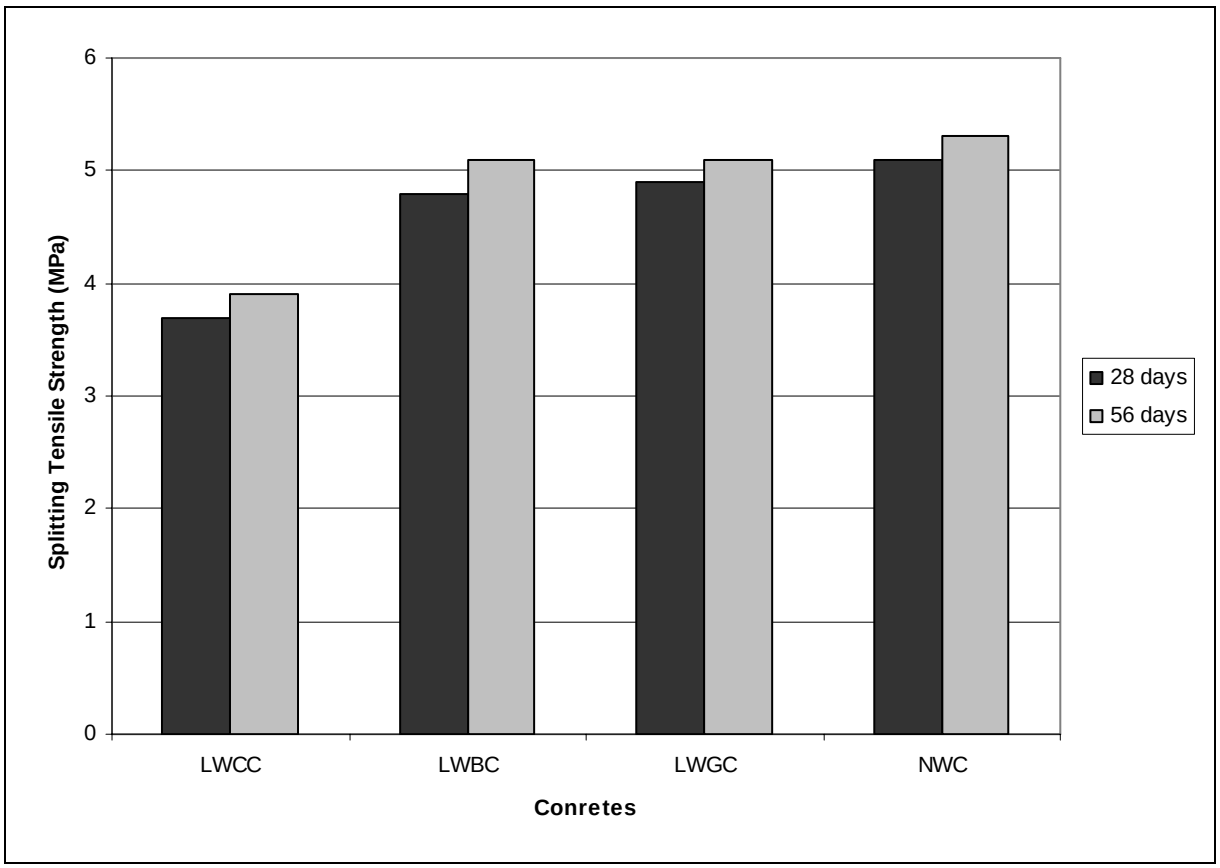

Figure 5.110.The splitting tensile strength values of 28-day and 56-day concrete specimens

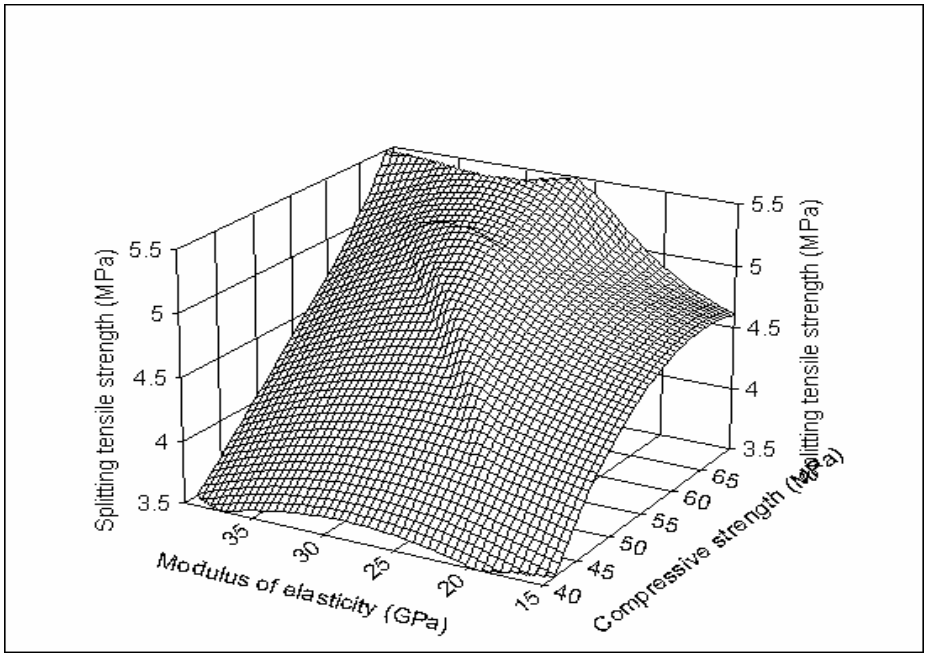

Figure 5.111. 3D view of experimental results of LWC and NWC

Using response surface methodology, the experimentally obtained compressive strength, modulus of elasticity and splitting tensile strength values were analyzed and the coefficients of the parameters were arrived at and given by the regression equation (which gives the predicted values). According to the obtained results the developed models are statistically accurate. The final model which is an empirical relationship between the splitting tensile strength (*Z*) and compressive strength (*X*) and modulus of elasticity (*Y*) is shown below:

$$\sigma_t = a + b*\sigma + c*E + d*\sigma^2 + e*E^2 + f*\sigma*E \qquad (5.52)$$

The significance of each coefficient was determined by Student's t-test and p-values (Table 5.40). Values of "Prob>F'' less than 0.0500 indicate that model terms are significant. The larger the magnitude of the t-value and the smaller the p-value, the more significant is the corresponding coefficient. The results indicated that linear effect of compressive strength, quadratic effect of compressive strength and modulus of elasticity and interaction effect between compressive strength and modulus of elasticity were highly significant ($p < 0.001$ or $p < 0.05$) for splitting tensile strength.

Table 5.40. Coefficients of the model given by software

Parm	Value	Std Error	t-value	P>|t|
a	-3,83125	0,423808	-9,04006	0,01202
b	0,198636	0,033285	5,967739	0,02695
c	0,099853	0,04233	2,358897	0,14233
d	-0,00275	0,000477	-5,76673	0,02878
e	-0,00785	0,000813	-9,64543	0,01058
f	0,006167	0,001072	5,75036	0,02894

Table 5.41. ANOVA for response surface fit to the experimental results

Source	Sum of Squares	DF	Mean Square	F value	P>F
Regr	2,518436	5	0,503687	3204,89	0,00031
Error	0,000314	2	0,000157		
Total	2,51875	7			

Table 5.42. Actual and predicted values by response surface fit for splitting tensile strength

X	Y	Z	Z Predicted	Residual	Residual %
42,3	19,6	3,7	3,703904	-0,0039	-0,10551
44,6	19,7	3,9	3,895524	0,004476	0,114776
53,5	26	4,8	4,791079	0,008921	0,185848
55,8	25,7	4,9	4,913583	-0,01358	-0,2772
59,5	26,3	5,1	5,096482	0,003518	0,068979
60,4	25,9	5,1	5,099233	0,000767	0,015043
62,9	36,8	5,1	5,101095	-0,0011	-0,02147
66	37,1	5,3	5,2991	0,0009	0,016975

The results of the response surface fitting in the form of analysis of variables are shown in Tables 5.41 and 5.42. The F value of the quadratic model and individual model terms helps in finding their significance. The F-test with a very low probability value showed a very high significance for the regression model. The regression model was highly significant ($p < 0.001$ or $p < 0.05$) with a satisfactory coefficient of determination

(R^2) 0.99 and adjusted determination coefficient (adjusted R^2) 0.99. The results demonstrated that the model developed was quite accurate as the percentages of error in prediction were in a good agreement (Table 5.42). Figure 5.122 illustrated 3D view of the predicted values obtained by the software.

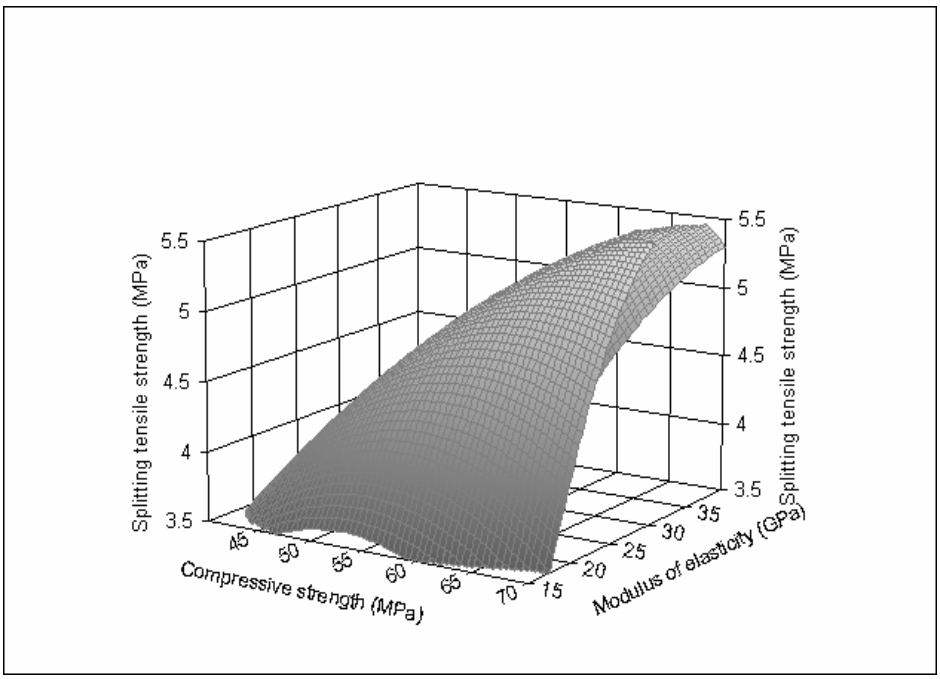

Figure 5.112. 3D view - response surface plot showing the effect of compressive strength and modulus of elasticity on splitting tensile strength

The relationship between splitting tensile strength and compressive strength was studied for concretes. The expressions obtained were below:

$$\sigma_t = 0{,}1109\ \sigma^{0{,}9389},\ R = 0{,}9912 \text{ for LWC in 28 and 56 days} \quad (5.53)$$

$$\sigma_t = 0{,}0738\ \sigma^{1{,}046},\ R = 0{,}9971 \text{ for LWC in 28 days} \quad (5.54)$$

$$\sigma_t = 0{,}1253\ \sigma^{0{,}9053},\ R = 0{,}9990 \text{ for LWC in 56 days} \quad (5.55)$$

$$\sigma_t = 0{,}1572\ \sigma^{0{,}8496},\ R = 0{,}9682 \text{ for LWC and NWC in 28 days} \quad (5.56)$$

$$\sigma_t = 0{,}1721\ \sigma^{0{,}8239},\ R = 0{,}9893 \text{ for LWC and NWC in 56 days} \quad (5.57)$$

$$\sigma_t = 0{,}171\ \sigma^{0{,}8269},\ R^2 = 0{,}9781 \text{ for LWC and NWC in 28 and 56 days} \qquad (5.58)$$

where σ_t is the splitting tensile strength in MPa and σ is the compressive strength in MPa.

In the past, a number of empirical relationships between compressive strength and tensile strength have been suggested [125]. Many of them are presented in the following form:

$$\sigma_t = k * \sigma^a \qquad (5.59)$$

where k and a are coefficients and the values of a have been suggested between 0.5 and 0.75. British Code of Practice BS 8007:1987 also suggests similar form of relationship and the values for k and a as 0.12 and 0.70, respectively. In another study [125], the relationship between the compressive strength and the tensile strength was developed as shown as follows:

$$\sigma_t = 0.14 * \sigma^{0.85}\ (R^2=0.95) \qquad (5.60)$$

It is worth noting here that the above relationship and the suggested one by BS 8007 are similar to those of Equations 5.53-5.58 derived in this investigation. It can be observed that the concrete mixes containing lightweight aggregates behave in a similar manner to that of normalweight concrete.

The compressive strength of the lightweight concretes was related to splitting tensile strength as well as modulus of elasticity, a strong dependency being observed (Figure 5.113). Power regression model was used to correlate the compressive strength and splitting tensile strength. R values were close and high in all different conditions. However, the largest R values were observed when the normalweight concretes were not taken into account.

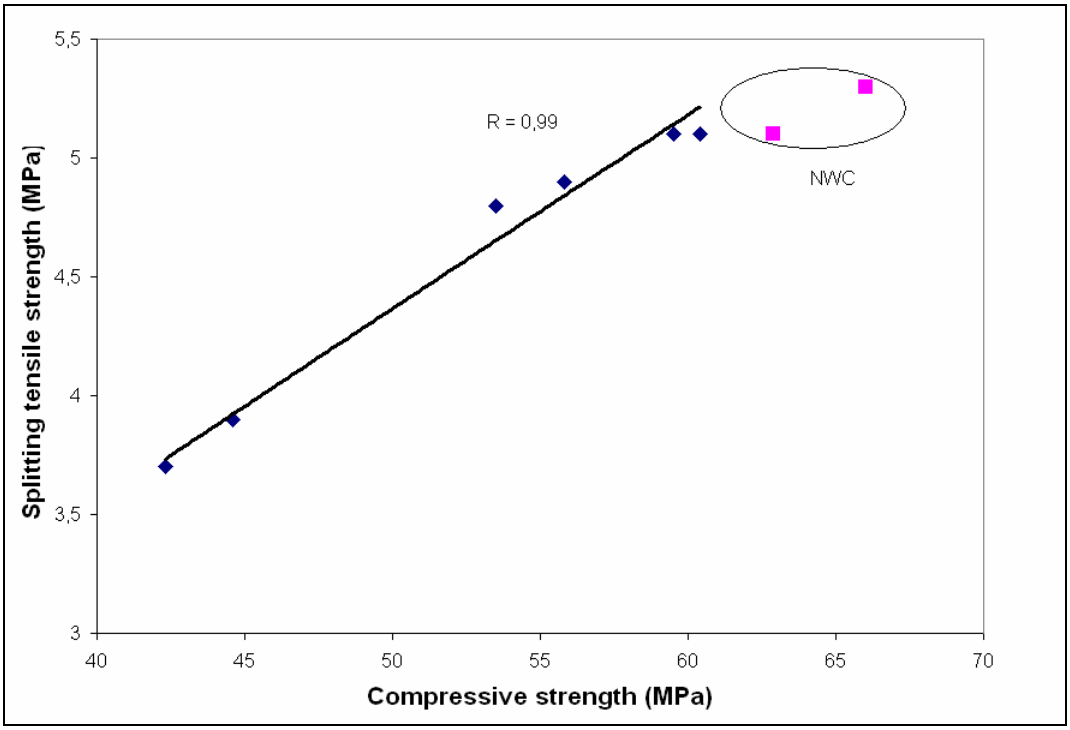

Figure 5.113. Relationship between splitting tensile strength and compressive strength

5.3.4. Rapid Chloride Permeability

The test results are summarized in Table 5.43 and Figure 5.114. LWBC showed the best performance among the concretes in the rapid chloride permeability test. The penetration of water, chloride and other aggressive ions into concrete is the most important factor in the physical and chemical process of deterioration, and it is the microstructure of concrete that mainly controls the physical/chemical phenomena associated with water movements and the transport of ions in concrete [126]. In some aggressive environments, concrete structures are also subjected to chloride ion penetration [14]. Buildings located near the sea shore or concrete roads and bridges that get sprayed by salt to prevent ice formation are examples of such structures. In those environments, steel reinforcement can quickly be contaminated with chloride ions. Such contamination may cause pitting corrosion and thus cause serious reduction in the effective steel reinforcement. It may also cause spalling and further deterioration. The combination of lightweight aggregate with silica fume and/or fly ash has produced high-strength lightweight concrete for structural applications [51]. This type of concrete has become popular in off-shore structures. Therefore it is very important to evaluate the performance of such concrete for durability, especially in marine environments where chloride initiated corrosion is likely to be the

most significant cause of possible deterioration. The permeability of concrete is not a simple function of its porosity, but depends also on the size, distribution, shape, tortuosity, and continuity of the pores [127]. Since high resistance to chloride penetration can be directly related to low permeability that dominates the deterioration process in concrete structures, the resistance to chloride penetration is one of the simplest measures to determine the durability of concrete. Thus, high-performance concrete may be defined as the concrete having high resistance to chloride penetration as well as high strength.

All concrete specimens at all ages showed very low chloride permeability except the LWCC at 28 days which was rated as low chloride permeability. The chloride permeability of all concrete specimens markedly decreased at 56 days owing to the very fine particles of silica fume with high pozzolanic reactivity. The silica fume densified the microstructure of concrete through filling of the finer pores. Also, in some studies [43, 52, 94, 125 and 126], the decrease of permeability of concretes containing silica fume and fly ash was attributed to the microfiller effect and high pozzolanic reactivity, leading to the denser, stronger and a fine and discontinuous pore structure. However, although for the 28-day concretes the pozzolanic reaction has not fully developed, they exhibited very low permeability. In the same study [126], it is shown that non air-entrained concrete had a lower permeability than air-entrained one. However, air-entrainment did not seem to have a great influence on the chloride permeability compared with water-to-binder ratio and mineral admixtures. In our study, it is obvious that all concretes exhibited low and very low permeability although they were all nearly 4 % air-entrained. This can provide a firm basis for the use of high-performance concrete having very low permeability and high durability in the actual structures under severe conditions. In an investigation [51], it is reported that lightweight aggregate concrete had the least chloride concentration and even lower than similar strength normal weight concrete. The explanation to this phenomenon was likely to be the reservoir action of the lightweight aggregates possessing high absorption capacity that ranges from around 8 % to sometimes more than 20 %. These aggregates would act as protective reservoirs to the rest of the matrix and would absorb the chloride laden solution. However, this test was performed on dry specimens immersing them in a sodium chloride solution. Thus, this explanation is not valid for our study. All the specimens were in SSD condition, therefore, instead of acting as protecting reservoirs, cold bonded aggregates transported chloride ions more quickly due to their high open porosity. Moreover, in high-

strength concrete, whether normal weight or lightweight, the matrix is very rich with cementitious materials and the pores are expected to be discontinuous. This would limit the ingress of chloride ions within the matrix.

LWCC and LWBC showed the highest and the lowest chloride permeability with total charge passed values of 1464 and 586 coulombs at 28 days and 748 and 264 coulombs at 56 days, respectively. The chloride permeability values of concretes at 56 days were less than half of the permeability values at 28 days. Although the variation in chloride permeability among concretes was not large, the permeability of concrete containing cold-bonded aggregates was higher than other concretes. This could be attributed to the high absorption and open porosity of cold-bonded aggregates. Concretes with sintered aggregates showed significantly lower penetration value than its natural aggregate counterpart. These results show that concretes with sintered lightweight aggregates provide high level protection to reinforcement as far as corrosion is concerned. The results also suggested that strength and durability are not always synonymous. The NWC had the highest compressive strength, whereas it exhibited higher permeability than both LWGC and LWBC.

Table 5.43. Results of rapid chloride permeability

Concretes	Charge passed, (coulombs)	
	28 day	56 day
LWCC	1464	748
LWBC	586	264
LWGC	701	295
NWC	729	308

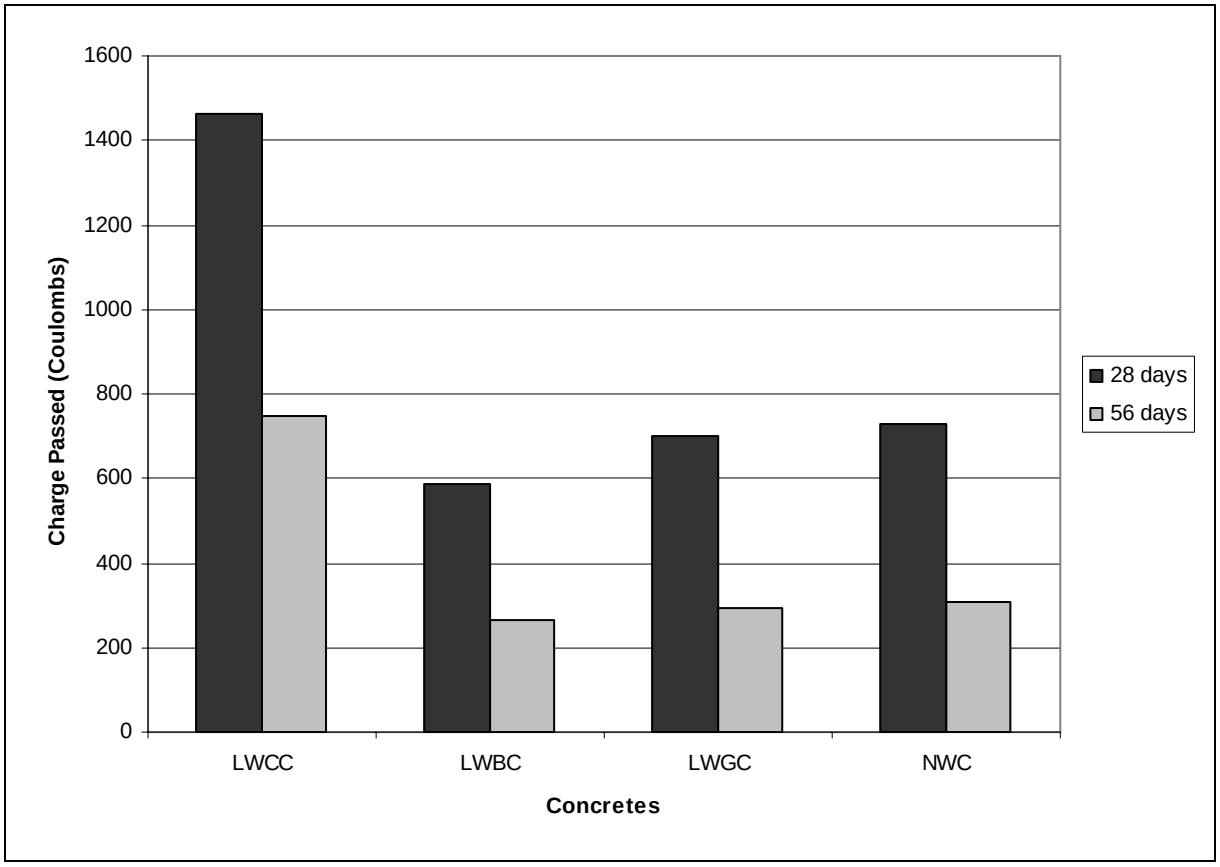

Figure 5.114.The rapid chloride permeability values of 28-day and 56-day concrete specimens

In practice, the quality of concrete and its fitness for purpose is often judged by its compressive strength. Therefore, the relationship between compressive strength and durability-related properties is of particular interest. The relationships between compressive strength and permeability and between splitting tensile strength and permeability are shown in Figures 5.115 and 5.116 and the equations are presented as follows:

$$Q = 2E+09\ \sigma^{-3,7659},\ R = 0,8856 \text{ for LWC in 28 and 56 days} \quad (5.61)$$

$$Q = 1E+08\ \sigma^{-3,0786},\ R = 0,9469 \text{ for LWC in 28 days} \quad (5.62)$$

$$Q = 2E+08\ \sigma^{-3,313},\ R = 0,9901 \text{ for LWC in 56 days} \quad (5.63)$$

$$Q = 2E+06\ \sigma^{-1,9543},\ R = 0,8063 \text{ for LWC and NWC in 28 days} \quad (5.64)$$

$$Q = 1E+07\ \sigma^{-2,6149},\ R = 0,9252 \text{ for LWC and NWC in 56 days} \quad (5.65)$$

$$Q = 4E+07\ \sigma^{-2,7975},\ R = 0,7572 \text{ for LWC and NWC in 28 and 56 days} \quad (5.66)$$

where:

Q = Total charge passed in coulombs

σ = Compressive strength in MPa

$$Q = 179497\ \sigma_t^{-3,7964},\ R = 0,8458 \text{ for LWC in 28 and 56 days} \quad (5.67)$$

$$Q = 73641\ \sigma_t^{-3,0017},\ R = 0,9685 \text{ for LWC in 28 days} \quad (5.68)$$

$$Q = 111229\ \sigma_t^{-3,6753},\ R = 0,9953 \text{ for LWC in 56 days} \quad (5.69)$$

$$Q = 39475\ \sigma_t^{-2,5474},\ R = 0,9222 \text{ for LWC and NWC in 28 days} \quad (5.70)$$

$$Q = 64778\ \sigma_t^{-3,2931},\ R = 0,9703 \text{ for LWC and NWC in 56 days} \quad (5.71)$$

$$Q = 105454\ \sigma_t^{-3,4009},\ R = 0,7781 \text{ for LWC and NWC in 28 and 56 days} \quad (5.72)$$

where:

Q = Total charge passed in coulombs

σ_t = Splitting tensile strength in MPa

It can be seen from Figures 5.115 and 5.116 that lightweight concretes gave better correlation when normalweight concretes were exported. As the strength increased, the permeability reduced as expected. It is interesting to note that the variations between the lightweight concretes became smaller and less significant as the age increased. Similar relationship was obtained when comparing tensile strength with permeability.

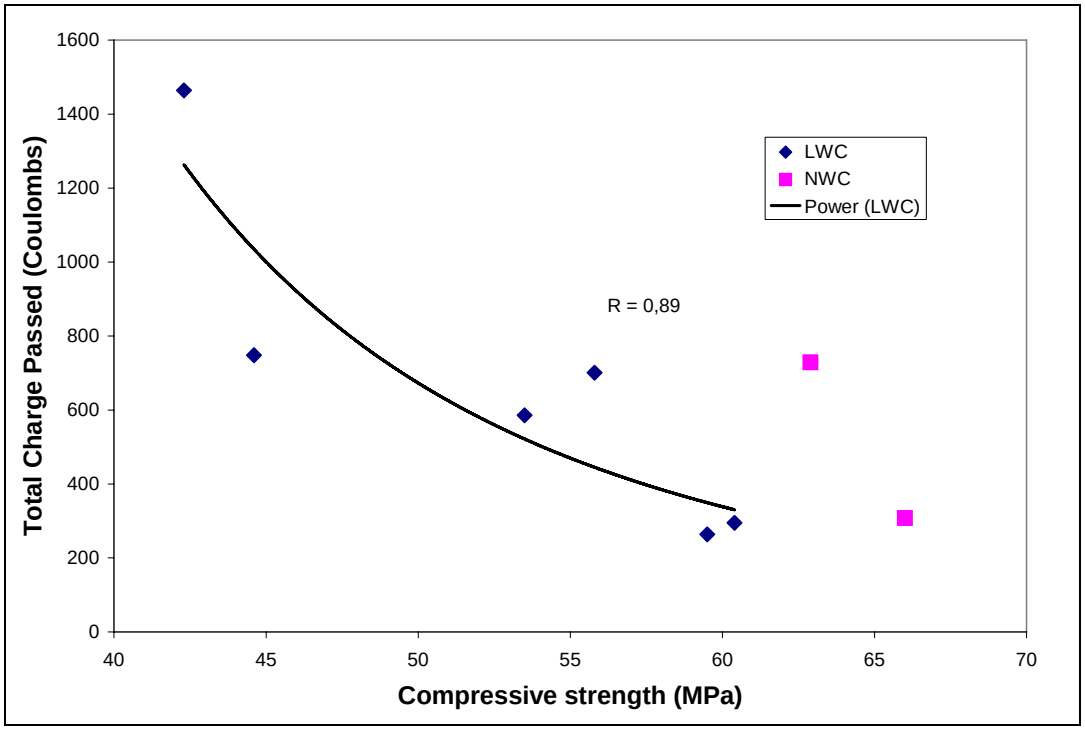

Figure 5.115. Relationship between total charge passed and compressive strength of lightweight concretes

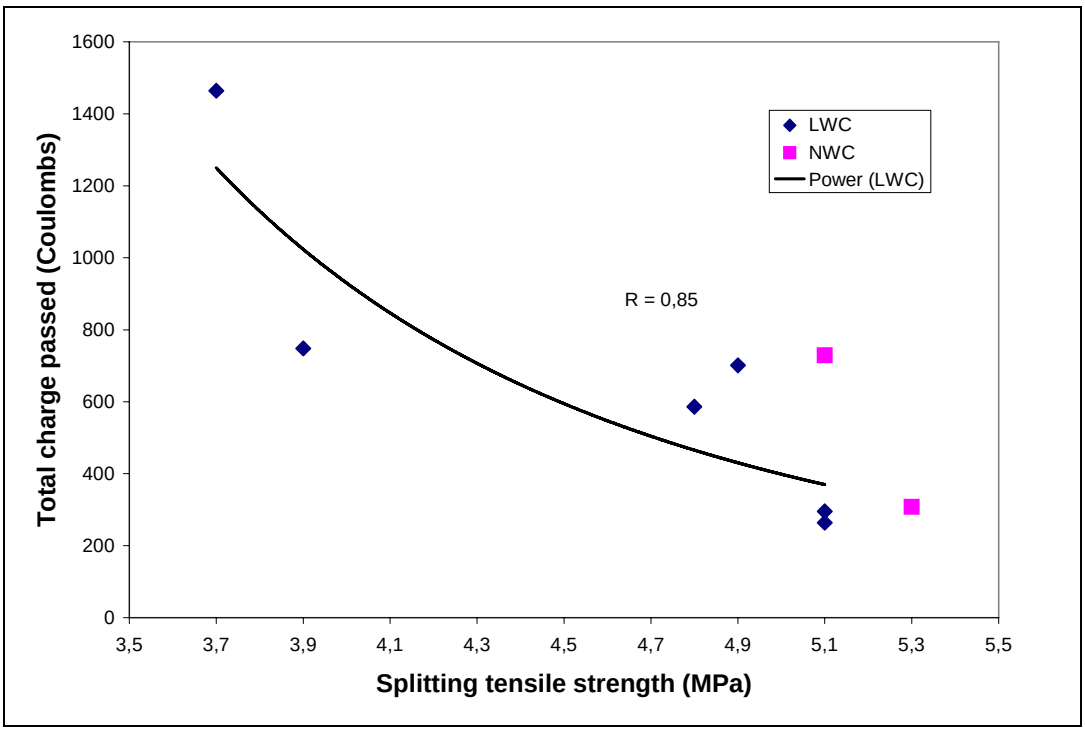

Figure 5.116. Relationship between total charge passed and splitting tensile strength of lightweight concretes

5.3.5. Accelerated Corrosion Test

The time-current curves and time to initiation of corrosion for lightweight and normalweight concretes are shown in Figure 5.117 and Table 5.44. Besides the strength/weight ratio, the other factor that is of significant importance for structures is the long-term durability. This is affected to a large extent by the permeability of concrete. Concrete with high permeability will provide ready access for both water and harmful substances resulting in deterioration of either concrete or steel reinforcement embedded in the concrete or a combination of both. Chloride-induced corrosion of reinforcing steel is one of the most pressing problems worldwide that the construction industry is facing today [52].

The time of reinforcement corrosion can be determined by observing a sudden rise in the current followed by occurence of crack of concrete specimens. The potential measurements in mV were taken and these potential values, then were converted to current by the aid of resistor used in the test. At the beginning of the test, the potential of LWCC was nearly 150 mV, while the potentials of LWBC, LWGC and NWC were close to each other and 54, 53 and 56 mV, respectively. However, the crack propagation was observed immediately after a sudden rise of the current. Thus, the last recorded potential before the crack occurence was approximately 200 mV. At the beginning of experiment and due to the constant potential impressed, the steel bar in concrete was anodic [128]. However, the anodic reaction or the corrosion reaction rate on the steel bar surface was very slow because of the limited access of chloride ions and oxygen to the surface of the steel bar which explained the initial low current at the beginning of the test. As the experiment was continued, corrosion of the steel bar kept more or less steady until the time when crack was developed through surrounding concrete and as a consequence the electrical resistivity between the anode and the cathode was sharply reduced with a simultaneous increase in current. Cracking of the surrounding concrete allowed easy access of the chloride ions and oxygen to the surface of the steel and hence increased the corrosion rate. It was possible to determine the corrosion tendency of the reinforcement in the seawater environment by employing this test method, whereas in a study [129], the researchers stated that it was difficult by employing the standard test method for half-cell potential measurement described in ASTM C876 (for atmospheric environment). This is because potential

measurements indicate only the local probability of corrosion and not the actual corrosion rates.

LWBC exhibited the longest corrosion time with 123 days, followed by LWGC with 106 days, NWC with 66 days and LWCC with 28 days. In the case of LWCC, the corrosion time increase was 75 % at 56 days. The result further confirms that whereas cold bonded fly ash aggregate increased the porosity of lightweight concrete, the silica fume would partly compensate the detrimental effect caused by cold bonded lightweight aggregate on the permeability. The replacement of 10B1200 and 10G1200 lightweight aggregates for normalweight crushed stone caused 86 % and 61 % increase in corrosion time, respectively. Similar trend was also observed in accelerated corrosion test as in rapid chloride permeability test. Keeping in mind the results of chloride permeability and the corrosion time increase in LWCC at 56 days and also considering the positive effect of silica fume especially at later ages, the corrosion time of 56-day concretes would be at least twice of 28-day concretes, coming to mean that longer time to corrode. Therefore, the 56-day concretes containing sintered lightweight and normalweight aggregates could not be tested. However, in the test set up, the concentration of solution or the voltage applied could be increased to obtain short corrosion time.

The action of acids on cement paste consists in an attack on the components of the hardened cement paste [130]. It is believed that this action leads to a conversion of all the calcium compounds, unreacted residue of C_3S and C_2S in cement grains, calcium hydroxide, calcium silicate hydrate, and calcium aluminate hydrate to the calcium salt of the attacking acid. As a result of the conversion, the binding capacity of the hardened cement is destroyed. It is accepted that the rate of attack would depend on quality of the concrete and also on the solubility of the resulting calcium salt and the permeability of precipitates. In this study, all constituents and their contents but aggregates were same. In the light of this explaination, although the behavior of the hardened cement paste part of all concretes against the acids was same, the concretes with cold-bonded aggregates was more vulnerable than other concretes to acid attack due to difference in chemical and phase composition of aggregates. The cold-bonded aggregate was rich in calcium due to presence of residues of C_2S and C_3S, portlandite [$Ca(OH)_2$], and C-S-H in fly ash and cement composition. These calcium-containing compounds in the aggregates reacted with the acid

during test. Calcium ions with their solubility left the cement paste and cold-bonded aggregates. Decalcified C-S-H and silica gel have no structural properties. In other words, the decalcification of C-S-H destroys the binding capacity of C-S-H and leads to a loss of adhesion and strength in concrete as also reported in another study [131]. As a result of these reactions, expansion and cracking are caused, directly or indirectly, by ettringite and gypsum formation, while softening and disintegration are caused by destruction of C-S-H. As a result of this, concrete and cold bonded aggregate surfaces became soft and could be removed, thus, exposing the interior concrete layers to deterioration. This is attributable to the poor performance of concretes with cold bonded aggregates, besides the high open porosity of these aggregates. The water absorptions of sintered aggregates and normalweight aggregates were similar, however, concretes with sintered aggregates were more stable in the acid solution than normalweight concrete. The normalweight crushed stone used in concrete was calcerous that reacted with the acid, resulting in softening of aggregate surface and ITZ deterioration. This evidence provided a support for the reason of rapid deterioration of concretes with aggregates containing calcium compounds. This result was also confirmed by XRD studies (Figure 5.47), detecting calcite minerals present in cold-bonded aggregates. It was reported that the permeability of lightweight concrete was extremely low and generally equal to or significantly lower than that reported for the normalweight concrete specimens [123]. Similar results and conclusions by Russian, Japanese and English investigators confirmed these findings. All attributed the low permeability to the profound influence of the high-integrity contact zone possessed by lightweight concrete. The results obtained from this test is consistent with comparative results of RCPT and water permeability test.

Crack shapes of all concretes were observed after the exposure testing. A fast longitudinal crack was dedected for all concretes. However, in some investigations [81, 127], researchers noticed that crack propagations were different for some specimens. In these studies, close to transverse cracks and a slow and curved multidirectional cracks were observed in addition to the longitudinal cracks.

Table 5.44. Corrosion time of concretes

Concretes	Corrosion time (Days)
LWCC28	28
LWCC56	49
LWBC28	123
LWGC28	106
NWC28	66

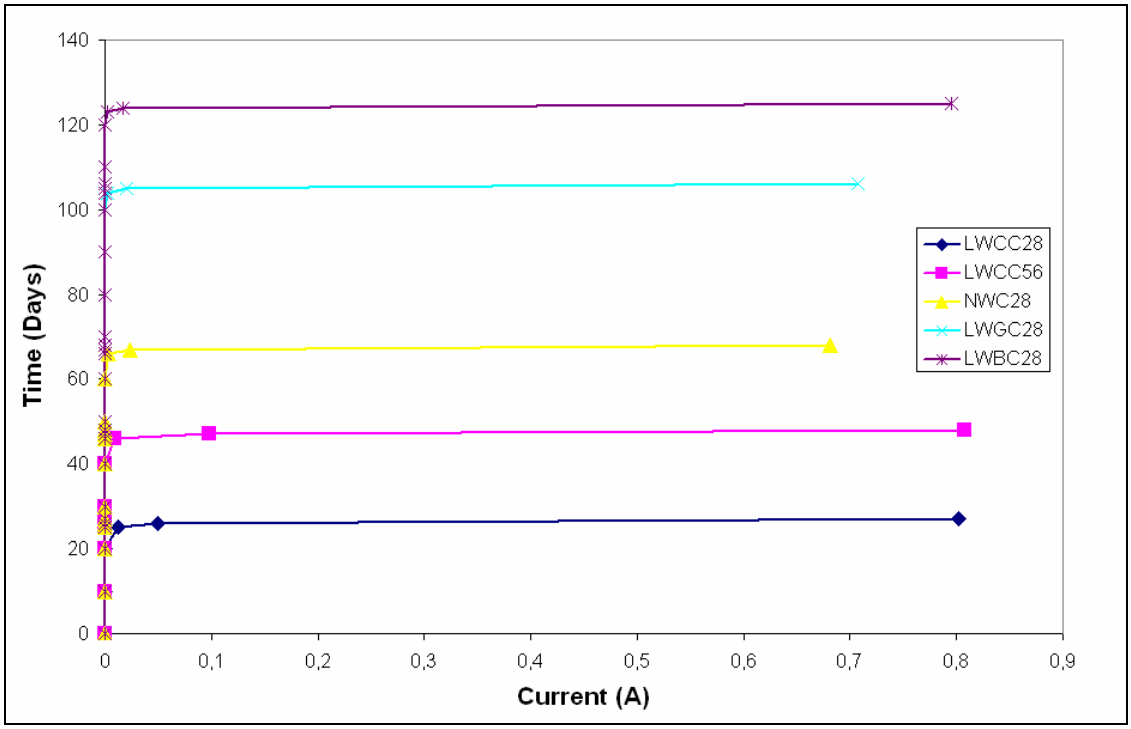

Figure 5.117. Curve of corrosion current

The relationships between corrosion time and compressive strength, between corrosion time and tensile strength and between corrosion time and total charge passed are exhibited in Figures 5.118-5.120 and equations derived from regression models are as below:

$$t = 26{,}06\sigma^{0{,}1674},\ R = 0{,}6714 \quad (5.73)$$

$$t = 2{,}111\ \sigma_t^{0{,}1828},\ R = 0{,}8352 \quad (5.74)$$

$$t = 9737{,}4Q^{-0{,}5841},\ R = 0{,}9663 \quad (5.75)$$

where:

t = corrosion time in days

σ = compressive strength in MPa

σ_t = splitting tensile strength in MPa

Q = total charge passed in coulombs

The relations between the corrosion time and other tests were established from the experimental results. Power regression models gave the largest R values among other regression models for all analysis. It can be seen that there is a poor relationship between the compressive strength and corrosion time with a small R value of 0.67, showing that the regression was established under poor fit. A remarkably high variation was present in the corrosion time and compressive strength results. Corrosion time correlated better with splitting tensile strength than with compressive strength with a R value of 0.84. The reason could be attributed to the fact that cracking which was a consequence of the corrosion, was related more with the tensile strength of concretes. Similar trend was observed as can be seen in Figures 5.118 and 5.119 for both compressive srength and splitting tensile strength. However, the best correlation was obtained with total charge passed with R value of 0.97 which was high enough to apply the model to calculate corrosion time from the total charge passed. As can be seen from the Figure 5.120, as the total charge passed increased, corrosion time decreased.

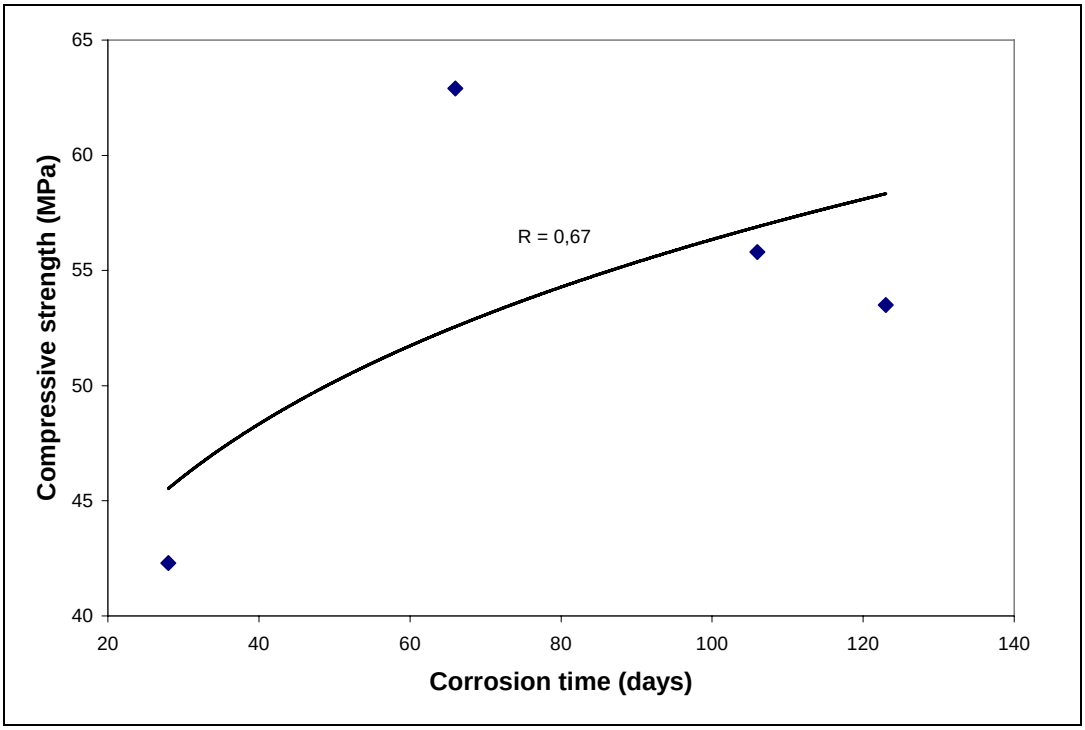

Figure 5.118. Relationship between corrosion time and compressive strength of 28-day concretes

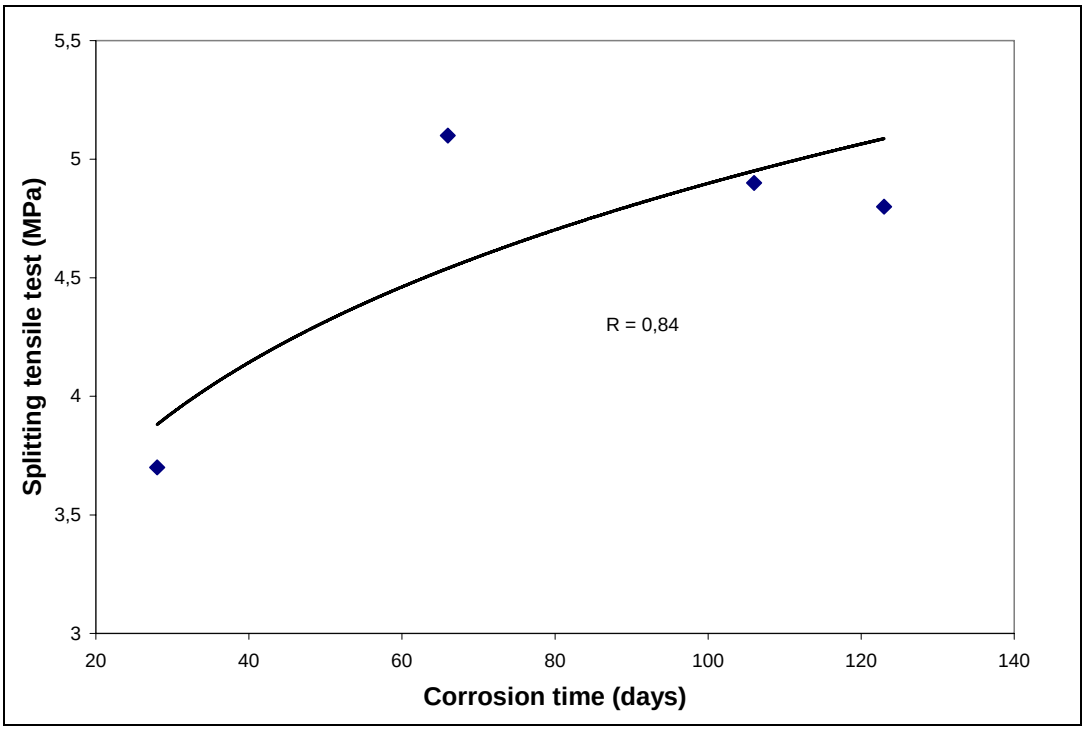

Figure 5.119. Relationship between corrosion time and splitting tensile strength of 28-day concretes

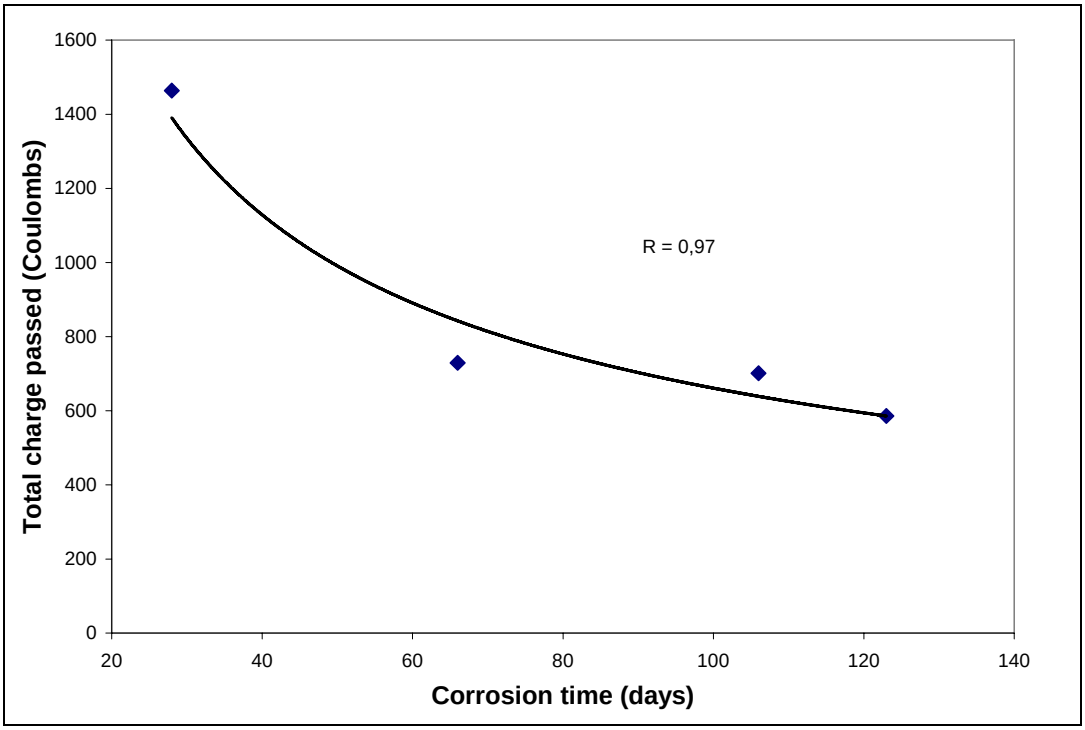

Figure 5.120. Relationship between corrosion time and total charge passed of 28-day concretes

5.3.6. Water Permeability Test

The water permeability values of concretes are illustrated in Tables 5.45 and 5.46 and Figure 5.122. Permeability or, more importantly, penetrability is the principal factor influencing durability of concrete [37]. As usual, the water permeability of concretes practically decreases as the age increases [94]. However, as can be seen from the results, 28-day water permeability values were lower than the 56-day values due to the sample conditioning process indicated previously. The occurence of microcracks owing to the temperature in the oven at 56 days increased the water penetration depths. Some researchers [81, 94] also explained this difference by the change of the microstructure of the concrete: oven drying induces micro cracking of concrete, supplementary connections of previously disconnected or ‘‘dead end’’ pores. It is believed that when concrete specimens are exposed to medium temperature, the total pore volume increases, which affects the distribution of pore sizes and creates additional pore space in hardened cement paste. The increase in porosity due to increased temperature leads to a decrease in the bulk mass density of cement paste. Although low water/cement ratio was used that contributed to minimize the volume of porosity, quick drying under 110 ^{o}C would lead to localized

areas of high porosity in the hydrated cement paste and an increase in the water permeability of concretes. Second, it may be due to microcracks or shrinkage cracks resulting from thermal stresses occurred during drying at 110 ^{o}C. Under these conditions, the presence of microcracks on the surface area and at the transition zone of the specimens could have a major influence on the results of the 56-day concretes.

LWCC was more permeable than the others. This is because the cold bonded aggregate had the highest open porosity among other aggregates. The water absorption and volume of permeable pore space of the lightweight and normalweight concretes was evaluated according to ASTMC 642. 28-day test results are shown in Table 5.45 for the normalweight and lightweight concretes. Most artificial lightweight concrete exhibits significantly higher water absorption than normal weight concrete [118, 132]. Nevertheless, in this study, especially concretes containing lightweight sintered aggregates showed similar values with normalweight concrete. LWCC had the largest water absorption and permeable void values as 8.9 and 17 %, respectively, whereas other concretes had lower values than did LWCC, ranged from 2.8 to 3.3 % for water absorption and from 5.6 to 6.4 % for permeable pores. Also, results of the water permeability test indicated that compared to other three concretes, LWCC had a poor performance, showing 36 mm of the depth of water penetration at 28 days. The other concretes showed almost similar behavior in water permeability. LWBC exhibited the least permeability both at 28 and 56 days having 19 and 39 mm, respectively. In studies [37, 52], it is demonstrated that the water penetrability of the LWC is comparable to the NWC of similar strength grade and equivalent mix proportion. The same result was also obtained in this investigation. The lower permeability of the LWC was probably due to a denser interfacial zone between the aggregate and the mortar matrix compared with that of the NWC. The frequency of microcracking in the former was probably also lower due to less difference in the modulus of elasticity between the aggregate and the mortar matrix compared with that in the latter. The depth of water penetrations were close to the results of other studies investigating the lightweight concrete with same strengths [37, 38 and 52]. Although NWC showed the second worst performance for rapid chloride permeability and accelerated corrosion tests, it exhibited a slightly higher performance in 28 days for water permeability test. In a study [52], the lower water permeability of the LWC compared with that of the NWC did not correlate to the chloride penetrability of the concrete. The discrepancy may be related to

the different transport mechanisms involved in the water permeability test and the chloride penetration tests. Permeability refers to the amount of water migration through concrete when the water is under pressure or the ability of concrete to resist water penetration [118]. Permeability of concrete is a function of permeability of paste, permeability and gradation of aggregate, paste-aggregate transition zone and paste to aggregate proportion. Permeability also depends on w/c (increase with the increase of w/c) and initial curing conditions. However in this study, w/c and curing conditions were same for all concretes. It is also concluded that to be watertight, structural concrete should have a w/c of not more than 0.48 for exposure to fresh water and not more than 0.44 for exposure to seawater. In current study, w-c ratio was much lower than the indicated values. It appeared that replacement of lighweight sintered fly ash aggregates for the normalweight crushed aggregates prevented concrete from water penetration. In comparison with 28-day permeability, 56-day water permeability was two times larger. The percentages of increase rate in water permeability from 28 days to 56 days were 119 %, 105 %, 78 % and 105 % for LWCC, LWBC, LWGC and NWC, respectively. It can be concluded that LWCC was more sensitive to heat than the other concretes. The water permeability increase rate was proportional to the water absorption of aggregates. LWCC possessed the highest amount of water in SSD state before drying. Therefore, larger thermal stresses occurred in larger moisture environment leading to microcracks or shrinkage cracks during drying. LWGC had the lowest water absorption and permeable voids and the lowest increase rate showing the least affected concrete due to drying process. Also, it is obvious that this fully drying process in oven at 110 ^{o}C prior to testing terminated the filling and pozzolanic effect of silica fume as discussed earlier. The permeability of mortar or concrete is higher than that of the corresponding cement paste because of the micro-cracks that are present in the interface zone between the aggregate and cement paste [126]. This fact exhibits the importance of interfacial transition zone between aggregate and cement paste for permeability properties. If the same sample conditioning process was applied to 56-day concretes just like the 28-day concretes, the any possible beneficial effect of silica fume on the water permeability could be investigated. It is apparently visible that the permeability would be very low or negligible. This assumption can be proved by the SEM images of ITZ of concretes (Figures 5.142, 5.144, 5.146 and 5.148). The other permeability test results were in good agreement with water permeability test results.

Figure 5.121. Determination of water penetration depth on splitted cubic specimen

Table 5.45. 28-day water absorption and volume of permeable voids of the concretes

Concretes	28- day Water absorption (%)	28-day Permeable pore volume (%)
LWCC	8,9	17,0
LWBC	3,3	6,4
LWGC	2,8	5,6
NWC	3,1	6,3

Table 5.46. Depths of water penetration of the concretes

Concretes	Water penetration, mm	
	28 days	56 days
LWCC	36	79
LWBC	19	39
LWGC	23	41
NWC	21	43

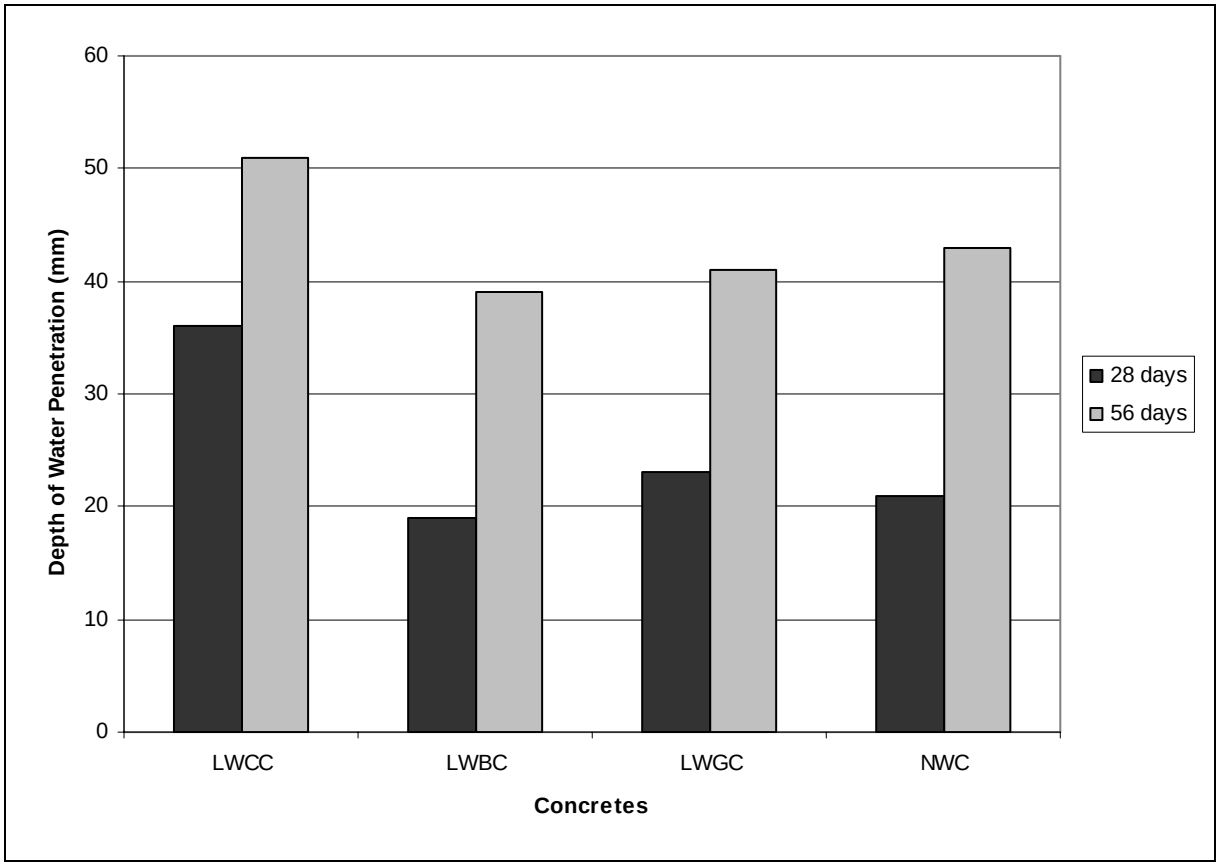

Figure 5.122. The water permeability values of 28-day and 56-day concrete specimens

In this investigation, a relationship between 28-day compressive strength and water penetration depth of concretes was established. Also, the 28-day water penetration depth was related to the splitting tensile strength, total charge passed, corrosion time, water absorption and volume of permeable voids as shown in Figures 5.123-5.128, respectively. Equations are as follows:

$$d = 7063{,}4\ \sigma^{-1{,}4315},\ R = 0{,}8438 \quad (5.76)$$

$$d = -11{,}516\ \sigma_t + 78{,}011,\ R = 0{,}9439 \quad (5.77)$$

$$d = 0{,}019\ Q + 8{,}2502,\ R = 0{,}9903 \quad (5.78)$$

$$d = 123{,}03\ t^{-0{,}3849},\ R = 0{,}9096 \quad (5.79)$$

$$w = 0{,}3656\ d - 4{,}5243,\ R = 0{,}9598 \quad (5.80)$$

$$v = 0{,}6847\ d - 8{,}1219,\ R = 0{,}9623 \quad (5.81)$$

where:

d = depth of water penetration in mm

σ = compressive strength in MPa

σ_t = splitting tensile strength in MPa

Q = total charge passed in coulombs

t = corrosion time in days

w = water absorption in %

v = volume of permeable pore space in %

It can be seen that there are good agreements between the results obtained from the tests. The water permeability correlated better with splitting tensile strength than with compressive strength with R values of 0.94 and 0.84, respectively. It is noteworthy that while the power regression model gave the high R value in the case of compressive strength, a strong linear relationship was observed with splitting tensile strength. Also, the best fit linear model was obtained with the correlation of total charge passed with an R value of 0.99. Water penetration decreased with increase in compressive and splitting tensile strength and increase with total charge passed increase. The R value of 0.91 was given by the power model in relationship between corrosion time and water permeability. Linear models were selected when analyzing the relationships between water absorption and permeable voids due to high R values of 0.9598 and 0.9623, respectively achieved with these models. As water absorption and permeable voids increased, the water penetration increased. All models presented high R values which were evidences of good correlations. Therefore, by using the proposed models, calculation of depth of water penetration of concretes could give accurate results.

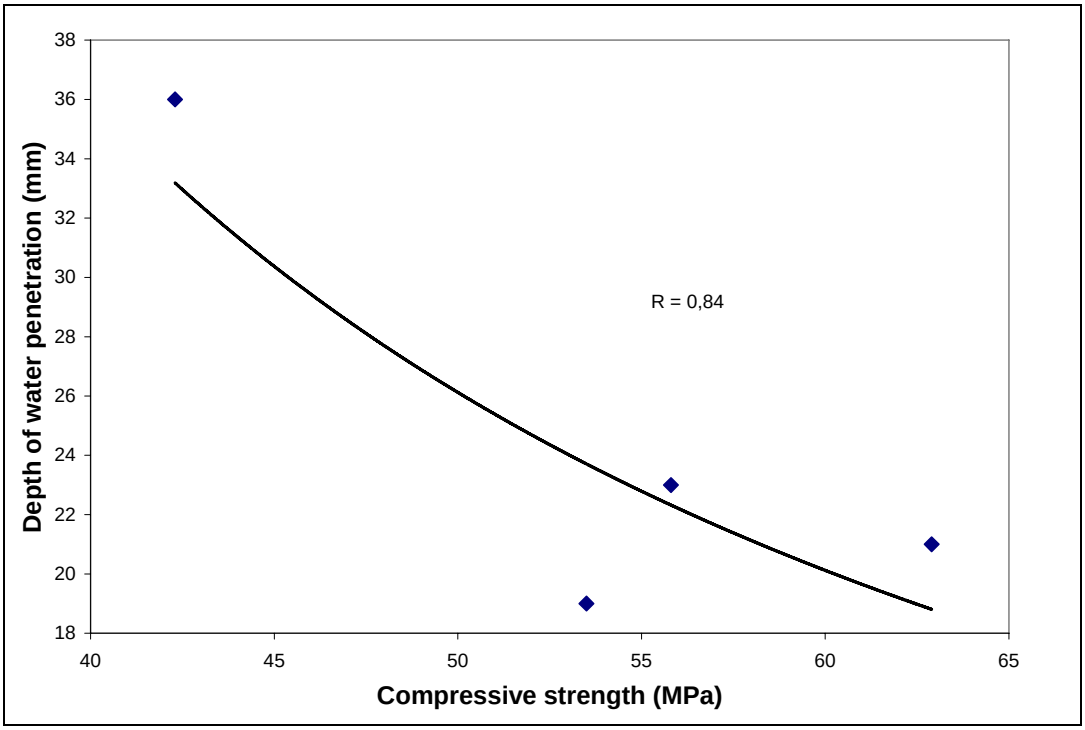

Figure 5.123. Relationship between depth of penetration and compressive strength of 28-day concretes

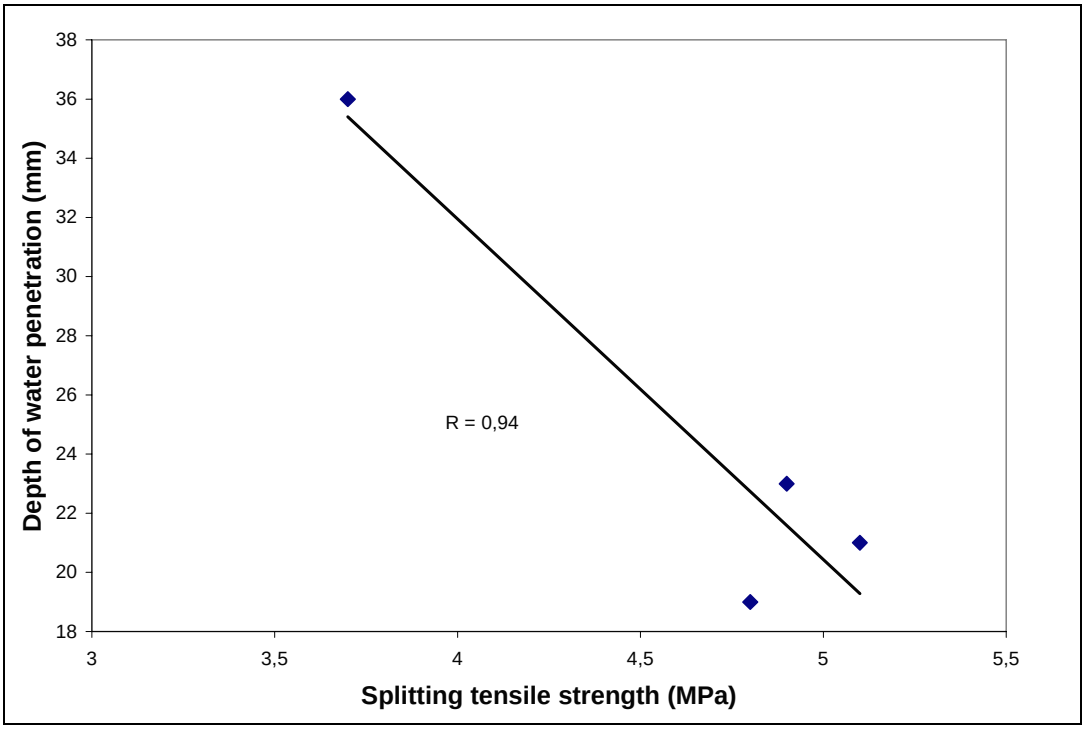

Figure 5.124. Relationship between depth of penetration and splitting tensile strength of 28-day concretes

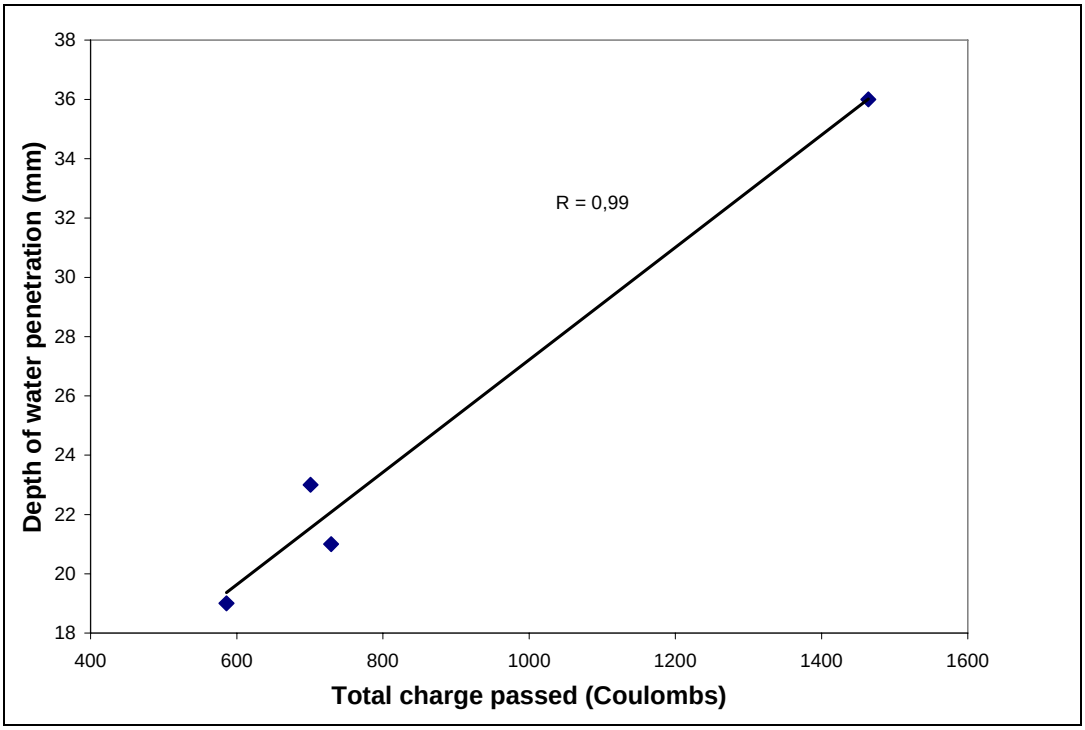

Figure 5.125. Relationship between depth of penetration and total charge passed of 28-day concretes

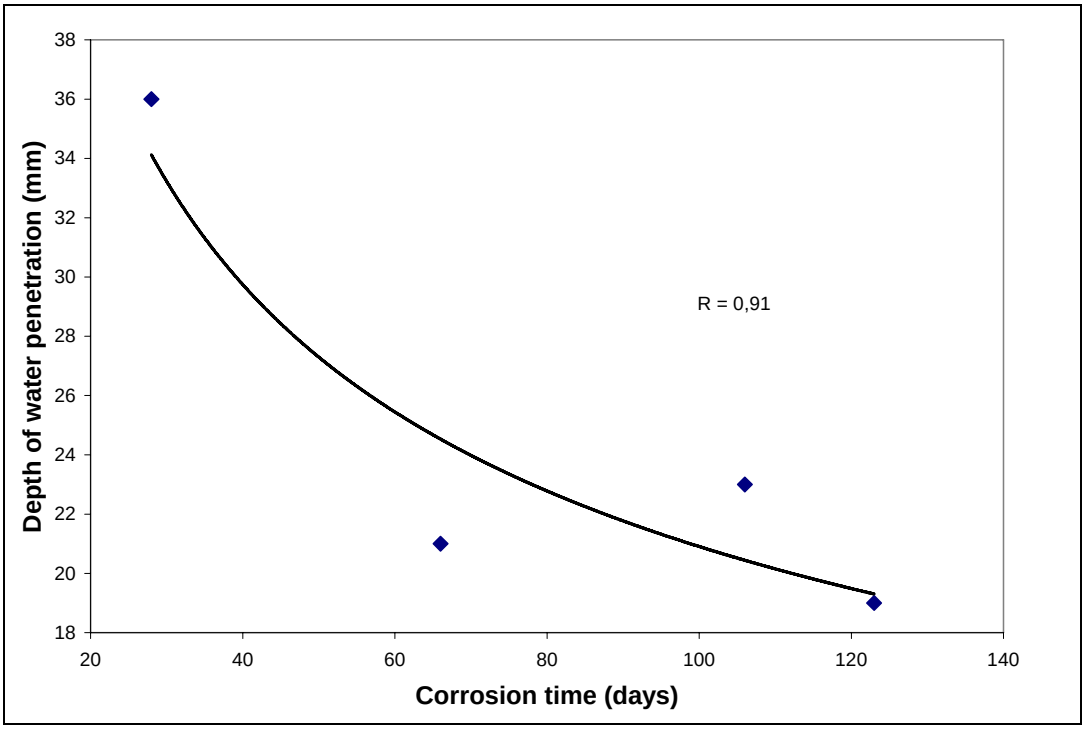

Figure 5.126. Relationship between depth of penetration and corrosion time of 28-day concretes

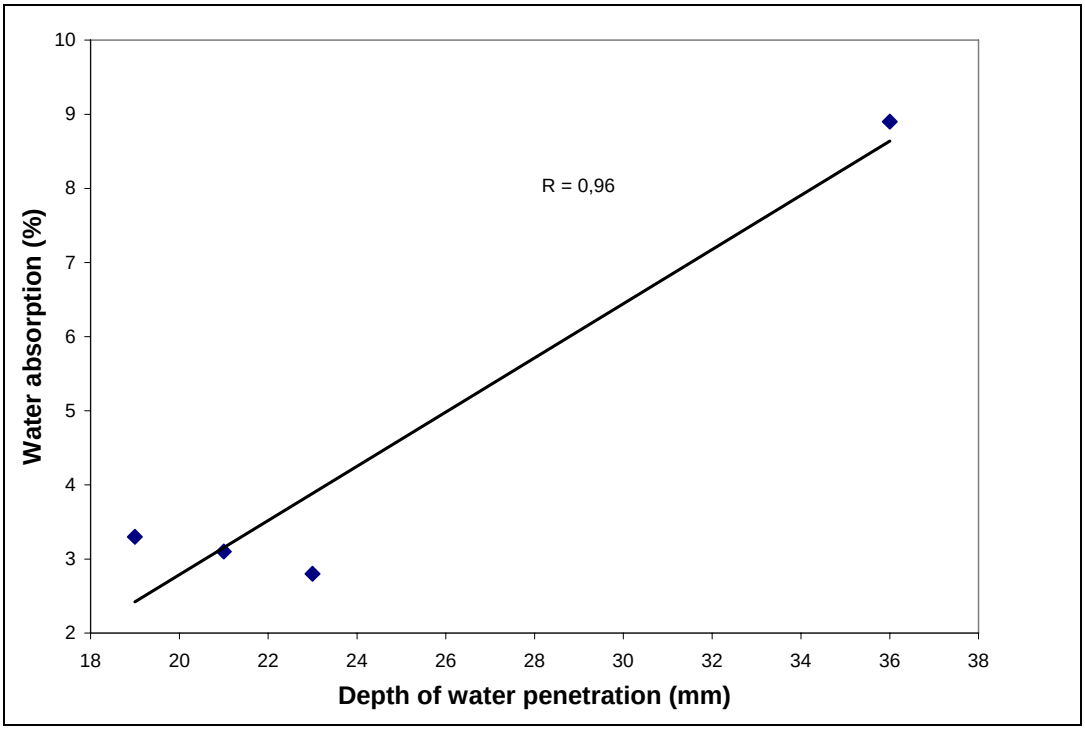

Figure 5.127. Relationship between depth of penetration and water absorption of 28-day concretes

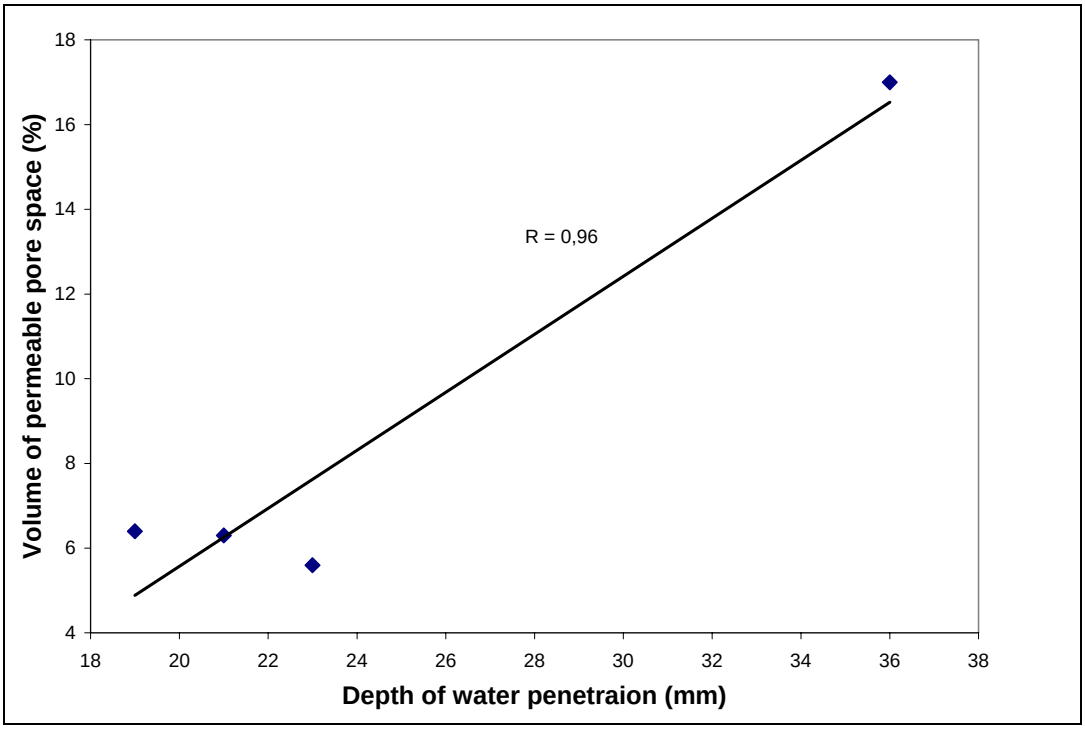

Figure 5.128. Relationship between depth of penetration and volume of permeable pore space of 28-day concretes

5.3.7. Rapid Freezing and Thawing Test

The rapid freeze and thaw cycling test is beneficial to determine the frost resistance of concrete specimens by comparing the durability performance of concretes. The properties of lightweight aggregates are enhanced by the improvements in the production methods and processes. However, the resistance of lightweight aggregate concrete to freeze–thaw cycling is still unclear. Table 5.47, Figures 5.129 and 5.130 show relative dynamic modulus of elasticity and durability factor of concretes in the rapid freze-thaw cycling test.

Concrete that has the ability to resist the destructive forces imposed upon it, by environmental constraints and without requiring excessive maintenance, is termed durable concrete [133]. Factors such as freeze–thaw cycling can cause deterioration of concrete in a relatively short period of time. Therefore, concrete durability is directly correlated to its state of deterioration. The water present in concrete, exposed to freezing conditions, undergoes an expansion process. This is primarily due to the 9 % expansion of the water in the concrete. As the water in the moist concrete freezes, it produces osmotic and hydraulic pressures in the cement paste and the aggregate. As these pressures increase, micro-cracks begin to form leading to rupture. Rupture occurs as the pressure exceeds the tensile strength of the paste or aggregate. Resistance to freezing and thawing depends on many factors: permeability, degree of saturation, amount of freezable water, and rate of freezing. Freeze–thaw resistance can be increased with the selection of good quality aggregate, the low water/cement ratio, the right amount of cement content, and the proper curing conditions.

The relative dynamic modulus of elasticity of a durable concrete specimen exposed to accelerated freze-thaw cycling should be equal to or greater than 60 % of the initial value after 300 cycles. The freeze and thaw test can be ideal for determining relative durability. It is not intended for quantitative analysis but rather to compare the durability performance of different concretes. The durability factor is found by determining the number of cycles (N) at which the relative dynamic modulus of elasticity reached 60 % as previously indicated. A part of micro-cracks occured in hardening stage may collect moisture that may be frozen and expand at low temperatures, through which cracks may

propagate and join each other and ultimately damage the microstructure of concrete [134]. Meanwhile, concrete under the repeated freeze–thaw cycling produces new micro-cracks, which mostly fall into the range of 0.1–10 microns in size. The formation of these micro-cracks is the result of the repeated opposite direction of thermal stresses developed within the microstructure. The decrease in values of the relative dynamic modulus of elasticity results from the fact that the repeated freezing and expansion stresses coupled with the thermal stresses have exceeded the tensile strength of concrete, which leads to the formation of micro-cracks.

In this study, all the 28- day and 56-day concrete specimens had a durability factor greater than 85 and 90 respectively, which met the requirement for freeze-thaw durability. LWCC showed the relatively poor performance at 28 and 56 days due to the existence of large amount of voids in the lightweight aggregates resulting in increase of the amount of freezable water and saturation degree of concrete. However the durability factor of LWBC was the highest (92.8) at 56 days which indicates a significant resistance against freze-thaw. The use of water-saturated aggregates (approaching the 24 hr water absorption) at the time of mixing generally reduces freezing and thawing resistance of lightweight concrete [16]. As the degree of saturation of the concrete increases dramatically, damage arises much faster in wet frost testing [135]. NWC exhibited also lower frost resistance as compared to concretes with sintered aggregates. The results revealed that all specimens possesed high and similar resistance to freze-thaw exposure. It is important to note that the concretes were cured for 28 and 56 days before exposure to freeze thaw cycling. The results may have been quite different if the specimens were cured for a shorter period of time as specified in ASTM C 666. It is widely recognized that while the ASTM Test Method for Resistance of Concrete to Rapid Freezing and Thawing (C 666) provides a useful comparative testing procedure, there remains an inadequate correlation between accelerated laboratory test results and the observed behavior of mature concrete exposed to natural freezing and thawing [123]. When freezing-and-thawing tests are conducted, ASTM C 330 requires the following modification to the procedures of ASTM C 666, “Unless otherwise specified, remove the lightweight concrete specimens from moist curing at an age of 14 days and allow to air-dry for another 14 days exposed to a relative humidity of 50 ± 5% and a temperature of 73.5 + 3.5 °F (23 ± 2 °C). Then submerge the specimens in water for 24 h before the freezing and thawing test.” In addition, all concretes contained

nearly 4 % air content which reduced the negative effect of freeze thaw cycling. As in normal weight concretes, it is demonstrated that air entrainment provides a high degree of protection to lightweight concretes exposed to freezing and thawing [16]. All concretes contained silica fume leading to increase in the density of microstructure and thus improvement of durability. Also it is known that concretes in the lower strength ranges had relatively poor freeze-thaw resistance than high strength concretes. In a study [135], hydraulic flow into voids in high performance concrete during wet freeze/thaw was also studied and found that high performance concrete could be very freeze/thaw resistant when properly cured. Many lightweight concretes can perform equivalent to or better than normal weight concretes. However, in a study [136], it was observed that the relative dynamic modulus of elasticity of concretes started to increase slightly through the freezing-and-thawing test and it was still greater than 90 and 110 %, even after 320 cycles. According to previous researchers, low water-cement ratio concrete can resist frost attack even without aerated treatments [134]. However, there are other research works demonstrating that low water-cement ratio concrete still suffers from frost attack, while directly correlating low void ratios to frost resistance has simplified the scenario. As a result, it is common to find a large variation in testing results and even contradictory conclusions for the same specimen. These results show that there are some inconsistensies in freeze thaw test results obtained in different investigations.

The results of weighing specimens presented that all concrete types lost small amount of mass during cycles. However they maintained their integrity. Also, no cracks or spalling was observed visually. For concrete to perform satisfactorily in severe exposure conditions, it is essential that a good bond develops and is maintained between the aggregate and the enveloping continuous mortar matrix [123]. A high incidence of interfacial cracking or aggregate debonding would have a serious effect on durability if these cracks fill with water and subsequently freeze. In conclusion, all concretes showed quite perfect resistance to freeze-thaw.

Table 5.47. Results of freeze thaw cycling test of concretes

Cycles	0	50	100	150	200	250	300
Concretes	Relative dynamic modulus of elasticity (%)						
LWCC28	100	98.3	97.8	96.3	93.4	90.0	86.1
LWCC56	100	98.6	97.9	97.0	96.3	93.9	90.2
LWBC28	100	99.0	97.4	96.8	94.8	92.2	88.1
LWBC56	100	99.1	98.6	98.0	97.2	94.3	92.8
LWGC28	100	98.3	97.6	96.3	94.0	92.1	87.9
LWGC56	100	99.7	99.1	98.9	98.1	96.1	92.3
NWC28	100	99.3	97.0	96.3	94.7	91.1	87.1
NWC56	100	99.8	99.3	98.6	97.6	94.1	91.3

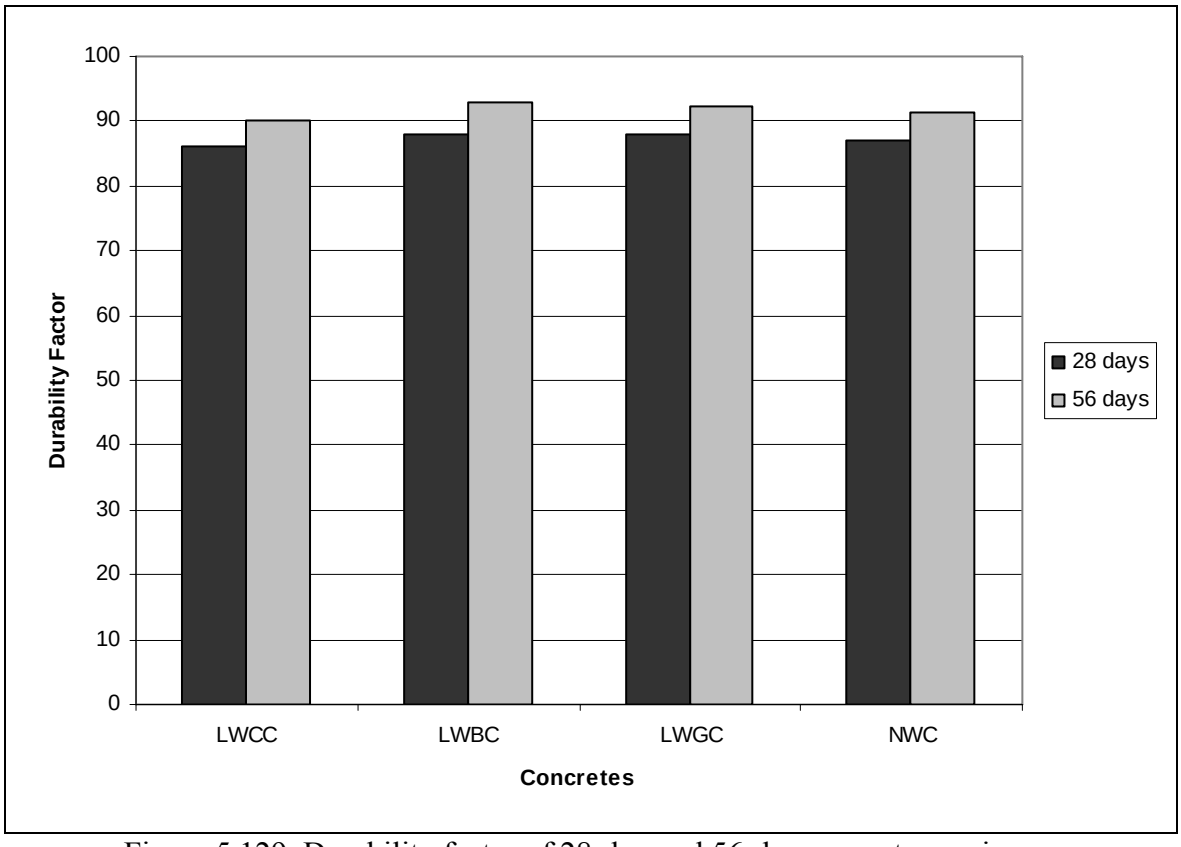

Figure 5.129. Durability factor of 28-day and 56-day concrete specimens

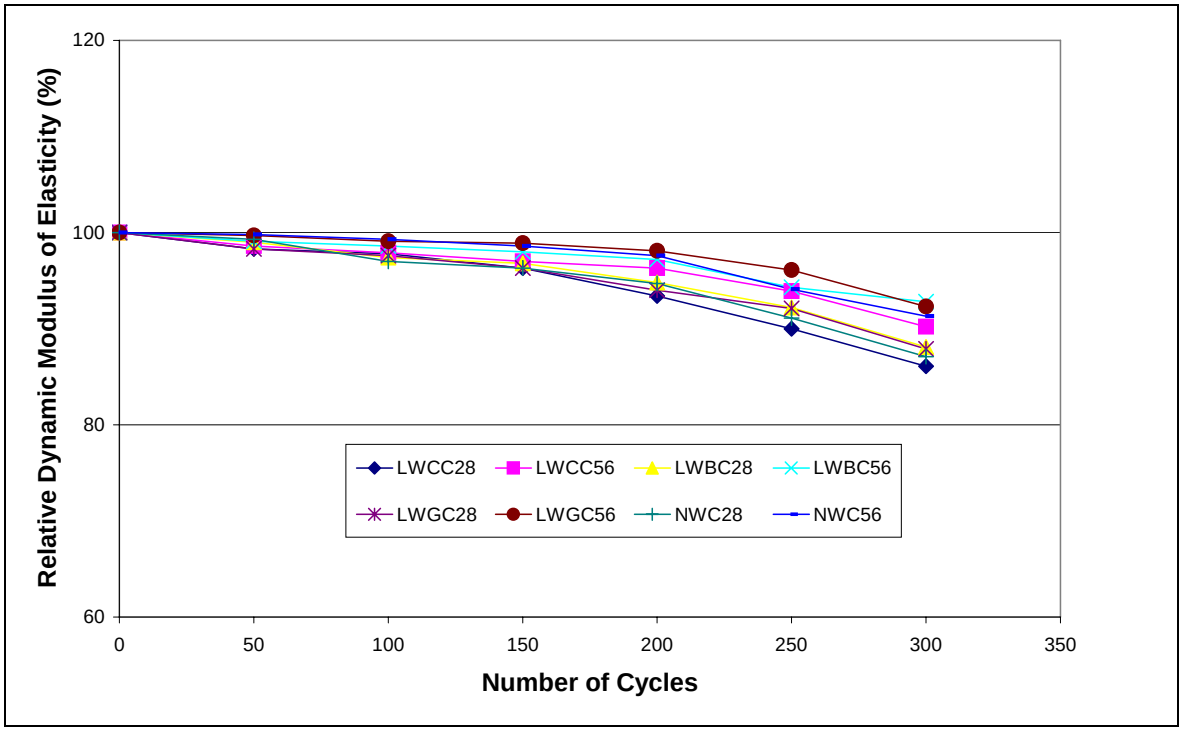

Figure 5.130. Relative dynamic modulus of elasticity of 28-day and 56-day concrete specimens

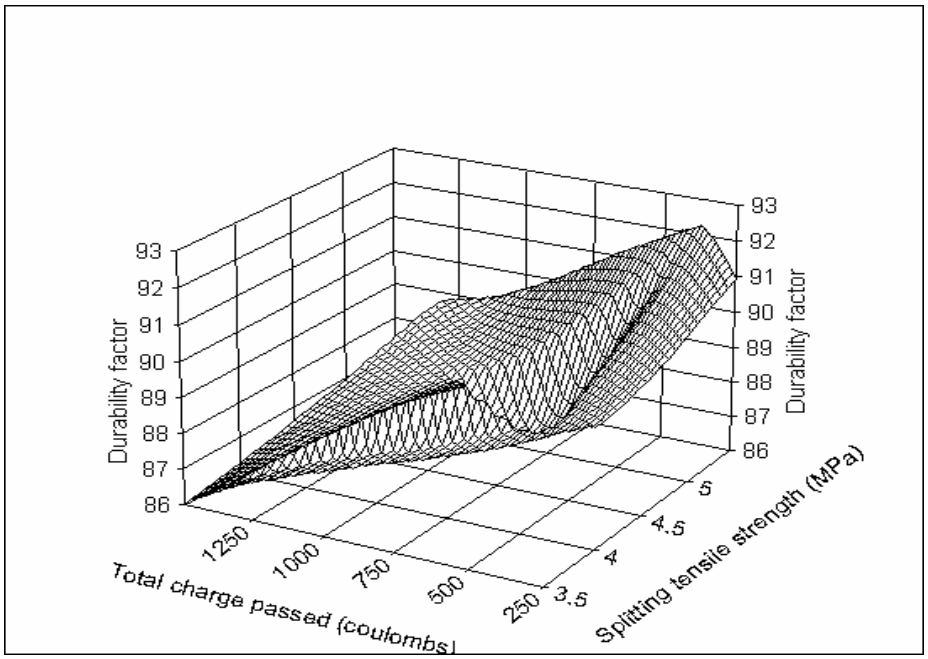

Figure 5.131. 3D view of experimental results

The below equation is based on the quadratic model between the durability factor (*Z*) and splitting tensile strength (*X*) and total charge passed (*Y*) suggested by the software against other models since this model fitted well with the experimental data.

$$D=a+b*\sigma_t+c*Q+d*Q^2 \quad (5.82)$$

The significance of each coefficient was determined by Student's t-test and p-values (Table 5.48). Values of "Prob>F'' less than 0.0500 indicate that model terms are significant. The results demonstrated that the factor most significant for the durability factor was the linear effect of total charge passed and the next was the linear effect splitting tensile strength and quadratic effect of total charge passed. There was no interaction effect between splitting tensile strength and total charge passed were significant for durability factor.

Table 5.48. Coefficients of the model given by software

Parm	Value	Std Error	t-value	P>|t|
a	111,2245269	3,787969028	29,36257557	0,00001
b	-2,79755173	0,668759665	-4,18319447	0,01388
c	-0,01786403	0,002541537	-7,02882812	0,00216
d	5,33E-06	1,39E-06	3,833267344	0,01857

The quadratic model was found to fit the experimental data best with standard deviation of 0.06028 with correlation coefficient (R^2 value) of 0.967, indicating that the fitnesses of the selected model is good. The results of the response surface fitting in the form of analysis of variables are shown in Tables 5.49 and 5.50. The F-test with a low probability value showed a high significance for the regression model. The value of the adjusted determination coefficient (adjusted $R^2 = 0.923$) is also very high which indicates a high significance for the model. Figure 5.131 and 5.132 illustrated 3D view of theexperimental results and predicted values obtained by the software, respectively.

Table 5.49. ANOVA for response surface fit to the experimental results

Source	Sum of Squares	DF	Mean Square	F value	P>F
Regr	42,84139	3	14,28046	39,2964	0,002
Error	1,453615	4	0,363404		
Total	44,295	7			

Table 5.50. Actual and predicted values by response surface fit for durability factor

X	Y	Z	Z Predicted	Residual	Residual %
3,7	1464	86,1	86,15399	-0,05399	-0,0627
3,9	748	90,2	89,93644	0,263562	0,292198
4,8	586	88,1	89,15979	-1,05979	-1,20294
4,9	701	87,9	87,6152	0,284798	0,324002
5,1	264	92,8	92,6127	0,187299	0,201831
5,1	295	92,3	92,15136	0,148643	0,161043
5,1	729	87,1	86,76909	0,330909	0,379919
5,3	308	91,3	91,40143	-0,10143	-0,1111

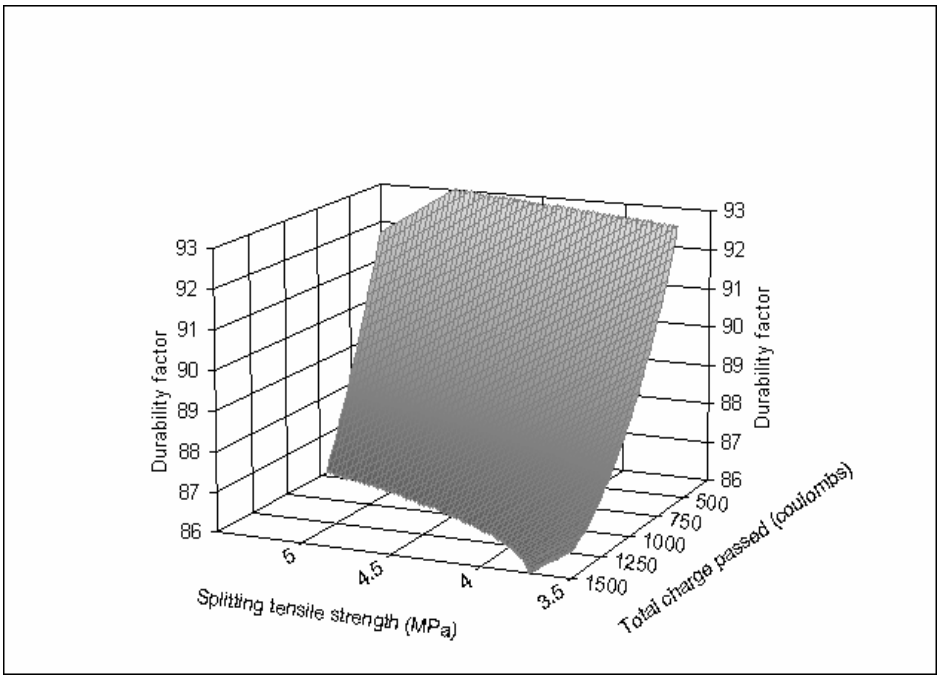

Figure 5.132. 3D view - response surface plot showing the effect of splitting tensile strength and total charge passed on durability factor

Regression analysis was performed on the durability factor related with other experimental results which gave the best fits against other regression models shown in Figures 5.133-5.139 with the following equations:

$$D = 64{,}874\ \sigma^{0{,}0801},\ R = 0{,}4583 \text{ for compressive strength at all ages} \quad (5.83)$$

$$D = 53{,}65\ \sigma^{0{,}1295},\ R = 0{,}6551 \text{ for compressive strength of LWC at all ages} \quad (5.84)$$

$$D = 8E\text{-}18\sigma^{9{,}6863},\ R = 0{,}6083 \text{ for compressive strength at 28 days} \quad (5.85)$$

$$D = 75{,}034\ \sigma^{0{,}0495},\ R = 0{,}6693 \text{ for compressive strength at 56 days} \quad (5.86)$$

$$D = 1{,}9643\ \sigma_t + 80{,}169,\ R = 0{,}4690 \text{ for splitting tensile strength at all ages} \quad (5.87)$$

$$D = 2{,}5238\ \sigma_t + 77{,}999,\ R = 0{,}5901 \text{ for splitting tensile strength of LWC at all ages} \quad (5.88)$$

$$D = 2E\text{-}21\ \sigma_t^{11{,}003},\ R = 0{,}7875 \text{ for splitting tensile strength at 28 days} \quad (5.89)$$

$$D = 82{,}31\ \sigma_t^{0{,}0683},\ R = 0{,}7702 \text{ for splitting tensile strength at 56 days} \quad (5.90)$$

$$D = 117{,}35Q^{-0{,}0431},\ R = 0{,}9110 \text{ for total charge passed at all ages} \quad (5.91)$$

$$D = 117{,}39Q^{-0{,}0427},\ R = 0{,}9178 \text{ for total charge passed of LWC at all ages} \quad (5.92)$$

$$D = 102{,}82Q^{-0{,}0244},\ R = 0{,}9424 \text{ for total charge passed at 28 days} \quad (5.93)$$

$$D = 105{,}31Q^{-0{,}0235},\ R = 0{,}9004 \text{ for total charge passed at 56 days} \quad (5.94)$$

$$D = 81{,}695t^{0{,}0156},\ R = 0{,}9950 \text{ for corrosion time at 28 days} \quad (5.95)$$

$$D = -0{,}1041d + 89{,}877,\ R = 0{,}8775 \text{ for water penetration depth at 28 days} \quad (5.96)$$

$$D= -0,2722w + 88,531,\ R = 0,8775 \text{ for water absorption at 28 days} \quad (5.97)$$

$$D = -0,1473v+ 88,6,\ R = 0,8832 \text{ for permeable voids at 28 days} \quad (5.98)$$

where:

D = durability factor

σ = compressive strength in MPa

σ_t = splitting tensile strength in MPa

Q = total charge passed in coulombs

t = corrosion time in days

d = depth of water penetration in mm

w = water absorption in %

v = volume of permeable pore space in %

The linear models showed the linearity between the durability factor and splitting tensile strength, water penetration depth, water absorption and volume of permeable voids. The durability factor was directly proportional to these results of hardened concrete. The positive sign of the equations showed that the durability factor increased with increasing the results, whereas negative sign of the equations showed that the durability factor increased with decreasing the results. Large R values of models showed that the regression was established under good fit, which means that there was no remarkable variation in the durability factor and other experimental results of concrete. In contrast, small R values demonstrated that the model was established under poor fit with considerable scatter. When the values of normalweight concrete were exported, the R values increased. Also, separately 28-day values showed larger R values than both 56-day and 28 and 56-day values except compressive strength which had the largest 56-day R value among other ages. In addition, relationship between durability factor and mechanical properties exhibited smaller R values than permeability properties.

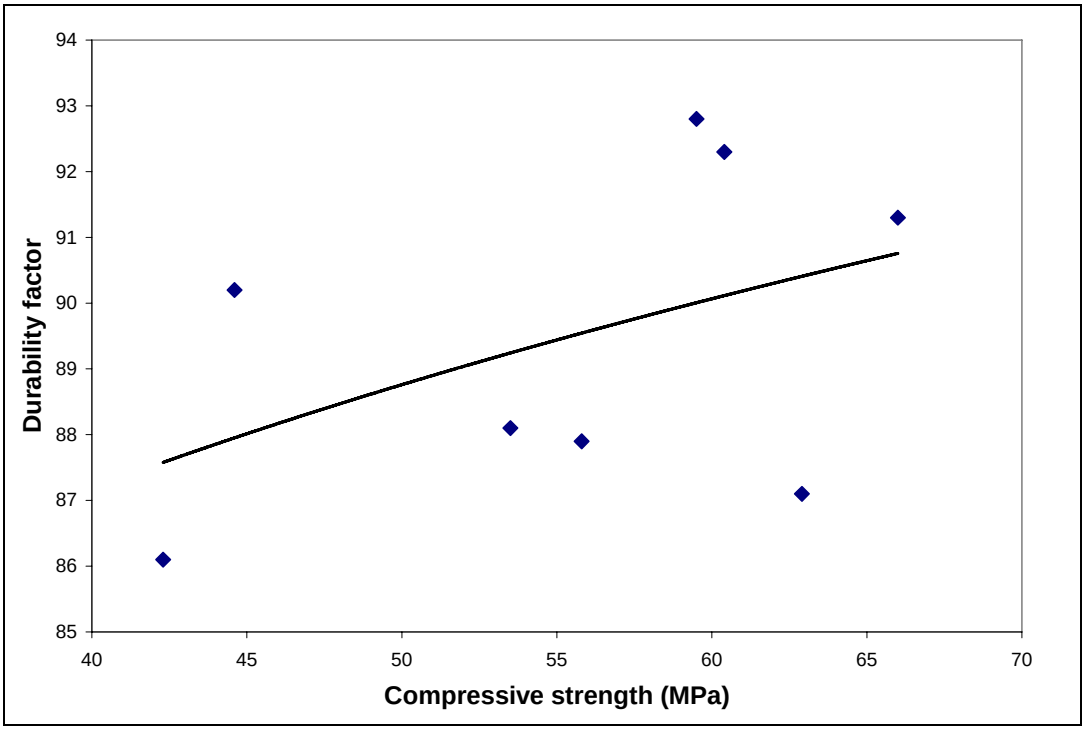

Figure 5.133. Relationship between durability factor and compressive strength

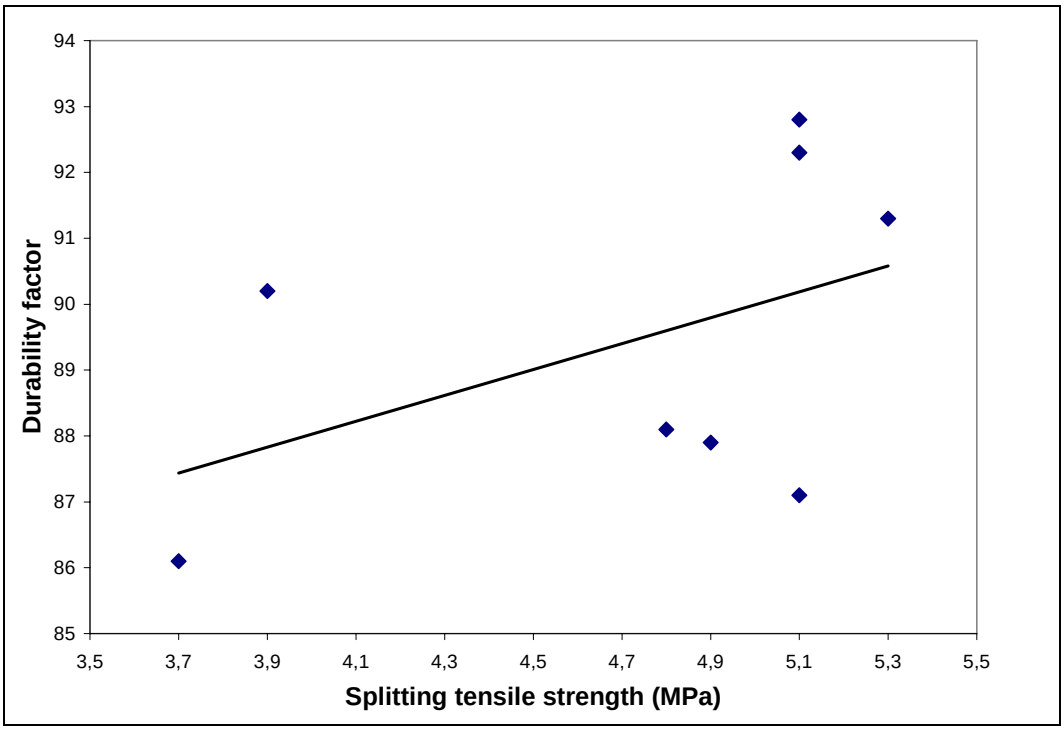

Figure 5.134. Relationship between durability factor and splitting tensile strength

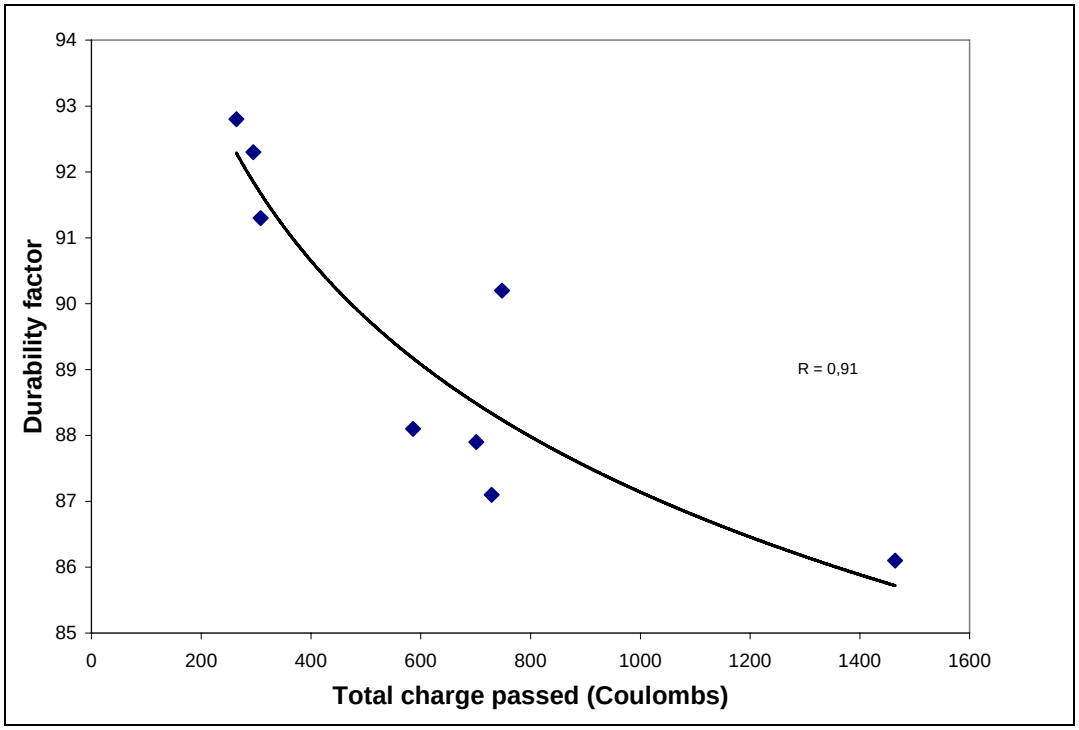

Figure 5.135. Relationship between durability factor and total charge passed

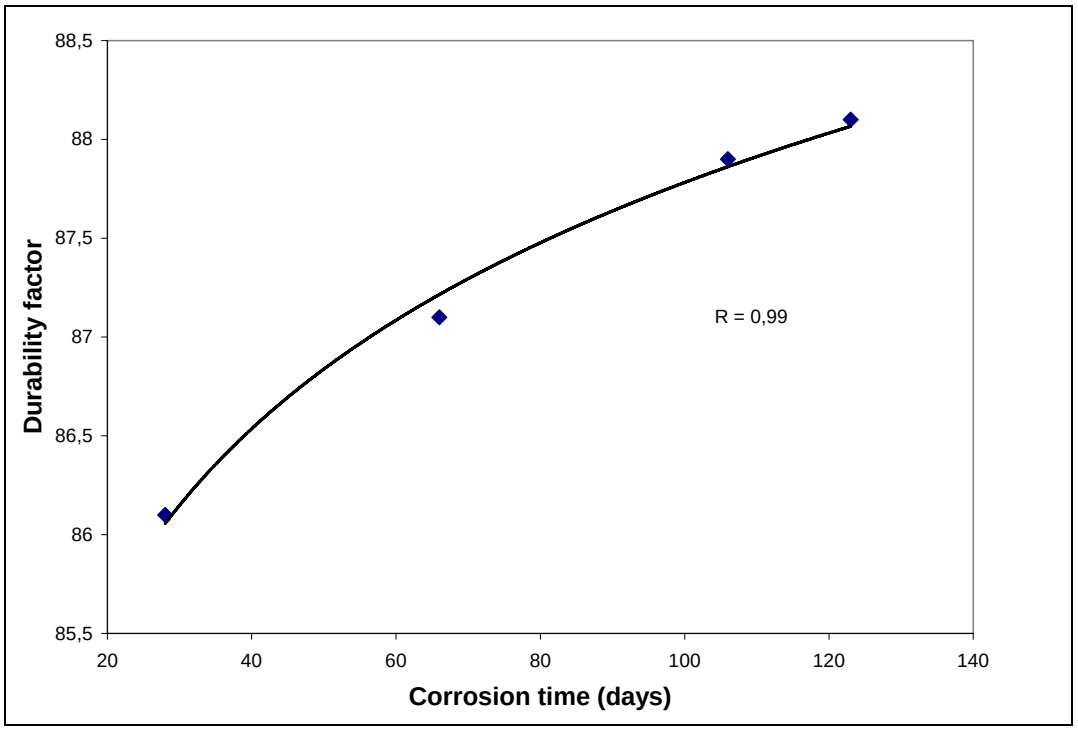

Figure 5.136. Relationship between durability factor and corrosion time of 28-day concretes

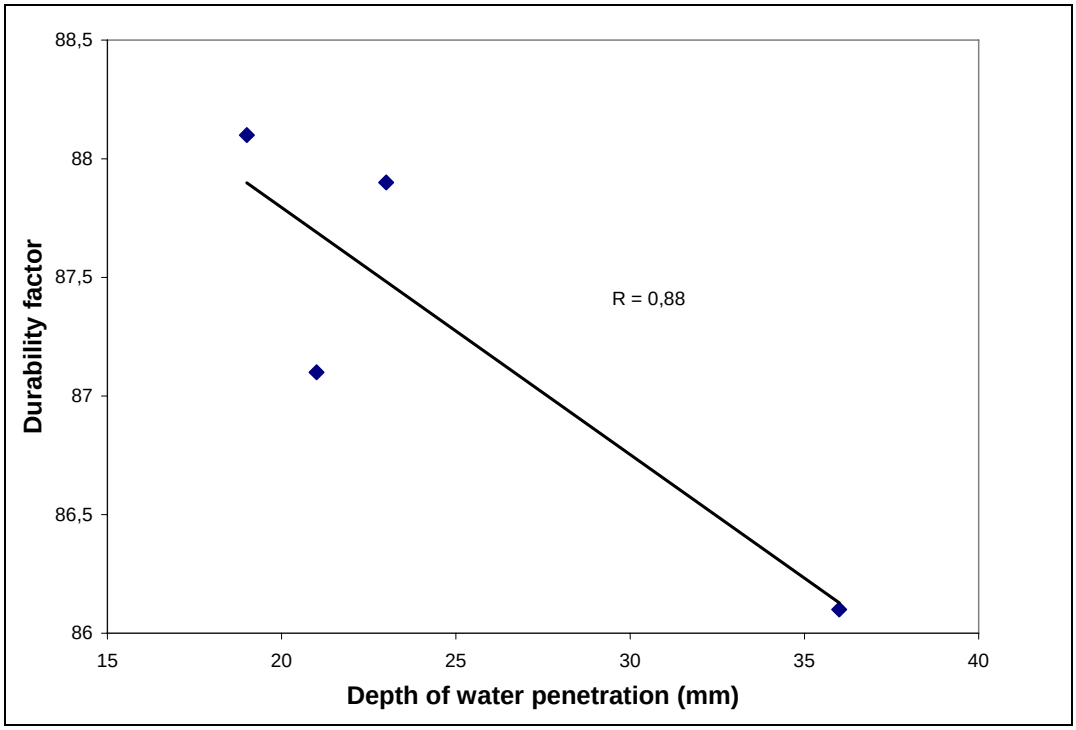

Figure 5.137. Relationship between durability factor and depth of water penetration of 28-day concretes

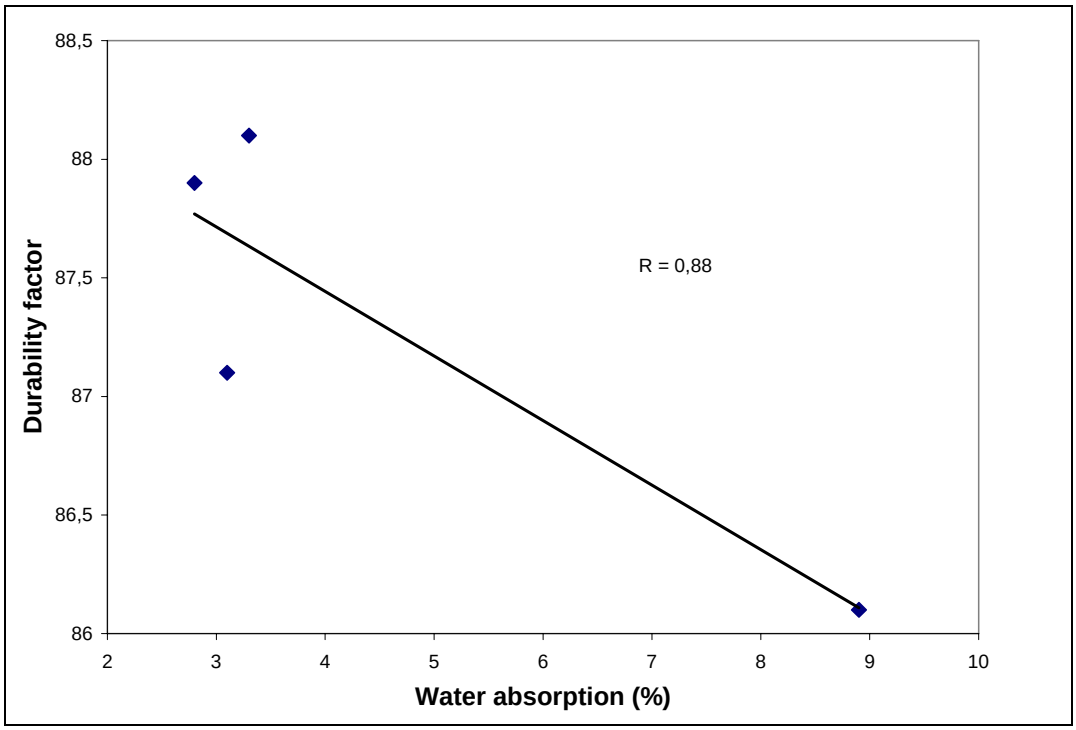

Figure 5.138. Relationship between durability factor and water absorption of 28-day concretes

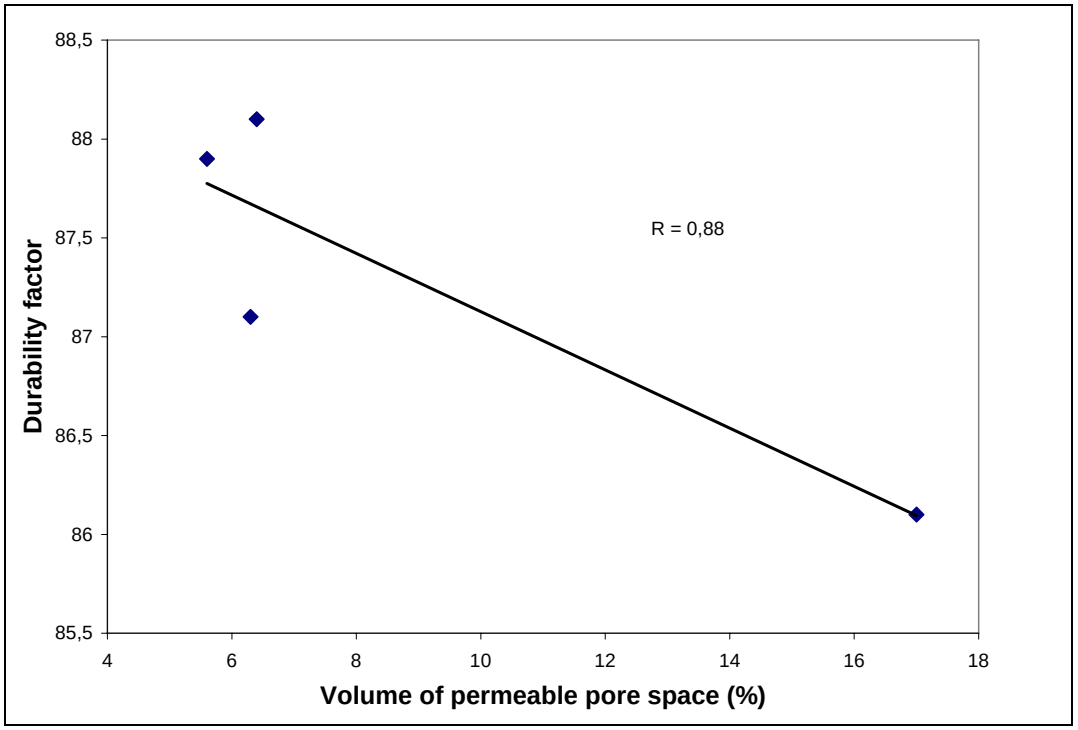

Figure 5.139. Relationship between durability factor and permeable voids of 28-day concretes

5.3.8. SEM Observations of Hardened Concretes

Figures 5.141-5.148 show the transition zone between the cement paste and the normalweight and the lightweight aggregates at the age of 28 and 56 days. Also, Figure 5.140 shows the cement paste matrix of concretes having entrained air voids with nearly 10-100 microns diameter, uniformly distributed and spherical in shape in the cement paste phase.

Before any systematic work is done to understand the cement matrix microstructure aiming to increase the concrete properties, studies which approach the improvement of the ITZ between the aggregate and the cement matrix should be prioritized, since many important properties of the concrete are significantly influenced by the characteristics of that ITZ [137]. However, the nature of the contact between cement paste and aggregate (large and small) which occurs in mortar and concrete has been and still remains somewhat of an enigma [138]. Various groups and individuals have studied the interfacial regions and observed a number of interesting phenomena. For example, the transition in physical properties one observes as one crosses an aggregate-paste boundary is not a sharp

discontinuity, but a gradual one. The so-called "Aureole de transition" (transition zone) has both a real extent and thickness, and as such it can be considered as a separate entity having discrete intrinsic properties, properties which impact on the performance of mortars and concrete. To date, it has been demonstrated that the interfacial region has a finite thickness and enhanced porosity. As such, it is often referred to as the weakest part of concrete, where fracture is initiated, and as an avenue of attack for corrosive chemical agents.

The contact zone is the transition layer of material connecting the coarse-aggregate particle with the enveloping continuous mortar matrix [123]. Analysis of this linkage layer requires consideration of more than the adhesion developed at the interface (contact zone) and should include the transitional layer that forms between the two phases. Collapse of the structural integrity of a conglomerate may come from the failure of one of the two phases or from a breakdown in the contact zone causing a separation of the still-intact phases. The various mechanisms that act to maintain continuity, or that cause separation, have not received the same attention as has the air-void system necessary to protect the paste. Aggregates are often inappropriately dismissed as being inert fillers and, as a result, they and the associated transition zone have until recently received very modest attention.

The images were selected to be representative as far as the condition of the cement paste and the interface of paste–aggregate were concerned. There was not any considerable differentiation among the cement matrix of concretes. In all samples, the cement paste appears to be uniform in color. Besides, the entrapped air is uniformly distributed in the form of small rounded bubbles. Separation of most aggregates and cement matrix in contact zone could take place during preparation of samples for SEM observations.

Some researches present results demonstrating that the mineral additions can produce a significant reduction in the thickness of the matrix-aggregate ITZ, besides the densification of such region, contributing to an improvement of the properties related to mechanical strength and concrete durability [137]. In this study, this phenomenon indicated that in the case of cold bonded aggregates, the fly ash and cement reacted with calcium hydroxide made by C_2S and C_3S and produced C-S-H at 56 days as can be seen Figure 5.152. Furthermore, cold bonded lightweight aggregates strengthened and narrowed

the transition zone because of consuming the calcium hydroxide. The reaction of CH and fly ash forms CSH gel, which results in increased compressive strengths. Fly ash tends to have a low reaction rate [133]. At 28 days, the degree of fly ash reaction rate is slightly more than 10%. Furthermore, only 20% of the fly ash reacts after 90 days. One explanation for the low activity of fly ash at room temperature is that the pH of the solution 13 does not meet the requirements of fly ash, 13.3. In the normalweight concrete, mechanical bonding of normalweight aggregates with the cement paste matrix was observed due to their more angular shapes (Figures 5.147 and 5.148). The strong bond was also detected in the case of sintered aggregates resulting in concrete strength increase (Figures 5.143-5.146). Also, silica fume is considered a very effective mineral addition in the reduction of the thickness of the matrix-aggregate ITZ. The reduction in porosity of concrete incorporating silica fume can be linked to improvements that occur on the interfacial transition zones between the cement matrix and the aggregate. In the lightweight and normalweight concretes, it is possible to observe an improvement in the matrix-aggregate ITZ characteristics, such as reduction of porosity.

The contact zone in lightweight concrete is the interface between two porous media: the lightweight-aggregate particle and the hydrating cement binder [123]. This porous media interface allows for hygral equilibrium to be reached between the two phases, thus eliminating weak zones caused by water concentration. In contrast, the contact zone of normalweight concrete was an interface between the nonabsorbent surface (wall effect) of the dense aggregate and a water-rich binder. The accumulation of water at that interface is subsequently lost during drying, leaving a porous, low-quality matrix at the interface.

In any composite material, the properties of the constituents and the interactions between them determine the behaviour of the material [52]. Concrete is a composite material with coarse and fine aggregates embedded in a cement paste matrix. As such, the aggregate and the cement paste as well as the interfacial zone between them affect the mechanical behaviour and permeability, thus durability of concrete. In concrete, it is generally not the porosity but the pore structure that is essential in establishing the permeability. In addition to that, microcracks in the matrix may contribute significantly to the permeability. In the light of this explanation, in this study, the interface zone was in tight and locking bond between the two phases of all concretes. Cracking did not initiate in

the interface but rather was arrested at the interfacial zone. This means that cracks that may occur in the aggregate itself did not spread uncontrollably through the matrix [14]. This is due to both the strength of the interfacial zone and the strength of the matrix itself.

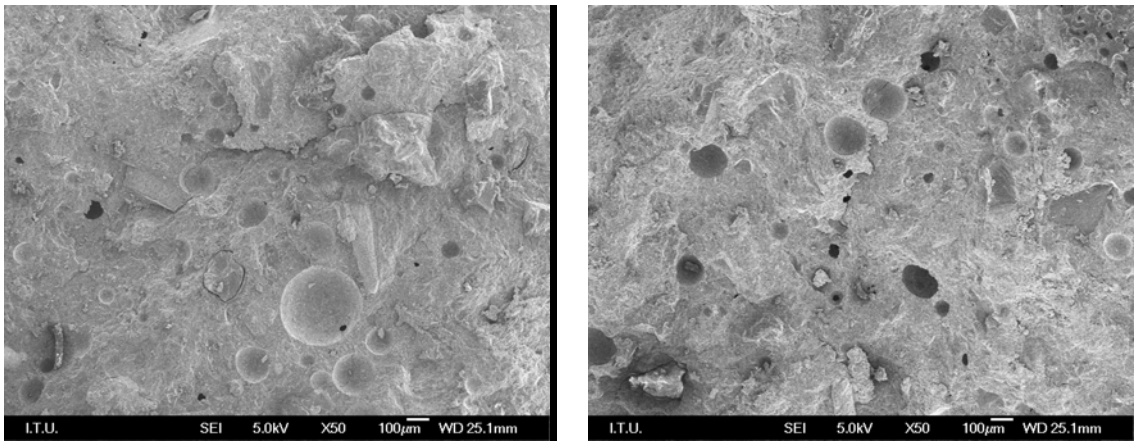

Figure 5.140. Scanning electron micrograph of air-entrained cement paste of concretes

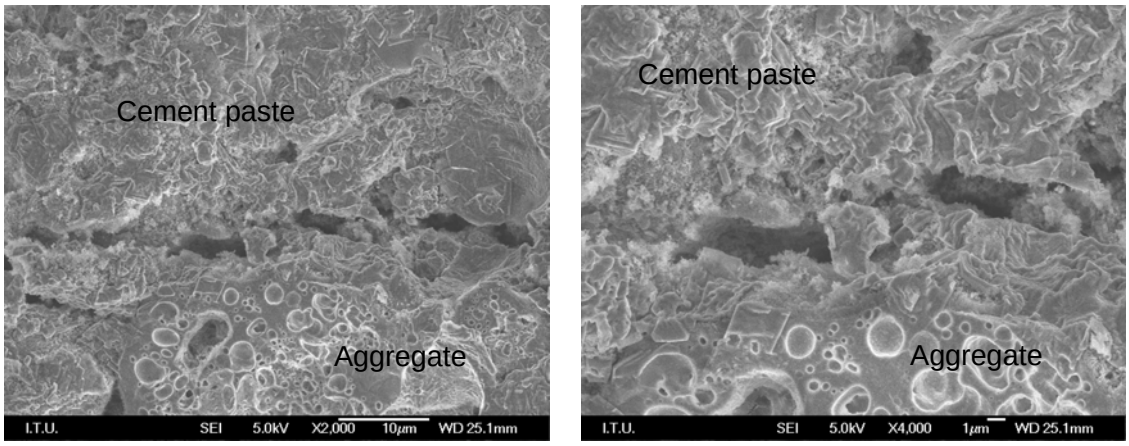

Figure 5.141. The interface of paste–aggregate of LWCC in 28 days with magnifications of x2000 and x4000

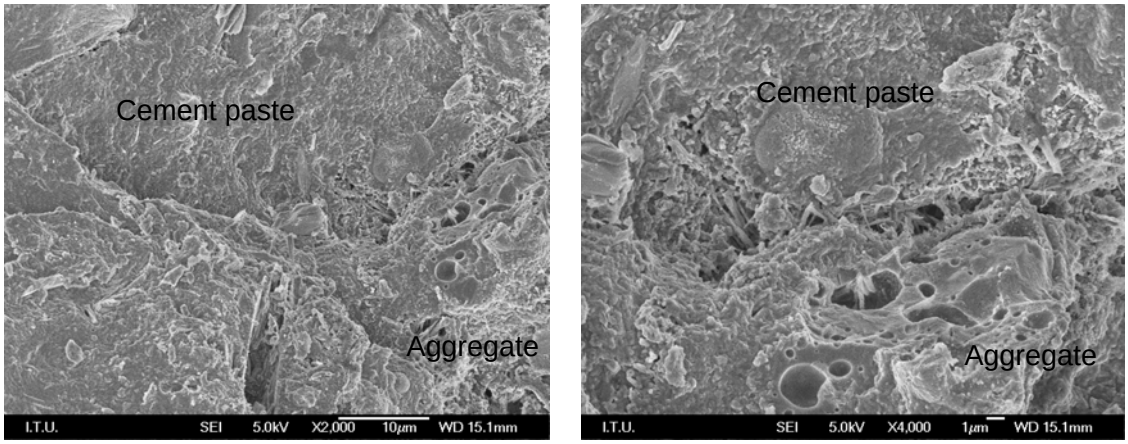

Figure 5.142. The interface of paste–aggregate of LWCC in 56 days with magnifications of x2000 and x4000

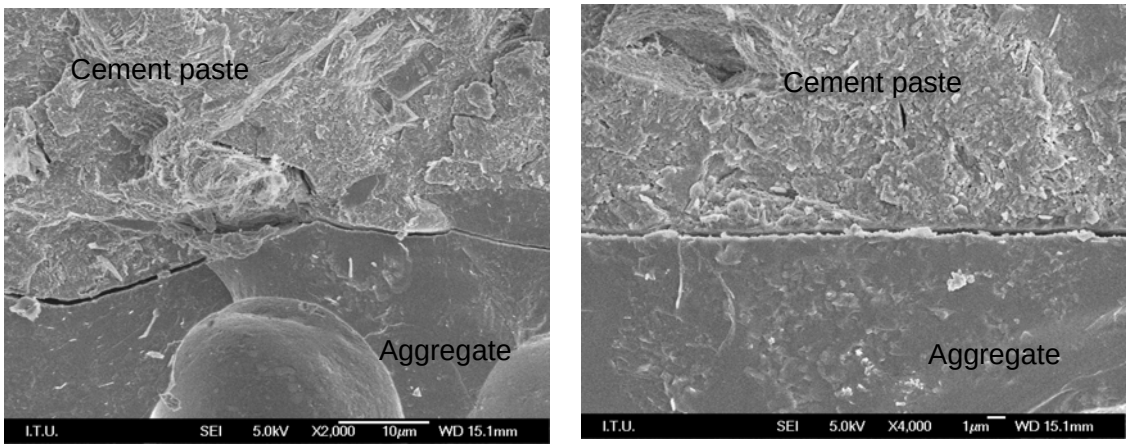

Figure 5.143. The interface of paste–aggregate of LWBC in 28 days with magnifications of x2000 and x4000

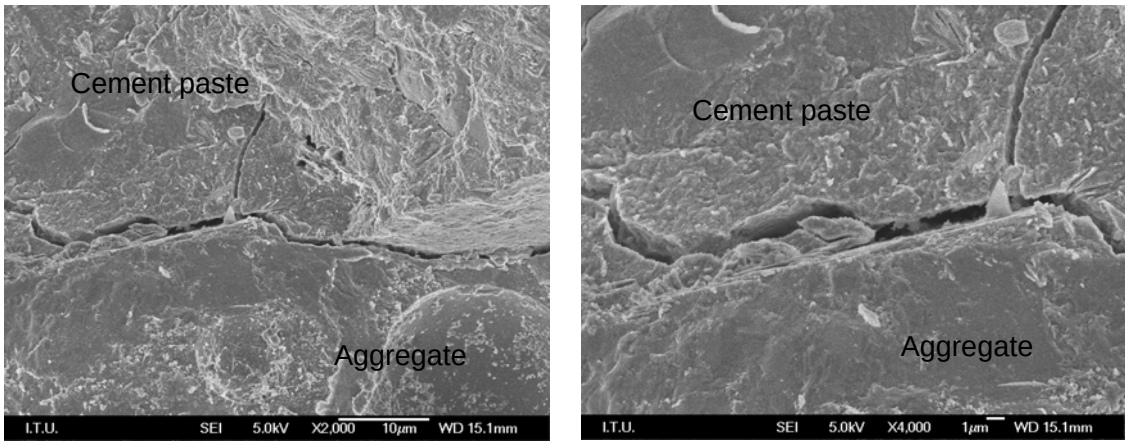

Figure 5.144. The interface of paste–aggregate of LWBC in 56 days with magnifications of x2000 and x4000

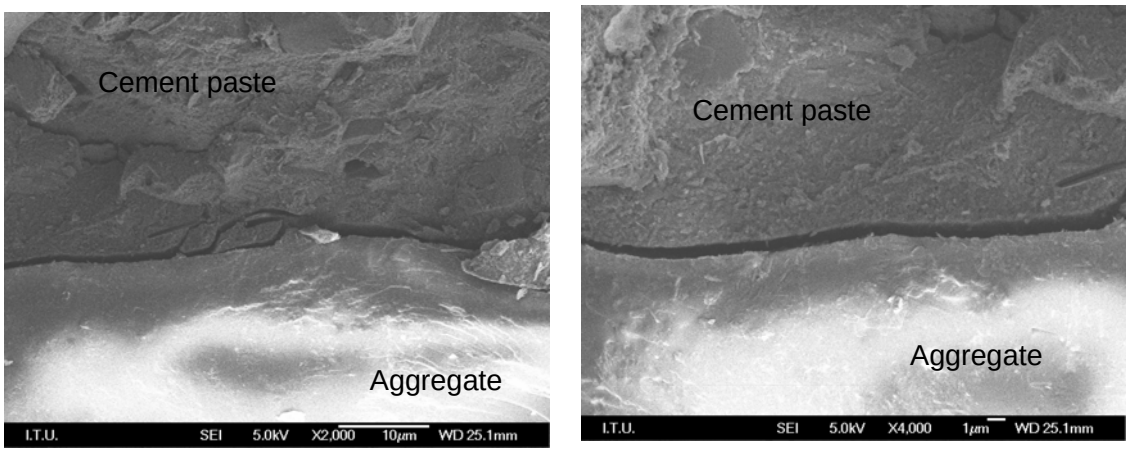

Figure 5.145. The interface of paste–aggregate of LWGC in 28 days with magnifications of x2000 and x4000

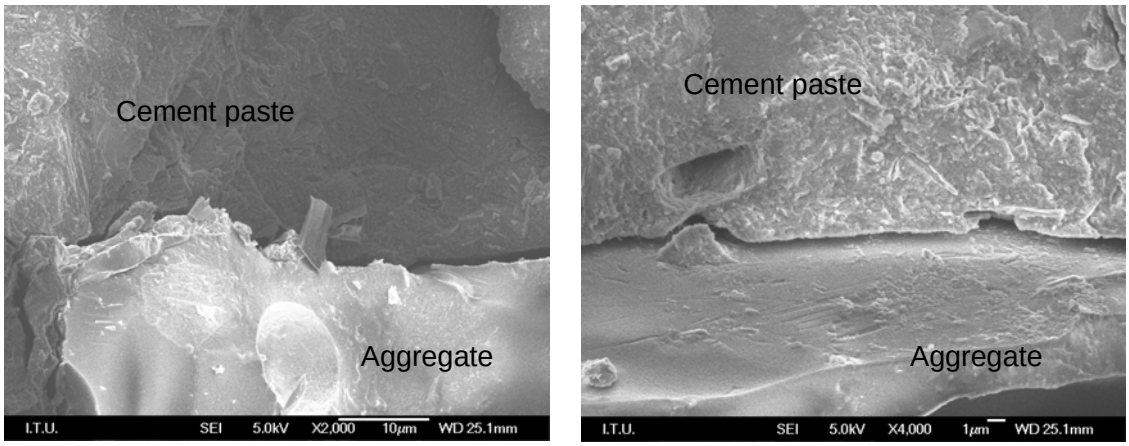

Figure 5.146. The interface of paste–aggregate of LWGC in 56 days with magnifications of x2000 and x4000

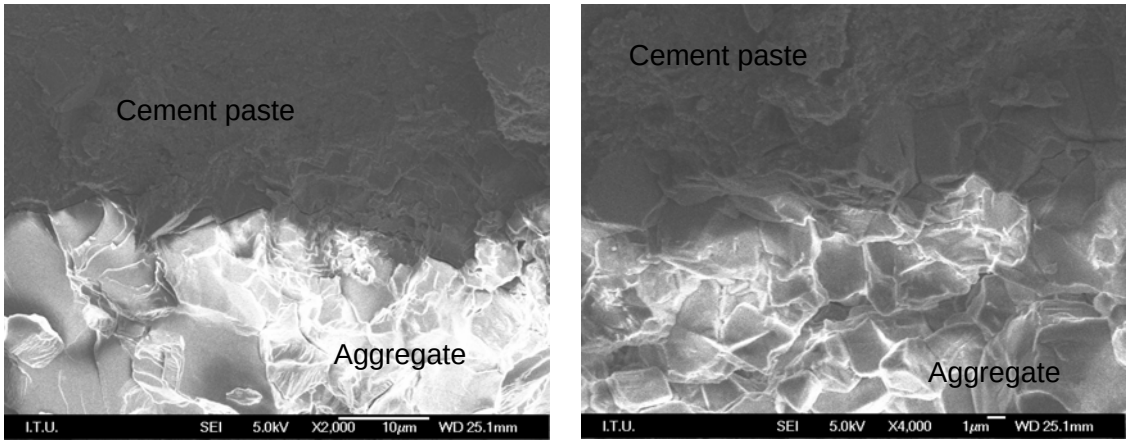

Figure 5.147. The interface of paste–aggregate of NWC in 28 days with magnifications of x2000 and x4000

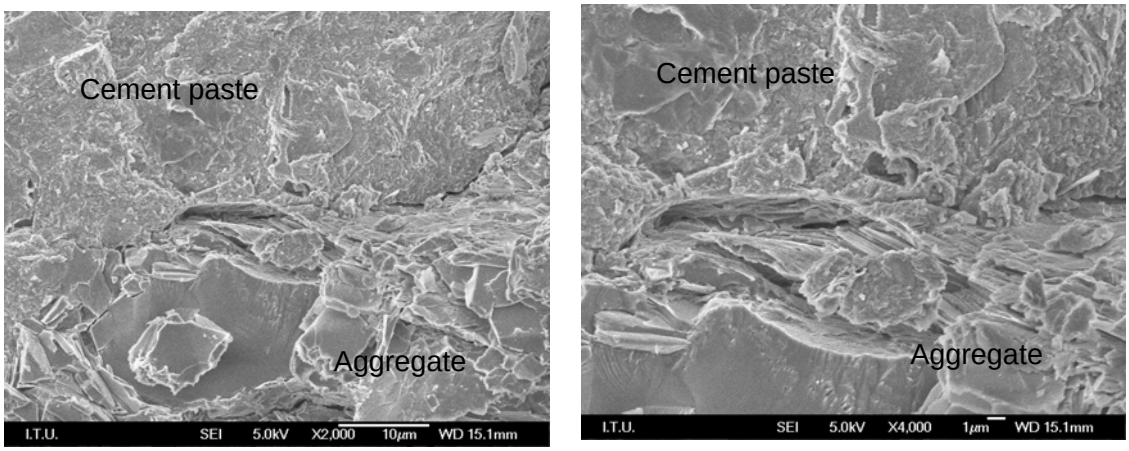

Figure 5.148. The interface of paste–aggregate of NWC in 56 days with magnifications of x2000 and x4000

6. CONCLUSIONS AND RECOMMENDATIONS FOR FUTURE WORKS

6.1. Conclusions

The following conclusions and recommendations were drawn from this study:

For lightweight fly ash aggregates:

- The highest and the lowest specific gravity values for only fly ash aggregates (OFA) were obtained by sintering at 1200 ^{o}C and 1100 ^{o}C, whereas for aggregates with binder sintered at 1150 ^{o}C and 1200 ^{o}C, mostly gave the highest and lowest specific gravities, respectively.

- Specific gravity values continuously increased with increasing the sintering temperature in the case of OFA aggregates. At the temperatures 1100 and 1150 ^{o}C, increasing bentonite content increased the specific gravity, however increasing glass powder content caused reduction in dry basis specific gravity. The results indicated that the use of glass powder and bentonite as binders in fly ash led to a significant reduction in specific gravity in the resulting aggregate sintered at 1200 ^{o}C. The effect was more prominent in the aggregates containing higher content of binders.

- Cold-bonded fly ash lightweight aggregate had specific gravities of 1.61 and 1.30 in saturated surface dry and oven dry condition, respectively. For specific gravity in SSD condition, its specific gravity was among the lowest ones and for OD condition it had the lowest specific gravity in oven-dry condition among other aggregate types due to its excessive internal porosity.

- The water absorption of all aggregate types declined with the increase in temperature. Only fly ash aggregates (OFA) showed linear decrease, however aggregates with binders exhibited a significant decrease up to 1150 ^{o}C, then the drop was slight up to

1200 ^{o}C. Increasing binder content reduced the water absorption at all temperatures. The water absorption of cold-bonded aggregates was 23.9 % which was the highest absorption among all aggregate types, followed by OFA1100 with a value of 18.4 %.

- In the case of total porosity of OFA aggregates, similar trend was observed as in water absorption. There was a linear reduction in porosity of OFA aggregates. The addition of binders reduced the total porosity at 1100 and 1150 ^{o}C, however the total porosity increased with the use of binders at 1200 ^{o}C. Generally, the critical pore diameters of aggregates showed paralellism with the total porosity values. The critical diameter decreased with temperature in aggregates without binders. However, aggregates with binders showed decrease up to 1150 ^{o}C, then rise with further increase in temperature.

- The crushing strength of aggregates with bentonite slightly increased by the content of bentonite at these mentioned temperatures, however aggregates with glass powder exhibited a slight decrease with content increase at 1150 ^{o}C. The highest strength values were obtained for OFA aggregates by sintering at 1200 ^{o}C, for aggregates with binders by sintering at 1150 ^{o}C. The strength of all aggregates decreased with increasing the binder content at 1200 ^{o}C. Bentonite was more effective in strength rise than glass powder especially at 1150 ^{o}C. The strength of aggregates with glass powder was lower than that of aggregates with bentonite at all temperatures. The strengths of aggregates with binders showed the same trend of pellet densities with increasing temperature, increasing to a maximum value and then decreasing, as expected. The crushing strength of cold-bonded lightweight aggregates was 3.7 MPa which was the lowest value among all sintered aggregates.

- In the DTA thermogram of the fly ash, one endothermic peak was recorded at 440 ^{o}C, due to the glass transition and formation of CO_2 from carbon compounds, followed by one exhotermic peak at 623 ^{o}C due to the ferrous and sulphides oxidation and combustion of organic materials. However, although endotermic peaks were observed for all aggregates, exhotermic peaks began to disappear by increase in binder content. The TGA curves of the materials used in aggregate production showed different weight loss trend due to various reasons. The reasons of the weight losses were unburned

carbon, organic materials, sulfide, hydrate, carbonate, iron, oxide present in the materials.

- According to SEM results, only fly ash aggregates sintered at 1100 ^{o}C exhibited poorly sintered structure with very few necks between the particles, resulting in poor mechanical properties, low density and high water absorption. With increasing temperature, fly ash particles coalesce forming necks among the particles and resulting in higher density and under some conditions good mechanical properties starting at 1150 ^{o}C. With the addition of binders, the neck growth rate and neck size increased greatly starting at 1100 ^{o}C. The SEM test was also performed to visually examine the resulting hydration products of cold bonded aggregates. Aggregates with low water absorption and high strength can be attributed to the discontinuous porosity, dense structure and small pore size at 1150 °C. However, the water absorption, specific gravity and strength values were low for aggregates containing binders at 1200 °C owing to the large pores, formation of glassy texture on the surface and closed porosity.

- Fly ash and other sintered aggregates presented a crystalline formation and amorphous phase. The broad hump was observed due to the glass content, present in the diffraction spectrum at around 23^{o}. The reduction of quartz peaks was observed for all aggregate types with temperature increase. Also, cold-bonded aggregates presented formation of calcite with the quartz, and mullite peaks as the main crystalline phases.

- The optimization results obtained by Design Expert software demonstrated that, whatever the optimization criteria, aggregates with the highest binder contents sintered at high temperature have the highest desirabilities among all aggregates that would lead to minimum specific gravity and water absorption and maximum strength.

- The experimental observations were consistent with the SEM images, DTA and XRD trends.

For lightweight aggregate concretes:

- It is clear that in order to obtain similar slump and air content value for lightweight concretes as compared to normal weight concrete, a lower amount of superplasticizer and air entraining agent was needed. When natural coarse aggregate was replaced by lightweight aggregates, there was a significant reduction in the density of fresh and hardened concrete. All of the lightweight concretes had a fresh and oven-dry density lower than 2000 kg/m^3. Although LWCC had a greater fresh density than the other lightweight concretes, its oven-dry density was lower than the others due to the porosity of cold-bonded aggregate.

- The use of lightweight fly ash aggregate in concrete led to a higher reduction in the modulus of elasticity and compressive strength than in the splitting tensile strength, the percentage of this reduction decreased in 56 days. Although replacement of lightweight aggregates for normalweight aggregates in concrete production decreased the strength, lightweight concretes improved the resistance to permeability and freeze-thaw cycling of the concretes.

- In the normalweight concrete, mechanical bonding of normalweight aggregates with the cement paste matrix was observed due to their more angular shapes. The strong bond was also detected in the case of sintered aggregates resulting in concrete strength increase. In the case of cold bonded aggregates, the fly ash and cement reacted with calcium hydroxide made by C_2S and C_3S and produced C-S-H at 56 days. Furthermore, cold bonded lightweight aggregates strengthened and narrowed the transition zone because of consuming the calcium hydroxide.

- The results of this study showed that the production of high-strength air-entrained lightweight aggregate concretes were achieved by using sintered and cold-bonded fly ash aggregates.

6.2. Recommendations for Future Works

In this study, fly ash used was very coarse. Powders with fine particle size distributions have advantageous sintering characteristics because the high surface area to volume ratio increases diffusion of small particles through the liquid phase to the larger particles. The binders and fly ash can be milled prior to sintering to improve its particle size distribution for processing. Wet milling can be preferred because it has been found to provide more uniform particle size distribution, the liquids used in the wet milling process tend to break up agglomerates and reduce welding of powder particles. Alternatively, dry milled in a hammer mill can be applied.

The aggregates were agglomerated prior to sintering to create agglomerates having a desired size and shape to form the sintered aggregate and to improve concrete properties. Pelletization was agglomeration method in this study. Other methods can be used to obtain aggregates such as crushing after sintering.

Three different temperatures were selected based on the proportion of binders to fly ash to make an aggregate having desired density and other properties, such as water absorption and strength. Decrease in sintering temperature can be achieved resulting in lower cost and energy. Thus, binders other than bentonite and glass powder and different proportions of binders can be used. Also, heating rate was constant in this study. Aggregate properties can be investigated by selecting different heating rates.

Different sintered lightweight fly ash aggregates were chosen for use in high-strength lightweight concrete according to both trial mixes and optimization results obtained from Design Expert software. Other aggregates produced in this study with relatively high densities that are impermeable to water ingress with high strengths can be used as replacement aggregates in conventional (normal weight) concrete.

APPENDIX A: ACTUAL AND PREDICTED VALUES OF RESPONSES BY D-OPTIMAL DESIGN

Table A.1. Actual and predicted values of specific gravity

Standard Order	Temperature ^{o}C	Binder content	Binder type	Actual Value	Predicted Value	Residual	Error
1	1100	5	B	1,75	1,72	0,029447	1,68
2	1150	0	B	1,74	1,81	-0,06521	3,75
3	1150	10	B	1,94	1,86	0,083225	4,29
4	1200	5	B	1,63	1,71	-0,07828	4,80
5	1100	0	G	1,49	1,50	-0,01179	0,79
6	1200	10	G	1,6	1,59	0,010978	0,69
7	1100	10	G	1,77	1,80	-0,03276	1,85
8	1150	5	G	1,93	1,90	0,032412	1,68
9	1200	0	G	1,93	1,89	0,043664	2,26
10	1100	0	B	1,51	1,50	0,007821	0,52
11	1200	0	B	1,92	1,79	0,130947	6,82
12	1150	0	G	1,73	1,85	-0,12365	7,15
13	1100	10	B	1,77	1,85	-0,08289	4,68
14	1100	5	G	1,81	1,70	0,114709	6,34
15	1200	10	G	1,58	1,59	-0,00902	0,57
16	1150	10	B	1,93	1,86	0,073225	3,79
17	1100	0	G	1,52	1,50	0,018214	1,20
18	1200	5	B	1,61	1,71	-0,09828	6,10
19	1100	10	G	1,76	1,80	-0,04276	2,43

Table A.2. Actual and predicted values of water absorption (%)

Standard Order	Temperature °C	Binder content	Binder type	Actual Value	Predicted Value	Residual	Error
1	1100	5	B	8,4	9,97	-1,57101	18,7
2	1150	0	B	10,1	9,30	0,801705	7,9
3	1150	10	B	0,7	1,68	-0,98087	140,1
4	1200	5	B	0,8	0,01	0,789595	98,7
5	1100	0	G	18,8	18,78	0,018314	0,1
6	1200	10	G	0,6	0,64	-0,04124	6,9
7	1100	10	G	8	8,18	-0,18171	2,3
8	1150	5	G	3,4	3,90	-0,50496	14,9
9	1200	0	G	2	2,65	-0,64753	32,4
10	1100	0	B	18,4	18,01	0,393378	2,1
11	1200	0	B	2,4	3,75	-1,34917	56,2
12	1150	0	G	10,7	9,14	1,564995	14,6
13	1100	10	B	7,8	6,09	1,707647	21,9
14	1100	5	G	11,6	11,40	0,196779	1,7
15	1200	10	G	0,8	0,64	0,158757	19,8
16	1150	10	B	0,8	1,68	-0,88087	110,1
17	1100	0	G	18	18,78	-0,78169	4,3
18	1200	5	B	1,1	0,01	1,089595	99,1
19	1100	10	G	8,4	8,18	0,218288	2,6

Table A.3. Actual and predicted values of crushing strength (MPa)

Standard Order	Temperature °C	Binder content	Binder type	Actual Value	Predicted Value	Residual	Error
1	1100	5	B	13,1	11,9	1,171467	8,9
2	1150	0	B	9,2	10,3	-1,08568	11,8
3	1150	10	B	24,0	18,7	5,328435	22,2
4	1200	5	B	13,7	17,0	-3,32871	24,3
5	1100	0	G	4,8	5,4	-0,58354	12,2
6	1200	10	G	10,1	10,5	-0,38408	3,8
7	1100	10	G	12,0	11,9	0,100964	0,8
8	1150	5	G	15,6	11,3	4,273769	27,4
9	1200	0	G	19,0	17,5	1,461736	7,7
10	1100	0	B	5,1	4,3	0,756831	14,8
11	1200	0	B	19,6	16,2	3,371818	17,2
12	1150	0	G	8,0	11,5	-3,4609	43,3
13	1100	10	B	13,7	19,5	-5,8139	42,4
14	1100	5	G	9,7	8,6	1,058713	10,9
15	1200	10	G	9,0	10,5	-1,48408	16,5
16	1150	10	B	22,2	18,7	3,528435	15,9
17	1100	0	G	5,3	5,4	-0,08354	1,6
18	1200	5	B	13,1	17,0	-3,92871	30,0
19	1100	10	G	11,0	11,9	-0,89904	8,2

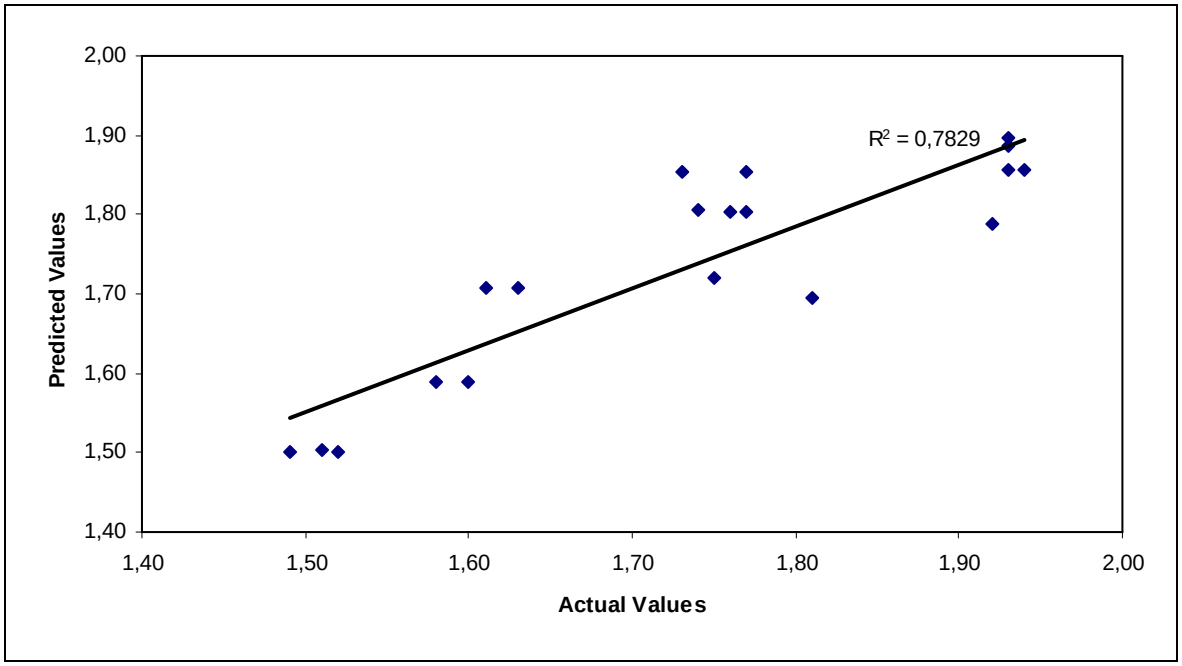

Figure A.1. Predicted vs actual values of specific gravity (gr/cm3)

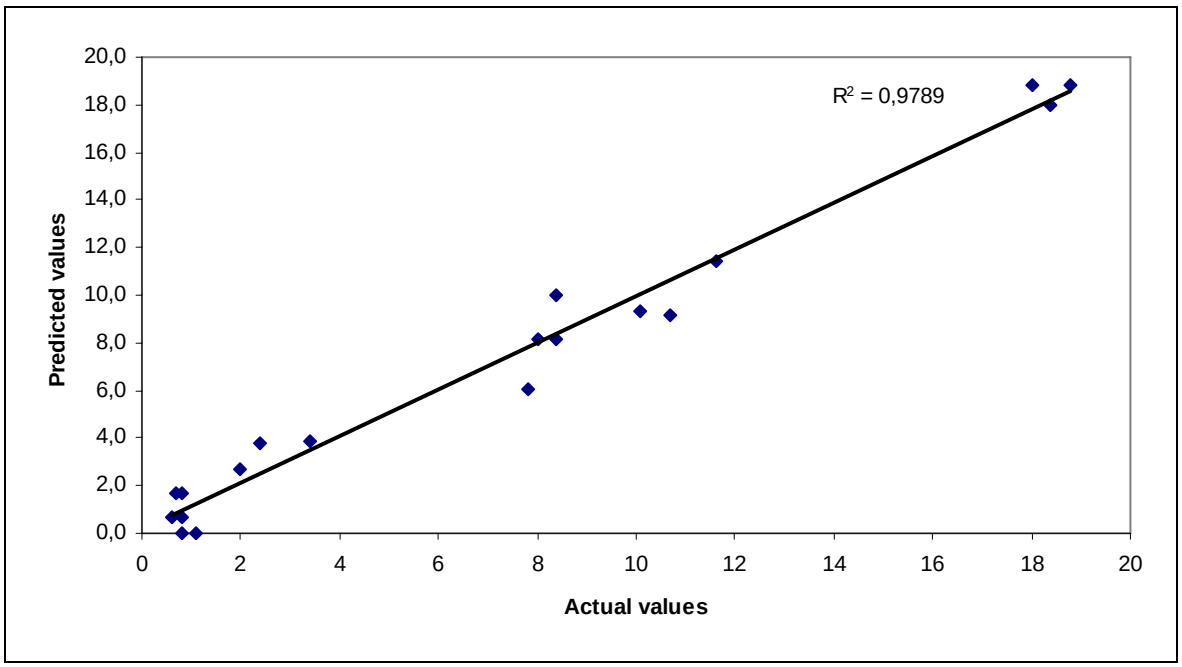

Figure A.2. Predicted vs actual values of water absorption (%)

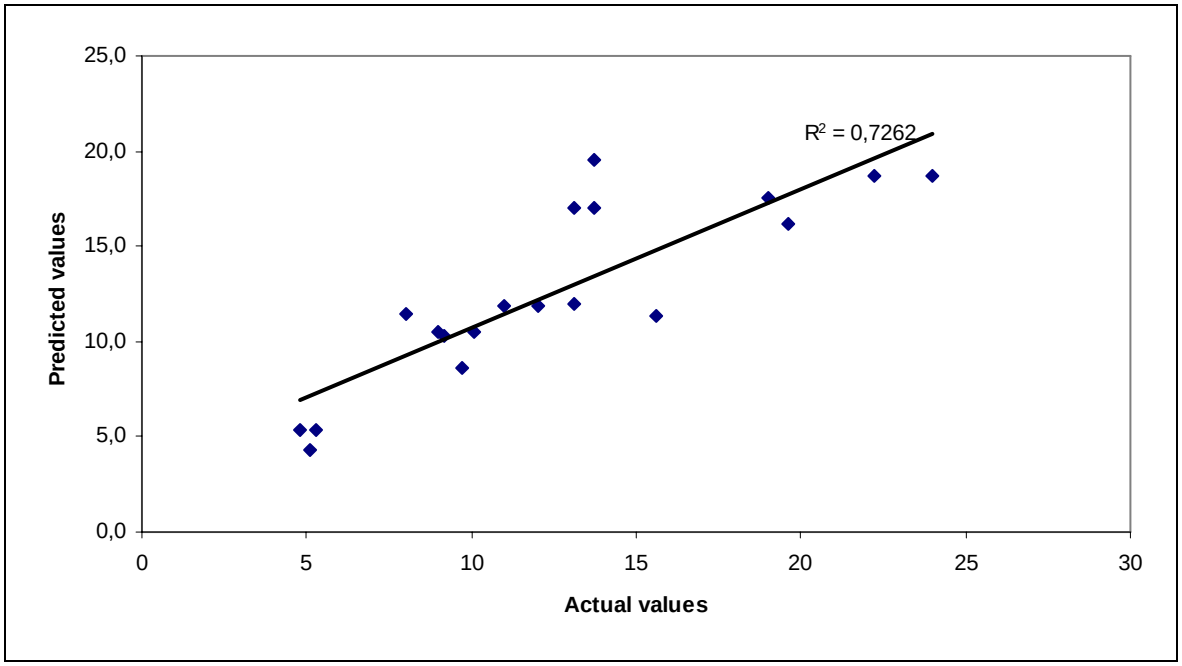

Figure A.3. Predicted vs actual values of crushing strength (MPa)

APPENDIX B: ACTUAL AND PREDICTED VALUES OF RESPONSES BY HISTORICAL DATA DESIGN

Table B.1. Actual and predicted values of specific gravity (OD)

Standard Order	Temperature °C	Binder content	Binder type	Actual Value	Predicted Value	Residual	Error
1	1100	0	G	1,51	1,52	-0,00764	0,51
2	1100	5	G	1,81	1,72	0,090278	4,99
3	1100	10	G	1,77	1,83	-0,06347	3,59
4	1150	0	G	1,74	1,83	-0,09139	5,25
5	1150	5	G	1,93	1,88	0,047778	2,48
6	1150	10	G	1,85	1,84	0,005278	0,29
7	1200	0	G	1,92	1,85	0,073194	3,81
8	1200	5	G	1,66	1,75	-0,08639	5,20
9	1200	10	G	1,59	1,56	0,032361	2,04
10	1100	0	B	1,51	1,50	0,007917	0,52
11	1100	5	B	1,75	1,71	0,0375	2,14
12	1100	10	B	1,77	1,83	-0,06458	3,65
13	1150	0	B	1,74	1,81	-0,07417	4,26
14	1150	5	B	1,9	1,87	0,026667	1,40
15	1150	10	B	1,93	1,84	0,085833	4,45
16	1200	0	B	1,92	1,83	0,092083	4,80
17	1200	5	B	1,62	1,74	-0,11583	7,15
18	1200	10	B	1,56	1,56	0,004583	0,29

Table B.2. Actual and predicted values of specific gravity (SSD)

Standard Order	Temperature ^{o}C	Binder content	Binder type	Actual Value	Predicted Value	Residual	Error
1	1100	0	G	1,79	1,81	-0,02111	1,18
2	1100	5	G	2,02	1,92	0,104722	5,18
3	1100	10	G	1,91	1,97	-0,05611	2,94
4	1150	0	G	1,92	1,99	-0,07444	3,88
5	1150	5	G	2,0	1,98	0,023889	1,19
6	1150	10	G	1,9	1,90	-0,00444	0,23
7	1200	0	G	1,97	1,90	0,070556	3,58
8	1200	5	G	1,68	1,76	-0,07861	4,68
9	1200	10	G	1,6	1,56	0,035556	2,22
10	1100	0	B	1,79	1,78	0,010556	0,59
11	1100	5	B	1,89	1,88	0,009722	0,51
12	1100	10	B	1,88	1,93	-0,04778	2,54
13	1150	0	B	1,92	1,98	-0,05778	3,01
14	1150	5	B	2,01	1,96	0,053889	2,68
15	1150	10	B	1,94	1,88	0,058889	3,04
16	1200	0	B	1,97	1,90	0,072222	3,67
17	1200	5	B	1,64	1,75	-0,11361	6,93
18	1200	10	B	1,57	1,56	0,013889	0,88

Table B.3. Actual and predicted values of apparent specific gravity

Standard Order	Temperature °C	Binder content	Binder type	Actual Value	Predicted Value	Residual	Error
1	1100	0	G	2,09	2,14	-0,04972	2,38
2	1100	5	G	2,29	2,14	0,150278	6,56
3	1100	10	G	2,06	2,12	-0,05806	2,82
4	1150	0	G	2,12	2,17	-0,05472	2,58
5	1150	5	G	2,07	2,08	-0,01222	0,59
6	1150	10	G	1,95	1,97	-0,01806	0,93
7	1200	0	G	2,02	1,95	0,071944	3,56
8	1200	5	G	1,69	1,76	-0,07306	4,32
9	1200	10	G	1,60	1,56	0,043611	2,73
10	1100	0	B	2,09	2,08	0,013611	0,65
11	1100	5	B	2,04	2,06	-0,02472	1,21
12	1100	10	B	2,00	2,03	-0,03139	1,57
13	1150	0	B	2,12	2,15	-0,03306	1,56
14	1150	5	B	2,13	2,05	0,081111	3,81
15	1150	10	B	1,96	1,92	0,036944	1,88
16	1200	0	B	2,02	1,97	0,051944	2,57
17	1200	5	B	1,65	1,77	-0,12139	7,36
18	1200	10	B	1,58	1,55	0,026944	1,71

Table B.4. Actual and predicted values of water absorption (%)

Standard Order	Temperature ^{o}C	Binder content	Binder type	Actual Value	Predicted Value	Residual	Error
1	1100	0	G	18,4	19,1	-0,68472	3,72
2	1100	5	G	11,6	11,3	0,294444	2,54
3	1100	10	G	8,2	7,9	0,290278	3,54
4	1150	0	G	10,4	9,4	1,019444	9,80
5	1150	5	G	3,4	3,9	-0,53889	15,85
6	1150	10	G	2,6	2,9	-0,28056	10,79
7	1200	0	G	2,2	3,0	-0,80972	36,81
8	1200	5	G	1,1	-0,1	1,2	108,59
9	1200	10	G	0,7	1,2	-0,48472	69,25
10	1100	0	B	18,4	18,0	0,365278	1,99
11	1100	5	B	8,4	9,7	-1,33889	15,94
12	1100	10	B	6,9	5,8	1,073611	15,56
13	1150	0	B	10,4	9,1	1,336111	12,85
14	1150	5	B	2,3	3,1	-0,80556	35,02
15	1150	10	B	0,8	1,5	-0,73056	91,32
16	1200	0	B	2,2	3,4	-1,22639	55,74
17	1200	5	B	1	-0,2	1,2	119,44
18	1200	10	B	0,7	0,6	0,131944	18,85

Table B.5. Actual and predicted values of porosity (%)

Standard Order	Temperature ^{o}C	Binder content	Binder type	Actual Value	Predicted Value	Residual	Error
1	1100	0	G	19,1	18,42	0,683333	3,58
2	1100	5	G	13,6	16,90	-3,3	-24,26
3	1100	10	G	11,3	9,23	2,066667	18,29
4	1150	0	G	13,3	9,69	3,608333	27,13
5	1150	5	G	7,3	9,85	-2,55	-34,93
6	1150	10	G	3,9	3,86	0,041667	1,07
7	1200	0	G	6,5	10,27	-3,76667	-57,95
8	1200	5	G	16,9	12,10	4,8	28,40
9	1200	10	G	6,2	7,78	-1,58333	-25,54
10	1100	0	B	19,1	19,20	-0,1	-0,52
11	1100	5	B	15,3	18,37	-3,06667	-20,04
12	1100	10	B	15,1	11,38	3,716667	24,61
13	1150	0	B	13,3	10,04	3,258333	24,50
14	1150	5	B	10,1	10,88	-0,78333	-7,76
15	1150	10	B	2	5,58	-3,575	178,75
16	1200	0	B	6,5	10,18	-3,68333	-56,67
17	1200	5	B	17,6	12,70	4,9	27,84
18	1200	10	B	8,4	9,07	-0,66667	-7,94

Table B.6. Actual and predicted values of crushing strength (MPa)

Standard Order	Temperature °C	Binder content	Binder type	Actual Value	Predicted Value	Residual	Error
1	1100	0	G	5,1	4,9	0,2	3,92
2	1100	5	G	9,7	9,4	0,333333	3,44
3	1100	10	G	11,5	13,8	-2,33333	20,29
4	1150	0	G	8,6	11,3	-2,7	31,40
5	1150	5	G	15,6	11,8	3,833333	24,57
6	1150	10	G	14,7	12,2	2,466667	16,78
7	1200	0	G	19,3	17,7	1,6	8,29
8	1200	5	G	11,8	14,2	-2,36667	20,06
9	1200	10	G	9,6	10,6	-1,03333	10,76
10	1100	0	B	5,1	5,5	-0,43333	8,50
11	1100	5	B	13,1	12,2	0,933333	7,12
12	1100	10	B	13,7	18,8	-5,1	37,23
13	1150	0	B	8,6	11,7	-3,06667	35,66
14	1150	5	B	20,4	14,3	6,1	29,90
15	1150	10	B	23,1	16,9	6,166667	26,70
16	1200	0	B	19,3	17,8	1,5	7,77
17	1200	5	B	13,4	16,4	-3,03333	22,64
18	1200	10	B	12	15,1	-3,06667	25,56

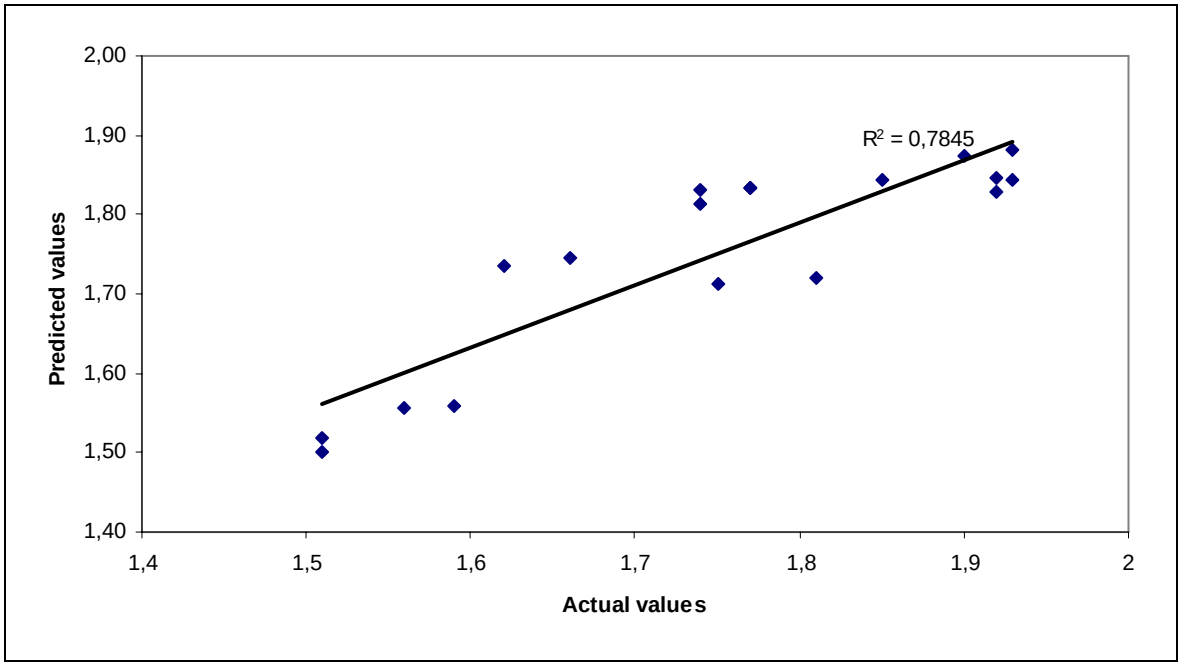

Figure B.1. Predicted vs actual values of specific gravity (OD) (gr/cm3)

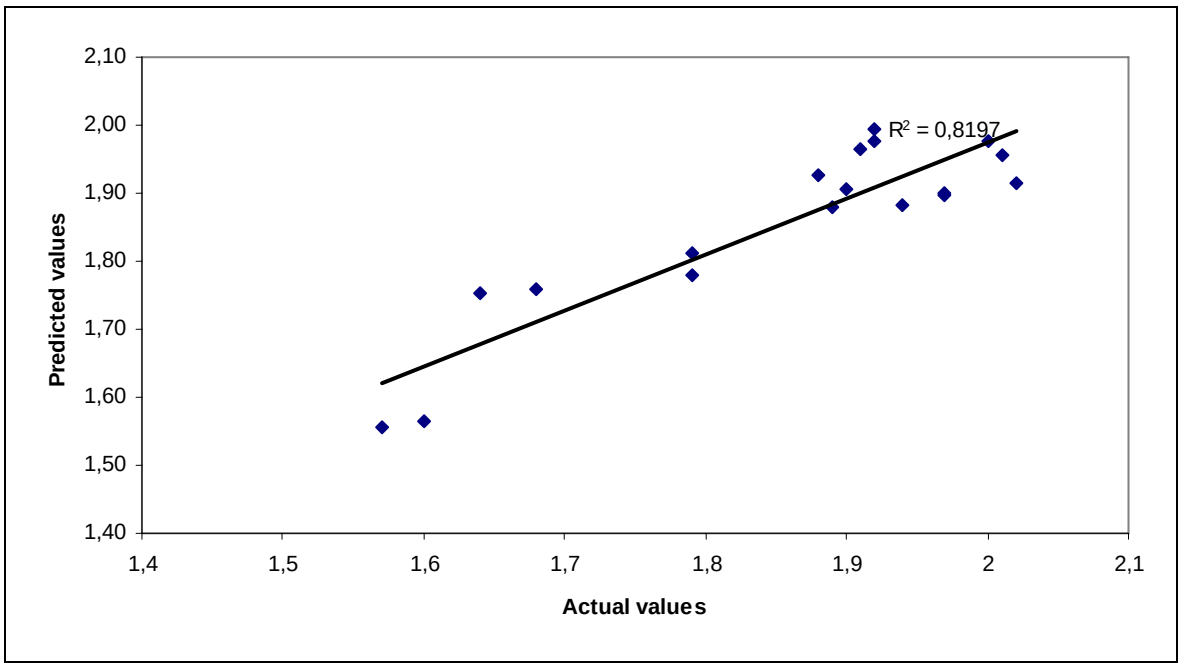

Figure B.2. Predicted vs actual values of specific gravity (SSD) (gr/cm3)

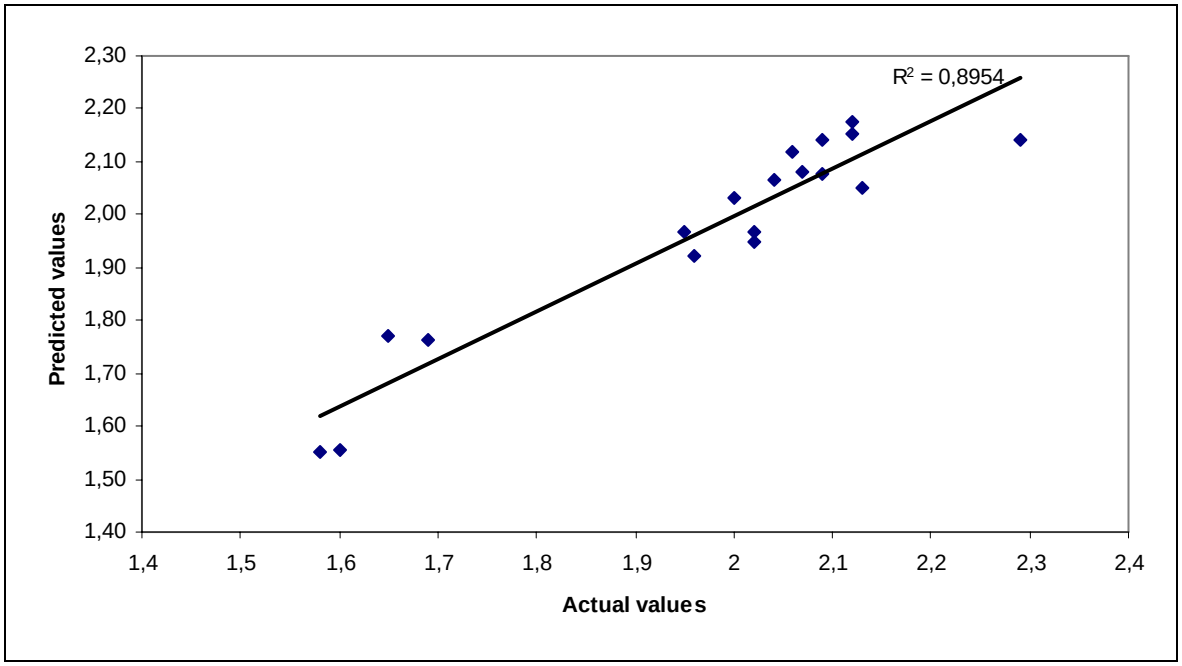

Figure B.3. Predicted vs actual values of apparent specific gravity (gr/cm3)

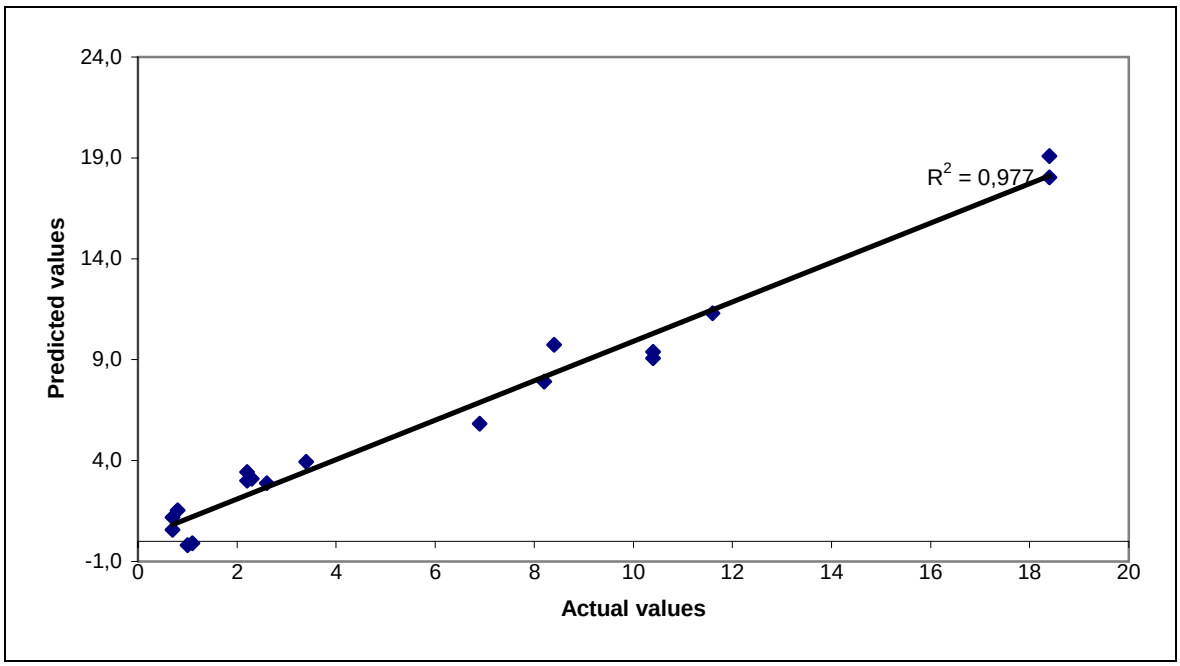

Figure B.4. Predicted vs actual values of water absorption (%)

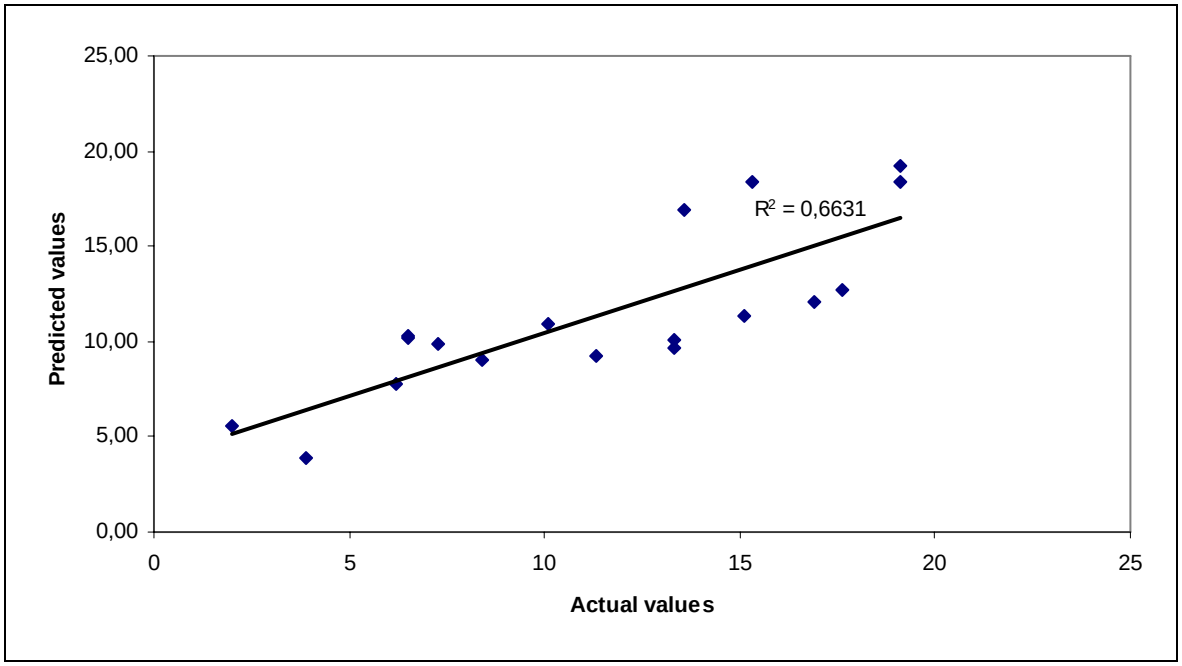

Figure B.5. Predicted vs actual values of porosity (%)

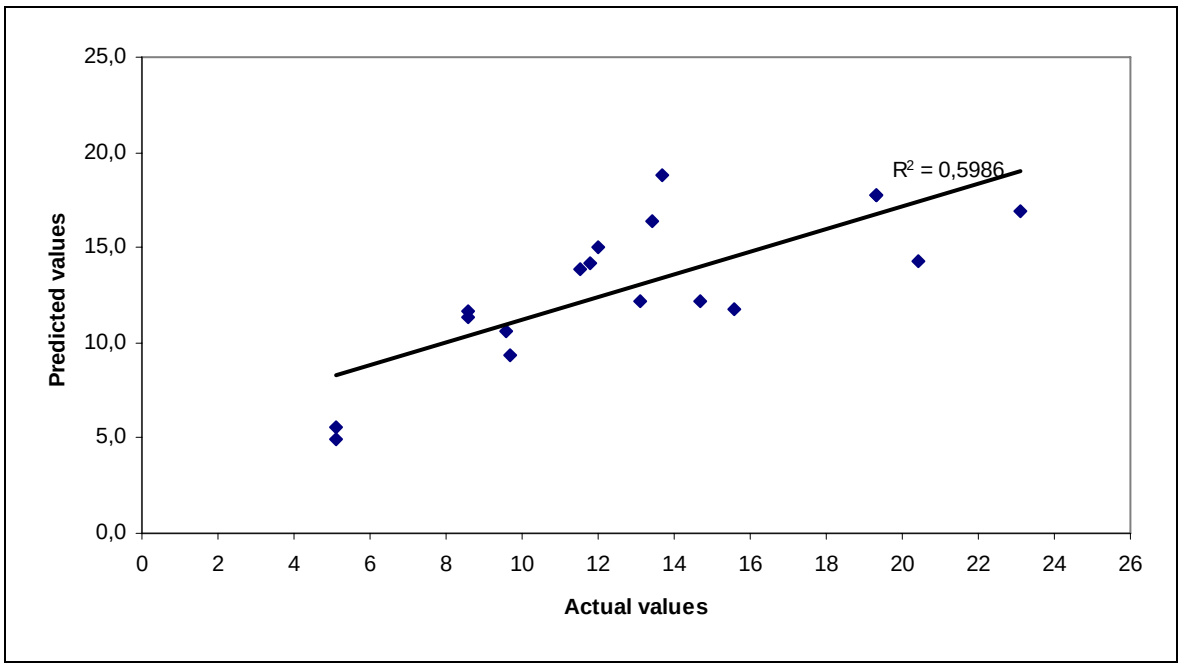

Figure B.6. Predicted vs actual values of crushing strength (MPa)

REFERENCES

1. Bethani, S., "Pyroprocessed Aggregates Comprising IBA and Low Calcium Silicoaluminous Materials And Methods For Producing Such Aggregates", *The Patent Cooperation Treaty*, World Intellectual Property Organization, WO 2006/074945, Geneva, 2006.

2. Biernacki, J. J., A. K. Vazrala and H. W. Leimer, "Sintering of A Class F Fly Ash", *Fuel*, Vol. 87, No. 6, pp. 782-792, May 2008.

3. Erol, M., S. Küçükbayrak and A. Ersoy-Meriçboyu, "Characterization of sintered Coal Fly Ashes", *Fuel*, Vol. 87, No. 7, pp. 1334-1340, June 2008.

4. Ćojbašić, L., G. Stefanović, Ž. Sekulić and S. Heckmann, "Influence Of The Fly Ash Chemical Composition on the Portland Cement and Fly Ash Mixture Hydration Mechanism", *Mechanical Engineering*, Vol. 3, No. 1, pp. 117 – 125, October 2005.

5. Foletto, E. L., C. Volzone and L. M. Porto, "Performance of An Argentinian Acid-Activated Bentonite in the Bleaching of Soybean Oil", *Brazilian Journal of Chemical Engineering*, Vol. 20, No.2, São Paulo, Apr./June 2003.

6. Al-Bahar, S. and V.T.L. Bogahawatta, "Development of Lightweight Aggregates in Kuwait", *The Arabian Journal for Science and Engineering,* Vol. 31, No. 1C, pp. 231-239, June 2006.

7. Verma, C. L., S. K. Handa, S. K. Jain and R. K. Yadav, "Techno-commercial Perspective Study For Sintered Fly Ash Light-weight Aggregates in India" *Construction and Building Materials*, Vol. 12, No. 6-7, pp. 341-346, September 1998.

8. Ramamurthy, K. and K.I. Harikrishnan, "Influence of Binders on Properties of Sintered Fly Ash Aggregate", *Cement and Concrete Composites*, Vol. 28, No. 1, pp. 33-38, January 2006.

9. Ripke, S. J. and S. K. Kawatra, "Can Fly-Ash Extend Bentonite Binder For Iron Ore Agglomeration?", *International Journal of Mineral Processing*, Vol. 60, No. 3-4, pp. 181-198, December 2000.

10. Ansari, F. and A. Maher, "Recycled Materials in Portland Cement Concrete", *Department of Transportation, In cooperation with New Jersey Department of Transportation Division of Research and Technology and U.S. Department of Transportation Federal Highway Administration*, FHWA NJ 2000-03, New Jersey, June 2000.

11. Shayan, A.and A. Xu, "Value-added Utilisation of Waste Glass in Concrete", *Cement and Concrete Research*, Vol. 34, No. 1, pp. 81-89, January 2004.

12. Poon, C. S. and D. Chan, "Effects of Contaminants on the Properties of Concrete Paving Blocks Prepared with Recycled Concrete Aggregates" *Construction and Building Materials*, Vol. 21, No. 1, pp. 164-175, January 2007.

13. Shi, C., Y. Wu, C. Riefler and H. Wang, "Characteristics and Pozzolanic Reactivity of Glass Powders" *Cement and Concrete Research*, Vol. 35, No. 5, pp. 987-993, May 2005.

14. Kayali, O., "Fly Ash Lightweight Aggregates in High Performance Concrete", *Construction and Building Materials*, October 2007.

15. Lo, T. Y. and H. Z. Cui, "Properties of green lightweight aggregate concrete", *International Wokshop on Sustainable Development and Concrete Technology*, Iowa State University/Tsinghua University, Beijing, PRC, pp. 113-118, 20-21 May 2004.

16. ACI Committee 213, *Guide for Structural Lightweight Aggregate Concrete*, ACI 213R-87, 1987.

17. Bremner, T. W. and M. D. A. Thomas, *Learning Module on Traditional and Non Traditional Uses of Coal Combustion Products (CCP)*, http://www.unb.ca/civil/bremner/CIRCA/TextofCourse/TextofCourse.doc.

18. Mun, K. J., "Development and Tests of Lightweight Aggregate Using Sewage Sludge For Nonstructural Concrete", *Construction and Building Materials*, Vol. 21, No. 7, pp. 1583-1588, July 2007.

19. Ramachandran, V.S., "Waste and By-Products as Concrete Aggregates", *Canadian Building Digest CBD-215*, National Research Council Canada, http://irc.nrc-cnrc.gc.ca/pubs/cbd/cbd215_e.html, April 1981.

20. Nabozny, M., J. Nocon, Z. Wozniacki and J. Pasierb, J., " Processing of Residues from Power Generation into Sintered Aggregate: Process Requirements", *Energy Sources*, Vol. 27, pp. 1375-1383, 2005.

21. Cheeseman, C.R. and G.S. Virdi, "Properties and Microstructure of Lightweight Aggregate Produced From Sintered Sewage Sludge Ash" *Resources, Conservation and Recycling*, Vol. 45, No. 1, pp. 18-30, September 2005.

22. Cheeseman, C. R., A. Makinde and S. Bethanis, "Properties of Lightweight Aggregate Produced by Rapid Sintering of Incinerator Bottom Ash", *Resources, Conservation and Recycling*, Vol. 43, No. 2, pp. 147-162, January 2005.

23. Wasserman, R. and A. Bentur, "Effect of Lightweight Fly Ash Aggregate Microstructure on the Strength of Concretes", *Cement and Concrete Research*, Vol. 27, No. 4, pp. 525-537, April 1997.

24. Li-xiong, G., Y. Yan and W. Ling, "Research on Sintered Fly Ash Aggregate of High Strength and Low Absorption of Water", *Proceedings of the International Workshop on Sustainable Development and Concrete Technology*, pp. 151-157, Beijing, May 20–21, 2004.

25. Brite EuRam III, "The Effect of the Moisture History on the Water Absorption of Lightweight Aggregates", *EuroLightCon Economic Design and Construction with Light Weight Aggregate Concrete*, Document BE96-3942/R20, June 2000.

26. Duvarcı, Ö. Ç., Y. Akdeniz, F. Özmıhçı, S. Ülkü, D. Balköse and M. Çiftçioğlu, "Thermal Behaviour of A Zeolitic Tuff", *Ceramics International*, Vol. 33, No. 5, pp. 795-801, July 2007.

27. Huang, S., F. Chang, S. Lo, M. Lee, C. Wang and J. Lin, "Production of Lightweight Aggregates From Mining Residues, Heavy Metal Sludge, and Incinerator Fly Ash", *Journal of Hazardous Materials*, Vol. 144, No. 1-2, pp. 52-58, June 2007.

28. Hung, M. and C. Hwang, "Study of Fine Sediments For Making Lightweight Aggregate", *Waste Manage Res*, Vol. 25, pp. 449–456, 2007.

29. Chiou, I., K. Wang, C. Chen and Y. Lin, "Lightweight Aggregate Made From Sewage Sludge and Incinerated Ash", *Waste Management*, Vol. 26, No. 12, pp. 1453-1461, 2006.

30. Show, K., D. Lee, J. Tay, S. Hong and C. Chien, "Lightweight Aggregates From Industrial Sludge–Marine Clay Mixes", *Journal of Environmental Engineering*, Vol. 131, No. 7, July 2005.

31. Yang, C. C. and R. Huang, "Approximate Strength of Lightweight Aggregate Using Micromechanics Method", *Advanced Cement Based Materials*, Vol. 7, pp. 133–138, 1998.

32. Tangtermsirikul, S. and A. C. Wijeyewickrema, “Strength Evaluation of Aggregate Made From Fly Ash”, *ScienceAsia*, Vol. 26, pp. 237-241, 2000.

33. Mangialardi, T., “Sintering of MSW Fly Ash For Reuse As A Concrete Aggregate”, *Journal of Hazardous Materials*, B87, pp. 225–239, 2001.

34. Wang, K. S., C. J. Sun and C. C. Yeh, “The Thermotreatment of MSW Incinerator Fly Ash For Use As An Aggregate: A Study Of The Characteristics Of Size Fractioning”, *Resources, Conservation and Recycling*, Vol. 35, pp. 177–190, 2002.

35. Tsai, C., K. Wang and I. Chiou, “Effect of Sio_2–Al_2O_3–Flux Ratio Change on the Bloating Characteristics of Lightweight Aggregate Material Produced From Recycled Sewage Sludge”, *Journal of Hazardous Materials*, Vol. 134, No. 1-3, pp. 87-93, June 2006.

36. Aineto, M., A. Acosta, J. M. Rincon and M. Romero, “Production of Lightweight Aggregates From Coal Gasification Fly Ash and Slag”, *World of Coal Ash*, Lexington, Kentucky, 2005.

37. Al-Khaiat, H. and M. N. Haque, “Effect of Initial Curing on Early Strength and Physical Properties of A Lightweight Concrete”, *Cement and Concrete Research*, Vol. 28, No. 6, pp. 859-866, June 1998.

38. Al-Khaiat, H. and N. Haque, “Strength and Durability of Lightweight and Normal Weight Concrete”, *Journal of Materials in Civil Engineering*, Vol. 11, No. 3, pp. 231-235, 1999.

39. Kayali, O., M. N. Haque and B. Zhu, “Some Characteristics of High Strength Fiber Reinforced Lightweight Aggregate Concrete” *Cement and Concrete Composites*, Vol. 25, No. 2, pp. 207-213, February 2003.

40. Kayali, O., M. N. Haque and B. Zhu, "Drying Shrinkage of Fibre-Reinforced Lightweight Aggregate Concrete Containing Fly Ash", *Cement and Concrete Research*, Vol. 29, No. 11, pp. 1835-1840, November 1999.

41. Zhou, F. P., R. V. Balendran and A. P. Jeary, "Size Effect on Flexural, Splitting Tensile, and Torsional Strengths of High-Strength Concrete", *Cement and Concrete Research*, Vol. 28, No. 12, pp. 1725-1736, December 1998.

42. Chiaia, B., J. G. M. van Mier and A. Vervuurt, "Crack Growth Mechanisms in Four Different Concretes: Microscopic Observations and Fractal Analysis", *Cement and Concrete Research*, Vol. 28, No. 1, pp. 103-114, 1998.

43. Yun, B., I. Ratiyah and P. A. M. Basheer, "Properties of Lightweight Concrete Manufactured with Fly Ash, Furnace Bottom Ash, and Lytag", *International Wokshop on Sustainable Development and Concrete Technology*, Beijing, pp. 77 88, May 2004.

44. Wang, H.Y. and K.C. Tsai, "Engineering Properties of Lightweight Aggregate Concrete Made From Dredged Silt", *Cement and Concrete Composites*, Vol. 28, No. 5, pp. 481-485, May 2006.

45. Brite EuRam III, "A Rational Mix Design Method for Lightweight Aggregate Concrete Using Typical UK Materials", *EuroLightCon Economic Design and Construction with Light Weight Aggregate Concrete*, Document BE96-3942/R5, January 2000.

46. Behera, J. P., B. D. Nayak, H. S. Ray and B. Sarangi, "Light Weight Concrete with Sintered Flyash Aggregate : A Study on Partial Replacement to Normal Granite Aggregate", *IE (I) Journal*, Vol. 85, pp. 84-87, August 2004.

47. Chi, J. M, R. Huang, C. C. Yang and J. J. Chang, "Effect of Aggregate Properties on the Strength and Stiffness of Lightweight Concrete", *Cement and Concrete Composites*, Vol. 25, No. 2, pp. 197-205, February 2003.

48. Döven, A. G., *Lightweight Fly Ash Aggregate Production Using Cold Bonding Agglomeration Process*, Ph.D. Thesis, Boğaziçi University, 1998.

49. Gesoğlu, M., *Effects of Lightweight Aggregate Properties on Mechanical, Fracture, and Physical Behavior of Lightweight Concretes*, Ph.D. Thesis, Boğaziçi University, 2004.

50. Faust, T. and G. König, "High Strength Lightweight Aggregate Concrete", *2nd International PhD Symposium in Civil Engineering*, pp. 1-8, Budapest, 1998.

51. Kayali, O. and B. Zhu, "Chloride Induced Reinforcement Corrosion in Lightweight Aggregate High-Strength Fly Ash Concrete", *Construction and Building Materials*, Vol. 19, No. 4, pp. 327-336, May 2005.

52. Chia, K. S. and M. Zhang, "Water Permeability and Chloride Penetrability of High-Strength Lightweight Aggregate Concrete", *Cement and Concrete Research*, Vol. 32, No. 4, pp. 639-645,April 2002.

53. Bethani, S., "Pyroprocessed Aggregates Comprising IBA and PFA and Methods for Producing Such Aggregates", *The Patent Cooperation Treaty*, World Intellectual Property Organization, WO 2006/074944, Geneva, 2006.

54. Manikandan, R. and K. Ramamurthy, "Influence of Fineness of Fly Ash on the Aggregate Pelletization Process", *Cement and Concrete Composites*, Vol. 29, No. 6, pp. 456-464,July 2007.

55. Baykal, G. and A. G. Döven, "Utilization of Fly Ash by Pelletization Process; Theory, Application Areas and Research Results", *Resources, Conservation and Recycling*, Vol. 30, No. 1, pp. 59-77, July 2000.

56. Harikrishnan, K.I. and K. Ramamurthy, "Influence of Pelletization Process on the Properties of Fly Ash Aggregates", *Waste Management*, Vol. 26, No. 8, pp. 846-852, 2006.

57. Kingery, W. D., "Sintering from Prehistoric Times to the Present", *Proceedings of the Fifth International Symposium on the Science and Technology of Sintering*, Vol. 25-26, pp. 1-10, Vancouver, 1992.

58. Upadhyaya, G. S., *Sintered Metallic and Ceramic Materials*, John Wiley and Sons, England, 2000.

59. Kang, S. L., *Sintering Densification, Grain Growth and Microstructure*, Elsevier, 2005.

60. Mackenzıe, J. K. and R. Shuttleworth, "A Phenomenological Theory of Sintering", *Proc. Phys. Soc. LXII*, pp. 833-852, 1949.

61. German, R. M., *Sintering Theory and Practice*, John Wiley and Sons, New York, 1996.

62. Upadhyaya, G. S., *Powder Metallurgy Technology*, Cambridge International Science Publishing, England, 2002.

63. Li, Y., D. Wu, J. Zhang, L. Chang, D. Wu, Z. Fang and Y. Shi, "Measurement and Statistics of Single Pellet Mechanical Strength of Differently Shaped Catalysts", *Powder Technology*, Vol. 113, No. 1-2, pp. 176-184, November 2000.

64. Yashima, S., Y. Kanda, S. Sano, "Relationship between Particle Size and Fracture Energy or Impact Velocity Required to Fracture as Estimated from Single Particle Crushing", *Powder Technology*, Vol. 51, No. 3, pp. 277–282, 1987.

65. Diamond, S., "Mercury Porosimetry: An Inappropriate Method for the Measurement of Pore Size Distributions in Cement-Based Materials", *Cement and Concrete Research*, Vol. 30, No. 10, pp. 1517-1525, October 2000.

66. Moon, H. Y., H. S. Kim and D. S. Choi, "Relationship between Average Pore Diameter and Chloride Diffusivity in Various Concretes", *Construction and Building Materials*, Vol. 20, No. 9, pp. 725-732, November 2006.

67. Yang, C.C., "On the Relationship between Pore Structure and Chloride Diffusivity from Accelerated Chloride Migration Test in Cement-Based Materials", *Cement and Concrete Research*, Vol. 36, No. 7, pp. 1304-1311, July 2006.

68. Xue, Y., S. Wu, H. Hou and J. Zha, "Experimental Investigation of Basic Oxygen Furnace Slag Used as Aggregate in Asphalt Mixture", *Journal of Hazardous Materials*, Vol. 138, No. 2, pp. 261-268, November 2006.

69. Lu C. and H. C. Jong, "Sımplified Model for the Water Permeability of Porous OPC Mortar", *Journal of The Institution of Engineers, Singapore*, Vol. 44, No. 1, pp. 11-19, 2004.

70. Brow, R. K., *DTA/Crystallization*, http://web.mst.edu/~brow/ws2004_cer122_dta.pdf, 2003.

71. WHD Microanalysis Consultants, *Concrete Examination by SEM*, http://www.whd.co.uk/Concrete/concretebysem.html, 2007.

72. Ward, C. R. and D. French, "Relation between Coal and Fly Ash Mineralogy, Based on Quantitavive X-Ray Diffraction Methods", pp. 1-14.

73. Ward, C. R. and D. French, "Determination of Glass Content and Estimation of Glass Composition in Fly Ash Using Quantitative X-Ray Diffractometry", *Fuel*, Vol. 85, pp. 2268–2277, 2006.

74. Muthukumar, M., D. Mohan and M. Rajendran, "Optimization of Mix Proportions of Mineral Aggregates Using Box Behnken Design of Experiments", *Cement & Concrete Composites*, Vol. 25, pp. 751–758, 2003.

75. Benyounis, K.Y., A.G. Olabi and M.S.J. Hashmi, "Multi-Response Optimization of CO_2 Laser-Welding Process of Austenitic Stainless Steel" ,*Optics & Laser Technology*, Vol. 40, pp. 76–87, 2008.

76. Çelik, B., *Recycled Aggregate Concrete at Elevated Temperatures*, Ph.D. Thesis, Boğaziçi University, 2007.

77. Liyana-Pathirana, C. and F. Shahidi, "Optimization of Extraction of Phenolic Compounds from Wheat Using Response Surface Methodology", *Food Chemistry*, Vol. 93, pp. 47–56, 2005.

78. Benyounis, K.Y., A.G. Olabi and M.S.J. Hashmi, "Optimizing the Laser-Welded Butt Joints of Medium Carbon Steel Using RSM", *Journal of Materials Processing Technology*, Vol. 164–165, pp. 986–989, 2005.

79. Jo, B., S. Park and J. Park, "Properties of Concrete Made with Alkali-Activated Fly Ash Lightweight Aggregate (AFLA)", *Cement & Concrete Composites*, Vol. 29, pp. 128–135, 2007.

80. Lo, T.Y., H.Z. Cui and Z.G. Li, "Influence of Aggregate Pre-Wetting and Fly Ash on Mechanical Properties of Lightweight Concrete", *Waste Management*, Vol. 24, pp. 333–338, 2004.

81. Zaharieva, R., F. Buyle-Bodin, F. Skoczylas and E. Wirquin, "Assessment of the Surface Permeation Properties of Recycled Aggregate Concrete", *Cement & Concrete Composites*, Vol. 25, pp. 223–232, 2003.

82. Rossignolo, J. A. and M. V. C. Agnesini, "Durability of Polymer-Modified Lightweight Aggregate Concrete", *Cement & Concrete Composites*, Vol. 26, pp. 375–380, 2004.

83. Diamond, S. and J. Huang, "The ITZ in Concrete-A Different View Based on Image Analysis and SEM Observations", *Cement and Concrete Composites*, Vol. 23, pp. 179-188, 2001.

84. Diamond, S., "Considerations in Image Analysis as Applied to Investigations of the ITZ in Concrete", *Cement and Concrete Composites*, Vol. 23, pp. 171-178, 2001.

85. Liao, K., P. Chang, Y. Penga and C. Yang, "A Study on Characteristics of Interfacial Transition Zone in Concrete", *Cement and Concrete Research*, Vol. 34, pp. 977–989, 2004.

86. Kayali, O., "Flashag-New Lightweight Aggregate for High Strength and Durable Concrete", *World of Coal Ash*, Lexington, Kentucky, 2005.

87. Aineto, M., A. Acosta, J. M. Rincon and M. Romero, "Thermal Expansion of Slag and Fly Ash from Coal Gasification in IGCC Power Plant", *Fuel*, Vol. 85, pp. 2352–2358, 2006.

88. Adell, V., C.R. Cheeseman, M. Ferraris, M. Salvo, F. Smeacetto and A.R. Boccaccini, "Characterising the Sintering Behaviour of Pulverised Fuel Ash Using Heating Stage Microscopy", *Materials Characterization*, Vol. 58, No. 10, pp. 980-988, October 2007.

89. Adell, V., C.R. Cheeseman, A. Doel, A. Beattie and A.R. Boccaccini, "Comparison of Rapid and Slow Sintered Pulverised Fuel Ash", *Fuel*, Vol. 87, pp. 187–195, 2008.

90. Styszko-Grochowiak, K., J. Golas, H. Jankowski and S. Kozinski, "Characterization of the Coal Fly Ash for the Purpose of Improvement of Industrial On-Line Measurement of Unburned Carbon Content", *Fuel*, Vol. 83, pp. 1847–1853, 2004.

91. Furlani, E., S. Bruckner, D. Minichelli and S. Maschio, "Synthesis and Characterization of Ceramics from Coal Fly Ash and Incinerated Paper Mill Sludge", *Ceramics International*, 2007.

92. Dong, Y., X. Feng, X. Feng, Y. Ding, X. Liu and G. Meng, "Preparation of Low-Cost Mullite Ceramics from Natural Bauxite and Industrial Waste Fly Ash", *Journal of Alloys and Compounds*, 2007.

93. Zhang, S. and M. Zhang, "Hydration of Cement and Pore Structure of Concrete Cured in Tropical Environment", *Cement and Concrete Research*, Vol. 36, pp. 1947– 1953, 2006.

94. Cui, L. and J. H. Cahyadi, "Permeability and Pore Structure of OPC Paste", *Cement and Concrete Research*, Vol. 31, pp. 277-282, 2001.

95. Ilica, M., C. Cheeseman, C. Sollars and J. Knight, "Mineralogy and Microstructure of Sintered Lignite Coal Fly Ash", *Fuel*, Vol. 82, pp. 331–336, 2003.

96. Riley, C. M., "Relation of Chemical Properties to the Bloating of Clays" *J. Am. Ceram. Soc.*, Vol. 34, No.4, pp. 121–128, 1951.

97. Li, R., L. Wang, T. Yang and B. Raninger, "Investigation of MSWI Fly Ash Melting Characteristic by DSC–DTA", *Waste Management*, Vol. 27, pp. 1383–1392, 2007.

98. Öveçoğlu, M. L., B. Kuban and H. Özer, "Characterization and Crystallization Kinetics of a Diopside-Based Glass-Ceramic Developed from Glass Industry Raw Materials", *Journal of the European Ceramic Society*, Vol. 17, pp. 957-962, 1997.

99. Jozic, D. and J. Zelic, "The Effect of Fly Ash on Cement Hydration in Aqueous Suspensions", *Ceramics − Silikáty*, Vol. 50, No. 2, pp. 98-105, 2006.

100. Onal, M., Y. Sarıkaya, T. Alemdaroğlu and İ. Bozdoğan, "The Effect of Acid Activation on Some Physicochemical Properties of a Bentonite", *Turk J Chem*, Vol. 26, pp. 409-416, 2002.

101. Cheng, T.W. and Y.S. Chen, "On Formation of $CaO–Al_2O_3–SiO_2$ Glass–Ceramics by Vitrification of Incinerator Fly Ash", *Chemosphere*, Vol. 51, pp. 817–824, 2003.

102. Cheng, T.W. and Y.S. Chen, "Characterisation of Glass Ceramics Made from Incinerator Fly Ash", *Ceramics International*, Vol. 30, pp. 343–349, 2004.

103. Karamanova, A., M. Pelinoa, M. Salvob and I. Metekovits, "Sintered Glass-Ceramics from Incinerator Fly Ashes. Part II. The Influence of the Particle Size and Heat-Treatment on the Properties", *Journal of the European Ceramic Society*, Vol. 23, pp. 1609–1615, 2003.

104. De Casa, G., T. Mangialardi, A.E. Paolini and L. Piga, "Physical-mechanical and Environmental Properties of Sintered Municipal Incinerator Fly Ash", *Waste Management*, Vol. 27, pp. 238–247, 2007.

105. http://www.hca.com/pages/english/glossar.html

106. Khoury, N. N., M. Zaman and J. G. Laguros, "Use of XRD Patterns to Evaluate Compressive Strength of Stabilized Aggregates", *JCPDS - International Centre for Diffraction Data 2004, Advances in X-ray Analysis*, Vol. 47, pp. 379 384, 2004.

107. Wey, M., K.Liu, T. Tsai and J. Chou, "Thermal Treatment of the Fly Ash from Municipal Solid Waste Incinerator with Rotary Kiln", *Journal of Hazardous Materials*, Vol. B137, pp. 981–989, 2006.

108. Karamberi, A. and A. Moutsatsou, "Participation of Coloured Glass Cullet in Cementitious Materials", *Cement & Concrete Composites*, Vol. 27, pp. 319–327, 2005.

109. Nakamura, Y. K., T. N. Murakami, N. Y. Iwata, Y. Hirano, Y. Tokuoka and N. Kawashima, "Preparation of Porous Diopside Microspheres from Spherical Silica Gels Impregnated with $Ca(NO_3)_2$ and $MgCl_2$", *Journal of the Ceramic Society of Japan*, Vol. 112, No. 3, pp. 133-137, 2004.

110. Cheng, T.W., "Effect of Additional Materials on the Properties of Glass-Ceramic Produced from Incinerator Fly Ashes", *Chemosphere*, Vol. 56, pp. 127–131, 2004.

111. Monkman, S.and Y. Shao, "Assessing the Carbonation Behavior of Cementitious Materials", *Journal of Materials in Civil Engineering*, Vol. 18, No. 6, pp. 768-776, December 1, 2006.

112. Antiohos, S.K. and S. Tsimas, "A Novel Way to Upgrade the Coarse Part of A High Calcium Fly Ash for Reuse into Cement Systems", *Waste Management*, Vol. 27, pp. 675–683, 2007.

113. Walenta, G. and T. Füllmann, "Advances in Quantitative XRD Analysis for Clinker, Cements, and Cementitious Additions", *JCPDS - International Centre for Diffraction Data 2004, Advances in X-ray Analysis*, Vol. 47, pp. 287-296, 2004.

114. Ubbriaco, P. and D. Calabrese, "Solidification and Stabilization of Cement Paste Containing Fly Ash from Municipal Solid Waste", *Thermochimica Acta*, Vol. 321, pp. 143-150, 1998.

115. Sanjiv K. D., L. Young and P. Storer, "Automatic Control of Cement Quality Using On-Line XRD", *IEEE*, pp. 289-305, 2006.

116. Mannan, S., A. Fakhru'l-Razi, M. Z. Alam, "Optimization of Process Parameters for The Bioconversion of Activated Sludge by *Penicillium Corylophilum,* Using Response Surface Methodology", *Journal of Environmental Sciences*, Vol. 19, pp. 23-28, 2007.

117. Azargohar, R. and A.K. Dalai, "Production of Activated Carbon from Luscar Char: Experimental and Modeling Studies", *Microporous and Mesoporous Materials*, Vol. 85, pp. 219–225, 2005.

118. Hossain, K. M. A., "Properties of Volcanic Pumice Based Cement and Lightweight Concrete", *Cement and Concrete Research*, Vol. 34, pp. 283–291, 2004.

119. Weber, S., *Curing of High Strength Concrete Using Light-weight Aggregates*, www.iwb.uni-stuttgart.de/bibliothek/festschr/weber.pdf, pp. 377-391.

120. Nemes, R. and Z. Józsa, "Strength of Lightweight Glass Aggregate Concrete", *Journal of Materials in Civil Engineering*, Vol. 18, No. 5, pp. 710-714, October 1, 2006.

121. Lijiu, W., Z. Shuzhong and Z. Guofan, "Investigation of the Mix Ratio Design of Lightweight Aggregate Concrete", *Cement and Concrete Research*, Vol. 35, pp. 931–935, 2005.

122. Lo, T.Y., H.Z. Cui and Z.G. Li, "Influence of Aggregate Pre-wetting and Fly Ash on Mechanical Properties of Lightweight Concrete", *Waste Management*, Vol. 24, pp. 333–338, 2004.

123. ACI Committee 213, *Guide for Structural Lightweight Aggregate Concrete*, ACI 213R-03, 2003.

124. Nassif, H., "Development of High-Performance Concrete for Transportation Structures in New Jersey", *Department of Transportation, In cooperation with New Jersey Department of Transportation Division of Research and Technology and U.S. Department of Transportation Federal Highway Administration*, FHWA NJ 2003-016, New Jersey, August 2003.

125. Khan, M.I. and C.J. Lynsdale, "Strength, Permeability, and Carbonation of High-Performance Concrete", *Cement and Concrete Research*, Vol. 32, pp. 123–131, 2002.

126. Oh, B. H., S. W. Cha, B. S. Jang and S. Y. Jang, "Development of High-Performance Concrete Having High Resistance to Chloride Penetration", *Nuclear Engineering and Design*, Vol. 212, pp. 221–231, 2002.

127. Tsivilis, S., J. Tsantilas, G. Kakali, E. Chaniotakis and A. Sakellariou, "The Permeability of Portland Limestone Cement Concrete", *Cement and Concrete Research*, Vol. 33, pp. 1465–1471, 2003.

128. Al-Zahrani, M.M., S.U. Al-Dulaijan, M. Ibrahim, H. Saricimen and F.M. Sharif, "Effect of Waterproofing Coatings on Steel Reinforcement Corrosion and Physical Properties of Concrete", *Cement & Concrete Composites*, Vol. 24, pp. 127–137, 2002.

129. Ahna, W. and D.V. Reddy, "Galvanostatic Testing for the Durability of Marine Concrete under Fatigue Loading", *Cement and Concrete Research*, Vol. 31, pp. 343-349, 2001.

130. Bakharev, T., J. G. Sanjayana and Y. B. Cheng, "Resistance of Alkali-Activated Slag Concrete to Acid Attack", *Cement and Concrete Research*, Vol. 33, pp. 1607–1611, 2003.

131. Bakharev, T., J.G. Sanjayana and Y.-B. Cheng, "Sulfate Attack on Alkali-Activated Slag Concrete", *Cement and Concrete Research*, Vol. 32, pp. 211–216, 2002.

132. Rossignolo, J. A. and M.V. C. Agnesini, "Mechanical Properties of Polymer-Modified Lightweight Aggregate Concrete", *Cement and Concrete Research*, Vol. 32, pp. 329–334, 2002.

133. Toutanji, H., N. Delatte, S. Aggoun, R. Duval and A. Danson, "Effect of Supplementary Cementitious Materials on The Compressive Strength and Durability of Short-Term Cured Concrete", *Cement and Concrete Research*, Vol. 34, pp. 311–319, 2004.

134. Gao, X.F., Y. T. Lo and C. M. Tam, "Investigation of Micro-Cracks and Microstructure of High Performance Lightweight Aggregate Concrete", *Building and Environment*, Vol. 37, pp. 485 – 489, 2002.

135. Jacobsen, S., "Calculating Liquid Transport into High-Performance Concrete During Wet Freeze/Thaw", *Cement and Concrete Research*, Vol. 35, pp. 213–219, 2005.

136. Shi, C. and Y. Wu, "Mixture Proportioning and Properties of Self-Consolidating Lightweight Concrete Containing Glass Powder", *ACI Materials Journal*, Vol. 102, No. 5, pp. 355-363, September-October 2005.

137. Rossignolo, J. A., "Effect of Silica Fume and SBR Latex on the Paste-aggregate Interfacial Transition Zone", *Materials Research*, Vol. 10, No. 1, pp. 83-86, 2007.

138. Roy, D. M., M. W. Grutzeck, D. Shi and G. Lui, *Cement Paste Aggregate Interface Microstructure*, Strategic Highway Research Program, National Research Council, Washington, DC 1993.